Effect of thermal fluctuations on the binding properties of biological membranes

Der Einfluss von thermischen Fluktuationen auf die Bindungseigenschaften biologischer Membranen

Der
Naturwissenschaftlichen Fakultät
der
Friedrich-Alexander-Universität Erlangen-Nürnberg

---

zur
Erlangung des Doktorgrades Dr. rer. nat.

vorgelegt von
Daniel Thomas Schmidt
aus
Stuttgart, Deutschland

Als Dissertation genehmigt
von der naturwissenschaftlichen Fakultät
der Friedrich-Alexander-Universität Erlangen-Nürnberg

Tag der mündlichen Prüfung:	XX.XX.2016
Vorsitzender des Promotionsorgans:	Prof. Dr. Jörn Wilms
Gutachter	Prof. Dr. Ana-Sunčana Smith
	Prof. Dr.

Contents

Acknowledgements

An dieser Stelle möchte ich mich bei allen bedanken, die zum Gelingen dieser Doktorarbeit beigetragen haben. Besonders bedanken möchte ich mich bei

- Prof. Dr. Ana-Sunčana Smith für die exzellente Betreuung in den mittlerweile mehr als sechs Jahren intensiven Zusammenarbeit. In meinem Wachstumsprozess von der Studentischen Hilfskraft zum Diplomanden und dann Doktoranden fühlte ich mich immer in den besten Händen, stets motivierend zu neuen Bestleistungen und die Grenzen der Wissenschaft ein wenig zu erweitern. Durch die geschäftige Art der Arbeit und der Einbindung von Familie in den Beruf habe ich nicht nur auf wissenschaftlicher Ebene sehr viel gelernt, sondern auch die persönliche Hingabe zum Beruf erfahren.

- Prof. Dr. Udo Seifert für die Einführung in die Theoretische Physik beginnend mit der ersten Kursvorlesung "Klassische Mechanik" bis zur vollendeten Ausbildung zum promovierten Physikjünger. Ich glaube, dass ich erst hier am II. Institut für Theoretische Physik an der Uni Stuttgart, das ist mir in den vielen Jahren eine zweite Heimat geworden ist, klares analytisches und allumfassendes Denken gelernt habe.

- Dr. Timo Bihr für die jahrelange, gemeinsame und erfolgreiche Arbeit an der Modellierung von Membranadhäsion und die täglichen Gespräche und Diskussionen über so ziemlich jedes Thema.

- unseren experimentellen Kollegen Prof. Dr. Rudolf Merkel, Dr. Kheya Sengupta, Dr. Susanne Fenz und Dr. Cornelia Monzel für die

langjährige, erfolgreiche und intensive Zusammenarbeit. Im Laufe der Zeit habe ich gelernt, dass regelmäßig von experimentellen Messwerten auf den Boden der Tatsachen geholt zu werden, durchaus Freude bereiten kann. Auch wenn das Auswerten und Interpretieren von Messwerten und mit der Theorie in Einklang bringen mir so manches Haar gekostet hat.

- der gesamten Erlanger Crew, bestehend aus Zlatko Brkljača, Mislav Cvitković, Sara Kaliman, Zoran Miličević, Jayant Pande, Damir Vurnek, Robert Stepić, Robert Blackwell, Matthias Späth, Henning Stumpf, Simone Gehrer, David Jung und Oleg Trosman, für eine stets freundliche Aufnahme in den Erlanger Büros. So mancher Abend wurde erst durch euch spannend, lustig, unterhaltsam, etc.

- den Stuttgarter Kollegen. Namentlich handelt es sich um Dr. Punyabrata Pradhan, Dr. Andre Barato, Dr. Benedikt Sabaß, Dr. Boris Lander, Dr. David Abreu, Dr. Timo Bihr, Dr. Eva Zimmermann, Dr. Eckhard Dieterich, Dr. Kay Brandner, David Hartich, Michael Bauer, Patrick Pietzonka, Robert Wulfert, Sebastian Goldt, Jan Reinke, Matthias Uhl, Boris Bonev und noch einige mehr. Ich war nun fast 6 Jahre beinahe täglich am II. Institut für Theoretische Physik, und das Wohlbefinden steht und fällt mit den Kollegen im direkten Umfeld. Ich konnte mich nie beklagen, auch wenn so manche Kaffee-Mittagsrunde in erbitterten Diskussionen über so wichtige Themen wie z.B. die theoretische Höchstgeschwindigkeit eines Fahrrads (Lösung: halbe Lichtgeschwindigkeit in einer halbphysikalischen Rechnung), geendet ist.

- den Studenten Matthias Uhl, Boris Bonev, Matthias Späth und Henning Stumpf, die ich in ihren Bachelor- oder Masterarbeiten betreuen durfte. Ich konnte sehr viel durch unsere Diskussionen lernen. Vielen Dank für euren Einsatz (z.T. bis zum physisch machbaren) und die vielen lustigen Gespräche.

- Anja Steinhauser für die Einführung in die große und weite Welt der universitären Verwaltung. So manche Verwaltungsabläufe sind mir noch immer ein Rätsel. Doch wann immer wir gemeinsam versuchten ein Problem zu verstehen, lernte ich mehr und mehr, dass zum erfolgreichen wissenschaftlichen Arbeiten die ganzen administrativen Kleinigkeiten notwendige Voraussetzung sind. Außerdem möchte ich mich für Ihr stets offenes Ohr bei Problemen und Fragen jeder Art herzlichst bedanken.

- Waltraud Meineke, Ira Röllinghoff und Dragana Vurnek für die Hilfe bei allen Problemen bezüglich der Uni Erlangen und meinen vielen Dienstreisen von und nach Erlangen. Allein die Buchungsanfragen bei diversen Hotels in Erlangen ersparten mir bestimmt mehrere Stunden Arbeit.

- meinen Vereinskameraden des Yom Chi Kwan Taekwon-Do Ditzingen e.V. und des TSV Schmiden Abteilung Taekwon-Do, sowie in den letzten Wochen meiner Promotionszeit auch der Taekwon-Do Academy in Fürth für die Möglichkeit eines beinahe täglichen Trainings. So manche gedankliche Blockaden konnte ich durch ein anstrengedes und schweißtreibendes Training lösen.

- meinen Vorstandskollegen in den genannten Vereinen, sowie im ITF-D Landesverband Baden-Württemberg und dem nationalen Verband ITF-D für eine langjährige erfolgreiche Zusammenarbeit. Die alltäglichen Probleme und Aufgaben des Vereins- und Verbandslebens haben mir gezeigt, dass es auch noch andere Probleme im Leben gibt als die Probleme der Theoretischen Physik.
  Taekwon!

- meinen Eltern und Geschwistern, die mich immer in meinem Physikstudium unterstützt haben.

Part I

Summary

1 Summary

Cells connect to other cells with the help of highly specific membrane-anchored adhesion proteins. This adhesion process is typically regulated by the complex biochemical network of the cell. However, on the molecular level, thermal fluctuations dominate every motion of the proteins, the cell membrane and the surrounding water. These thermal fluctuations and their influence on the adhesion process between two adjacent cell membranes are the core of this thesis.

The work presented in this thesis is based on a wide range of methods, from minimal theoretical models for adhesion proteins to simulations of the growth of large adhesion domains involving thousands of adhesion proteins and to contributions to a novel experimental method for detecting membrane fluctuations with an unprecedented combination of temporal and spatial resolution. Most of the work combines different methods of the three pillars of empirical science - experiment, theory, and simulations. For a graphical illustration of the methods used in the papers that were submitted to or published in distinguished peer-reviewed scientific journals see Fig. I.1.1. In the following, I sketch briefly the work of this thesis that resulted in eight publications.

Measuring the membrane shape and fluctuations requires experimental techniques that are inherently associated with finite resolution limits in space and time such that the fluctuations measured in the experiment are not identical to the true membrane fluctuations. By convoluting the true membrane fluctuations with the appropriate spatial and temporal resolution functions, I calculated the apparent membrane fluctuations for two different experimental techniques, reflection interference contrast microscope (RICM) and a novel technique called dynamical optical displacement spectroscopy (DODS) (see publications P1 - P3). I found that the

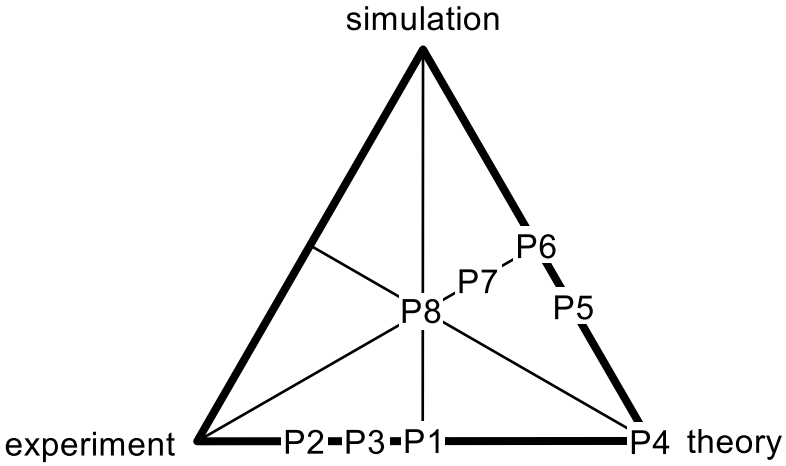

Figure I.1.1: Graphical classification of the publications presented in part "III Publications" of this thesis with respect to the method.

temporal resolution limits in RICM reduce the measured membrane fluctuations by a factor of about five compared to the true fluctuations (Fig. 6 in publication P1 and Fig. 3 in publication P3). In contrast, the excellent temporal resolution in the novel technique DODS renders the measured fluctuations close to the true fluctuations (Fig. 3 in publication P3). Additional to resolution limits of the experimental technique, each camera based technique is sensitive to the shot noise of the camera. In RICM, the shot noise is an important factor to deconvolve the true fluctuations from measured ones (see publication P1). All in all, my contributions to experimental analysis established, finally, a clear path from measured to true fluctuations and further to membrane parameters in theoretical model systems.

Vesicles approaching a substrate establish a non-specific interaction that is modelled by a interaction potential for the membrane. Typically, and especially in the presence of a flat substrate, the interaction potential is approximated by a harmonic potential. As long as the system stays in non-specific adhesion and only moderate fluctuations exist, the harmonic interaction potential is sufficient. However, for the transition from non-specific to specific adhesion, the membrane leaves the minimum of the interaction potential and the harmonic approximation fails. For an experimentally designed geometry of specific and non-specific adhesion, I calculated the membrane shape and fluctuation maps for a harmonic and a simple non-harmonic interaction potential (see publication P1). While I was able to stress the importance of the general form of the interaction potential being non-harmonic when it comes to transitions from non-specific

to specific adhesion, the precise form of the non-harmonic interaction potential is still to be determined.

For specific adhesion, I analysed the equilibrium and the kinetics of adhesion domains. First, for an infinite adhesion domain, where the bonds are placed on a regular lattice, I found a new bond configuration that is meta-stable due to a combination of membrane transmitted correlations between the bonds (see publication P4). Discussing the domain stability of smaller and smaller domains leads ultimately to a discussion of the stability of a single bond. I showed theoretically that the main parameter determining bond stability, i.e., binding affinity, for an adhesion protein in solution is different from the binding affinity of the same adhesion protein if bound to a membrane due to energetic and entropic contributions from the membrane upon binding (see publications P4 and P6). The mutual interplay between the adhesion protein and the membrane affects not only the bond stability but static and dynamic membrane mechanics, too. While the static membrane mechanics are well known, I contributed to the description of membrane dynamics with a phenomenological first order correction to the membrane's damping coefficients (see publication P5). With the dynamics of the bound membrane, temporal correlations of a stochastically bound membrane can be addressed and for which I predict some non-trivial effects in both, the membrane fluctuations and the temporal correlations (see publication P6). Moreover, with full knowledge of the binding affinity, the binding kinetics of a single bond can be constructed in a thermodynamically consistent manner, which I applied for three different levels of coarse-graining from microscopic reaction rates of the individual bond to effective reaction rates that include the binding configurations of nearby adhesion proteins (see publication P6). In the last step, a finite adhesion domain can be constructed from its building blocks. I contributed in particular to two questions: (i) how can ring-like structured adhesion domains form in a non-regulated reaction-diffusion system of adhesion proteins and (ii) what role plays the membrane in formation of adhesion domains. Concerning the first question, I found in a simulation study that bulky adhesion proteins and a circular contact zone being a subset of the protein reservoir is sufficient to form stable ring-like adhesion domains (see publication P7). If the proteins are small and crowding plays no role, the ring is only transient and finally the full contact zone is covered by the domain. In a reaction-diffusion system, the growth of the transient ring is theoretically described and in full agreement with the simulations results. To the second question concerning finite adhesion domains, I contributed to the theoretical description that showed that slight changes in the mean membrane height or the fluctuation amplitude by few

nanometers have tremendous impact on the domain growth types and kinetics. Moreover, experiments with model membranes showed that the membrane acts possibly as a matchmaker for the cell adhesion process (see publication P8).

In summary, this thesis provides comprehensive insights into the physics of the cell adhesion process and how the omnipresent thermal environment of the cell influences the equilibrium and kinetics of adhesion.

2 Zusammenfassung

Biologische Zellen bilden stabile Kontakte mit anderen Zellen mittels hochspezifischer, membrangebundener Adhäsionsproteine. Der Adhäsionsprozess wird typischerweise durch das komplexe biochemische Netzwerk der Zelle reguliert. Auf der molekularen Ebene jedoch werden sämtliche Bewegungen von Proteinen, der Membran oder des umgebenden Wassers von thermische Fluktuationen dominiert. Diese thermische Fluktuationen und ihr Einfluss auf den Adhäsionsprozess zwischen zwei Zellmembranen sind die Kernthemen dieser Dissertation.

In dieser Arbeit werden verschiedene Methoden verwendet, welche von minimale theoretische Modelle für Adhäsionsproteine über die Simulation des Wachstums von großen Adhäsionsdomänen mit mehreren tausend Proteinen bis zur Einführung einer neuen experimentellen Technik zur Bestimmung von Membranfluktuationen mit einer bislang unerreichter Genauigkeit in der Kombination von zeitlicher und räumlicher Auflösung reichen. Die meisten Projekte kombinieren mehrere Methoden der drei Säulen der empirischen Wissenschaften - Experiment, Theorie und Simulation. Eine grafische Darstellung der verwendeten Methoden für die aus dieser Dissertation erfolgten Veröffentlichungen ist in Bild I.2.1 gezeigt. Im Weiteren werde ich die Arbeit dieser Dissertation mit ihren acht Publikationen kurz zusammenfassen.

Um Membranprofile und -fluktuationen messen zu können, werden experimentelle Methoden benötigt, die an sich endliche Auflösungsgrenzen in Raum und Zeit enthalten, so dass die experimentell gemessenen Fluktuationen nicht mit den wahren Fluktuationen übereinstimmen müssen. Durch eine Faltung der wahren Fluktuationen mit passenden Funktionen für die räumliche und zeitliche Auflösung habe ich die sichtbaren Membranfluktuationen für zwei verschiedene experimentelle

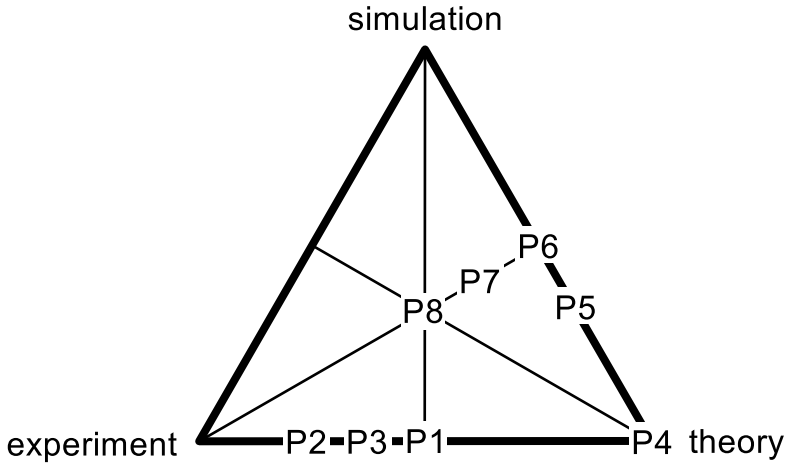

Figure I.2.1: Grafische Einordnung der in Teil "III Publications" dieser Dissertation gezeigten Veröffentlichungen bezüglich ihrer Methode.

Techniken, Reflection Interference Contrast Microscopy (RICM) die neue Methode Dynamical Optical Displacement Spectroscopy (DODS), berechnet (siehe Veröffentlichungen P1-P3). Dabei habe ich herausgefunden, dass die zeitliche Auflösungsgrenzen in RICM die gemessenen Membranfluktuationen gegenüber den wahren Fluktuationen um einen Faktor fünf reduzieren (Fig. 6 in der Veröffentlichung P1 und Fig. 3. in der Veröffentlichung P3). Im Gegensatz dazu sind durch die exzellente zeitliche Auflösung in DODS die gemessenen Fluktuationen sehr nahe an den wahren Fluktuationen (Fig. 3. in der Veröffentlichung P3). Über die Auflösungsgrenzen der experimentellen Techniken hinaus reagiert jede Messung mit einer Kamera-basierte Technik empfindlich auf das Rauschen der Kamera. In RICM ist das Kamerarauschen ein wichtiger Faktor um die wahren Fluktuationen von den gemessenen zu extrahieren. Insgesamt zeigen meine Beiträge zur Auswertung der Experimente schlussendlich einen eindeutigen Weg von den gemessenen Fluktuationen hin zu wahren Fluktuationen und machen es nun möglich darüber hinaus Membranparameter in theoretischen Modellen zu bestimmen.

Vesikel in Substratnähe erfahren eine nicht-spezifische Wechselwirkung, die durch ein Wechselwirkungspotential für die Membran modelliert wird. Typischerweise, und für ein ebenes Substrat im Besonderen, wird das Wechselwirkungspotential durch ein harmonisches Potential genähert. Solange das System in der nicht-spezifischen Adhäsion verbleibt und nur moderate Fluktuationen existieren, reicht die harmonische Näherung aus. Für den Übergang von nicht-spezifischer zu spezifischer Adhäsion muss die Membran jedoch das Minimum des Wech-

selwirkungspotentials verlassen und die harmonische Näherung versagt. Für diesen Fall berechnete ich für eine experimentell vorgegebene Geometrie von Bereichen nicht-spezifischer und spezifischer Adhäsion die Membranprofile und Fluktuationskarten für sowohl ein harmonisches als auch für ein einfaches nicht-harmonisches Wechselwirkungspotential (siehe Veröffentlichung P1). Während ich die Bedeutung eines im Allgemeinen nicht-harmonischen Wechselwirkungspotentials für den Übergang von nicht-spezifischer zu spezifischer Adhäsion betonen konnte, bleibt die Bestimmung der genauen Form der nicht-harmonischen Wechselwirkung eine Aufgabe für die Zukunft.

Im Bereich der spezifischen Adhäsion habe ich sowohl das Gleichgewicht als auch die Reaktions- und Wachstumskinetik von Adhäsionsdomänen untersucht. Für eine unendlich ausgedehnte Adhäsionsdomäne, in welcher die Bindungen auf einem regelmäßigen Gitter platziert sind, habe ich eine neue Bindungskonfiguration gefunden, die metastabil durch eine Kombination von membranvermittelten Korrelationen zwischen verschiedenen Bindungsstellen ist (siehe Veröffentlichung P4). Eine Diskussion der Stabilität von immer kleineren Adhäsionsdomänen führt schlussendlich zur Diskussion über die Stabilität einer einzelnen Bindung. Ich konnte theoretisch zeigen, dass die Bindungsaffinität, d.h. der wichtigste Parameter zur Bestimmung der Stabilität, eines gelösten Adhäsionsproteins sich von der Bindungsaffinität des selben Proteins, das an die Membran gebunden ist, unterscheidet (siehe Veröffentlichungen P4 und P6). Der Grund dafür liegt in den energetischen und entropischen Beiträgen der Membran durch die Bindung. Der gegenseitige Einfluss zwischen Adhäsionsproteinen und der Membran beeinflusst nicht nur die Bindungsstabilität sondern auch die statischen und dynamischen mechanischen Eigenschaften der Membran. Während die statischen Eigenschaften der gebundenen Membran ausreichend bekannt sind, konnte ich zur Beschreibung der dynamischen Membraneigenschaften durch eine phänomenologische Korrektur in erster Ordnung zu den Dämpfungskoeffizienten beitragen (siehe Veröffentlichung P5). Mit Hilfe der Dynamik einer gebundenen Membran können die zeitliche Korrelationen einer stochastisch gebundenen Membrane angegangen werden und für diesen Fall sage ich nichttriviale Effekte für die Membranfluktuationen und die zeitlichen Korrelationen voraus (siehe Veröffentlichung P6). Darüber hinaus kann mit der Kenntnis der Bindungsaffinität die Bindungskinetik einer einzelnen Bindung in einer thermodynamisch konsistenten Art und Weise konstruiert werden, welche ich auf drei verschiedene Ebenen von Vergröberungen angewendet habe - von mikroskopischen Reaktionsraten einer einzelnen

Bindung hin zu effektiven Reaktionsraten, die die Bindungskonfiguration der umliegenden Bindungen mit einbezieht (siehe Veröffentlichung P6). Im letzten Schritt kann nun eine endliche Adhäsionsdomäne aus ihren Bausteinen aufgebaut werden. Ich habe hier insbesondere zur Beantwortung der folgenden zwei Fragen beigetragen: (i) Wie können sich ring-ähnliche Adhäsionsdomänen in einem unregulierten Reaktions-Diffusions-System von Adhäsionsproteinen formen und (ii) welche Rolle spielt die Membran in der Bildung von Adhäsionsdomänen. Bezüglich der ersten Frage fand ich in einer simulationsbasierten Arbeit, dass voluminöse Adhäsionsproteine und eine kreisförmige Kontaktzone ausreichen, um eine stabile ring-ähnliche Adhäsionsdomäne zu bilden (siehe Veröffentlichung P7). Wenn die Proteine dagegen klein sind und damit eine Blockade der Proteine keine Rolle spielt, dass ist der Ring nicht stationär und zuletzt wird die komplette Kontaktzone von Bindungen besetzt sein. In einem Reaktions-Diffusions-System wird das Wachstum des nicht-stationären Rings theoretisch beschrieben und zeigt vollste Übereinstimmung mit der Simulationsergebnissen. Die zweite Frage die endliche Adhäsionsdomänen betreffend konnte ich zu der theoretischen Beschreibung beitragen, die gezeigt hat, dass kleinste Änderungen in der Membranhöhe oder den Fluktuationen schon von wenigen Nanometern enormen Einfluss auf den Typ des Domänenwachstums und die zugehörige Kinetik hat (siehe Veröffentlichung P8). Des Weiteren konnte dieser Effekt auch in Experimenten mit Modellmembranen gefunden werden, so dass die Membran auch als ein Vermittler des Adhäsionsprozesses in biologischen Membranen agieren könnte.

Zusammenfassend zeigt diese Dissertation einen umfassenden Einblick in die Physik des Zelladhäsionsprozesses und wie die allgegenwärtige thermische Umgebung der Zelle das Gleichgewicht und die Kinetik der Adhäsion beeinflusst.

Part II

General introduction

3

Adhesion of biological membranes from a physicists perspective

From the perspective of a physicist, the biological membrane is a fascinating field of research. Recently, advances in experimental techniques provide on the one hand imaging up to molecular resolution and on the other hand detailed control over constituents of the membrane (see Fig. II.3.1). The emerging experimental techniques now grant access for investigations and theoretical modelling from the physics point of view in fields concerning the cell and the biological membrane. Some of these fields include the biological membrane itself [2–6], the cytoskeleton [7–11], molecular motors attached to the cytoskeleton [12–17] or the membrane [18, 19] and, of course, the fascinating field of immune response, exemplified at the immunological synapse [20–27], only to mention few. Due to their complexity, only a combination of state-of-the-art experimental techniques with detailed theoretical models can fully explain a biological membrane. Elaborate theoretical models give access to, e.g., conformation of membranes [28–30], budding and vesiculation in membranes [30–34], or kinetics of membrane adhesion [35–37]. Combining the experimentally accessible fields with the theoretical modelling opens a very wide field of research related to biological membranes.

A core function of cells and biological membranes in multicellular organisms is the formation of permanent cell-cell contacts in a process that is known as adhesion. A biological cell is equipped with many tools to connect its cell membrane permanently with an adjacent cell or with the extracellular matrix [38]. A cell can form different types of junctions, which are classified in four main types: anchoring junctions, tight junctions, channel forming junctions, and signal-relaying junctions. In general, each junction

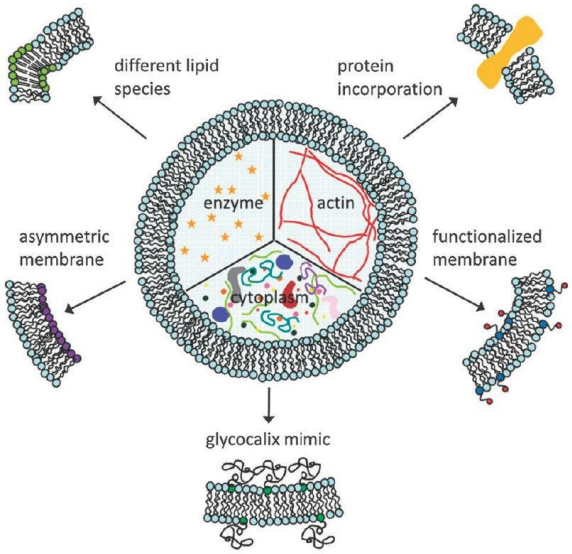

Figure II.3.1: Sketch of a giant unilamellar vesicle and how it can be modified to mimic different cases of interest to physical studies. Adopted from [1].

is formed with highly specific adhesion proteins. The most famous adhesion proteins as, e.g., classical cadherins belong to the class of anchoring junctions and transmit stresses between neighbouring cells by connecting their cytoskeletons. With the four main classes of junctions, a cell has a wide spectrum of possibilities to inter-connect with its environment.

The backbone of a biological membrane is a bilayer that is formed from lipids. In general, a lipid is an amphiphilic molecule with a hydrophilic head and a hydrophobic tail. Suspended in an aqueous solution, lipids try to minimize the contact of the hydrophobic tail with water [39, 40]. In consequence, lipids arrange in a process of self-organisation into structures as, e.g., micelles, liposomes and lipid bilayers. The lipid composition of a biological membrane is manifold. Most of the membrane lipids belong to the large group of glycerophospholipids that contain a glycerol core linked to two fatty acid tails and to one phosphate head group. From this lipid group, biological membranes mostly consist of phosphatidylcholine (PC), phosphatidylethanolamine (PE) and phosphatidylserine (PS). Other lipids found in biological membranes belong to the groups of sphingolipids (e.g. sphingomyelin) and sterol lipids (e.g. cholesterol) [38]. With this variety of different lipids, each biological membrane can be unique just by the lipid composition and, thus, modelling a biological membrane can become very challenging. One very famous model for biological membranes is the so

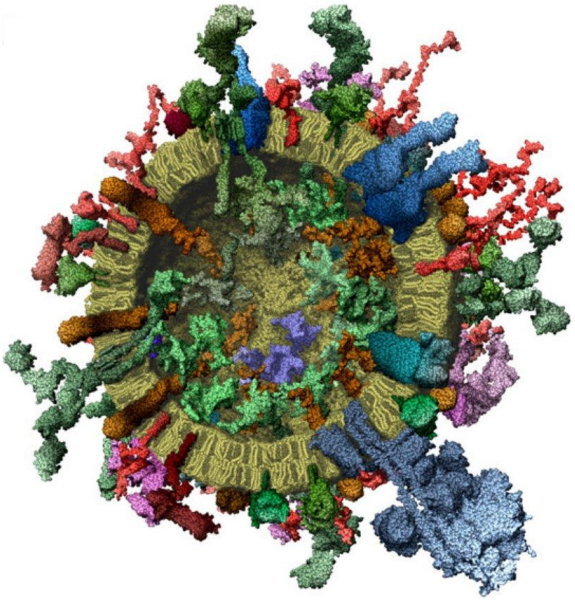

Figure II.3.2: Artistic view of a section of a biological membrane at near atomic resolution. The lipid bilayer is crowded with various types of proteins, including cholesterol, ATPases and GTPases, typical for a synaptic vesicle. Adopted from [43].

called fluid mosaic model by Singer and Nicolson [41] in which the membrane is a lipid bilayer that contains a low density of proteins embedded. Nowadays, it seems clear that the fluid mosaic model is a first idea for a model of a biological membrane and a typical membrane is not decorated now and then with a protein but rather crowded with all types of proteins ([42], for an artistic view see Fig. II.3.2). While each protein is relevant for one or few functions, packing the membrane full of proteins is the only way to achieve the very different functions of biological membranes.

Besides interactions with and at the biological membrane based on the chemical and biological functions of its constituents, the membrane experiences an omnipresent interaction with the environment that is of physical origin, namely thermal fluctuations of the membrane. Since Schrödinger's book "What is life?" [44], published for the first time more than 70 years ago, the interplay between the physical world, determined by thermodynamics and statistics, and the biological world was studied intensively. Cells and vesicles experience stochastic "kicks" from the environment that lead to membrane shape undulations, called membrane fluctuations, and possibly play a crucial role in many biological functions [45]. Compared to the membrane that is few nanometers thick [46], membrane

fluctuations can be rather large with an amplitude that can easily exceed the membrane thickness by more than an order of magnitude [47]. Understanding thermal fluctuations of biological membranes and their mechanical properties has gathered a lot of interest in the last decades and many elaborate experiments, which reproduce biophysical effects of the cell, have been performed and explained [28–30, 42, 48–51].

The physics of cells and biological membranes is often studied with biomimetic model systems [45, 52–54]. A biomimetic model system is a model that reproduces a certain biophysical effect of the cell. For instance, in experiments addressing cell adhesion, a biological membrane is reduced to a pure lipid bilayer that contains the most important adhesion proteins to build a cell adhesion system with the minimal number of relevant constituents. One appropriate model system is, e.g., a giant unilamellar vesicle (GUV, for a review see [1]) that adheres to an opposing membrane with well defined geometry and molecular structure. The opposing membrane can be, e.g., a supporting lipid bilayer (SLB) [55] or another GUV. A possible biomimetic model system for specific membrane adhesion is shown in Fig. II.3.3. This model system consists of a GUV where a fraction of the lipids are decorated with a biotinylated head group and, opposing to the GUV, a supported lipid bilayer of similar constituents. Adding derivatives of the biotin-binding protein avidin to the system forms biotin-avidin bonds which connect the SLB and the GUV, making this particular system ideal to study the effect of interplay between single bonds and the mechanical response of the membrane. A biomimetic model system provides control over the main players in the adhesion process; however, to study the physics of a model system, nanometric measurements of the instantaneous membrane shape are needed.

The standard technique to measure membrane fluctuations is Reflection Interference Contrast Microscopy (RICM). The concept of RICM was developed in the 1960s [56] and has benefited from several refinements recently (for a review see [57]). RICM measures membrane fluctuations close to a glass substrate, where the latter is used to guide the monochromatic illuminating light to the membrane. Reflections of the light at every interface, e.g., glass-water, water-membrane, etc., are collected and brought to interference with the illuminating beam. The distance between the glass and the membrane influences the interference pattern. Consequently, the interference intensity is associated with a height between glass and membrane. Some other experimental techniques use the same physical concept to reconstruct the height of the membrane (for an overview see [58]). Still, RICM is the best technique to measure membrane displacements with nanometric resolution. For instance, a recent improvement to

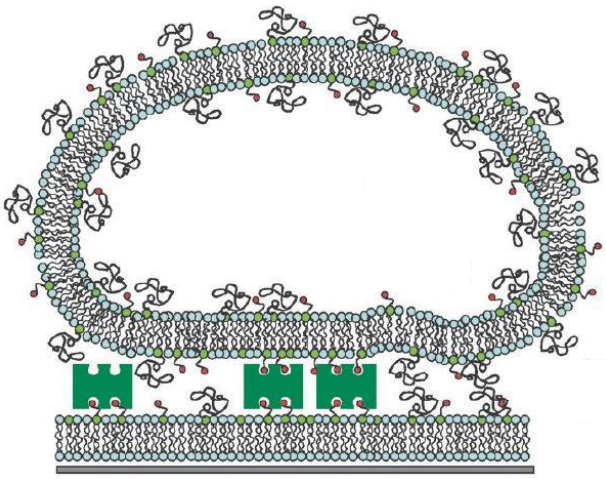

Figure II.3.3: Sketch of a biomimetic model system with a giant unilamellar vesicle (GUV) and a supporting lipid bilayer (SLB). With this system, specific adhesion of the GUV to the SLB can be studied. Adopted from [1].

dual wavelength RICM [59, 60] enables for measuring membrane heights up to 800 nm above the substrate with height resolution down to 2 nm. Moreover, RICM resolves a large area of several μm^2 of the contact zone of the membrane with lateral resolution limited by the pixel size of the camera (typically around 300 nm lateral resolution; see publication P1). With a temporal resolution limit in RICM of about 50 ms, the limits of RICM are reached if fast recording of membrane positions is required as, e.g., for measuring temporal correlations between membrane fluctuations. In such a situation other experimental techniques are needed.

The novel technique Dynamical Optical Displacement Spectroscopy (DODS, introduced in publication P2) provides nanometric vertical resolution (about 20 nm) and temporal resolution increased by about four orders of magnitude compared to RICM and is now in the microsecond range, which allows for measuring the full temporal auto correlation function of a fluctuating membrane. In DODS, the membrane is coated with a high concentration of fluorescent markers, brought into a confocal detection volume and intensity fluctuations are recorded. While the set up is very similar to the well known technique Fluctuation Correlation Spectroscopy (FCS), intensity fluctuations in DODS arise from spatial fluctuations of the membrane. The sensitivity of DODS is largest if the mean membrane height is matched with the inflection point of the confocal detection volume. Another advantage of DODS over RICM is that it is independent of a substrate and membrane fluctuations can be measured at

any position of a biomimetic model system or a biological membrane of a cell. However, in the presence of a substrate, RICM measures the absolute height of the membrane with greater precision than in DODS (see publication P3). Additionally, with DODS the displacement of only a single point of the membrane is recorded, whereas with RICM a whole map of membrane displacements is measured. Finally, DODS requires the addition of fluorescent markers to the membrane which could modify the mechanical of physiological properties of the membrane. However, with respect to the mechanical properties of a membrane, in publication P3 we were able to achieve excellent agreement between an unlabelled membrane measured by RICM and a fluorescently labelled membrane observed with DODS. In conclusion, we retain for the novel technique DODS an excellent combination of small vertical resolution and, simultaneously, an exceptional temporal resolution which renders DODS the ideal method to measure temporal correlations in nanometric displacements of biological and model membranes.

4

Membrane physics - from vesicles to non-specific adhesion

The aim of membrane physics is to understand the static and dynamic mechanical properties of biological membranes, i.e., equilibrium shape, fluctuation amplitude, lateral and temporal correlation functions. To omit the huge molecular complexity of a biological membrane, the considered membrane is reduced to a minimal model in experiment and theory. From the experimental perspective, modelling the mechanical structure of a biological membrane, the biological membrane is often reduced to an artificial lipid bilayer which is build from one or few types of lipids. The aim of using an artificial lipid bilayer is to achieve full control of the system that leads to insights from reproducible experiments. In theoretical modelling, the membrane is regarded as a two dimensional, flexible sheet in a three dimensional environment. Here, properties as shear and bending moduli are assigned to the model membrane and the static and dynamic properties of the membrane are recovered.

In the first part, we will follow the historical path of membrane physics ad deal with the theoretical description of a vesicle. In the second part of this section, we will focus on the non-specific adhesion of vesicles discussing its origin, appropriate theoretical modelling and the static and dynamic mechanical properties of vesicle membranes in non-specific adhesion.

4.1 Fundamentals in membrane physics

In the early days of membrane physics, thermal membrane displacements of red blood cells were observed [47]. This so called flickering of red blood

cells was observed for the first time more than 120 years ago [61] and, for a long time, the thermal origin was unclear. However, associating the flickering with thermal fluctuations of the membrane turned out to be the key to understand the flickering. Moreover, describing the membrane as a two dimensional sheet in a three dimensional environment, decorated with a set of mechanical properties and in contact with an environment exerting stochastic forces onto the membrane provides a system with a minimal number of parameters. Finally, the continuum modelling of the membrane was proven to be a suitable tool for the theoretical modelling of flickering of membranes.

The most important mechanical characteristic of a fluctuating membrane is its bending, which requires re-organisation of lipids on a molecular level and, thus, costs free energy. Bending of membranes was first described in the continuum modelling in the pioneering work of Canham [62] and Helfrich [48, 63] in the early 1970s (for a recent review, see [64]). Helfrich associated the bending of a membrane with an energetic term $\mathcal{H}_b$ being a function of the curvature of the membrane,

$$\mathcal{H}_b = \oint \mathrm{d}A \left(\frac{\kappa}{2}(2H - c_0)^2 + \kappa_G K \right). \tag{4.1}$$

Here, the integral is a surface integral over the membrane area A. The elastic parameters κ and κ_G are the bending rigidity and the Gaussian rigidity, respectively. The spontaneous curvature c_0 accounts for a preferentially curved membrane shape, which is zero for symmetric bilayers. The mean curvature and the Gaussian curvature are denoted by H and K, respectively. According to the Gauss-Bonnet-theorem, the Gaussian curvature term is a constant as long as the topology of the vesicle is constant and in this situation it introduces only an offset to the Hamiltonian. For quantities derived from the Hamiltonian, e.g., mean membrane shape or fluctuations, only variations of the Hamiltonian and not its absolute value are of interest. Consequently, we will neglect the Gaussian curvature term whenever the absolute value of the membrane energy is not of interest and just the term with mean curvature remains. Additionally, we will reduce to symmetric bilayers ($c_0 = 0$) motivated by the experimental model system. The bending term is key in describing a membrane by theoretical means, however, it is not the only term of the Hamiltonian.

For describing vesicles in the continuum picture, membrane tension is a second parameter next to bending rigidity. Microscopically, the membrane area is given by the number of lipids in the membrane and, thus, the membrane area is a constant. In a theoretical description, membrane ten-

sion σ appears as a Lagrange multiplier to constrain the membrane area [65]. The total Hamiltonian becomes

$$\mathcal{H} = \oint \mathrm{d}A \left(\frac{\kappa}{2}(2H)^2 + \sigma \right) \tag{4.2}$$

and includes the membrane tension σ and the bending term in the case of a vesicle built from a symmetric lipid bilayer at a constant topology.

In recent years, the question of what the true definition of the membrane tension is has been debated [66–68]. The discussion started with various definitions of membrane tension. For instance, in experiments measuring membrane tension by, e.g., micropipette aspiration [69], analysis of the fluctuation spectrum [70] or the fluctuation amplitude (see [71] or publication P1), the tension builds up in vesicles due to osmotic pressure differences between the inside and the outside of the vesicle. However, a tensionless membrane in an experiment, i.e., with osmotic balance between the inside and the outside the vesicle, has a non-vanishing σ in the understanding of eq. (4.2). Thus, it is claimed, the $\sigma = 0$ case is often only of theoretical interest [72]. All in all, it is clear that the definition of a membrane tension is understood in various publications in different ways, mostly depending on the background of the scientist. To avoid any misunderstanding, in this thesis we stick to the membrane tension as introduced in eq. (4.2).

The Helfrich Hamiltonian including a membrane tension term, despite its simple structure, allows for explanation of a handful of experiments. For instance, in the early 1990s, different experimentally observed vesicle shapes were explained summing up all possible vesicle shapes in a phase diagram [30, 73–75]. The main order parameter in this context is the reduced volume, defined as the fraction of the vesicle volume and the volume of a sphere with the vesicle's membrane area. Several vesicle shapes found in biological systems, such as discocytes and stomatocytes were explained on these grounds using basic physics and a minimal model system (see fig. II.4.1). Another successful example for describing the membrane with a Hamiltonian was the calculation of thermal fluctuations in quasi-spherical vesicles in the 1980s [76, 77]. Comparison with experiments showed convincing agreement.

In the last decades of the 20th century, the emerging field of computer simulations allowed for the simulation of the membrane model described by the Helfrich Hamiltonian beyond analytical and numerical calculations. For instance, in the early days of computer simulations in membrane physics, the interaction of a fluctuating membrane with a wall was

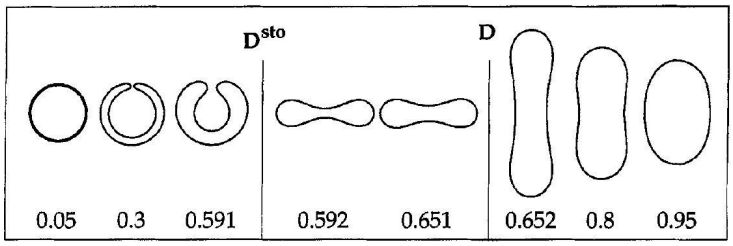

Figure II.4.1: Equilibrium vesicle shapes for several values of the reduced volume (from [73]). Here, the membrane has no spontaneous curvature.

investigated [78, 79]. In the late 1970s, Helfrich derived a steric repulsion that is proportional to $1/h^2$, with the distance h from the wall [63]. The steric repulsion originates from occasional kicks of the membrane to the hard wall. However, the correct form of the proportionality constant for the repulsion was debated up to the late 1980s as an analytical solution of the constant was not yet found. Monte Carlo simulations, accounting for the membrane bending in a discretized manner, confined the membrane between two walls or pushed the membrane towards the wall with an external potential and, finally, shed light on that problem [78–80]. In the late 1990s, the constant was calculated analytically in a variational perturbation theory that was extrapolated to order infinity by Bachmann et al. [81], confirming the simulations. Apart from the strength of steric repulsion of a membrane close to a hard wall, computer simulations of continuum membranes are used to study, e.g., unbinding transitions [82–84], shape deformations of planar membranes due to anchored proteins [50, 85, 86], or adhesion of membranes to a surface [87, 88]. However, with stronger computer hardware and development of efficient algorithms, computer simulations established as a tool for membrane physics beyond a continuum description of the membrane.

Simulations considering all atoms of each lipid of the membrane, in so called molecular dynamic simulations, contributed to the field of membrane physics, too. For instance, fusion of vesicle membranes [89, 90] or the fluidity of lipids in the membrane [91] are interesting questions that were addressed by molecular dynamic simulations. These simulations are an independent tool confirming theoretical findings, e.g., in the field of phase transitions of lipid bilayers from the liquid-ordered to the liquid-disordered phase. Moreover, for situations which are a bit more challenging to tackle than single-component lipid bilayer phase transitions, molecular dynamics simulations are still a powerful tool to go beyond what is analytically understood [66, 92–96].

4.2 Non-specific membrane adhesion

4.2.1 The origin of non-specific interactions

If a vesicle adheres to another vesicle or a planar scaffold, it first forms a contact zone which is parallel to the opposing sheet. Thus, the membrane in the contact zone is on average planar and exhibits only small fluctuations. In this limit, the membrane profile is described in Monge representation, i.e., each point on the membrane is characterized by its height $h(\mathbf{x})$ above a planar reference plane with coordinates $\mathbf{x}$. Typically, the reference plane is identified with the planar scaffold or the opposing vesicle. The Monge representation describes the membrane profile unambiguously if the assumption of small fluctuations is applicable. In this situation the mean curvature $2H$ of the membrane transforms to $\nabla^2 h(\mathbf{x})$ while the tension term becomes $\sigma(\nabla h(\mathbf{x}))^2/2$, both in second order approximations. At the same time, the integral in eq. (4.2) changes from a surface integral over the total membrane area to an integral over the projected area of the membrane onto the reference sheet. With these modifications, the Hamiltonian is written as

$$\mathcal{H} = \int_A \mathrm{d}\mathbf{x} \left[\frac{\kappa}{2} (\nabla^2 h(\mathbf{x}))^2 + \frac{\sigma}{2} (\nabla h(\mathbf{x}))^2 \right]. \tag{4.3}$$

and the almost planar geometry of the contact zone is fully included into the Hamiltonian description of the membrane. While the almost planar membrane is described by the Hamiltonian, however, an interaction between membrane and the opposing surface, i.e., the origin for the almost planar geometry, is not included in eq. (4.3).

Interactions of the vesicle with the scaffold can be attractive or repulsive, adding up to an effective interaction potential. First, the opposing sheet, set to $h = 0$ without loss of generality, restricts the membrane to positions $h \geq 0$ and, consequently, the main repulsive interaction between membrane and scaffold arises from steric repulsion due to hard wall interactions [63, 97]. Besides repulsive interactions, various attractive interactions between membrane and scaffold exist. Possible attractive interactions might emerge from electrostatic interactions between charged or polarized surfaces [98], from van-der-Waals interactions or from gravity if a vesicle sediments towards a scaffold, to mention only a few (for a review see, e.g., [99, 100]). Generally speaking, combining all individual interaction potentials from long-range attractive and short-range repulsive interactions will constitute an interaction potential with a minimum at a

finite distance h_0 from the scaffold. For moderate fluctuations, we may approximate the non-specific interaction potential by a harmonic potential of strength γ around the minimum at h_0. Adding the non-specific interaction between membrane and scaffold to the Hamiltonian yields

$$\mathcal{H} = \int_A \mathrm{d}A \left[\frac{\kappa}{2} (\nabla^2 h(\mathbf{x}))^2 + \frac{\sigma}{2} (\nabla h(\mathbf{x}))^2 + \frac{\gamma}{2} (h - h_0)^2 \right]. \tag{4.4}$$

This Hamiltonian is referred to as the standard Helfrich Hamiltonian for an almost planar membrane.

The limits of a harmonic interaction potential in the Hamiltonian, eq. (4.4), may be reached easily. For large membrane displacements or pulling the membrane out of the potential minimum towards the substrate, the limits of the harmonic approximation for the interaction potential are stressed and a more realistic, non-harmonic interaction potential has to be used. In publication P1, we present such a case and compare theoretical results to experimental observations of the membrane shape for pinning the membrane in a well defined geometry on the substrate. Recording mean membrane shapes of vesicles pinned to the structured substrate reveals differences for the membrane parameters (membrane tension σ or the strength γ of the interaction potential) in the range of several orders of magnitude using a non-harmonic approximation, e.g., a $(4, 2)$-Mie potential instead of the harmonic approximation of eq. (4.4).

4.2.2 Static and dynamic properties

In the following, we will review static and dynamic measures for a membrane in non-specific adhesion. In detail, we will mention the mean membrane profile, the fluctuation amplitude, the lateral correlation function, and temporal correlations. In this section, we will follow detailed reviews written by Lipowsky [29] and Seifert [30].

The membrane in the non-specific interaction potential has a uniform mean membrane shape. The mean membrane shape is found by minimizing the membrane Hamiltonian, eq. (4.4). Obviously, a flat membrane resting in the minimum of the interaction potential $\langle h(\mathbf{x}) \rangle = h_0$ minimizes the Hamiltonian by setting each of the quadratic terms of the Hamiltonian identically to zero. Any other membrane conformation is associated with a positive Hamiltonian due to its quadratic term.

Like the mean membrane shape, the fluctuation amplitude of the membrane is non-specific adhesion is uniform, too. The fluctuation amplitude $\langle \Delta h^2 \rangle$ is found from the second variation of the Hamiltonian. In partic-

ular, we expand the instantaneous membrane profile in Fourier modes, $h(\mathbf{x}) = \sum_{\mathbf{q}} h_{\mathbf{q}} \exp(i\mathbf{q}\mathbf{x}) + h_0$, where we impose a finite membrane sheet and periodic boundary conditions. Next, we assign each mode with $k_B T/2$ accordingly to the equipartition theorem and correlations between Fourier modes are determined. Because of translational invariance of the system and a Hamiltonian that is quadratic in the membrane profile, the correlations between Fourier modes are delta correlated, $\langle h_{\mathbf{q}} h^*_{\mathbf{q}'} \rangle \sim \delta_{\mathbf{q},-\mathbf{q}'}$. With correct correlations in Fourier space, the fluctuation amplitude in real space is found easily,

$$\langle \Delta h^2 \rangle = \frac{1}{(2\pi)} \int \mathrm{d}q \frac{q}{\kappa q^4 + \sigma q^2 + \gamma} = \frac{1}{2\pi} \frac{\arctan(\sqrt{4\kappa\gamma - \sigma^2}/\sigma)}{\sqrt{4\kappa\gamma - \sigma^2}}, \quad (4.5)$$

which reduces to $1/(8\sqrt{\kappa\gamma})$ for a tensionless membrane. Here, we set $k_B T \equiv 1$, as throughout the thesis. It is worth noting that the height probability distribution for the membrane fluctuating in the harmonic non-specific interaction potential is a Gaussian distribution for each lateral position with mean membrane shape as the first moment and fluctuation amplitude as the second moment of the distribution. Calculating the height probability distribution of the non-specifically adhered membrane with the help of functional integrals proves the Gaussian type of the height probability distribution with moments higher than second order being identically zero. The height probability distribution is a great tool for calculating the mean membrane shape and fluctuation amplitude, however, for mechanical properties determined from different lateral positions, e.g., the lateral correlation function, the height probability distribution is impractical.

Lateral correlations between two lateral positions $\mathbf{x}_1$ and $\mathbf{x}_2$ are found with the help of the correlations in Fourier space identified from the equipartition theorem. In a straightforward manner, the lateral correlation function becomes

$$\langle \Delta h(\mathbf{x}_1) \Delta h(\mathbf{x}_2) \rangle = \frac{1}{(2\pi)} \int \mathrm{d}q \frac{q J_0(qr)}{\kappa q^4 + \sigma q^2 + \gamma}, \quad (4.6)$$

where we used $r \equiv |\mathbf{x}_1 - \mathbf{x}_2|$ and the Bessel function $J_0(qr)$ of the first kind. For $\mathbf{x}_1 = \mathbf{x}_2$, the Bessel function $J_0(0)$ becomes unity and the fluctuation amplitude, eq. (4.5), is recovered. In the case of a tensionless membrane with $\sigma = 0$ the integral in the lateral correlation function can be evaluated analytically becoming a Kelvin function with lateral correlation length $\xi = \sqrt[4]{\kappa/\gamma}$ [101, 102]. In case of a tense membrane, the lateral cor-

relation length will increase due to coupling of long-ranging modes by the tension term [71].

With the mean membrane shape, the fluctuation amplitude and the lateral correlation function all static properties of a non-specifically adhered membrane are identified and we can turn to its dynamic properties. The temporal correlation function of a membrane fluctuating in the non-specific potential were calculated from basic principles in the 1990s. Here, thermal excitations of the membrane dissipate into the fluid of viscosity η. A straightforward technique starts with Stokes equations for the aqueous solution surrounding the membrane [103]. In that picture, the membrane acts as a boundary to two compartments of fluids above and below the membrane. Each membrane mode with amplitude q decays exponentially with damping coefficient

$$\Gamma(q) = \frac{\kappa q^4 + \sigma q^2 + \gamma}{4\eta q}, \tag{4.7}$$

using the viscosity η of the surrounding fluid. For the case of two different fluids above and below the membrane, the viscosity in eq. (4.7) becomes the arithmetic mean of the viscosities of the surrounding fluids (a calculation is shown in the supporting information of publication P3). Putting it all together, the temporal correlation function is given by

$$\langle \Delta h(\mathbf{x}, t) \Delta h(\mathbf{x}, t + \Delta t) \rangle = \frac{1}{2\pi} \int_0^\infty \mathrm{d}q \, \frac{q \exp(-\Gamma(q)\Delta t)}{\kappa q^4 + \sigma q^2 + \gamma}. \tag{4.8}$$

As long as the membrane is described in a translational invariant Hamiltonian, the temporal correlations take the form of the above equation. However, the damping coefficient might be changed. For instance, for a membrane in a non-specific interaction potential in the presence of an impermeable wall, hydrodynamic interaction of the membrane with the wall become important and the damping coefficients change sensibly [103].

5 Specific membrane-scaffold interactions

In this chapter, we will discuss specific membrane adhesion of membrane-anchored adhesion proteins that form bonds and bind the membrane locally to a scaffold. The interaction between membranes and bonds is mutual. Bonds deform or, at least, affect the membrane's mean shape and fluctuations which, in turn, influence the formation and stability of bonds.

Membrane-anchored adhesion proteins play a crucial role in many biological processes. A particularly intriguing example of studies of adhesion proteins investigates the stability of focal adhesions [104]. In general, focal adhesion points enable the cell to apply stress to the specific adhesion points and, thereby, provide motility. It was found experimentally that adhesions are most stable if the adhesion molecules are spaced by a specific distance [105], hinting at the interplay between individual adhesion proteins and the mechanistic behaviour of the membrane and the cytoskeleton. Motivated by such experiments, we will investigate the mutual interplay of point-like bonds and the membrane.

In comparison to the non-specific interaction discussed in the previous section, which is described by a laterally homogeneous interaction potential, specific interactions form from localized adhesion proteins described by a locally inhomogeneous interaction potential. In detail, the specific interaction potential is non-zero only for positions with an adhesion protein. In combination with a homogeneous, non-specific interaction potential, a theoretical description becomes challenging, taking into account the inhomogeneous nature of specific interactions.

A first approach to consider specific interactions is restricted to systems with a high density of adhesion proteins. Here, a mean-field description of the specific interactions is applicable. Combining both, the non-specific and the specific interaction potentials compose a laterally homogeneous

double-well interaction potential [106, 107] and specific adhesion can be understood as a first-order dewetting transition from non-specific adhesion [108]. However, with lateral distance between adhesion proteins of the size of the membrane's lateral correlation length, local changes in the mean membrane shape and fluctuation amplitude play a crucial role for bond kinetics and bond stability [109].

5.1 The single bond

A single bond connects two membranes, which are a fluctuating membrane above a rigidly supported lipid bilayer. We call the adhesion protein on the fluctuating membrane the ligand whereas the protein on the scaffold is called receptor and both proteins form a ligand-receptor bond. In biology, there is a huge variety of adhesion proteins, however, in experimental model systems used for publications P1 - P3, P7, and P8 we deal with only few types of adhesion proteins. In particular, proteins used in those publications are the biotin-avidin bond, one of the strongest bonds known, and extracellular domains of E-cadherins forming homophilic bonds. The large avidin molecule is bound only to the supporting lipid bilayer on the substrate. Biotins and the extracellular domains of E-cadherins are bound covalently to lipid head groups of the fluctuating membrane such that, to a good approximation, the mechanic properties of the fluctuating membrane are undisturbed whether there are unbound adhesion proteins attached to the membrane or not. Therefore, the non-specifically bound, fluctuating membrane is described by the Hamiltonian of eq. (4.4) and the modification due to specific adhesion is accounted for by adding a term for the bond. In a second order approximation, the bond is a harmonic spring of stiffness λ and rest length l_0. With this modified Hamiltonian all mechanic properties of the membrane and the bond are obtained. The Hamiltonian describes the membrane in the unbound and in the bound state, however, to model the binding process of the bond further information is necessary.

The molecular details of the binding process of a ligand and a receptor to a bond are complex. In a simplifying theoretical approach, the ligand and receptor can form a bond if they come into binding range. Molecular complexation of the bond is associated with a release of free energy which is referred to as binding affinity. Breaking a bond is associated with an energetic cost of the same amount. Measuring the binding affinity of membrane-anchored adhesion proteins includes energetic and entropic contributions of the membrane, too. For instance, the mean membrane de-

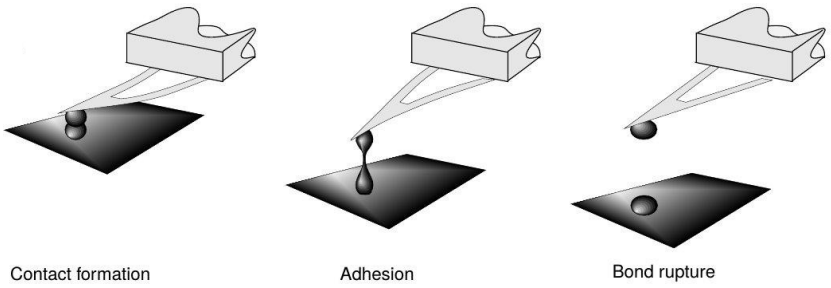

Figure II.5.1: Sketch of an experiment measuring rupture forces between single bonds or, here, between individual cells. Determining force-distance curves reveal for a cell contact experiment possibly single bond rupture events. Adopted from [116].

formation due to forces transmitted by the bond is connected to an energetic term [106]. Additionally, reduction of membrane fluctuations due to bond formation is associated with an entropic cost the system has to pay [110]. Consequently, the same adhesion protein dissolved in solution or attached to membranes obeys different binding affinities [111–113], which might amount to several $k_\mathrm{B}T$. For our purposes, the intrinsic binding affinity is the binding affinity of the protein in solution and the binding affinity in membrane adhesion is to be determined.

In publications P4 and P5, we obtained the binding affinity of the membrane-bound adhesion proteins by explicitly calculating the free energy difference between bound and unbound state. The free energy difference consists of three terms. The first term is the deformation energy of the membrane and of the bond and the second term is the entropic contribution due to confining the fluctuations of the membrane and the receptor to each other. The third term is the intrinsic binding affinity of the protein. Possible additional entropic effects may arise if the individual adhesion proteins are mobile in the unbound state but immobile in the bound state, which would require a term associated with the immobilization of the proteins. Then, the number of possibilities to find a ligand and a receptor at the same lateral position have to be counted, which was done in some models in an elaborate way [109, 114, 115]. For the discussion of a single bond, the ligand and the receptor are assumed to be immobile and at the same lateral position.

In early experimental attempts, the binding affinity or rupture forces of single bonds were measured with the atomic force microscope (AFM, [117–121]). In these experiments, a ligand is attached to the tip of an AFM. Bringing the tip in contact with a solid, receptor-coated substrate forms a

ligand-receptor bond. Increasing the distance between tip and substrate gives rise to force-distance measurements revealing the free energy landscape of the molecular changes during rupture of the bond (for an illustration of the experiment see Fig II.5.1). The field of single molecule force spectroscopy [116, 122, 123] developed rapidly since then. Nowadays, force measurements are applied to various situations of rupture experiments and have become a standard tool to address very different questions. For instance, rupture experiments of single- and double-stranded DNA [124–127] are used, e.g., to tackle fundamental questions in stochastic thermodynamics [128]. Apart from atomic force microscopy, other methods in single molecule experiments are, e.g., magnetic beads, optical tweezers, glass microneedles or the biomembrane force probe apparatus (for an overview see ref. [129]). In conclusion, recent experimental techniques measure the properties of single bonds qualitatively and quantitatively to an accuracy that allows a direct comparison to theoretical models.

5.1.1 A permanent bond

In this section, we are interested first in the effects of a bond on the membrane mechanics. Consequently, we neglect binding kinetics and keep the bond permanently formed. The mutual interplay between membrane and bond will be discussed in the next section "A stochastic bond".

The effect of a single permanent bond on the mean membrane shape is well known. The ligand-receptor bond deforms the membrane to minimize the total free energy of the system consisting of the bond and the membrane. The deformation is proportional to the difference between the position of the minimum of the interaction potential h_0 and the rest length of the receptor l_0 [130, 131]. The membrane deformation decays for a tensionless membrane with the Kelvin function kei_0 on the length scale of the lateral correlation length [101, 102]. Whenever the mean membrane shape is deformed, a deformation energy due to bending of the membrane and pulling it out of the minimum of the interaction potential is stored in the membrane. The deformation energy is proportional to $(h_0 - l_0)^2$ (see refs. [102, 106] and publication P4).

The membrane fluctuations in the vicinity of a single bond are suppressed locally as a function of the distance to the bond. At the position of a bond, the fluctuations are determined by a model of two springs in parallel. One spring describes the bond, the other spring describes the membrane. The fluctuations of the construct are given by the inverse of the sum of both spring stiffness's. In the immediate proximity of the bond, the

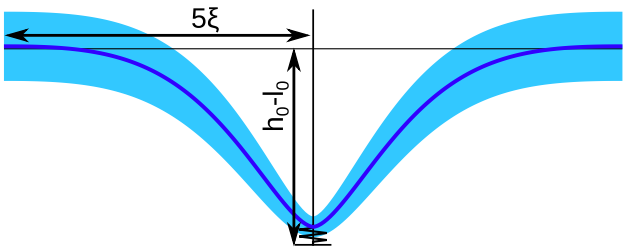

Figure II.5.2: Mean membrane profile (blue curve) and fluctuation amplitude (light-blue area) of a single, permanently bound ligand-receptor pair (sketched by the spring). Thereby, all units are rescaled and the membrane is tensionless. The ligand-receptor bond is $10\times$ stiffer than the membrane and $h_0 - l_0 \simeq 5.5\sqrt{\langle \Delta^2 \rangle}$.

fluctuation amplitude increases almost linearly resembling a cone that was found for pinning a membrane without an interaction potential [130]. Further apart from the receptor, the membrane fluctuations are determined by the non-specific interaction potential. The functional dependence of the membrane fluctuation amplitude on the distance to the bond is given by the square of the lateral correlation function. In fig. II.5.2, we show the mean membrane deformation (dark blue line) and the fluctuation amplitude (light blue shaded area).

Lateral correlations of a permanently bound membrane show some interesting features, which can be understood intuitively. First, the lateral correlation length of $\langle h(\mathbf{0})h(\mathbf{x})\rangle$ of a permanently bound membrane, i.e., the correlation length measured from the position of the bond, is identical to the correlation length of an unbound membrane (see publication P5). Second, while the lateral correlation length is unchanged, the amplitude of the lateral correlation function is altered comparing the unbound and the permanently bound membrane. For the permanently bound membrane, the amplitude of the correlation function at the position of the bond is given by the fluctuation amplitude as described in the previous paragraph. The core characteristics of the lateral correlation function, correlation length and amplitude, are fully understood and, in summary, all static properties of a pinned membrane were discussed.

Temporal correlations of a permanent single bond attached to the membrane are difficult to calculate analytically and have been addressed with several methods in the last years. Temporal correlations are described by the temporal height-height auto-correlation function or its Fourier transform, the power spectral density [132, 133]. Temporal correlations are determined by the hydrodynamic interplay between membrane and

surrounding fluids. In detail, the Stokes equations have to be solved and all forces perpendicular to the membrane plane have to balance. For the unbound membrane an expansion in plane waves allowed for an analytical solution for each fluctuation mode individually. However, for the permanently bound membrane, irrespective of an expansion in plane waves or in eigenmodes of the system, all fluctuation modes couple due to translational invariance of the system. First steps to understanding temporal correlations of a pinned membrane were achieved by dynamic membrane simulations [134, 135] and by numerically calculating the fluctuation spectrum of a discretized membrane [86, 136, 137]. However, a discretized membrane possesses only a few fluctuation modes and full understanding of hydrodynamic interactions of a localized pinning site attached to the membrane is still unsolved. Recently, with a phenomenological ansatz, we derived a first order correction to the damping coefficients of each fluctuation mode (see publication P5). Moreover, we found temporal correlations of the pinned membrane to be independent of mean membrane shape deformations.

5.1.2 A stochastic bond

Binding kinetics

After dealing with the effect of a permanent bond on the membrane, we will shift our focus in this section towards the effect of the membrane on the bond. Nowadays, it is well known that binding and unbinding rates of adhesion proteins react in a unique way to forces. Here, we will first account for a thermodynamically consistent formulation of force-dependent reaction rates that we will then use to determine rates for several levels of coarse graining which will finally recover the correct force dependence of the reaction rates.

Historically, in the work of Bell in the late 1970s the binding and unbinding process was described in a simple model [138]. The binding of a bond was assumed to run in two steps. First, the ligand and the receptor have to come into binding range and, second, the actual binding occurs. Unlike to proteins dissolved in solution, binding of membrane-anchored proteins immobilized on the membrane surface depends strongly on membrane fluctuations. The actual binding occurs for membrane-anchored proteins in the same way as for proteins in solution. In a next step, whenever a bond was formed, it can undergo the unbinding procedure. According to Bell's work, the unbinding rate increases exponentially with the force applied on the bond. Consequently, the life time

of a bond decreases with increasing force. A bond that follows the simple model of Bell is called a normal bond and was experimentally confirmed in the 1990s by several groups [139–141].

However, some bonds cannot be described by Bell's model. A bond that counter-intuitively has an increased life time with increasing the force applied to it is called a catch bond [142, 143]. This type of bonds was proposed by Dembo [144] and experimentally observed for the first time by Marshall et al. [145]. The molecular mechanisms of catch bonds are elusive, yet, recent molecular dynamic simulations show that forces applied to the bond allow for the formation of additional hydrogen bonds stabilizing the whole construct, which might offer an explanation [146]. The discussion of normal and catch bonds became recently even more complex when classical E-cadherins were found to behave as either normal bonds or catch bonds, depending on their conformation [147]. This observation boosts speculations of the cells adopting the conformation of adhesion proteins to increase or reduce the stability of individual bonds and accordingly the stability of adhesion domains and tissue.

In our model for the binding kinetics, three levels of reaction rates can be distinguished (see publication P6). On an almost molecular level, instantaneous reaction rates $k^{\pm}$ depend on the actual position of the receptor and the membrane. The reaction rates fulfil local detailed balance for a thermodynamically consistent model and the general form is comparable to Arrhenius rates [148]. On a somewhat coarse grained level, reaction rates $k_{\mathrm{on/off}}$ integrate the fluctuations of the receptor. Consequently, the rates $k_{\mathrm{on/off}}$ depend only on the membrane position and resemble characteristics of the phenomenologically motivated rates by Bell and Dembo [138, 144]. We use $k_{\mathrm{on/off}}$ for a simulation scheme which renders the membrane fluctuations explicitly in Langevin dynamics [109, 113, 131]. The third level of modelling reaction rates integrates the membrane position, too, resulting in effective reaction rates $K^{\mathrm{on/off}}$. These effective rates are applicable for a time scale separation between the characteristic time of membrane and receptor fluctuations on the one side and life times of the unbound or bound state on the other side. These rates account in particular for cooperation between bonds [109, 131]. A simulation scheme based on effective reaction rates is very efficient in rendering adhesion dynamics of specific membrane-scaffold interactions, opening the possibilities to investigate the adhesion processes on the scale of a cell for several hundreds of seconds (see [109] and publications P7 and P8).

Fluctuations and temporal correlations of a stochastic bond

A single bond experiment typically deals with the stochastic formation of the bond, i.e., the bond opens and closes several times during the measurement. The amplitude of fluctuations fluctuations or the temporal autocorrelation function of the binder distance can be measured (a recent experiment is shown in, e.g., [128]). For the case of a stochastic bond, we will review the fluctuation amplitude and temporal correlations of the membrane. The main idea is that the trajectory of the membrane height at the position of the bonds is the result of three different stochastic processes, namely the fluctuations of the membrane in the (i) unbound and (ii) bound state and (iii) fluctuations associated with a two state process for opening and closing of the bond. By measuring the membrane height at the position of a stochastic bond for a sufficiently long time to record several opening and closing events, the mean membrane height and the membrane fluctuation can be extracted. In the measurement, for a fraction p_u of the total time the bond is open, whereas for a fraction $p_b = 1 - p_u$ the bond is formed. For a mean membrane height $h_u = h_0$ of the unbound membrane and a mean membrane height h_b in the bound state, the mean membrane height of the stochastic bond is given by

$$h_s = p_u h_0 + (1 - p_u) h_b. \tag{5.1}$$

If the equilibrium heights of the unbound bond and the minimum of the membrane coincide, i.e., $l_0 = h_0$, the mean membrane height in the bound state becomes $h_b = h_0$ and the mean membrane height of the stochastic bond becomes $h_s = h_0$, too. In this case, the membrane fluctuation amplitude of the stochastic bond is simply the mean of the fluctuation amplitudes in the given states, $\langle \Delta h^2 \rangle_s = p_u \langle \Delta h^2 \rangle_u + (1 - p_u) \langle \Delta h^2 \rangle_b$ with the fluctuation amplitudes $\langle \Delta h^2 \rangle_u$ in the unbound state and $\langle \Delta h^2 \rangle_b$ in the bound state. However, if $l_0 \neq h_0$ the mean membrane height of unbound and bound state differ from each other and the fluctuation amplitude of the stochastic bond is a sum of three terms, namely the fluctuation amplitude in the unbound and in the bound state and a term for switching between the states,

$$\langle \Delta h^2 \rangle_s = p_u \langle \Delta h^2 \rangle_u + (1 - p_u) \langle \Delta h^2 \rangle_b + p_u (1 - p_u)(h_0 - h_b)^2. \tag{5.2}$$

The additional term is due to fluctuations in a two state process of different heights. Combining the three terms shows that the fluctuation amplitude of the stochastic bond $\langle \Delta h^2 \rangle_s$ can easily exceed the individual fluctuation amplitude in the unbound or bound state, $\langle \Delta h^2 \rangle_u$ or $\langle \Delta h^2 \rangle_b$, respectively

(see Fig. 4 in publication P6).

Experimentally, the fluctuation amplitude of a stochastic bond has been measured, e.g., in an experiment of specific adhesion of a vesicle to a supported lipid bilayer via biotin-avidin bonds [149]. Here, the height trajectory of the membrane was observed with dynamic RICM and the mean membrane height and the fluctuation amplitude were extracted. At the position of a nucleation seed, the membrane goes in the early stages from an unbound state to a stochastic bond and, after agglomeration of additional bonds, the nucleation seed is stabilized. From an unbound membrane to a stabilized nucleation seed, the mean membrane height is monotonically pulled towards the substrate and the fluctuation amplitude first increases from the unbound fluctuation amplitude and, later, decreases to the fluctuation amplitude of the bound membrane. While in the experiment many bonds are involved, the characteristics of the fluctuation amplitude of a stochastic bond are clearly identifiable.

Beyond mean membrane heights and fluctuation amplitudes, temporal correlations of the stochastic bond are easily accessible. The three stochastic processes applicable to the stochastic bond obey, typically, three different characteristic time scales. Thus, in an analysis of temporal correlations each of the processes should be visible, even more prominently than in the fluctuation amplitude. The power spectral density is an ideal tool for studying temporal correlations of a stochastic bond. The power spectral densities for the bound and unbound membrane are given by the respective power spectral densities discussed above. The power spectral density of a stochastic two-state process as a Bernoulli process is a Lorentzian with a low frequency limit proportional to $(h_0 - l_0)^2$ and a characteristic frequency $\omega^* \equiv (K_{\mathrm{on}} + K_{\mathrm{off}})^{-1}$, using the effective reaction rates $K_{\mathrm{on/off}}$ jumping between both states. Combining all three individual power spectral densities, full knowledge about the power spectral density of a stochastic bond is gained (see, e.g., in publication P6 where we found excellent agreement between simulations and the calculated results of the model without any fit parameter).

5.2 Domain formation and membrane-transmitted correlations

In a biological context, a single bond is rarely involved in adhesion. Consequently, the question arises what happens if many bonds interact with each other and how the properties of a single bond are modified. In terms

of stability, a single bond is stable if the energetic gain at least compensates for energetic and entropic costs forming the bond. However, a domain achieves stability if the energetic gain of all bonds compensates for all energetic and entropic costs. In other words, a domain profits from cooperation in the deformation energy, and suffers from entropic costs of suppressed membrane fluctuation modes in a lattice. Comparing the numbers of gains and costs, a domain can be stable even in cases where a single bond is unstable.

In this section, we first consider the case of an infinitely large domain, i.e., all bonds arranged on an infinite lattice are permanently bound. In a second paragraph, we discuss the formation of a domain from a single bond to a stable nucleation seed as well as further growth dynamics of the domain.

5.2.1 An infinite domain

We consider an infinite domain of regularly arranged bonds where the characteristic parameter describing the domain is the bond density defined by the number of bonds per area. From a physicists perspective, specific adhesion points arranged on a regular lattice give rise to a lattice gas description [102, 150, 151]. Here, bonds with nearest-neighbour interactions are considered and the formation of adhesion domains can be studied. While the lattice gas description provides first approximative results, it turns out that the interaction between bonds is more complex, driven by rather long-range membrane-transmitted interactions. Thus, a lattice gas description lacks important details of cooperativity between bonds.

For discussing domain stability, the free energy difference per area, i.e., a free energy density, is a suitable tool. The free energy density has a global minimum when, in the limit of point-like bonds, the bonds approach close packing, i.e., the packing distance d between two bonds approaches $d \to 0$. In this theoretical limit, the membrane is flat and pulled to the rest length of the receptors, i.e., the total deformation energy for a piece of the membrane of area A is given by $A\gamma(h_0 - l_0)^2/2$. At the same time, the energetic gain is given by the number of bonds times the intrinsic binding affinity. However, for $d \to 0$ and a constant chemical potential for the unbound binders, an infinite number of bonds is placed below the membrane of area A. Imposing biological relevant intrinsic binding affinities of few k_BT exceed the entropic costs for close packing of bonds and suppression of any fluctuations by far and, consequently, the free energy density diverges to a global minimum and close packing becomes the preferred state for an

infinite domain. Another obvious binding state of an infinite domain is the unbound state, i.e., the limit $d \to \infty$. If the bonds maximize the spacing between each other, cooperativity is lost and a discussion of individual single bonds follows. The free energy density approaches zero for large bond distances because of the finite free energy difference of single bonds divided by a huge area per bond. Interesting for a discussion of domain stability on grounds of the free energy density is the question whether the free energy density curve approaches zero for $d \to \infty$ from positive or negative values rendering the domain unstable or stable, respectively. Both states, close packing and the unbound state, exist independently of membrane-transmitted cooperativity. For finite bond distances, due to a subtle combination of membrane deformations and taking advantage of membrane-transmitted correlations, we found a local free energy density minimum (see publication P4). Consequently, specific binding of a membrane in an infinite domain can occur in three possible ways: it can be unbound ($d \to \infty$), it can be bound in a metastable dilute domain (finite d) and it can be bound in close packing ($d \to 0$). A hint for experimental observation of the dilute domain might be the observation that focal adhesions are most stable if the adhesion molecules are spaced in a specific distance [105, 152]. While the stability of focal adhesions is tightly connected to the cytoskeleton of a cell, dilute spacing of bonds due to membrane cooperativity might support the stability even further.

For bonds placed on a regular lattice, the mean membrane shape can be obtained by minimizing the Hamiltonian within a unit cell of the lattice and imposing periodic boundary conditions. Alternatively, calculating the height probability distribution for the unit cell yields the mean membrane shape as its first moment. Additionally, the second moment of the height probability distribution is identified with the fluctuation amplitude. Calculating the height probability distribution without periodic boundary conditions and implementing all bonds explicitly, the mean membrane shape and the fluctuation map for an arbitrary bond configuration can be determined (see [131] and publications P4 and P5). Thus, the mean membrane shape and the fluctuation amplitude are found for all bond configurations in finite and in infinite domains.

Regarding temporal correlations of the membrane bound to a bond lattice, we found in publication P5 phenomenologically that membrane-transmitted correlations can be treated effectively on a single bond level. To determine the temporal correlations of the membrane bound to a single bond, we found a first order correction to the damping coefficients depending on the fluctuation amplitude of the membrane. In a bond lattice with membrane-transmitted correlations between bonds, the fluctuation

amplitude of the membrane changes locally. Using the local fluctuation amplitude of the membrane in a bond lattice for the first order correction of the damping coefficients results in temporal correlations that agree well with simulations of the full bond lattice. This phenomenological approach to the temporal correlations is a first step towards full understanding of the membrane dynamics in infinite domains.

5.2.2 A finite domain

Growth of adhesion domains depends on individual bonds aggregating to the domain. Combining deformations of neighboring bonds is associated with an energetic gain that pushes the bonds together. The initial step of the formation of a domain is a stable nucleation seed. In a capillary approximation counting energetic contributions of the adhesion domain and its edges it was found for biological relevant parameters that typically a few bonds in a domain are sufficient to stabilize the seed [131]. If the nucleation seed is stable, the growth dynamics of the domain depends on the diffusion of adhesion proteins and bonds and on the molecular complexation of binders to bonds.

The formation of finite domains by lateral organisation of permanent bonds were studied previously. For a huge number of mobile binders, agglomeration of domains in the contact zone of two opposing membranes into a single large domains was identified due to minimizing the membrane deformation energy [88]. In comparable studies, binders of different lengths separate spatially forming domains containing only one type of binders due to the same membrane deformation argument [115, 153]. The costs for membrane deformation typically exceed the entropic costs of agglomeration of bonds in large domains. However, if the mean membrane shape is undisturbed upon bond formation, i.e., for $l_0 = h_0$, the entropic effects dominate. In this situation and on large scales, dilute organisation of bonds suppresses many membrane fluctuation modes, whereas a closer packing of the bonds allows more fluctuation modes. Thus, entropic effects can promote the formation of bond domains, too [154–156]. However, binding kinetics add another characteristic to the formation of finite domains.

The interplay between the diffusion of binders and their complexation to bonds leads immediately to a description of the domain growth in a reaction-diffusion system. In principle, whenever binders of opposing membrane sheets meet, they can form a bond that can later break again. In a reaction-diffusion system, two competing time scales determine the

domain growth: the time scale of diffusion of binders and the time scale of the binding kinetics. In describing membrane adhesion in a reaction-diffusion system, the local binding kinetics is determined by the mean membrane shape and the fluctuation amplitude and, thus, by the local bond configuration [109, 131]. The analytical description of a reaction-diffusion system is possible in two limits: the reaction-limited and the diffusion-limited regime. In the diffusion-limited regime a bond is formed whenever a ligand and a receptor meet and the growth dynamics is limited by the density and the diffusion of the bonds. The morphology of the bond domains in the diffusion-limited regime is characterized by few nucleation seeds that grow, in a homogeneous system, radially. A theoretical description of the domain growth is given by a radially symmetric diffusion equation [35–37, 113]. In a system of vesicle adhesion to a flat substrate with a circular contact zone and a finite reservoir for the binders, the diffusion-limited regime shows domains that grow radially from the rim of the contact zone inwards (publication P7). In the reaction-limited regime, the morphology is characterized by many nucleation seeds that form and grow independent of each other until neighboring seeds merge. A suitable model for this type of domain growth is the Johnson-Mehl-Avrami-Kolmogorov model [157, 158]. In an experimental system, both growth regimes might be complemented by other growth dynamics and morphologies due to, e.g., bulky binders, that can form impermeable barriers and facilitate crowding (see publication P7).

Part III

Publications

P1

Signature of a non-harmonic potential as revealed from a consistent shape and fluctuation analysis of an adherent membrane

Signature of a non-harmonic potential as revealed from a consistent shape and fluctuation analysis of an adherent membrane

D. Schmidt[1], C. Monzel[2,3,4], T. Bihr[1], R. Merkel[2], U. Seifert[1], K. Sengupta[3], and A.-S. Smith[5]

[1] II. Institut für Theoretische Physik, Universität Stuttgart, 70569 Stuttgart, Germany
[2] Institute of Complex Systems 7: Biomechanics, Forschungszentrum Jülich GmbH, 52425 Jülich, Germany
[3] Aix-Marseille Université, CNRS, CINaM UMR 7325, 13288 Marseille, France
[4] Institute for Physical Chemistry, University of Heidelberg, 69120 Heidelberg, Germany
[5] Institut für Theoretische Physik, Friedrich Alexander Universität Erlangen-Nürnberg, 91052 Erlangen, Germany

Phys. Rev. X, **4** (2014) 021023

DOI: 10.1103/PhysRevX.4.021023
http://journals.aps.org/prx/pdf/10.1103/PhysRevX.4.021023

ABSTRACT The interaction of fluid membranes with a scaffold, which can be a planar surface or a more complex structure, is intrinsic to a number of systems – from artificial supported bilayers and vesicles to cellular membranes. In principle, these interactions can be either discrete and protein mediated, or continuous. In the latter case, they emerge from ubiquitous intrinsic surface interaction potentials as well as nature-designed steric contributions of the fluctuating membrane or from the polymers of the glycocalyx. Despite the fact that these nonspecific potentials are omnipresent, their description has been a major challenge from experimental and theoretical points of view. Here we show that a full understanding of the implications of the continuous interactions can be achieved only by expanding the standard superposition models commonly used to treat these types of systems, beyond the usual harmonic level of description. Supported by this expanded theoretical framework, we present three independent, yet mutually consistent, experimental approaches to measure the interaction potential strength and the membrane tension. Upon explicitly taking into account the nature of shot noise as well as of finite experimental resolution, excellent agreement with the augmented theory is obtained, which finally provides a coherent view of the behavior of the membrane in a vicinity of a scaffold.

Signature of a Nonharmonic Potential as Revealed from a Consistent Shape and Fluctuation Analysis of an Adherent Membrane

Daniel Schmidt,[1] Cornelia Monzel,[2,3,4] Timo Bihr,[1,5] Rudolf Merkel,[2] Udo Seifert,[1] Kheya Sengupta,[3] and Ana-Sunčana Smith[5*]

[1]*II. Institut für Theoretische Physik, Universität Stuttgart, 70569 Stuttgart, Germany*
[2]*Institute of Complex Systems 7, Biomechanics, Forschungszentrum Jülich GmbH, 52425 Jülich, Germany*
[3]*Aix-Marseille Université, CNRS, CINaM UMR 7325, 13288 Marseille, France*
[4]*Institute for Physical Chemistry, University of Heidelberg, 69120 Heidelberg, Germany*
[5]*Institut für Theoretische Physik, Friedrich Alexander Universität Erlangen-Nürnberg, 91052 Erlangen, Germany*

(Received 26 September 2013; revised manuscript received 19 February 2014; published 5 May 2014)

The interaction of fluid membranes with a scaffold, which can be a planar surface or a more complex structure, is intrinsic to a number of systems from artificial supported bilayers and vesicles to cellular membranes. In principle, these interactions can be either discrete and protein mediated, or continuous. In the latter case, they emerge from ubiquitous intrinsic surface interaction potentials as well as nature-designed steric contributions of the fluctuating membrane or from the polymers of the glycocalyx. Despite the fact that these nonspecific potentials are omnipresent, their description has been a major challenge from experimental and theoretical points of view. Here, we show that a full understanding of the implications of the continuous interactions can be achieved only by expanding the standard superposition models commonly used to treat these types of systems, beyond the usual harmonic level of description. Supported by this expanded theoretical framework, we present three independent, yet mutually consistent, experimental approaches to measure the interaction potential strength and the membrane tension. Upon explicitly taking into account the nature of shot noise as well as the nature of finite experimental resolution, excellent agreement with the augmented theory is obtained, which finally provides a coherent view of the behavior of the membrane in the vicinity of a scaffold.

DOI: 10.1103/PhysRevX.4.021023 Subject Areas: Biological Physics, Soft Matter

I. INTRODUCTION

Phospholipid membranes in cellular and biomimetic systems exhibit significant fluctuations [1–6], which may be of thermal origin or may arise as a result of active processes in the environment [7–10]. Fluctuations play an important role in the regulation of the cell recognition process [6] and regulate the adhesiveness of membranes [11]. In the context of protein-mediated interactions, an important role of the fluctuations is to rescale the binding affinity for the macromolecular complexation [12] and to promote correlations between the binders, both in the plane of the membrane and while binding to surrounding scaffolds [13,14]. However, even the qualitative understanding of these processes is a challenge, while the quantitative description is in the nascent stage and is a very active field of research [15,16].

*Corresponding author.
smith@physik.uni-erlangen.de

The physical framework explaining the thermal membrane fluctuations was provided by Helfrich [17,18] who was the first to calculate the wave-vector–dependent fluctuation amplitude as a decreasing function of the membrane stiffness. Shortly after that, the effects of the tension originating from the finiteness of the cell or vesicle shape were introduced (for a review, see Ref. [19] and references therein), even though the precise definition of the tension is still being scrutinized [20–22]. Meanwhile, a number of methods have been developed to measure the fluctuations of free membranes [5,23–25], mostly in red blood cells [1,26,27] and phospholipid giant unilamellar vesicles [28–31]. These early measurements were in good agreement with the theoretical predictions [32] and were used to determine the tension and the bending stiffness of the membrane. However, very recent data acquired with unprecedented time and space resolution pointed to potential problems [33]. More specifically, data agreed well with the Helfrich model only after the viscosity of the surrounding fluid was set as a parameter, which upon fitting led to unexpectedly large magnitudes.

Fluctuations of membranes in the vicinity of scaffolds, as simple as a hard surface or another membrane, evoked even more deliberation. In the context of membrane-surface

interactions, the focus has often been on specific and discrete protein-mediated interactions [9,34–41]. However, in addition, there are a number of omnipresent contributions that build a nonspecific potential acting between the two interfaces. Prominent examples of these continuous potentials are the repulsion of the polymers in vesicles and of the glycocalyx of a living cell. Even more generic are Coulomb and hydration forces [42]. Equally important contributions to the intermembrane or membrane-substrate potential are the steric Helfrich repulsion and van der Waals attraction [43,44], but depending on the system, other potentials may also be involved. The presence of this ubiquitous nonspecific potential of course impacts the membrane fluctuations [45], which was well explained close to the unbinding transition [46–48]. When the system is below the critical temperature, a minimum in the potential is found to appear at finite distances [49], from a few up to 150 nm interfacial separations [29,50].

The nonspecific membrane-substrate interactions have been studied in adherent vesicles [29,50]. The difficulty, however, is that during the spreading of the vesicle in a wetting-like process [51], the tension in the vesicle increases, renormalizing the membrane fluctuations and thus the repulsive contribution to the effective potential [52]. In turn, this may affect the position of the minimum of the potential and its strength. Since both are coupled to the vesicle tension, all these parameters must, in principle, be determined self-consistently [49,52,53], as a function of the membrane stiffness. However, this coupling is still not fully understood when the system is of a finite size and away from the unbinding transition.

The effects of direct membrane-substrate interactions were introduced to theoretical modeling by a harmonic potential, whose strength and position are defined by the curvature and the position of the original potential, respectively [32,54]. From there on, this harmonic approximation has been used regularly in membrane-adhesion studies [29,55–57], even though the range of validity of this approximation has not been experimentally verified. Furthermore, the above-described interplay requires simultaneous determination of the tension and the potential strength. However, after the first encouraging attempts [29,55], this task has not been fulfilled successfully until now because of the limitations of available experimental techniques.

We developed an experimental model system with giant unilamellar vesicles, where the membrane is pinned in a controlled geometry, resulting in square-shaped segments within which the membrane-substrate interaction is purely nonspecific [50,58]. In this geometry, the membrane shape and fluctuations can be measured easily with dual-wavelength Reflection Interference Contrast Microscopy (RICM) [50,58], with an exposure time of 51 ms, vertical resolution of 5 nm, and 100 nm pixel size in our setup. Because the size of the patterned square is much larger than the lateral correlation length of the membrane [29], the membrane in the central part of the square is flat, on average, and fluctuates around the minimum of the membrane-substrate interaction potential. As such, this system is ideal to explore the nature and consequences of the nonspecific membrane-substrate interactions and to test the framework of the available theoretical models. However, for quantitative comparison of theory and experiments, finite time and space resolution of the experimental setup need to be integrated into the theoretical analysis.

In this work, we first provide a general theoretical framework to describe the measured fluctuation amplitudes in adherent membranes, taking into account the finite space and time resolution of the setup. This allows us to extract the true fluctuations from the measured apparent fluctuations. We then develop a procedure for determining the membrane tension and the strength of the membrane-substrate interaction potential. Three independent approaches are described: analysis of the shape of the membrane within a grid, analysis of the spatial correlation function, and analysis of the time correlation function. The three approaches yield very similar results with very good accuracy, independent of the choice of measurable. We show that for a holistic description, it is imperative to go beyond the limitations of the harmonic approximation, which particularly affects the average shape of the membrane. Consequently, we obtain the first coherent view of the behavior of the membrane in the vicinity of a substrate.

II. EXPERIMENTAL SETUP

A. Materials

Giant unilamellar vesicles (GUVs) and micropatterned substrates were prepared as described before [50,58]. In brief, GUVs composed from SOPC doped with 2mol% DOPE-PEG2000 and 5mol% DOPE-cap-biotin (Avanti Polar lipids, USA) were prepared by electro-swelling, and they are expected to have a membrane bending stiffness of $\kappa = 20 k_B T$ [2]. Here, k_B is the Boltzmann constant and T is the temperature. Substrates were prepared by microcontact printing of biotin-functionalized bovine serum albumin (BSA) in the form of square grids on ultraclean class cover slides, yielding an average layer thickness of 12 nm. The space within the grid, area 4 μm $\times$ 4 μm, was backfilled with BSA to provide a passive background. The grid itself was further functionalized with neutravidin (NAV). As a result, the biotin in the vesicle membrane binds to the neutravidin on the grid, which then pins the membrane to the pattern, leaving it only subject to the nonspecific membrane-substrate potential within the square and typically spreading over several squares, as observed by RICM (Fig. 1).

B. Imaging and observation

The GUV-substrate interaction was quantified using dual-wavelength Reflection Interference Contrast Microscopy as described before [25,50,58]. The data were acquired on an inverted microscope (Zeiss Axiovert 200, Carl Zeiss, Göttingen, Germany) equipped with a metal halogenide lamp (X-Cite, Exfo, Quebec, Canada), a dual-wavelength interference filter (546 nm and 436 nm), and a filter cube with crossed polarizers for illumination; a 63× Antiflex Plan-Neofluar oil objective; and two separate but synchronized charge-coupled device cameras (CCD cameras) (sensicam qe, PCO, Kehlheim, Germany) for detection in the two wavelength channels. The numerical aperture of illumination was set to 0.54. Typically, 2000 consecutive micrographs with a frame rate of ≃20 Hz were recorded.

C. Analysis

The recorded intensity images in each frame were converted to height maps following the procedure described previously [50,58]. This formalism takes into account all scaffold layers at which refraction occurs, the finite illumination aperture and, furthermore, removes the ambiguities arising from the periodic nature of the intensity-to-height relationship. Ambiguities arising from camera noise in a given pixel were accounted for by requiring space and time continuity [50]. The shape of the membrane patches (averaged over 1250 frames) can be extracted from this analysis (Fig. 1). The height fluctuations for each pixel (defined as the standard deviation of the height from the average, over 1250 frames) can then be extracted.

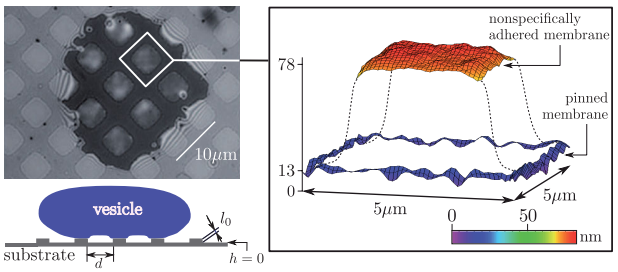

FIG. 1. RICM image of a vesicle pinned to a patterned substrate, with squares within which the membrane fluctuates in the nonspecific potential (upper-left diagram). The lower-left diagram is the schematic view. The reconstruction of the average membrane shape within one square is shown in the right panel. Only segments of a nearly planar membrane were processed to maintain accuracy in the height reconstruction [25]. The color code indicates the height above the substrate positioned at $h = 0$, while l_0 denotes the thickness of the adhesive pattern on the glass substrate. The vertical axis in the right figure is in units of nanometer.

D. Spatiotemporal resolution

The time resolution in this setup is limited by the camera speed, and for the present set of data, it is 51 ms. The lateral, in-plane resolution is about 0.25 μm. The pixel size of 0.1 μm corresponds to slight oversampling, which is advantageous for digital image processing, allowing localization precision of single objects of known shape to about 0.1 μm. The vertical resolution is set by the camera noise. The camera noise in this setup is dominated by the statistical shot noise, which is proportional to the square root of the intensity [25,58]. Typical out-of-plane resolution is 5 nm.

III. THEORETICAL FOUNDATION

We consider a membrane of bending stiffness κ and projected area S put under tension σ in the vicinity of a flat substrate. The membrane profile is parametrized in the Monge representation, whereby the membrane height $h(\mathbf{x})$ is determined for every vector $\mathbf{x}$ residing in the plane of the substrate. Hence, the Hamiltonian of the system can be written in the standard fashion

$$H = \int_S \mathrm{d}\mathbf{x}\left(\frac{\kappa}{2}(\nabla^2 h(\mathbf{x}))^2 + \frac{\sigma}{2}(\nabla h(\mathbf{x}))^2 + V(\mathbf{x})\right). \quad (1)$$

The first term in Eq. (1) is the contribution due to the bending of the membrane. The second term accounts for the surface tension, while the last term in Eq. (1) is related to the membrane-substrate interaction potential $V(\mathbf{x})$. Because of the Helfrich repulsion, this potential diverges at short distances and is dominated by attractive van der Waals interactions at large separations. At intermediate distances, other contributions to the potential may be significant. Nevertheless, a minimum typically appears at an intermediate height h_0, which has so far been reported in the range between 5 nm and 150 nm above the substrate

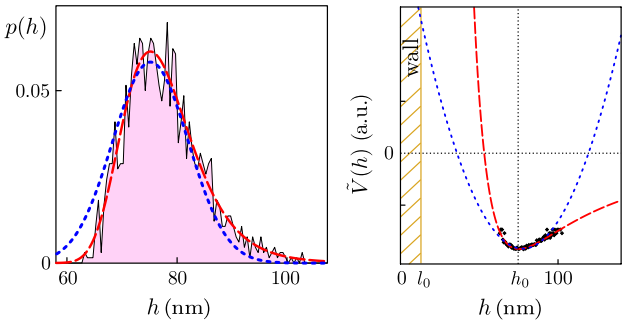

FIG. 2. Experimental height probability distribution (black line) and the respective effective potential (black symbols) are shown in the left and right panels, respectively. Fitting the data with a potential of the Mie or the harmonic form (right), and their Boltzmann factors (left), yields the red dashed and the blue dotted curves, respectively.

[25,44,57–60]. By definition, and independent of its exact form, the direct potential can be related to the height probability distribution at position $\mathbf{x}$ (Fig. 2, left panel),

$$p(h(\mathbf{x})) \sim \int Dh'(\mathbf{x}')\mathrm{e}^{-\mathcal{H}[h'(\mathbf{x}')]/k_\mathrm{B}T}\delta(h'(\mathbf{x}) - h(\mathbf{x})), \quad (2)$$

through a functional integral over all possible membrane profiles weighted by the Boltzmann factor (see Supplemental Material to Ref. [57]).

The above probability distribution can be measured and used to extract the signature of an effective substrate-membrane potential, the latter being defined as $\tilde{V}(h) \equiv -k_\mathrm{B}T \ln p(h)$ (right panel of Fig. 2). Within such a construction, the curvature of the minimum of this effective potential $\tilde{V}''(h_0)$ decreases when the fluctuation amplitude $\langle \Delta h^2 \rangle$ increases (angle brackets denote ensemble averaging), while it depends on all parameters of the entire Hamiltonian, comprising the direct potential, the tension, and the membrane stiffness.

In the current setup, the height probability distribution is obtained by sampling the heights of a small membrane segment in the middle of the square geometry (Fig. 1) to avoid the effects of the boundaries. Here, the image was typically averaged over a 5×5-pixel grid to reduce the effects of the camera noise. This height probability distribution has been evaluated in the literature in more complex systems involving ligand-receptor–mediated adhesion [59] or membranes composed of tertiary mixtures [61]. Therein, a Gaussian distribution of a width given by the mean fluctuation amplitude $\langle \Delta h^2 \rangle$ was used to describe the data, pointing to the quadratic form of the underlying Hamiltonian, which then implies a harmonic form of the direct membrane-substrate potential. Here, we find, for the free membrane segment, small, nevertheless, clear deviations from the Gaussian, whereby fluctuations appear suppressed on the side that is closer to the substrate (Fig. 2). Since the membrane is nearly flat, the quadratic description used for bending and tension terms seems sufficient, and the only term that can induce deviations from the Gaussian distribution is an anharmonic interaction potential.

A convenient way to account for the anharmonicity of the direct potential is to represent it by the (4, 2) Mie potential

$$V_\mathrm{M}(h) = \epsilon\left(\left(\frac{h_0}{h}\right)^4 - 2\left(\frac{h_0}{h}\right)^2\right). \quad (3)$$

Here, ϵ is the strength of the potential in the potential minimum at h_0, and the (4, 2) structure of $V_\mathrm{M}(h)$ has been chosen to facilitate further numerical calculations. This potential diverges at short distances, and following a minimum, it decays algebraically to zero at large distances from the substrate. This captures the key features of the true effective potential. In the two limits (very small and very large distances from the substrate), the Mie potential is, of course, not strictly correct. However, the geometry of the pattern ensures that these two limits are, in practice, not visited by the membrane. Furthermore, the shape of the Mie potential, particularly around the minimum, reproduces the true potential well. Another advantage of the (4, 2) potential is that it is defined by only two parameters, which allows a simple comparison with the harmonic potential.

Even though the physics of the problem suggests a more complex potential, so far theoretical modeling has been restricted to the harmonic approximation of the potential (blue dashed curves in Fig. 2) obtained when

$$V_\mathrm{HA}(h) = \frac{\gamma}{2}(h - h_0)^2 \quad (4)$$

is used in the Hamiltonian. Thereby, the curvature of the harmonic potential γ is the same as that of the Mie form in the minimum, yielding

$$\gamma = 8\epsilon/h_0^2.$$

The appeal for the harmonic approach not only arises from the fact that it results in a Hamiltonian with only quadratic terms, which is then technically easy to handle, but it also maintains consistency between the Monge parametrization (which assumes small curvatures of the membrane) and small (Gaussian) fluctuations around a minimum shape, where each mode is decoupled from others. However, if the membrane is pinned, as is the case in the patten produced herein, the membrane is significantly moved out of the minimum of the potential. This gives rise to relatively large contributions to the overall energetics of the system, and thus, more accurate treatments of the potential may be required. On the other hand, the nearly flat geometry of the pattern secures the accuracy of the Monge representation, and the fourth-order corrections to the bending and tension terms in the Hamiltonian should remain very small.

In the well-established circumstances of the harmonic approximation, the fluctuation amplitude $\langle \Delta h^2 \rangle$ is given by [32]

$$\langle \Delta h^2 \rangle = \frac{k_\mathrm{B}T}{(2\pi)^2}\int \mathrm{d}\mathbf{q}\,\frac{1}{\kappa q^4 + \sigma q^2 + \gamma}, \quad (5)$$

with the notation $\mathbf{q} \equiv (q_1, q_2)$ and $q \equiv |\mathbf{q}|$.

In the bending-dominated regime ($\sigma = 0$), the fluctuation amplitude is given by

$$\xi_\perp^2 \equiv \langle \Delta h^2 \rangle|_{\sigma=0} = \frac{k_\mathrm{B}T}{8\sqrt{\kappa\gamma}}. \quad (6)$$

This particular value for $\xi_\perp^2$ will henceforth be referred to as the vertical correlation length and is shown by the green line in Fig. 3 (left panel). In the tension-dominated regime,

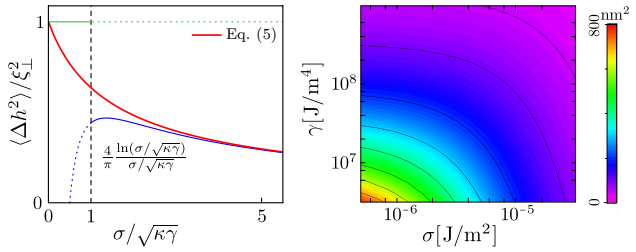

FIG. 3. Left panel: Fluctuation amplitude as a function of the membrane tension (red line). Approximations characteristic of the bending- and tension-dominated regime are shown in green and blue, respectively. Right panel: Fluctuation amplitude as a function of the tension and potential strength. Solid lines are contour lines of constant fluctuation amplitude.

the fluctuation amplitude decays with increasing tension (blue line in Fig. 3, left panel) [32]. However, independently of the parameter range, the fluctuation amplitude depends on both the potential strength and the tension (Fig. 3, right panel). Consequently, additional information about the fluctuation amplitude is necessary to unambiguously determine σ and γ.

One property that is attainable from the experiment is the equilibrium shape of the membrane itself. We reconstruct the shape from the measured data and compare it to the shape calculated theoretically by minimizing the Hamiltonian, Eq. (1). In this case, one could expect that the choice of the interaction potential between the membrane and the substrate may have a significant influence on the obtained result, simply because the harmonic approximation greatly underestimates the repulsion in the proximity of the substrate. On the other hand, small deviations from the Gaussian distribution (Fig. 2) suggest that the fluctuations of the membrane far away from the boundaries could still be treated within the harmonic approximation. These fluctuations may be evaluated through the height probability distribution, as shown above, or through the time correlation function at a given position $\mathbf{x}$,

$$\langle \Delta h(\mathbf{x},t)\Delta h(\mathbf{x},0)\rangle = \frac{k_B T}{(2\pi)^2}\int \mathrm{d}\mathbf{q}\,\frac{\mathrm{e}^{-\Gamma(q)t}}{\kappa q^4+\sigma q^2+\gamma}. \quad (7)$$

Here, $\Gamma(q)$ are mode-dependent damping coefficients for a membrane fluctuating in a potential close to a wall [62],

$$\Gamma(q)=\frac{(\kappa q^4+\sigma q^2+\gamma)}{4\eta q}\times\frac{2(\sinh(qh_0)^2-(qh_0)^2)}{\sinh(qh_0)^2-(qh_0)^2+\sinh(qh_0)\cosh(qh_0)+(qh_0)}, \quad (8)$$

with η being the viscosity of the surrounding fluid.

For the following, we define the lateral correlation length $\xi_\parallel$ and the characteristic correlation time τ^* of the membrane fluctuations,

$$\xi_\parallel \equiv \sqrt{\kappa/\gamma}, \qquad \tau^* \equiv \eta/\sqrt{\kappa\gamma^3}. \quad (9)$$

These values for a tensionless membrane provide the lower ($\xi_\parallel$) and upper (τ^*) bounds for the lateral correlation length and the correlation time, respectively, in the presence of tension. For typical experimental settings, they amount to $\xi_\parallel \simeq 200$ nm and $\tau^* \simeq 0.1$ ms. Under these circumstances, the correlation function given in Eq. (7) can be accurately evaluated only in the central segment of the free membrane patch. Because of the potential influence of the boundaries in the square geometry, two-point spatial correlations are not discussed.

IV. METHODS

In this section, we focus on the development of methods that allow the comparison of theoretical models and experimental measurables [58]. In particular, we calculate the shape of the membrane and relate the true correlation functions to apparent ones, which differ because of the finite resolution of the experimental setup. However, the final, experimentally recorded height integrates effects of thermal noise inherent to the data acquisition techniques, which we also account for in our discussions.

A. Calculation of the membrane shape

The equilibrium shape $\langle h(\mathbf{x})\rangle$ of the membrane has to fulfill the boundary conditions

$$\langle h(\mathbf{x})\rangle|_{\partial S} = l_0 \qquad \text{and} \qquad \nabla\langle h(\mathbf{x})\rangle|_{\partial S} = 0. \quad (10)$$

The first condition fixes the height of the membrane at the edge of the square frame of a surface S. The second condition ensures a finite bending energy of the membrane by requiring a zero contact angle along the frame.

For the calculation of the equilibrium shape $\langle h(\mathbf{x})\rangle$ in the harmonic potential (Fig. 4), with the above set of boundary conditions, the equilibrium shape $\langle h(\mathbf{x})\rangle$ is expanded into a set of orthonormalized functions $\Psi_{ij}(\mathbf{x})$,

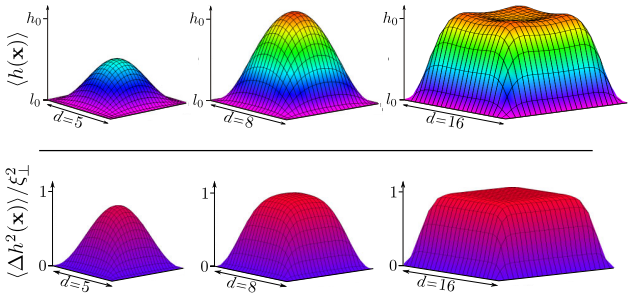

FIG. 4. Membrane in a nonspecific harmonic potential, with the minimum at the height h_0, pinned to a square of an edge length d (in units of $\xi_\parallel$). The universal mean membrane shape and the associated profile of the mean fluctuation amplitude (normalized by $\xi_\perp^2$) are shown in the top and bottom rows, respectively. All profiles are calculated for $\kappa = 20\ \mathrm{k_B T}$, $\sigma = 0$, and $\gamma = 2\times 10^7\ \mathrm{J/m^4}$.

$$\langle h(\mathbf{x})\rangle = \sum_{ij} a_{ij}\Psi_{ij}(\mathbf{x}) + l_0, \tag{11}$$

where each $\Psi_{ij}(\mathbf{x})$ is given by a product of two one-dimensional functions, $\Psi_{ij}(\mathbf{x}) = \psi_i(x_1)\psi_j(x_2)$, with x_1 and x_2 being components of the position vector $\mathbf{x}$. Each ψ_i is a stationary solution of the one-dimensional Hamiltonian [63] and satisfies the relevant boundary conditions. Thus, the membrane shape $\langle h(\mathbf{x})\rangle$ fulfills the boundary conditions for every possible set of expansion coefficients $\{a_{ij}\}$. The optimum shape is found by minimizing the entire Hamiltonian [Eq. (1)] with respect to the entire set $\{a_{ij}\}$.

In the Mie potential, the equilibrium shape cannot be minimized analytically. Therefore, the equilibrium shape is found numerically by discretizing the membrane on a mesh of 100×100 lattice segments and applying a steepest descent optimization to the membrane shape $\langle h(\mathbf{x})\rangle$.

As can be seen from Fig. 5, because the harmonic approximation significantly underestimates the repulsion between the membrane and the substrate, the shape of the profile is significantly different in the two approaches. We find that the harmonic approximation correctly predicts trends in the dependence of the shape on the tension and the potential strength of the membrane, but it cannot be used for quantitative understanding of experimentally obtained profiles. Consequently, anharmonic contributions are absolutely necessary to understand the observed fast decay of shapes close to the edge of the pattern.

B. Membrane fluctuations

The fluctuations in the harmonic potential are calculated in a similar way as the shape: The fluctuations $\Delta h(\mathbf{x}, t)$ of the membrane emerge from the instantaneous membrane conformations as small deviations from the equilibrium shape,

$$h(\mathbf{x}, t) = \langle h(\mathbf{x})\rangle + \Delta h(\mathbf{x}, t). \tag{12}$$

In order to calculate $\Delta h(\mathbf{x}, t)$, the fluctuating profile is expanded into the same set of orthogonal functions as the mean profile,

$$\Delta h(\mathbf{x}, t) = \sum_{ij} b_{ij}\Psi_{ij}(\mathbf{x}). \tag{13}$$

The second variation to the Hamiltonian is then related to the total energy of the fluctuations,

$$\delta^2 H = \frac{1}{2}\sum_{ijkl} b_{ij}E_{ijkl}b_{kl}, \tag{14}$$

with E_{ijkl} being the energy arising from coupling the (ij) with the (kl) mode. The mean-square deviations from the average shape fulfill the equipartition theorem, $\langle b_{ij}b_{kl}\rangle = k_{\mathrm{B}}T(E^{-1})_{ijkl}$, and thus

$$\langle \Delta^2 h(\mathbf{x})\rangle = k_{\mathrm{B}}T\sum_{ijkl}\Psi_{ij}(\mathbf{x})(E^{-1})_{ijkl}\Psi_{kl}(\mathbf{x}). \tag{15}$$

Consequently, the profile of the mean-square fluctuation amplitude can be evaluated numerically by determining the tensor E_{ijkl} (Fig. 4).

For determining the membrane fluctuations in the Mie potential, we use the same approach as for the fluctuations in the harmonic potential, which requires finding the second variation of the Hamiltonian with respect to the appropriate equilibrium shape (e.g., left panel in Fig. 5). In the current case, $V_M(h)$ is no longer harmonic, and the curvature of the potential affecting membrane fluctuations depends on the height that the membrane achieves along the profile. To obtain the second variation of a given profile $h(\mathbf{x})$, we thus expand $V_M(h)$ in orders of $\Delta h(\mathbf{x}, t)$, which results in a $\delta^2 H$ that is of the same form as in Eq. (14) and contains implicitly a distance-dependent γ_M given by the scaling function $g(\langle h(\mathbf{x})\rangle)$,

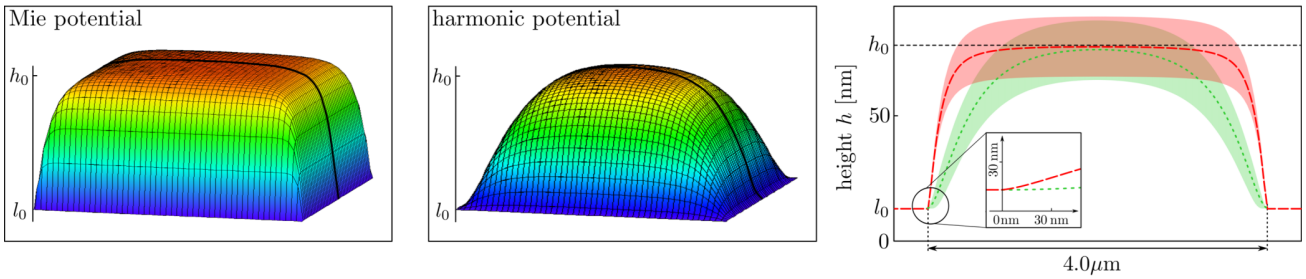

FIG. 5. Comparison of the mean membrane profile of a membrane residing in a Mie potential (left panel) and a harmonic potential of identical curvature (middle panel). The cross section through the center of the shapes is also shown, enveloped by the mean fluctuations of the shape (right panel). The profile associated with the Mie potential is shown in red, while the profile in the harmonic potential is shown in green. The inset shows a detailed view of the membrane shape near the pinning point. The shapes are determined for $\sigma = 6.6 \times 10^{-6}$ J/m^2 and $\gamma = 3.3 \times 10^7$ J/m^4, and $h_0 - l_0 = 65$ nm, as for vesicle segments shown later in Fig. 10.

$$\gamma_M \equiv V_M''(\langle h(\mathbf{x})\rangle) = \gamma g(\langle h(\mathbf{x})\rangle) = \frac{\gamma h_0^2}{4\langle h(\mathbf{x})\rangle^2}\left[10\left(\frac{h_0}{\langle h(\mathbf{x})\rangle}\right)^4 - 6\left(\frac{h_0}{\langle h(\mathbf{x})\rangle}\right)^2\right]. \quad (16)$$

For the membrane resting in the minimum h_0, the scaling function becomes unity, and thus, the fluctuations of an unbound membrane in the $V_M(h)$ are exactly the same as in the harmonic potential. For any height of the membrane somewhere between h_0 and l_0, the scaling function significantly increases the effective potential strength γ_M, resulting in strongly suppressed fluctuation amplitudes when the membrane deviates from the minimum of the potential (right panel in Fig. 5).

C. Accounting for the finite resolution of the acquisition system

Measuring membrane fluctuations is the key to determining the physical parameters of the system [1,53,54]. However, because of the finite temporal and spatial resolutions of the experimental techniques, only apparent fluctuation amplitudes are measured that may significantly differ from true fluctuations of the membrane (Fig. 6).

Because of a finite time resolution, modes with a lifetime smaller than τ^* cannot be detected. In the current system, spatial resolution almost matches the lateral correlation length $\xi_\parallel$, whereas the integration time by far exceeds the correlation time τ^*. Therefore, temporal integration has a particularly large effect (Fig. 6). Certain specialized techniques can create faster recording of intensity fluctuations [8,64,65], but these techniques acquire the information on the state of the membrane only in a single point and are not compatible with spatial imaging of the membrane. Consequently, developing procedures to interpret the measured fluctuations become imperative.

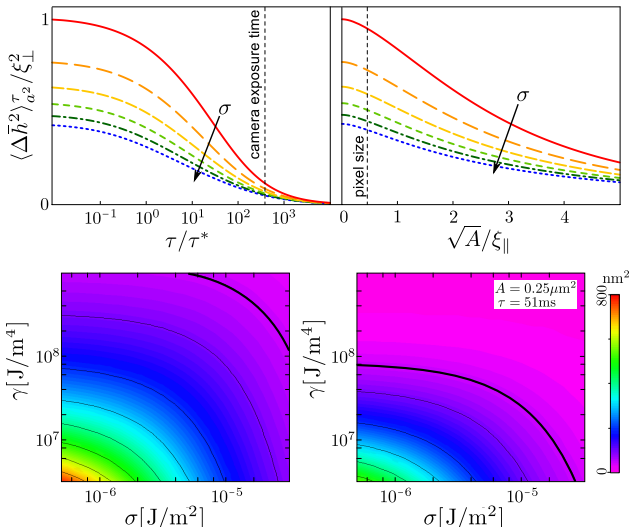

FIG. 6. Normalized apparent fluctuation amplitude as a function of temporal (upper left panel) and spatial resolution (upper right panel). The tension increases (in the direction of the arrow) from $\sigma = 0$ to $5\sqrt{\kappa\gamma}$. The true and the apparent fluctuation amplitudes are shown in the bottom left and bottom right panels, respectively. The latter has been calculated for a fixed integration time of $\tau = 51$ ms and is averaged over an area of $A = 0.5\ \mu\text{m} \times 0.5\ \mu\text{m} = 0.25\ \mu\text{m}^2$. Contour lines of constant mean-square fluctuation amplitudes are indicated. Specifically, the contour lines of the true and apparent fluctuation amplitude of 50 nm^2 are presented by the thick lines.

The effects of the temporal resolutions were first taken into account for the spectra obtained from measuring the fluctuations of the contour of a freely suspended giant vesicle [66]. Thereby, the vesicle shape was parametrized by spherical functions, and the temporal average of the time-dependent correlation function was performed. Here, we adapt this procedure to a situation where a flat segment of the membrane parametrized in the Monge representation fluctuates close to the wall. Consequently, the effects of the nonspecific potential are taken into account, and averaging is performed with the appropriate damping coefficients, given by Eq. (9).

The spatial averaging occurs because of the finite lateral resolution of the experiment. The camera averages the signal over an area A, and only fluctuation modes with a wavelength larger than $\sqrt{A}$ can be fully resolved.

As discussed, smearing the true membrane height at the position $\mathbf{x}$ and at the time t gives rise to the apparent membrane height $\bar{h}_A^\tau(\mathbf{x}, t)$, whereby the subscript A and the superscript τ indicate the spatial and temporal integration of the given measurement, expressed in square microns and milliseconds, respectively,

$$\bar{h}_A^\tau(\mathbf{x}, t) = \int_0^\tau \frac{\mathrm{d}t'}{\tau}\int_A \frac{\mathrm{d}\mathbf{x}'}{A} h(\mathbf{x}+\mathbf{x}', t+t'). \quad (17)$$

From Eq. (17), it is straightforward to derive the apparent time correlation function

$$\langle\Delta\bar{h}(\mathbf{x}, t)\Delta\bar{h}(\mathbf{x}, 0)\rangle_A^\tau = \int_0^\tau\int_0^\tau \frac{\mathrm{d}t_1'\mathrm{d}t_2'}{\tau^2}\iint_A \frac{\mathrm{d}\mathbf{x}_1'\mathrm{d}\mathbf{x}_2'}{A^2}\langle\Delta h(\mathbf{x}+\mathbf{x}_1', t+t_1') \times \Delta h(\mathbf{x}+\mathbf{x}_2', t+t_2')\rangle. \quad (18)$$

The true time correlation function $\langle\Delta h(\mathbf{x}, t)\Delta h(\mathbf{x}, 0)\rangle$ in real space is given in Eq. (7). The apparent time correlation function is found in Fourier space,

$$\langle\Delta\bar{h}(\mathbf{x}, t)\Delta\bar{h}(\mathbf{x}, 0)\rangle_A^\tau = \frac{k_\mathrm{B}T}{(2\pi)^2}\int \mathrm{d}\mathbf{q}\,\frac{\mathrm{e}^{-\Gamma(q)t}}{\kappa q^4 + \sigma q^2 + \gamma}\phi_A(\mathbf{q})\psi^\tau(\mathbf{q}), \quad (19)$$

as the convolution of the true correlations with the effects of the temporal and spatial averaging. Here, $\psi^\tau(\mathbf{q})$ is a function of the time component

$$\psi^{\tau}(\mathbf{q}) \equiv \int_0^{\tau}\int_0^{\tau}\frac{\mathrm{d}t_1'\mathrm{d}t_2'}{\tau^2}\mathrm{e}^{-\Gamma(\mathbf{q})|t_1'-t_2'|} = \frac{\mathrm{e}^{-\Gamma(q)\tau}-1+\Gamma(q)\tau}{\Gamma^2(q)\tau^2} \tag{20}$$

and $\phi_A(\mathbf{q})$ of the spatial component

$$\phi_A(\mathbf{q}) \equiv \iint_A \frac{\mathrm{d}\mathbf{x}_1'\mathrm{d}\mathbf{x}_2'}{A^2}\mathrm{e}^{-i\mathbf{q}(\mathbf{x}_1'-\mathbf{x}_2')}. \tag{21}$$

In principle, one could use any form of the patch A. In the special case of a square geometry of the adhesion pattern, it is convenient to follow the boundaries and keep the square geometry for the averaging procedure, which results in

$$\phi_A(\mathbf{q}) = \frac{16}{A^2}\frac{\sin(\frac{\sqrt{A}q_1}{2})^2\sin(\frac{\sqrt{A}q_2}{2})^2}{(q_1q_2)^2}. \tag{22}$$

For perfect temporal resolution, $\tau \to 0$ and $\psi^0(\mathbf{q}) \to 1$. Likewise, for perfect spatial resolution, $A \to 0$ and $\phi_0(\mathbf{q}) \to 1$. For objects of known shape, one could improve this procedure by using a more complex optical resolution function to deconvolute correlations between neighboring pixels [67].

The apparent mean-square fluctuation amplitude easily emerges from Eq. (19) for $t = 0$ as

$$\langle\Delta\bar{h}^2\rangle_A^{\tau} = \frac{k_\mathrm{B}T}{(2\pi)^2}\int \mathrm{d}\mathbf{q}\frac{1}{\kappa q^4+\sigma q^2+\gamma}\phi_A(\mathbf{q})\psi^{\tau}(\mathbf{q}). \tag{23}$$

In Fig. 6, we show the influence of temporal and spatial averaging of true fluctuations. The results show that the finite resolution of the experiment affects the apparent fluctuation amplitude by making it systematically smaller. Furthermore, we find that the limitations of the experimental technique have larger effects in systems subject to larger tensions and stronger interaction potentials.

D. Accounting for the background noise of the acquisition system

Another effect that impacts the experimental data is that of the background noise $\chi(\mathbf{x}, t)$ of the acquisition system. In the case of optical microscopy, the latter arises mostly from the intensity-dependent fluctuations in the number of photons reaching the detector. In principle, this shot noise is Poisson distributed, but because of the high number of photons detected in a typical RICM experiment, it can be treated as Gaussian distribution, leading to the noise increase with the square root of the intensity [50,58].

As the membrane height and the noise are assumed to be independent, the measured instantaneous membrane profile $\tilde{h}_A^{\tau}(\mathbf{x}, t)$ is given by

$$\tilde{h}_A^{\tau}(\mathbf{x}, t) = \bar{h}_A^{\tau}(\mathbf{x}, t) + \bar{\chi}_A^{\tau}(\mathbf{x}, t). \tag{24}$$

The first term on the right-hand side is the apparent height, and the second term is the contribution from the apparent noise, whereby the latter emerges from temporal and spatial averaging of the background noise $\chi(\mathbf{x}, t)$, over the time τ and area A, respectively. Similarly, the measured fluctuation amplitude of the membrane $\langle\Delta\tilde{h}^2(\mathbf{x})\rangle_A^{\tau}$ is the sum of the apparent membrane fluctuation amplitude [Eq. (23)], and the variance $\langle\bar{\chi}^2(\mathbf{x})\rangle_A^{\tau}$ is the ensemble average of the apparent noise,

$$\langle\Delta\tilde{h}^2(\mathbf{x})\rangle_A^{\tau} = \langle\Delta\bar{h}^2(\mathbf{x})\rangle_A^{\tau} + \langle\bar{\chi}^2(\mathbf{x})\rangle_A^{\tau}. \tag{25}$$

The time component of the apparent noise goes with $\sqrt{\tau}$, since it scales with the square root of the number of photons detected [50,58].

For a pixelated image, the height can be measured only at discrete positions $\mathbf{x}_i$, and the spatial resolution imposes the minimum area for averaging to be $A_{\mathrm{px}} = a^2$. As such, the measured height $\tilde{h}_{A_{\mathrm{px}}}^{\tau}(\mathbf{x}_i, t)$ of a single pixel inherently incorporates temporal and spatial averaging of noise on a level of a pixel $\bar{\chi}_{A_{\mathrm{px}}}^{\tau}(\mathbf{x}_i)$, the latter being of a particular background intensity.

We consider a segment of a pixelated membrane of an area A. This area can be of arbitrary shape as long as it consists of N pixels of identical background intensity (e.g., identical average height) for which noise is uncorrelated. In that case, the apparent noise is

$$\langle\bar{\chi}(\mathbf{x}_i)^2\rangle_A^{\tau} = \frac{1}{N^2}\sum_{\mathbf{x}_k,\mathbf{x}_l\in A}\langle\bar{\chi}_{A_{\mathrm{px}}}^{\tau}(\mathbf{x}_i+\mathbf{x}_k)\bar{\chi}_{A_{\mathrm{px}}}^{\tau}(\mathbf{x}_i+\mathbf{x}_l)\rangle = \frac{1}{N^2}\sum_{\mathbf{x}_k,\mathbf{x}_l\in A}\langle\bar{\chi}^2\rangle_{A_{\mathrm{px}}}^{\tau}\delta_{kl} = \frac{1}{N}\langle\bar{\chi}^2\rangle_{A_{\mathrm{px}}}^{\tau} = \frac{a^2}{A}\langle\bar{\chi}^2\rangle_{A_{\mathrm{px}}}^{\tau}. \tag{26}$$

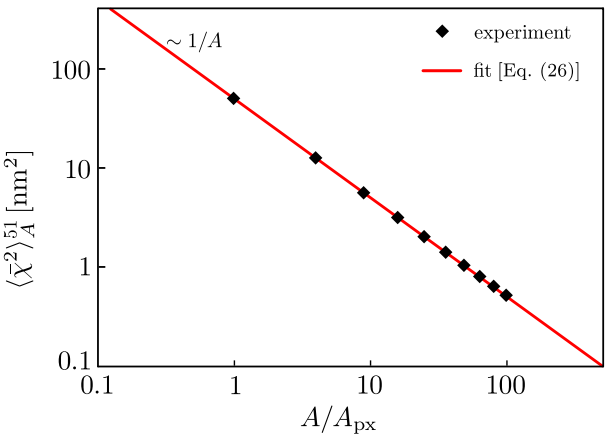

FIG. 7. The mean-square amplitude of the camera noise averaged over an area A containing N pixels of area A_{px}. The noise decreases exceptionally well with $1/A \sim 1/N$, proving the camera noise is independent for different pixels.

Here, we sum over all pixels within the considered area A. This result shows that averaging over several pixels may decrease the effect of the camera noise to negligible levels. For example, for the current experimental conditions, the variance of the apparent mean-square amplitude of the camera noise drops below 3 nm^2 upon averaging over 25 pixels (Fig. 7).

V. RESULTS

In the following, we develop three approaches to simultaneously determine the membrane tension σ and the strength γ of the membrane-substrate interaction potential. The common denominator to all of the approaches is determining the true mean fluctuation amplitude from the measured one. Thereby, it is assumed that the membrane resides in the minimum of the potential, which is well justified by the flatness of the membrane profile in the shape reconstruction (Fig. 1).

Determining the true fluctuation amplitude isolates the correct contour line (lower panel in Fig. 6). However, additional information is necessary to resolve the interdependence of $\langle \Delta h^2 \rangle$ on σ and γ. Such information can be provided by determining the shape of the membrane or the correlations. In the general case of adherent membranes, not all of these parameters can be determined, and the particular availability depends on the particular experimental situation. In the current setup, all possible measures are obtained simultaneously because of the particular design of the system. This allows us to take one measure at a time, deconvolve σ and γ, and compare the obtained results from different choices. However, if the theoretical model is complete, σ and γ are independent of the approach. Inability to obtain systematic values of the tension and the potential strength should point either to deficiencies of the theoretical description or to problems with the experimental technique.

A. Approach 1: Systematic spatial averaging

Within this approach, the measured fluctuation amplitude $\langle \Delta \tilde{h}^2(\mathbf{x}) \rangle_A^\tau$ of a flat segment of the membrane is determined as a function of the averaging area A. Thereby, A is varied by systematically increasing the number of pixels in the observed membrane segment (1×1 px, 2×2 px, 3×3 px, etc.), around the central pixel in the frame. This results in a square of length $a = 0.1\ \mu\mathrm{m}\sqrt{N}$, N being the number of pixels, for which the spatially averaged height $\tilde{h}$ is determined in each instance of time. This provides a sequence from which the mean height $\langle \tilde{h} \rangle_A^\tau$ and the mean-square deviation $\langle \Delta \tilde{h}^2(\mathbf{x}) \rangle_A^\tau$ are determined for each choice of a. The obtained data are shown with symbols in Fig. 8. To avoid influences from the boundaries, we restrict the total area of interest to a square of 1 μm^2 in the center of the pattern.

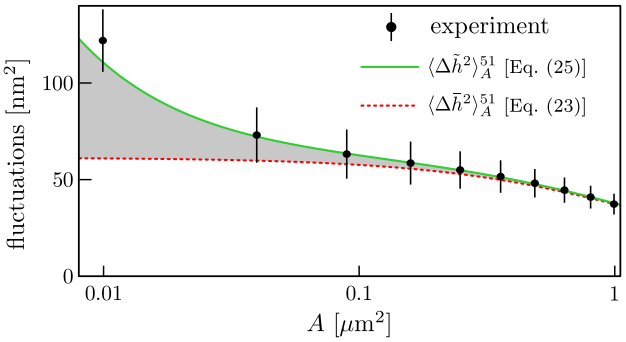

FIG. 8. Determining the tension and the potential strength by systematic spatial averaging over a square of area A. The best fit results in $\sigma = 5.0 \times 10^{-6}$ J/m^2 and $\gamma = 3.7 \times 10^7$ J/m^4.

To determine the tension and the potential strength, Eq. (25) is fitted to the data, with σ and γ being the fit parameters (Fig. 8). Thereby, the contribution from the apparent fluctuation in Eq. (25) is given by Eqs. (20), (22), and (23), whereas the contribution of the noise $\langle \bar{\chi}^2 \rangle_A^\tau$ is determined independently, for a pixel of the equivalent brightness. If the contribution from the noise is not known *a priori*, the procedure could be applied with a fit with three free parameters.

For the particular vesicle adhered to a pattern, as shown in Fig. 1, the camera noise is found to be $\langle \bar{\chi}^2 \rangle_A^\tau = 49$ nm^2. The systematic spatial averaging gives $\sigma = 5.0 \times 10^{-6}$ J/m^2 and $\gamma = 3.7 \times 10^7$ J/m^4. Thereby, the accuracy of the fit provides the mean-square amplitudes within the error bar of the experiment.

B. Approach 2: Time-dependent correlation function

Despite the somewhat limited time resolution of the setup, a quite sensitive approach to determining the tension and the nonspecific potential is fitting the measured time-dependent correlation function $\langle \Delta \tilde{h}(\mathbf{x}, t) \Delta \tilde{h}(\mathbf{x}, 0) \rangle$. The latter is still sensitive to the spatial resolution. It is instructive to use relatively large segments of the membrane to decrease the effects of the camera noise. Hence, we typically consider an area consisting of 5×5 pixels for which the spatial average height is calculated in each instance of time. This provides a sequence of heights $\tilde{h}(\mathbf{t})$ from which the time correlation function is calculated.

The reason for this sensitivity is the course of the time-dependent correlation function over a temporal regime (from $t = 0$ to $t < 3$ s). Within this range, the correlations decay from the fluctuation amplitude $\langle \Delta \tilde{h}^2 \rangle$ and ultimately reach zero. Therefore, the fitting curve has to match three characteristics: the fluctuation amplitude for $t = 0$, which is the mean fluctuation amplitude $\langle \Delta \tilde{h}^2 \rangle_A^\tau$; the long-time behavior (visible beyond $t \simeq 1$ s); and the characteristic decay time (see Fig. 9). These stringent restrictions make it rather simple to find appropriate parameters.

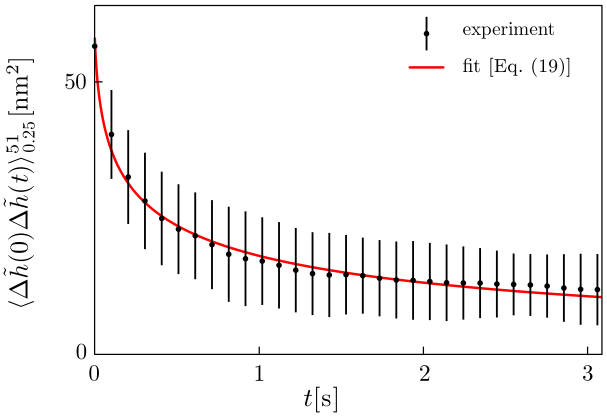

FIG. 9. Measured temporal correlation function (every second data point presented) is fitted with the expression given in Eq. (19). The fitting procedure provides $\sigma = 13.0 \times 10^{-6}$ J/m^2 and $\gamma = 1.0 \times 10^{7}$ J/m^4.

Data fitting is performed by applying Eq. (20), with σ and γ being the free parameters. The best fitting values for averaging over $N = 25$ pixels are $\sigma = 13.0 \times 10^{-6}$ J/m^2 and $\gamma = 1.0 \times 10^{7}$ J/m^4, for the case of the vesicle discussed in approach 1.

C. Approach 3: The membrane shape

The last available free parameter is the very shape of the membrane. The membrane is expected to be flat and in the minimum of the potential. Hence, we obtain a large segment of the membrane. However, the regions along the pattern (dark areas in Fig. 1) can be regarded as a membrane residing in a different state, the latter being characterized by an effectively much stronger potential with a minimum very close to the substrate. The experimental design imposes the geometry and hence the occurrence of the two states. The transition of the membrane between the two states occurs within the pattern, providing a membrane interface that is, in principle, subject only to nonspecific interactions. Because the height difference between the two states is of the order of 50 nm, the deviations from the minimum of the effective nonspecific potential can no longer be regarded as small, necessitating the systematic use of the Mie potential.

The fitting procedure is performed in two steps. We first determine the mean fluctuation amplitude of the membrane $\langle \Delta\tilde{h}^2 \rangle_A^\tau$ in the center of the weakly adhered fragment of the membrane. Thereby, it is preferable to choose large A ($A = 0.25\ \mu$m^2) to avoid effects of the camera noise. Determining the mean fluctuation amplitude reduces the choice of σ and γ to a particular subset of values presented by the relevant contour line (Fig. 6). In the second step, a family of shapes with σ and γ along the contour line is calculated, and the shape of the smallest mean-square deviation from the experimental shape is determined. The best fitting shape ascertains σ and γ, whereby no additional constraints were imposed. For the vesicle treated in approaches 1 and 2, this procedure provides the shape shown in Fig. 10, which is associated with $\sigma = 6.6 \times 10^{-6}$ J/m^2 and $\gamma = 3.0 \times 10^{7}$ J/m^4.

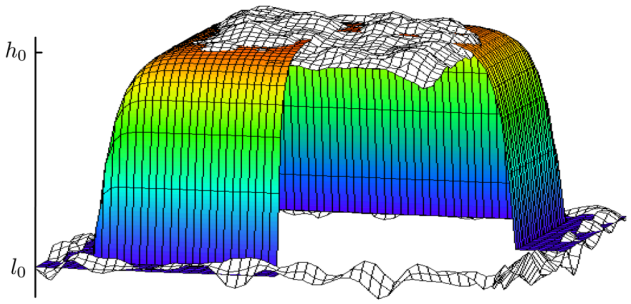

FIG. 10. Fitting the theoretically obtained mean shape (colored) to the experimentally determined mean profile of the membrane (gray). The best fit is found for $\sigma = 6.6 \times 10^{-6}$ J/m^2 and $\gamma = 3.0 \times 10^{7}$ J/m^4.

From the experimental point of view, it is only possible to reconstruct shapes of sufficient planarity at this stage. However, this affects the model reconstruction only slightly. Because the membrane in both adhesion states reaches the minimum of the potential at zero angles, the large section of the steep profile must be nearly linear. Hence, obtaining the width of the interface is almost equivalent to determining the overall shape. Here, the strong repulsion from the substrate in the Mie potential promotes steep interfaces, which is not the case for the harmonic potential. It is also worth noticing that the camera noise has no effect on the measured mean shape since $\langle \chi \rangle = 0$.

VI. DISCUSSION

In this work, we presented three independent methods to determine the strength of the nonspecific potential and the tension of membranes that weakly adhere in homogeneous potentials. All three methods were applied to the same sets of data, allowing for the first time, to our knowledge, the direct comparison between various approaches. After accounting for experimental limitations, all procedures provide values within the same order of magnitude for both the tension and the interaction potential strength, as can be seen in Fig. 11 and the related table. This is particularly important for the determination of the relevant parameters in more complex experimental situations where only one of these procedures can be used, depending on the circumstances.

To estimate the reliability of each approach, we first split the data into several subsamples, i.e., shorter time sequences of the membrane height, and perform the analysis on each subsample. From the set of results of the fits on the subsamples, we calculate the mean tension and potential strength, as well as their uncertainties, as the standard deviations from the means (shown as error bars in Fig. 12).

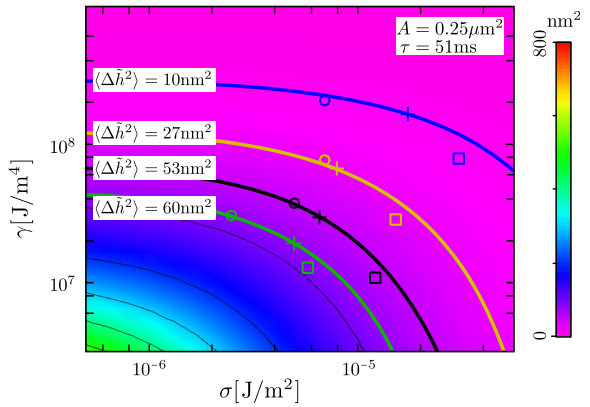

Method	σ [10^{-6}J/m^2]	γ [10^7J/m^4]
Systematic spatial averaging	5.0	3.7
Time correlations	13.0	1.0
Shape fitting	6.6	3.0

FIG. 11. A comparison of fitting procedures for a single vesicle is shown in the table and for four vesicles in the graph. The vesicle discussed in the manuscript and fittings shown in Figs. 7–10 is indicated by black lines and symbols. Circles denote results of determining the potential strength and the tension by the method of systematic averaging, while crosses and squares are obtained by fitting the shape and the time-dependent correlation function, respectively. Results of all fitting procedures for each vesicle lie very close to the appropriate contour line.

We present the outcome of this procedure for one patch with the low fluctuation amplitude and one patch with the high fluctuation amplitude [Fig. 12(a)]. We find the obtained uncertainties to be relatively small if the subsamples are sufficiently long (about 25 s), and the agreement between methods is better at higher fluctuation amplitudes. The single measurement associated with the entire sequence typically falls within the uncertainty of the mean obtained with each method. This, together with the good reproducibility of the fit results between the subsamples, strongly corroborates the reproducibility of results obtained by each method independently. Importantly, we find the uncertainties to be smaller than the uncertainty arising from the intrinsic experimental errors [25,50,58] and of the same magnitude as the uncertainty in determining the contour line in the phase diagram. Specifically, the small slope of the contour line suggests large uncertainties in the tension, while the large slope of the contour line is reflected in larger uncertainties in the potential strength. This is true even though determining the contour line is independent of the fitting procedures, at least in the case of spatial averaging and the time correlations. In the case of the latter, the tension is the most difficult to determine accurately because the contour line is nearly flat.

Another instructive analysis is to compare the results obtained from different squares on the same vesicle, where at least the tension is expected to be same. This analysis is

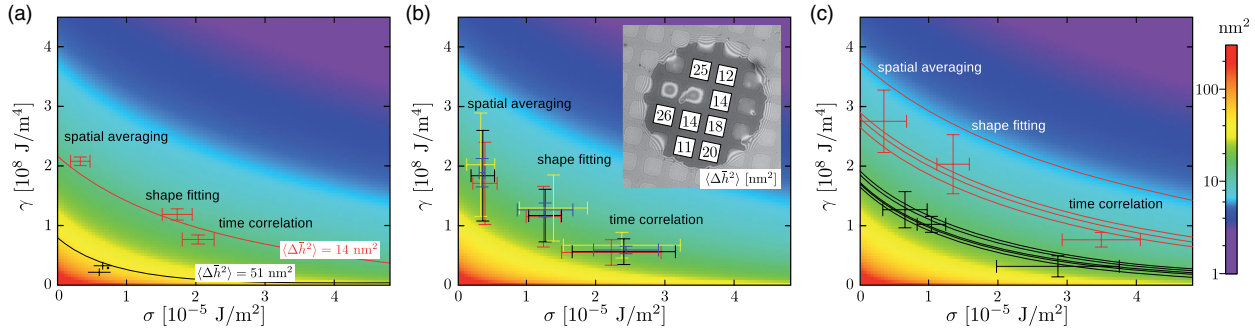

FIG. 12. Analysis of the reliability of the three approaches presented for extracting the potential strength and the tension in the membrane. The apparent fluctuation amplitude as a function of the potential strength and tension is shown as a background of each graph. The color code is given on the right. Contours associated with the apparent mean fluctuation amplitudes that are particular to each data set are displayed with solid lines. In all panels, the spatial and temporal averaging is performed with $A = 0.25$ μm^2 and $\tau = 0.51$ ms, respectively. (a) Mean values and standard deviations (error bars) associated with performing the analysis on several data recordings from the same patch. Results are presented for one patch with the low (red) and one patch with the high (black) mean apparent fluctuation amplitude (indicated by numbers on the relevant contour line). (b) Mean values and standard deviations associated with averaging the fit results over the eight patches on one vesicle. The patches and the vesicle are shown in the inset by a white square. The numbers within the squares indicate the apparent mean membrane fluctuation amplitude $\langle\Delta\tilde{h}^2\rangle$ for the particular membrane segment in units of nm^2. The analysis was performed on two short data sequences (two subsamples shown in red and yellow) and on a long sequence (black symbols). The results of averaging over three squares with the mean apparent fluctuation amplitude between 14 and 18 nm^2 are shown in blue. (c) Mean values and standard deviations associated with averaging over fitting results from membrane patches with similar mean apparent fluctuation amplitudes on different vesicles. The results for patches with small fluctuation amplitudes, ranging from 6 to 11 nm^2, are shown in red, while the results for large fluctuations, ranging from 18 to 20 nm^2, are shown in black.

presented in Fig. 12(b) for a vesicle that exhibits a statistically significant spread in mean fluctuation amplitudes of the patches, pointing to small variations in the substrate coating. The tension and the potential strength are found as the mean of values obtained from independent fits over eight squares (shown in the figure). Two short subsamples (red and yellow symbols) are compared to one long sequence (black symbols). The results from each subsample reproduce the results over the whole sequence, supporting the finding discussed above [Fig. 12(a)]. Interestingly, if the average is performed only over patches with a similar mean fluctuation amplitude (16 ± 2 nm^2), then the uncertainty in determining the effective potential with each method drops significantly [blue symbols in Fig. 12(b)], suggesting that the substrate is similarly coated below these parts of the vesicle. Apart from further confirming the reproducibility of our approaches used for data analysis, this investigation is indicative of the uniformity of the substrate. Actually, one could infer that the sensitivity in determining the uniformity of the substrate coating obtained by measuring the membrane fluctuations is significantly larger than that of other, more-established methods.

Finally, we analyze patches from different vesicles, which were all prepared in the same way. Here, one expects that patches with similar fluctuation amplitudes will yield similar values for the potential strength and tension, which is indeed the case [Fig. 12(c)]. This agreement is very important, as it clearly demonstrates the overall reproducibility of each approach independently and justifies their individual application when suitable. In this context, the spatial averaging method is perhaps the most limited, as it relies on relatively significant, apparent fluctuations of the membrane (weaker potentials and/or tensions). This is simply because at small fluctuation amplitudes, the averaging curve (Fig. 8) flattens very quickly, which affects the sensitivity of the fit.

Out of all three methods, obtaining the parameters from the shape may be technically most challenging, as it requires a nontrivial boundary problem to be solved numerically. As the first step in this procedure is determining the mean-square fluctuation amplitude, the fitting results for σ and γ of this method are always exactly on the contour lines in Fig. 11. Despite its somewhat technical nature, this method clearly points to limitations of the commonly used harmonic approximation. Here, we showed that systematic values of the tension and the potential strength can be obtained only after making a more appropriate approximation for the direct membrane-substrate potential. A simple harmonic approximation would systematically provide lower tensions and higher interaction potentials to provide a shape that reaches the minimum of the potential sufficiently fast. The difference in σ and γ may amount to a couple of orders of magnitude in a certain parameter range.

Even though all methods provided result within the same order of magnitude, the spatial averaging systematically provides the highest values of the potential strength and the smallest tension, while the time correlation function provides the opposite, all with uncertainties that are smaller than the differences between the means associated with different methods. While the spatial averaging and the shape fitting rely exclusively on the equilibrium properties of the system (and provide similar results if the anharmonic potential is taken into account), the construction of the time correlation function requires the correct reconstruction of the hydrodynamic interactions of the membrane with the surrounding fluid, the latter based in q-dependent damping coefficients for the membrane close to the substrate [62]. The observed systematic deviations of about a factor of 2 suggest that, despite good agreement, a more in depth study of time correlations may be required before the behavior of the membrane can be fully resolved from the theoretical point of view. This analysis, which combines modeling and experiments, should clarify the role of a potential volume constraint that was previously evoked in connection with the shape and fluctuations of adherent membranes [37]. On this note, our data suggest that changes in osmotic conditions will affect the volume below the patch, whereby we did not acquire any conclusive evidence that the volume constraint affects membrane fluctuations around an equilibrated shape. However, only a few modes are affected by the volume constraint in the square geometry, and hence different, more restrictive patterns should be used to fully understand its role.

VII. CONCLUSIONS

The framework presented herein provides a set of tools for a systematic study of membrane-substrate interaction potentials, which is a key step toward the understanding of the decades-old puzzle arising from inconsistencies in predictions and measurements of both the position of the minimum and the strength of the nonspecific potential. We have shown that this inconsistency can be removed to a large extent if a more realistic potential is used to reconstruct the shape of the membrane. For this purpose, we have chosen the (4, 2) Mie potential. Alternatively, we could have used the complete potential constructed by the superposition of the steric, hydration, van der Waals, and other potentials. Such an approach would have the advantage of connecting the material properties of the system to the current description. While we have shown previously that it is possible to account for some of the qualitative behavior of the membrane within this superposition approach (change of the position of the minimum while modulating the membrane tension), we have also shown that the individual potentials are associated with a number of unknown parameters, including the Hamaker constant, which cannot be measured independently [58]. In contrast, the (4, 2) Mie potential used here has the advantage of

being defined by only two parameters, yet it captures the key features of the true effective potential, particularly around the minimum. Of course, very close to and very far from the substrate, this potential is not correct. However, these two limits are irrelevant in practice because they are not visited by the membrane. Actually, the potential minimum is at relatively large distances from the substrate, and it is associated with relatively small fluctuation amplitudes. This result was also reported previously in Refs. [29–31,50]. This may be a hint that the very approach of constructing the complete potential by superimposing the contributing potentials may be questionable and that further studies of this potential are necessary. Our work here provides the key prerequisites for these next steps.

Irrespective of such details of the potential, we showed that the theoretical framework must be extended to account for anharmonic potentials. The first piece of evidence came from the reconstruction of the membrane shape. This method provided the membrane tension and potential strength consistent with the two methods relying on fluctuations only if the anharmonicity is taken into account. Some information about the functional form of the effective potential could be obtained by systematically inducing shape changes, yet the accuracy of such an approach is to be determined in the future.

The second piece of evidence for the anharmonic contributions came directly from measuring membrane fluctuations around the minimum (see Fig. 2). The latter can be reconstructed with great accuracy, and the RICM is particularly well suited for these measurements. Again, systematic changes of system parameters would be necessary to gain deeper insight into the functional form of the effective potential, which will be a focus of further studies.

The true strength of our approach is, however, to insist on the consistency between various methods. Actually, it was exactly this requirement that pointed to the insufficiency of the harmonic description. The notable discrepancy between equilibrium analysis and dynamic analysis suggests a further need for refinement of the theoretical treatment of hydrodynamic interactions.

In conclusion, determining the nonspecific potential between the membrane and another surface is a difficult problem because of the coupling between the membrane tension, the steric repulsion, and the direct interactions. Apart from putting into perspective the commonly used approximations, the work presented herein unambiguously shows that even small potentials affect the shape and the dynamics of the membrane significantly, suggesting that this potential needs to be treated earnestly in intermembrane and membrane-substrate studies. One of the problems in the past has been the lack of consistency in experimental results. With this work, this predicament can be fully circumvented, allowing us to tackle the conceptual challenge of understanding this elusive, yet so effective potential.

ACKNOWLEDGMENTS

We thank Susanne Fenz for useful discussions. A. S. S. and T. B. acknowledge the funding of the Cluster of Excellence: Engineering of Advanced Material at the University of Erlangen and the ERC StG 2013-337283 MembranesAct. C. M. is grateful for the support of the Deutsch-Franzsische Hochschule and the Exzellenzcluster Cellnetworks at the University of Heidelberg.

[1] F. Brochard and J. F. Lennon, *Frequency Spectrum of the Flicker Phenomenon in Erythrocytes*, J. Phys. (Les Ulis, Fr.) **36**, 11 (1975).

[2] E. Evans and W. Rawicz, *Entropy-Driven Tension and Bending Elasticity in Condensed-Fluid Membranes*, Phys. Rev. Lett. **64**, 2094 (1990).

[3] A. Zidovska and E. Sackmann, *Brownian Motion of Nucleated Cell Envelopes Impedes Adhesion*, Phys. Rev. Lett. **96**, 048103 (2006).

[4] A. E. Pelling, F. S. Veraitch, C. P.-K. Chu, B. M. Nicholls, A. L. Hemsley, C. Mason, and M. A. Horton, *Mapping Correlated Membrane Pulsations and Fluctuations in Human Cells*, J. Mol. Recognit. **20**, 467 (2007).

[5] T. Auth, S. A. Safran, and N. S. Gov, *Fluctuations of Coupled Fluid and Solid Membranes with Application to Red Blood Cells*, Phys. Rev. E **76**, 051910 (2007).

[6] A. Pierres, A.-M. Benoliel, D. Touchard, and P. Bongrand, *How Cells Tiptoe on Adhesive Surfaces Before Sticking*, Biophys. J. **94**, 4114 (2008).

[7] S. A. Safran, N. Gov, A. Nicolas, U. S. Schwarz, and T. Tlusty, *Physics of Cell Elasticity, Shape and Adhesion*, Physica (Amsterdam) **352A**, 171 (2005).

[8] T. Betz, M. Lenz, J.-F. Joanny, and C. Sykes, *ATP-Dependent Mechanics of Red Blood Cells*, Proc. Natl. Acad. Sci. U.S.A. **106**, 15320 (2009).

[9] B. Hampoelz, Y. Azou-Gros, R. Fabre, O. Markova, P.-H. Puech, and T. Lecuit, *Microtubule-Induced Nuclear Envelope Fluctuations Control Chromatin Dynamics in Drosophila Embryos*, Development (Cambridge, U.K.) **138**, 3377 (2011).

[10] B. Loubet, U. Seifert, and M. A. Lomholt, *Effective Tension and Fluctuations in Active Membranes*, Phys. Rev. E **85**, 031913 (2012).

[11] E. Sackmann and A.-S. Smith, *Physics of Cell Adhesion: Some Lessons from Cell-mimetic Systems*, Soft Matter **10**, 1644 (2014).

[12] D. Schmidt, T. Bihr, U. Seifert, and A.-S. Smith, *Coexistence of Dilute and Densely Packed Domains of Ligand-Receptor Bonds in Membrane Adhesion*, EPL **99**, 38003 (2012).

[13] S. F. Fenz, A.-S. Smith, R. Merkel, and K. Sengupta, *Inter-membrane Adhesion Mediated by Mobile Linkers: Effect of Receptor Shortage*, Soft Matter **7**, 952 (2011).

[14] E. Reister, T. Bihr, U. Seifert, and A.-S. Smith, *Two Intertwined Facets of Adherent Membranes: Membrane Roughness and Correlations between Ligand–Receptors Bonds*, New J. Phys. **13**, 025003 (2011).

[15] J. B. Huppa, M. Axmann, M. A. Mörtelmaier, B. F. Lillemeier, E. W. Newell, M. Brameshuber, L. O. Klein, G. J. Schütz, and M. M. Davis, *TCR-peptide-MHC Interactions in situ Show Accelerated Kinetics and Increased Affinity*, Nature (London) **463**, 963 (2010).

[16] J. Huang, V. I. Zarnitsyna, B. Liu, L. J. Edwards, N. Jiang, B. D. Evavold, and C. Zhu, *The Kinetics of Two-Dimensional TCR and pMHC Interactions Determine T-Cell Responsiveness*, Nature (London) **464**, 932 (2010).

[17] W. Helfrich, *Elastic Properties of Lipid Bilayers: Theory and Possible Experiments*, Z. Naturforsch. C **28**, 693 (1973).

[18] W. Helfrich, *Steric Interaction of Fluid Membranes in Multilayer Systems.*, Z. Naturforsch. A **33**, 305 (1978).

[19] U. Seifert, *Configurations of Fluid Membranes and Vesicles*, Adv. Phys. **46**, 13 (1997).

[20] J.-B. Fournier and C. Barbetta, *Direct Calculation from the Stress Tensor of the Lateral Surface Tension of Fluctuating Fluid Membranes*, Phys. Rev. Lett. **100**, 078103 (2008).

[21] J. Neder, B. West, P. Nielaba, and F. Schmid, *Coarse-Grained Simulations of Membranes under Tension*, J. Chem. Phys. **132**, 115101 (2010).

[22] F. Schmid, *Are Stress-Free Membranes Really Tensionless*, EPL **95**, 28008 (2011).

[23] E. A. Evans and V. A. Parsegian, *Thermal-Mechanical Fluctuations Enhance Repulsion between Bimolecular Layers*, Proc. Natl. Acad. Sci. U.S.A. **83**, 7132 (1986).

[24] J. T. Groves, *Bending Mechanics and Molecular Organization in Biological Membranes*, Annu. Rev. Phys. Chem. **58**, 697 (2007).

[25] L. Limozin and K. Sengupta, *Quantitative Reflection Interference Contrast Microscopy (RICM) in Soft Matter and Cell Adhesion*, ChemPhysChem **10**, 2752 (2009).

[26] K. Fricke, K. Wirthensohn, R. Laxhuber, and E. Sackmann, *Flicker Spectroscopy of Erythrocytes*, Eur. Biophys. J. **14**, 67 (1986).

[27] D. Boss, A. Hoffmann, B. Rappaz, C. Depeursinge, P. J. Magistretti, D. van de Ville, and P. Marquet, *Spatially-Resolved Eigenmode Decomposition of Red Blood Cells Membrane Fluctuations Questions the Role of ATP in Flickering*, PLoS One **7**, e40667 (2012).

[28] P. Méléard, J. F. Faucon, M. D. Mitov, and P. Bothorel, *Pulsed-Light Microscopy Applied to the Measurement of the Bending Elasticity of Giant Liposomes*, Europhys. Lett. **19**, 267 (1992).

[29] J. O. Rädler, T. J. Feder, H. H. Strey, and E. Sackmann, *Fluctuation Analysis of Tension-Controlled Undulation Forces between Giant Vesicles and Solid Substrates*, Phys. Rev. E **51**, 4526 (1995).

[30] J.-B. Manneville, P. Bassereau, S. Ramaswamy, and J. Prost, *Active Membrane Fluctuations Studied by Micropipet Aspiration*, Phys. Rev. E **64**, 021908 (2001).

[31] A.-S. Smith, K. Sengupta, S. Goennenwein, U. Seifert, and E. Sackmann, *Force-Induced Growth of Adhesion Domains Is Controlled by Receptor Mobility*, Proc. Natl. Acad. Sci. U.S.A. **105**, 6906 (2008).

[32] R. Lipowsky, Generic Interactions of Flexible Membranes, in *Structure and Dynamics of Membranes*, edited by R. Lipowsky and E. Sackmann (Elsevier, Amsterdam, 1995), Chap. 11, pp. 521–602.

[33] T. Betz and C. Sykes, *Time Resolved Membrane Fluctuation Spectroscopy*, Soft Matter **8**, 5317 (2012).

[34] T. R. Weikl, D. Andelman, S. Komura, and R. Lipowsky, *Adhesion of Membranes with Competing Specific and Generic Interactions*, Eur. Phys. J. E **8**, 59 (2002).

[35] N. Gov and S. Safran, *Pinning of Fluid Membranes by Periodic Harmonic Potentials*, Phys. Rev. E **69**, 011101 (2004).

[36] T. Auth and G. Gompper, *Fluctuation Spectrum of Membranes with Anchored Linear and Star Polymers*, Phys. Rev. E **72**, 031904 (2005).

[37] L. C.-L. Lin, J. T. Groves, and F. L. H. Brown, *Analysis of Shape, Fluctuations, and Dynamics in Intermembrane Junctions*, Biophys. J. **91**, 3600 (2006).

[38] L. C.-L. Lin and F. L. H. Brown, *Simulating Membrane Dynamics in Nonhomogeneous Hydrodynamic Environments*, J. Chem. Theory Comput. **2**, 472 (2006).

[39] G. Brannigan, L. C.-L. Lin, and F. L. H. Brown, *Implicit Solvent Simulation Models for Biomembranes*, Eur. Biophys. J. **35**, 104 (2006).

[40] H. Krobath, G. J. Schütz, R. Lipowsky, and T. R. Weikl, *Lateral Diffusion of Receptor-Ligand Bonds in Membrane Adhesion Zones: Effect of Thermal Membrane Roughness*, EPL **78**, 38003 (2007).

[41] H. Krobath, B. Rózycki, R. Lipowsky, and T. R. Weikl, *Line Tension and Stability of Domains in Cell-Adhesion Zones Mediated by Long and Short Receptor-Ligand Complexes*, PLoS One **6**, e23284 (2011).

[42] P. Pincus, J.-F. Joanny, and D. Andelman, *Electrostatic Interactions, Curvature Elasticity, and Steric Repulsion in Multimembrane Systems*, Europhys. Lett. **11**, 763 (1990).

[43] C. R. Safinya, D. Roux, G. S. Smith, S. K. Sinha, P. Dimon, N. A. Clark, and A. M. Bellocq, *Steric Interactions in a Model Multimembrane System: A Synchrotron X-ray Study*, Phys. Rev. Lett. **57**, 2718 (1986).

[44] M. Tanaka and E. Sackmann, *Polymer-Supported Membranes as Models of the Cell Surface*, Nature (London) **437**, 656 (2005).

[45] R. Lipowsky and B. Zielinska, *Binding and Unbinding of Lipid Membranes: A Monte Carlo Study*, Phys. Rev. Lett. **62**, 1572 (1989).

[46] R. Lipowsky and S. Leibler, *Unbinding Transitions of Interacting Membranes*, Phys. Rev. Lett. **56**, 2541 (1986).

[47] R. R. Netz, *Complete Unbinding of Fluid Membranes in the Presence of Short-Ranged Forces*, Phys. Rev. E **51**, 2286 (1995).

[48] M. Manghi and N. Destainville, *Statistical Mechanics and Dynamics of Two Supported Stacked Lipid Bilayers*, Langmuir **26**, 4057 (2010).

[49] R. R. Netz and R. Lipowsky, *Stacks of Fluid Membranes under Pressure and Tension*, Europhys. Lett. **29**, 345 (1995).

[50] C. Monzel, S. F. Fenz, R. Merkel, and K. Sengupta, *Probing Biomembrane Dynamics by Dual-Wavelength Reflection Interference Contrast Microscopy*, ChemPhysChem **10**, 2828 (2009).

[51] E. Sackmann and R. Bruinsma, *Cell Adhesion as Wetting Transition?*, ChemPhysChem **3**, 262 (2002).
[52] U. Seifert, *Self-Consistent Theory of Bound Vesicles*, Phys. Rev. Lett. **74**, 5060 (1995).
[53] K. R. Mecke, T. Charitat, and F. Graner, *Fluctuating Lipid Bilayer in an Arbitrary Potential: Theory and Experimental Determination of Bending Rigidity*, Langmuir **19**, 2080 (2003).
[54] R. Bruinsma, M. Goulian, and P. Pincus, *Self-Assembly of Membrane Junctions*, Biophys. J. **67**, 746 (1994).
[55] F. L. H. Brown, *Elastic Modeling of Biomembranes and Lipid Bilayers*, Annu. Rev. Phys. Chem. **59**, 685 (2008).
[56] T. Speck, *Effective Free Energy for Pinned Membranes*, Phys. Rev. E **83**, 050901 (2011).
[57] T. Bihr, U. Seifert, and A.-S. Smith, *Nucleation of Ligand-Receptor Domains in Membrane Adhesion*, Phys. Rev. Lett. **109**, 258101 (2012).
[58] C. Monzel, S. F. Fenz, M. Giesen, R. Merkel, and K. Sengupta, *Mapping Fluctuations in Biomembranes Adhered to Micropatterns*, Soft Matter **8**, 6128 (2012).
[59] A.-S. Smith, B. G. Lorz, U. Seifert, and E. Sackmann, *Antagonist-Induced Deadhesion of Specifically Adhered Vesicles*, Biophys. J. **90**, 1064 (2006).
[60] A.-S. Smith, S. F. Fenz, and K. Sengupta, *Inferring Spatial Organization of Bonds within Adhesion Clusters by Exploiting Fluctuations of Soft Interfaces*, EPL **89**, 28003 (2010).
[61] S. Marx, J. Schilling, E. Sackmann, and R. Bruinsma, *Helfrich Repulsion and Dynamical Phase Separation of Multicomponent Lipid Bilayers*, Phys. Rev. Lett. **88**, 138102 (2002).
[62] U. Seifert, *Dynamics of a Bound Membrane*, Phys. Rev. E **49**, 3124 (1994).
[63] T. R. Weikl, *Indirect Interactions of Membrane-Adsorbed Cylinders*, Eur. Phys. J. E **12**, 265 (2003).
[64] J. Pécréaux, H.-G. Döbereiner, J. Prost, J.-F. Joanny, and P. Bassereau, *Refined Contour Analysis of Giant Unilamellar Vesicles*, Eur. Phys. J. E **13**, 277 (2004).
[65] T. Franosch, M. Grimm, M. Belushkin, F. M. Mor, G. Foffi, L. Forró, and S. Jeney, *Resonances Arising from Hydrodynamic Memory in Brownian Motion*, Nature (London) **478**, 85 (2011).
[66] J. F. Faucon, M. D. Mitov, P. Méléard, I. Bivas, and P. Bothorel, *Bending Elasticity and Thermal Fluctuations of Lipid Membranes. Theoretical and Experimental Requirements*, J. Phys. (Les Ulis, Fr.) **50**, 2389 (1989).
[67] G. Wiegand, K. R. Neumaier, and E. Sackmann, *Microinterferometry: Three-Dimensional Reconstruction of Surface Microtopography for Thin-Film and Wetting Studies by Reflection Interference Contrast Microscopy (RICM)*, Appl. Opt. **37**, 6892 (1998).

P2

Measuring fast stochastic displacements of bio-membranes with dynamic optical displacement spectroscopy

Measuring fast stochastic displacements of bio-membranes with dynamic optical displacement spectroscopy

C. Monzel[1,2,†], D. Schmidt[3,4], C. Kleusch[1], D. Kirchenbüchler[1], U. Seifert[4], A.-S. Smith[3,5], K. Sengupta[2], and R. Merkel[1]

[1] Institute of Complex Systems 7 (ICS-7): Biomechanics, Forschungszentrum Jülich GmbH, 52425 Jülich, Germany
[2] Aix-Marseille Université, CNRS, Centre Interdisciplinaire de Nanoscience de Marseille UMR 7325, 13288 Marseille, France
[3] Institut für Theoretische Physik, Department für Physik, and the Excellence Cluster: Engineering of Advanced Materials, Friedrich Alexander Universität Erlangen-Nürnberg, 91058 Erlangen, Germany
[4] II. Institut für Theoretische Physik, Fakultät 8: Mathematik und Physik, Universität Stuttgart, 70550 Stuttgart, Germany
[5] Division of Physical Chemsitry, Ruđer Bošković Institute, 10000 Zagreb, Croatia
[†] Present addresses: Physical Chemistry, Institut Curie, CNRS UMR 168, 75248 Paris Cedex 5, France (C.M.); Weizmann Institute of Science, Department of Materials and Interfaces, Rohevot, Israel (D.K.)

Nat. Commun., **6** (2015) 8162

DOI: 10.1038/ncomms9162
http://www.nature.com/ncomms/2015/151006/ncomms9162/full/ncomms9162.html

ABSTRACT Stochastic displacements or fluctuations of biological membranes are increasingly recognized as an important aspect of many physiological processes, but hitherto their precise quantification in living cells was limited due to a lack of tools to accurately record them. Here we introduce a novel technique — dynamic optical displacement spectroscopy (DODS), to measure stochastic displacements of membranes with unprecedented combined spatio-temporal resolution of 20 nm and 10 ¯s. The technique was validated by measuring bending fluctuations of model membranes. DODS was then used to explore the fluctuations in human red blood cells, which showed an ATP-induced enhancement of non-Gaussian behaviour. Plasma membrane fluctuations of human macrophages were quantified to this accuracy for the first time. Stimulation with a cytokine enhanced non-Gaussian contributions to these fluctuations. Simplicity of implementation, and high accuracy make DODS a promising tool for comprehensive understanding of stochastic membrane processes.

nature COMMUNICATIONS

ARTICLE

Received 6 May 2015 | Accepted 25 Jul 2015 | Published 6 Oct 2015

DOI: 10.1038/ncomms9162 OPEN

Measuring fast stochastic displacements of bio-membranes with dynamic optical displacement spectroscopy

C. Monzel[1,2,†], D. Schmidt[3,4], C. Kleusch[1], D. Kirchenbüchler[1,†], U. Seifert[4], A-S Smith[3,5], K. Sengupta[2] & R. Merkel[1]

Stochastic displacements or fluctuations of biological membranes are increasingly recognized as an important aspect of many physiological processes, but hitherto their precise quantification in living cells was limited due to a lack of tools to accurately record them. Here we introduce a novel technique—dynamic optical displacement spectroscopy (DODS), to measure stochastic displacements of membranes with unprecedented combined spatio-temporal resolution of 20 nm and 10 μs. The technique was validated by measuring bending fluctuations of model membranes. DODS was then used to explore the fluctuations in human red blood cells, which showed an ATP-induced enhancement of non-Gaussian behaviour. Plasma membrane fluctuations of human macrophages were quantified to this accuracy for the first time. Stimulation with a cytokine enhanced non-Gaussian contributions to these fluctuations. Simplicity of implementation, and high accuracy make DODS a promising tool for comprehensive understanding of stochastic membrane processes.

[1] Institute of Complex Systems 7 (ICS-7): Biomechanics, Forschungszentrum Jülich GmbH, 52425 Jülich, Germany. [2] Aix-Marseille Université, CNRS, Centre Interdisciplinaire de Nanoscience de Marseille UMR 7325, 13288 Marseille, France. [3] Institut für Theoretische Physik, Department für Physik, and the Excellence Cluster: Engineering of Advanced Materials, Friedrich Alexander Universität Erlangen-Nürnberg, 91058 Erlangen, Germany. [4] II. Institut für Theoretische Physik, Fakultät 8: Mathematik und Physik, Universität Stuttgart, 70550 Stuttgart, Germany. [5] Division of Physical Chemistry, Ruđer Bošković Institute, 10000 Zagreb, Croatia. † Present addresses: Physical Chemistry, Institut Curie, CNRS UMR 168, 75248 Paris Cedex 5, France (C.M.); Weizmann Institute of Science, Department of Materials and Interfaces, Rehovot, Israel (D.K.). Correspondence and requests for materials should be addressed to K.S. (email: sengupta@cinam.univ-mrs.fr) or to R.M. (email: r.merkel@fz-juelich.de).

Stochastic remodelling of cellular membranes are essential for many life processes. For example, they play a significant role during cadherin and integrin mediated adhesion[1–3], they have an influence on substrate sensing and protrusion formation during migration[4,5] and facilitate vesicle budding and curvature induced trafficking processes[6,7]. Bending fluctuations of the membrane are an integral component of such remodelling process. In red blood cells (RBCs), such fluctuations are thought to prevent cell–cell adhesion and their modification is a marker of specific diseases[8–10]. In nucleated cells too, modification in fluctuations have been linked to pathology[11] and recent studies point to a critical role of nuclear envelope fluctuations for chromatin dynamics in *Drosophila* embryos and mouse embryonic stem cells[12,13]. The role of fluctuations in stabilizing mitochondria or the endoplasmic reticulum were mooted but are yet to be measured[14,15].

In the past, membrane fluctuations have mostly been quantified on giant unilamellar vesicles[16–22] (GUVs) or RBCs[23–26], with very few reports on nucleated cells[1,3]. The theory of thermally driven bending fluctuations of membranes was developed for both fluid membranes (relevant to GUVs[27–29]) and cytoskeleton scaffolded membranes (relevant for RBCs[23,26]). For fluid membranes, the theory is now considered to be well established but experiments at high frequencies and small bending fluctuations are still challenging[22,24,29]. In case of RBCs, in addition to thermal contribution, an additional active contribution has been suggested both theoretically[26] and experimentally[25] but this is still a matter of debate.

In the context of cells, stochastic activity is expected to be inherent to many membrane processes, for example those involving ion pumps[19]. However, due to the lack of suitable experimental tools to accurately measure membrane fluctuations in the complex optical environment of cells, the nature of active fluctuations in cellular membranes and their modulation during the life cycle of a cell is yet to be studied in detail. Several techniques have been developed to measure membrane fluctuations, including flicker spectroscopy[23], contour analysis[19], diffraction phase microscopy[25] and reflection interference contrast microscopy (RICM)[20,30]. These techniques often use camera based detection[17–23,25,29] with limited time resolution, and/or rely on refractive index induced contrast[17–25,28,29], which is impossible to accurately quantify in nucleated cells due to the presence of organelles and inhomogeneous protein distribution causing ill-defined variations in refractivity. Furthermore, in a given technique, only a specific part of the cell could be accessed—for example, along the equator[23,25] or close to a substrate[1,3,28].

A manifold of other technical advancement based on fluorescence correlation spectroscopy (FCS) has been reported during the last decade. These include two-focus or dual-color scanning approaches that provided novel insight into the structural organization of the cell membrane[31] and enabled quantification of binding affinities *in vivo*[32], and z-scan FCS[33], where measurements are recorded at subsequent points along the z axis, and which eliminates the need for an extrinsic calibration. Recent developments further combined spectroscopic and super-resolution techniques to reveal the dynamics of transient lipid aggregates at nanometric scales[34]. FCS maps of fast molecular dynamics inside living cells and tissues were realized in a spatially resolved manner using image correlation spectroscopy[35], spatiotemporal image cross-correlation spectroscopy, k-Space image correlation spectroscopy and raster image correlation spectroscopy[36] or the combined approaches of single plane illumination–FCS[37] and stimulated emission depletion–raster image correlation spectroscopy[38]. While these FCS related techniques are highly successful in characterizing the ensemble behaviour of individual molecules or small clusters, these techniques are not suitable to study the motion of huge molecular complexes such as bilayers, whose collective motion and bending fluctuations need to be detected with high precision over rapidly sampled time intervals.

In this work, we introduce a novel methodology called dynamic optical displacement spectroscopy (DODS) which circumvents these issues and can measure membrane fluctuations even in the complex optical environment of nucleated cells. The DODS set-up is based on FCS, which is currently a standard technique to measure molecular diffusion and interaction processes[31,39–41]. DODS takes advantage of the fast and sensitive detection inherent to FCS and thus measures membrane fluctuations with 20-nm axial and 10-μs temporal resolution. In addition, as in FCS, DODS measurements can be performed on any chosen part of the cell membrane.

We first validate DODS on model membranes and show that the values of known physical parameters are satisfactorily recovered using standard membrane theory. Next, using DODS to explore the flickering of RBCs, we recover reported results and show that addition of ATP indeed increases the non-Gaussian component but only at the rim. Finally, DODS is applied to a nucleated cell type—human macrophage—to measure hitherto undetectable displacements of the plasma membrane. Quantification of the displacement-histograms and auto-correlation functions shows substantial impact of cytokine stimulation.

Results

The principle. To perform DODS, the membrane under study is labelled with a fluorescent dye and placed in the illuminated confocal volume of a standard FCS set-up. In contrast to FCS, where intensity flickers arise from the diffusion of fluorophores, the key idea of DODS is to measure intensity variations originating exclusively from the physical motion of the membrane. This is possible, since (1) the intensity in the confocal volume follows a well-known distribution that can be measured accurately in each experiment and (2) any signals from diffusion processes are easily suppressed, as outlined below. Detected intensity flickers are then converted into membrane fluctuations in a highly controlled manner using an experimentally determined relation.

We demonstrate the principle of DODS using standard FCS as a starting point and GUV membranes as example: In FCS, the membrane is labelled with a fluorescent dye at low concentration (0.001%, see Methods section) and intensity variations $\delta I(t)$ result from the diffusion of a very small number of fluorophores in the confocal volume. Illustrated here as a model membrane (Fig. 1a,d,h), the membrane in our experiment is the distal surface of a GUV, which is tensed by immersion in a hypotonic solution. The tension thus generated in the membrane suppresses its bending fluctuations. When performing axial scans of the membrane (Fig. 1a–c), the Gaussian intensity distribution of the illuminating beam, I, is recovered and a value of the autocorrelation amplitude, ξ, at each axial position is obtained. In case of FCS, ξ exhibits a single peak distribution and measurements are performed at the central point of the confocal volume where the intensity signal is highest (Fig. 1h).

If the fluorophore concentration in the membrane is increased to 1%, the FCS signal vanishes and the autocorrelation function (ACF) flattens (Fig. 1b,e,i). The ACF, and consequently ξ, remain low at any point of the axial scan (Fig. 1i). In this case dye number fluctuations are so low that all signal originating from fluorophore diffusion is suppressed since it is lost in the noise. As a consequence this data defines the noise level of the system.

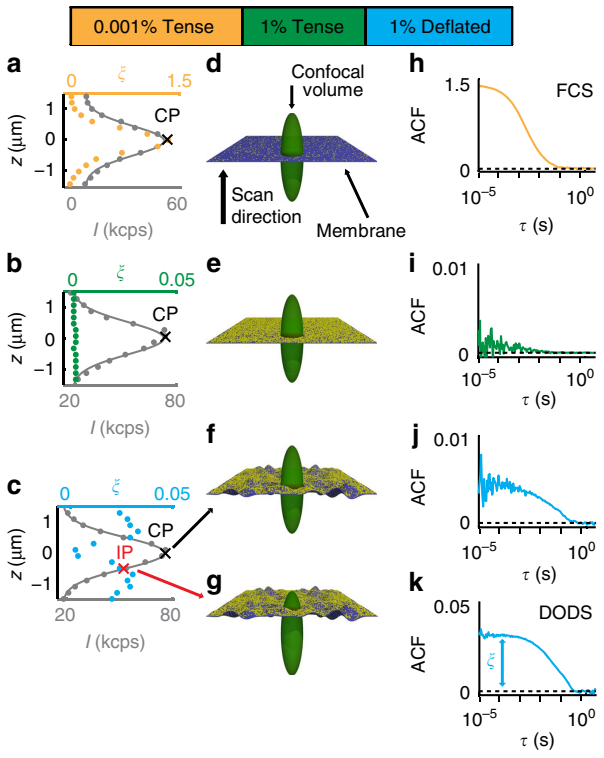

Figure 1 | From FCS to DODS. FCS and DODS measurements on the distal membrane of a GUV. (**a**-**c**) *z*-axial scans with measured intensity, *I*, (grey dots) and Gaussian fit (grey line) in kilo counts per second (kcps). ξ is the correlation amplitude of the recorded ACF (coloured dots); (**d**-**g**) sketch of the membrane (dark blue sheet) with different fluorophore concentration (yellow dots) in the confocal volume; (**h**-**k**) ACF measured at indicated point (central point, CP, or inflection point, IP). (**a**,**d**,**h**) standard FCS with tense, that is non-fluctuating membrane, low fluorophore concentration (ξ exhibits a single peak at CP, and ACF is recorded at the intensity peak CP); (**b**,**e**,**i**) suppression of FCS signal with high fluorophore concentration in tense membrane (ξ is low throughout the scan and ACF exhibits a very low signal at CP); (**c**,**f**,**j**) and (**g**,**k**)) DODS with deflated that is fluctuating membrane and high fluorophore concentration (ξ has peaks at the IPs of *I*(*z*), the ACF recorded at CP exhibits a low signal (**f**,**j**), while the signal at IP is high (**g**,**k**)).

Next, a GUV is immersed in a hypertonic solution and is thus rendered floppy. In this situation, its membrane undergoes strong bending fluctuations. Intriguingly, in this case, membrane displacements within the confocal volume with its inhomogeneous intensity distribution, give rise to a significant recovery of intensity flickers (Fig. 1c,f,g,j,k). For a deflated GUV with 1% fluorophore concentration, this signal is free of any diffusion contribution and $\delta I(t)$ results exclusively from physical displacements of the membrane. Note that presence of 1% labelled lipids is not expected to impact the fluidity or flexibility of the membrane (for example, compare concentrations for phase transition changes in refs 42,43). Furthermore, ξ exhibits a characteristic double peak shape (Fig. 1c). This is understood recalling the Gaussian intensity profile $I(z)$: At central point the fluctuating membrane is detected only via small intensity variations, while at the inflection point (IP), the membrane motion is reflected by a large range of intensities. As a consequence, the sensitivity of membrane fluctuation detection is highest at IP.

DODS geometry. To relate measured intensity flickers to membrane fluctuations quantitatively, the first step is to

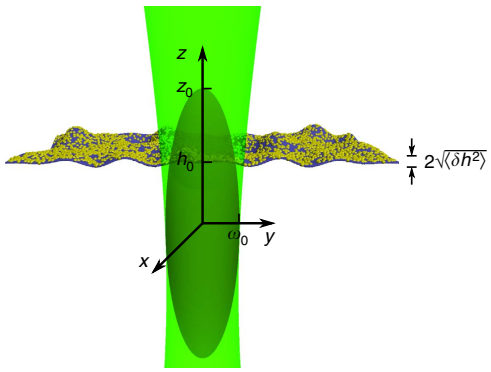

Figure 2 | Sketch of the membrane-confocal volume set-up for DODS. The coordinate system and notations are defined. The membrane is in the *x*-*y* plane and undergoes small displacements in the *z* direction. The membrane is positioned such that its average *z* position, h_0, is at the inflection point of the intensity distribution, *I*(*z*). ω_0 and z_0 are the radii of the beam waist in the radial and axial directions, respectively.

determine the axial intensity profile $I(z)$ of the confocal volume. Formally this is given by the Gaussian function

$$I(z) = I_{\max} \exp\left[-2\frac{z^2}{z_0^2}\right] + I_{\mathrm{Bg}}, \qquad (1)$$

where $I_{\max} = I_0 \frac{\pi c_0 \omega_0^2}{2}$ is the maximal intensity detected at the centre, z is the average membrane position within the confocal volume, I_{Bg} is the background intensity, c_0 is the fluorophore concentration and ω_0 and z_0 are the radial and axial radii of the confocal volume, respectively. $\omega_0 = 280 \pm 5$ nm and $z_0 = 1{,}285 \pm 10$ nm are measured independently using fluorescent beads of sub-resolution size ($N = 10$, data taken from two different experiments; all errors given are s.d., throughout, N is the number of measured objects which can be beads, GUVs or cells; see Supplementary Fig. 1 for an example of the shape of the confocal volume). Scans in the vertical direction confirm the Gaussian profile of $I(z)$ in all experimental cases, which is then fitted using equation (1) (Fig. 1a–c).

For a fluctuating membrane, the instantaneous vertical position z is time dependent and defined as $z = h(t) = h_0 + \delta h(t)$. $h_0 \equiv \langle h(t)\rangle$ is the mean membrane position and $\delta h(t)$ is the instantaneous membrane fluctuation (see Fig. 2). The relation between intensity and membrane fluctuations, $\delta I(t)$ and $\delta h(t)$, respectively, is obtained by expanding $I(z)$ in equation (1) around h_0 up to second order. At IP, which is the optimal position for membrane fluctuation measurements (Fig. 1c,g,k), the second derivative of $I(h_0)$ vanishes and the relation simplifies to:

$$\begin{aligned}\delta I(t) &= -I_{\max} \exp\left[-2\frac{h_0^2}{z_0^2}\right]\left\{\frac{4h_0\delta h(t)}{z_0^2}\right\} \\ &\equiv m \cdot \delta h(t).\end{aligned} \qquad (2)$$

Equation (2) can be used to calculate $\delta h(t)$ from $\delta I(t)$ via the slope m at IP, while m is determined in each measurement from the Gaussian intensity profile $I(z)$. Subsequently, the displacement autocorrelation function (dACF), $\langle \delta h(\tau)\delta h(0)\rangle$, is either built from the calculated $\delta h(t)$, or, equivalently, calculated directly from the recorded ACF through the relation:

$$\mathrm{ACF} = \frac{m^2}{\langle I(t)\rangle^2}\mathrm{dACF}. \qquad (3)$$

Detailed derivation is given in Supplementary Note 1. Note that use of the experimentally determined slope m, rather than a theoretical factor derived from system parameters, ensures that aberrations and image imperfections due to optical

inhomogeneity, which may be present in complex systems like nucleated cells, are automatically accounted for.

Axial and temporal resolution. The axial resolution, which is the smallest displacement that we can measure, is related to the shape of the confocal volume and the background noise and was determined to 20 nm by the following three approaches: (1) the spatial error introduced via the linear intensity-height approximation was checked using Taylor expansions of second or third order in $\delta h(t)$ for the conversion of intensity to membrane fluctuations. By comparison of the resulting traces with the linear expansion in $\delta h(t)$, a maximal error of 12 nm for the average stochastic displacement was found (see Supplementary Note 2 for examples and further details). (2) The axial resolution in the z direction can be calculated from data representing the detection limit, for example, bending fluctuation traces from tensed GUV or supported lipid bilayer (SLB) (see Supplementary Figs 2 and 3). Here, the maximum value of the correlation amplitude amounted to $\xi_{\mathrm{det}} = 0.0024$. At the IP, for a typical slope of $m = 130\,\mathrm{k.c.p.s.\,\mu m^{-1}}$ (k.c.p.s., kilo counts per second) and intensities of 50 k.c.p.s., equations (2) and (3) yield an axial resolution limit of $h_{det} = \sqrt{(50\,\mathrm{k.c.p.s.})^2 \cdot \xi_{det}/m^2} = 20\,\mathrm{nm}$. (3).

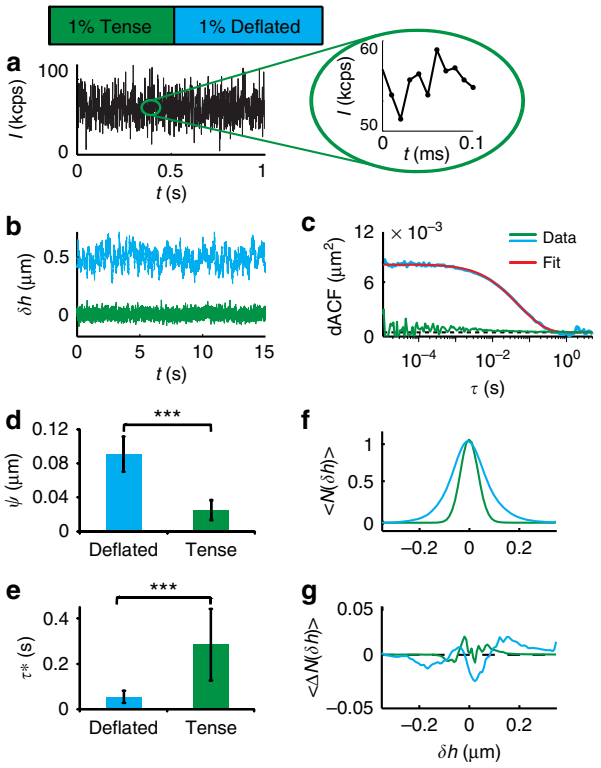

Figure 3 | DODS validation and application to GUVs. (**a**) A typical intensity trace recorded at IP (inset: zoom). (**b**) Displacement trace, δh, for tense and deflated GUV (the latter is shifted by $+0.5\,\mu$m for clarity) and (**c**) corresponding dACF. Fitting of dACF (red line) yields the fluctuation amplitude, $\psi = \sqrt{\langle \delta h^2 \rangle}$, and the relaxation time, τ^*, which define the membrane tension and the viscosity of the surrounding medium (see text for details). (**d**) ψ and (**e**) τ^* for deflated and tense GUVs. Significance levels, P, were evaluated by Mann–Whitney U-test: $P<0.001$ (***), $P<0.01$ (**) and $P<0.05$ (*). Error bars denote s.d. of results. (**f**) Histogram of membrane fluctuations, $\langle N(\delta h)\rangle$, and (**g**) deviation from a Gaussian fit, $\langle \Delta N(\delta h)\rangle$. Data represent the average of all tense ($N=10$, 3 experiments) and deflated ($N=46$, 9 different experiments) vesicles, respectively.

The influence of the signal-to-noise ratio on the axial resolution is estimated theoretically, calculating the error in fluctuations Δh for variable signal and background intensities. Here the conversion of intensities to $\delta h(t)$ at the IP is assumed. An increase in background intensity by ΔI_{Bg} and with the slope $m = \frac{2I_{max}}{z_0} \cdot 0.61$, then leads to the spatial error:

$$\Delta h = \frac{\Delta I_{Bg}}{m} = \frac{\Delta I_{Bg} \cdot z_0}{2 \cdot 0.61 \cdot I_{max}} \qquad (4)$$

Supplementary Fig. 4 shows the result of this calculation for fluorophore intensity counts between $I_{\mathrm{max}} = 0$–90 kcps and background intensities varying between $I_{Bg} = 0$–9 kcps. A lower limit of ΔI_{Bg} is given by the dark current of the avalanche photodiode detection amounting to 0.5 kcps. This is also a common background intensity for the experiments presented here. Clearly, for signal intensities of 50–90 kcps the error is well below 20 nm.

It should be noted, that other systems may exhibit higher ΔI_{Bg} values, resulting in a corresponding drastic increase in the spatial error and any uncorrelated background signal will further dampen the amplitude of the autocorrelation curve. For example, utilization of phenol red containing medium raised ΔI_{Bg} to 2 k.c.p.s. and increased the error in h to >20 nm. Its use was therefore avoided and care was taken to work with minimal possible background intensities.

The temporal resolution of DODS was determined to 10 μs, despite the fact that raw data are recorded at the rate of 200 ns per point. However, to obtain a reasonable signal-to-noise ratio, with uncertainties in the dACF shape well below the axial resolution, we integrate over 10 μs and record for a minimum of 25 s (see Supplementary Fig. 5 for a detailed analysis).

Validation and application to GUVs. We validated DODS by comparing bending fluctuations of model membranes with well-known theoretical predictions[28,29], previous experimental results[20,22,28,29] and comparison to dual-wavelength RICM (DW)–RICM[17,44]; see Supplementary Note 3). The amplitude of fluctuation $\psi = \sqrt{\langle \delta h^2 \rangle}$ and the relaxation time τ^* were obtained from dACFs measured at the distal surface of GUVs, which were also fitted with setup-specific theoretical expressions to obtain the membrane tension and viscosity (see Supplementary Note 4, Supplementary Equation (9))[28]. As expected, the fluctuations were stronger for the deflated GUVs (90 ± 20 nm, $N=46$), as compared with the tense GUVs (25 ± 4 nm, $N=10$) with an opposite trend for τ^* (0.06 s for deflated and 0.28 s for tense, see Fig. 3). Significance levels were determined by Mann–Whitney U-test, reported as $P<0.001$ (***), $P<0.01$ (**) and $P<0.05$ (*).

To test whether the method reflects the bending fluctuations of GUVs correctly, we extracted the trace δh over an interval of 60 s and plotted the probability distribution function of bending fluctuations, $N(\delta h)$. For all GUV of a specific condition, this was then averaged, yielding $\langle N(\delta h)\rangle$. In both, deflated and tense case, the fluctuation distribution was nearly Gaussian, as is expected for the case for a linear system under equilibrium. Deviations from the Gaussian were quantified by skewness (S), which is a measure of the asymmetry of the probability distribution, and kurtosis (K), which yields a measure of the 'peakedness' of the probability distribution. Here only slight deviations from zero ($S = 0.5 \pm 0.3$, $K = -0.8 \pm 0.2$ for deflated GUVs and $S = 0.2 \pm 0.2$ and $K = -0.7 \pm 0.2$ for tense GUVs; see Fig. 3) were obtained. Fitting of the dACF with Supplementary Equation (9) of Supplementary Note 4, yields the average tension and viscosity. The tension amounts to $\sigma = 0.5 \pm 0.3\,\mu\mathrm{J\,m^{-2}}$ for deflated GUV, which agrees well with literature[19,20,29]. The

viscosity (1.2 ± 0.6 mPas) is, as expected, close to that of water (1.0 mPas) with a slight deviation arising from the higher viscosity of the sucrose solution inside the vesicle $\eta = 1.4$ mPas. Comparative measurements of DODS and DW-RICM of the vesicle membrane near the substrate yield fluctuation values in high agreement for both techniques (see Supplementary Note 3). Amplitudes for fluctuations near the substrate amount to $\psi = 31 \pm 12$ (DODS) and 26 ± 21 nm (DW-RICM). In summary, bending fluctuations measured with DODS are fitted very well with existing theory and yield reliable values for fluctuation amplitudes, tension and dissipation. Having established DODS as an accurate and reliable technique, (see Supplementary Fig. 2 and Supplementary Note 2 and 5 for further specification and control measurements), we then applied it to progressively more complex systems—first RBCs and then nucleated cells.

Application to RBCs. RBCs are simple cells known to undergo bending fluctuations with a still debated contribution from active processes[24,25]. They exhibit a biconcave shape maintained by ATP powered remodelling of their membrane coupled spectrin network. In recent years, ATP has been proposed to also facilitate non-equilibrium dynamic fluctuations of the RBC membrane.[24–26] To further elucidate this aspect, we performed DODS measurements at the centre and at the rim of human RBCs, in the presence or absence of ATP (Fig. 4a,b). Fluctuation amplitudes are significantly larger at the rim (50 ± 10 nm, $N = 26$) in comparison to the centre (30 ± 10 nm, $N = 18$) and increase by a factor of 1.4 in the presence of ATP (rim: 74 ± 10 nm, $N = 31$, centre: 41 ± 10 nm, $N = 24$) in agreement with Tuvia *et al.*[45] and Park *et al.*[25] (Fig. 4c). The fluctuations relaxed much faster in ATP depleted cells, where only thermal fluctuations are expected ($\tau^* = 0.09 \pm 0.01$ s (centre) and 0.10 ± 0.01 s (rim)). Extracting the probability distribution function of the membrane fluctuations, ATP − cells, exhibited a Gaussian distribution, as expected. Skewness and kurtosis values (Fig. 4d, $S = 0.1 \pm 0.5$ (rim)/0.3 ± 0.6 (centre) and $K = -1.2 \pm 0.3$ (rim)/-1.0 ± 0.9 (centre)) were comparable to vesicles. For ATP + cells, the same was found at the centre, but unexpectedly, a deviation from a Gaussian distribution was found at the rim. As characterized by a non-zero skewness and kurtosis, this indicates a nonlinear behaviour of the system ($S = 0.1 \pm 0.6$ (rim)/1.1 ± 0.6 (centre) and $K = -1.9 \pm 0.6$ (rim)/-0.9 ± 0.3 (centre)).

Taken together, our results suggest that the RBC membrane is a metabolically regulated active structure, whose motion is dominated by thermal contributions, with residual ATP driven activity detectable at the rim of the cell.

Application to macrophages. Next we applied DODS to a complex cell and measured a change in stochastic displacements as a response to a biologically relevant stimulus: qualitative measurements on cells have been undertaken before, yet, so far it was not possible to quantify stochastic bending fluctuations to this accuracy. As an example, we probed the priming of human macrophages in response to stimulation by the soluble cytokine interferon gamma (IFNγ). IFNγ is known to augment many host-defense functions in macrophages and through its interplay with membrane bound activators it increases actin polymerization and ruffling activity[46]. With DODS, membrane dynamics were quantified measuring the stochastic displacements at the lamellipodium (lam) and at the edge of the cell body (body) (Fig. 5a). Correlation analysis was carried out for non-stimulated (IFNγ −, $N = 26$ lam, $N = 26$ body) and stimulated cells (IFNγ +, $N = 29$ lam, $N = 11$ body). IFNγ − macrophages exhibit comparable fluctuation amplitudes of about 45 nm at the lam and the body (40 ± 10 nm (lam) and 50 ± 20 nm (body)) (Fig. 5b). As expected, IFNγ treatment enhanced the fluctuation amplitude (80 ± 30 nm (lam) and 90 ± 30 nm (body), respectively, for IFNγ + cells). τ^* decreased from 0.8 ± 0.4 s (both lam and body) in untreated cells to about 0.5 s in primed cells (0.4 ± 0.3 s and 0.6 ± 0.2 s), which is opposite to the trend of enhanced fluctuations in RBCs (Fig. 5c). The stochastic membrane displacements in IFNγ − cells are nearly Gaussian ($S = -0.9 \pm 0.8$ (body)/0.8 ± 0.5 (lam) and $K = -1.0 \pm 0.3$ (body)/-0.8 ± 0.4 (lam)), but stimulation significantly increases both skewness and kurtosis indicating vastly increased active contributions (Fig. 5d, $S = 3.4 \pm 1.0$ (body)/3.8 ± 1.0 (lam) and $K = -5.1 \pm 1.1$ (body)/-2.4 ± 0.7 (lam)). Hence, our data suggests that amplitude, time correlation and the fluctuation distribution function are indicative of the cell's biological state.

Discussion

In this study, a new technique to quantify membrane fluctuations with unprecedented spatiotemporal accuracy was set-up. This technique, DODS, is a novel tool for basic research and future biomedical applications, and is particularly valuable as it measures stochastic displacements in living cells and, unlike existing techniques[21,25], does so at any chosen part of the cell. Crucially, the relation between displacement and intensity is

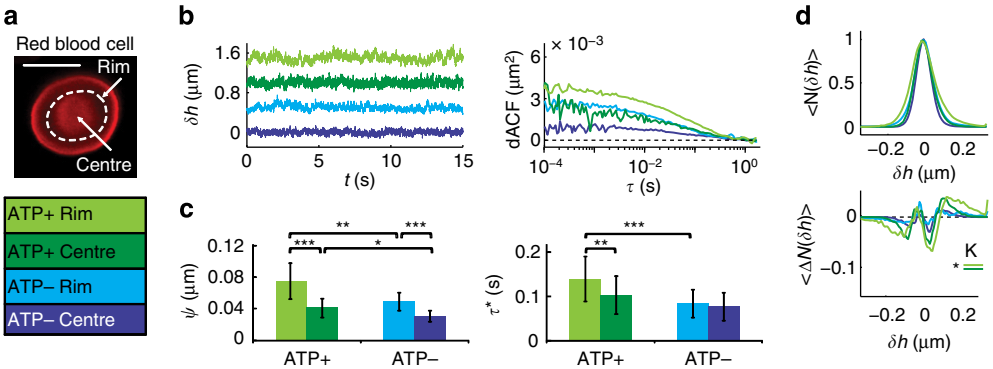

Figure 4 | DODS applied to RBCs. (**a**) Fluorescence image and measurement positions (white dashed lines) for a RBC, scale bar, 5 μm. (**b**) Displacement traces, δh, (shifted by + 0.5 μm for clarity) and dACFs (rim/centre, ATP +/ATP −). (**c**) Fluctuation amplitude, ψ, and relaxation time, τ^*. Error bars denote s.d. (**d**) Histogram of displacements, $\langle N(\delta h)\rangle$, and deviation from a Gaussian fit, $\langle \Delta N(\delta h)\rangle$, averaged for all cells (seven different ATP + experiments (rim: $N = 31$, centre: $N = 24$) and seven different ATP − experiments (rim: $N = 26$, centre: $N = 18$)). Significance levels for differences in skewness (S) and kurtosis (K) are indicated. Significance according to Mann–Whitney U-test $P < 0.001$ (***), $P < 0.01$ (**) and $P < 0.05$ (*).

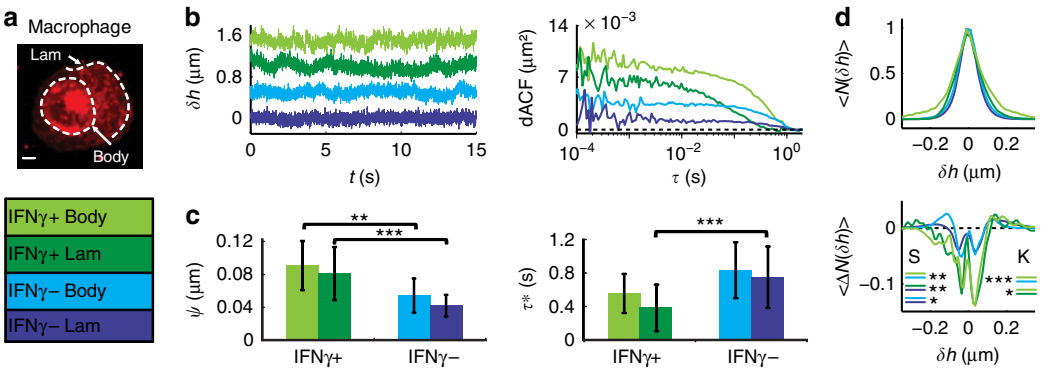

Figure 5 | DODS applied to macrophages. (**a**) Fluorescence image and measurement positions (white dashed lines) for a macrophage, scale bar, 5 μm. (**b**) Displacement traces, δh, (shifted by $+0.5$ μm for clarity) and dACFs (cell body (body)/lamellipodium (lam), IFNγ+/IFNγ−). (**c**) fluctuation amplitude, ψ, and relaxation time, τ^*. Error bars denote s.d. (**d**) Histogram of displacements, $\langle N(\delta h)\rangle$, and deviation from a Gaussian fit, $\langle \Delta N(\delta h)\rangle$, averaged for all cells (six different IFNγ+ experiments (lam: $N=29$ and body: $N=11$) and five different IFNγ− experiments (rim: $N=26$ and centre: $N=26$)). Significance levels for differences in skewness (S) and kurtosis (K) are indicated. Significance according to Mann–Whitney U-test $P<0.001$ (***), $P<0.01$ (**) and $P<0.05$ (*).

experimentally determined, thus no assumptions regarding the optics of the cell have to be made.

DODS was applied to the membranes of GUVs, RBCs and human macrophages. Tension ($0.5\,\mu J\,m^{-2}$) and viscosity (1.2 mPas) relevant to a freely fluctuating model membrane were determined for the first time. Previous attempts to measure bending fluctuations with enhanced accuracy were either limited by camera detection and substrate proximity[20] or led to an unreasonable high viscosity exceeding the expected value by $\times 20$ (ref. 24). The stochastic displacements of RBC membrane is a highly debated topic and our data contribute to the closure of the ongoing discussion on RBC membrane activity. Our proof-of-principle demonstration of the stochastic displacements of the plasma membrane of macrophages gives access to an entirely new kind of data that should provide insight into hitherto inaccessible stochastic cellular processes as well as may stimulate further theoretical development.

The axial resolution of DODS in the z direction, which is currently estimated to be 20 nm, can be improved using lateral instead of axial scans. In the lateral direction (x–y plane), the intensity Gaussian is narrower and simultaneously the slope at the IP is steeper. More precisely, at the IP, where $z_0=\pm 2h_0$ and equation (2) yield $m=\frac{2I_{max}}{z_0}\cdot 0.61$, lateral scans suggest a resolution enhancement by a factor 4, due to the exchange of z_0 for $\omega_0 \sim z_0/4$. Similarly, it may be improved by an order of magnitude using stimulated emission depletion (STED)–FCS[34,38], where the effective beam size is much smaller and therefore the intensity Gaussian much narrower. DODS can be extended to larger membrane movements by retaining higher order terms in the intensity-displacement relationship. An interesting extension concerns simultaneous measurement of diffusion and membrane fluctuations by using two different fluorophores at high (for DODS) and low (for FCS) molecular concentration. This has been attempted before by tracing a fluorescent molecule at low concentration close to a membrane exhibiting bending fluctuations[47]. However, a direct evidence separating the two contributions is still missing. Diffusion and membrane fluctuations are speculated to be correlated for model membranes[48] and may provide crucial data in the cellular context by linking membrane tension to molecular dynamics[49]. With axial resolution comparable to the established super-resolution techniques, and time resolution comparable to FCS, DODS will take advantage of ongoing improvements to FCS[34,38–41] and can be expected to be established as a companion technique to FCS-based diffusion and structural organization measurements[31], thus linking membrane scale phenomena to molecular scale events.

Methods

Data acquisition and analysis. DODS measurements were undertaken at a confocal laser scanning microscope (LSM710, Zeiss) equipped with a 5-mW HeNe laser ($\lambda=543$ nm) and two avalanche photodiodes (Perkin Elmer, Waltham, MA, USA) for photon counting detection. Appropriate filter sets were chosen (for the dyes used here: beam splitter 488/543 nm for excitation and 580-nm long pass filter for emission, Zeiss) and a water immersion objective (C-Apochromat, $\times 40$, numerical aperature 1.2, Zeiss) was used. Data acquisition and realtime autocorrelation were executed via the software ZEN (version 2008, Zeiss). Before the start of a DODS measurement, fluorescence and phase contrast images were acquired to determine the overall shape of the GUV or the cell and to choose the appropriate position. In a typical experiment, with the fluorescent membrane positioned inside the confocal volume, the excitation laser is attenuated until a maximum count I_{max} of $\sim$70–100 kcps is reached. Subsequently, a fast scan perpendicular to the membrane is recorded—this establishes the parameters of the Gaussian intensity distribution of the illuminating volume. The confocal spot is then positioned such that the mean position of the membrane is at the IP of the Gaussian (given by the intensity $I_{IP}=0.61\cdot I_{max}$). Intensity fluctuations are recorded for a specific time interval and the ACF is calculated. Tests were undertaken to ensure that at the applied excitation intensities bleaching was negligible and that fluorophore response was linear. Ergodicity and stationarity of data were tested by calculating the deviation between the ACF over the total recording time and the ACF over a subset of $5\times x$ s, x$\in\{1$–$10\}$ duration (Supplementary Note 2). Twenty-five seconds were determined to be minimal recording time t_{min}, which ensures ergodicity and the complete build-up of the dACF. For GUVs and RBCs data were recorded for 2–3 min. In case of macrophages, cell movement limited measurement times to 40–120 s, which is nevertheless $\gg t_{min}$ and therefore sufficient to build the ACF.

To compare DODS with a different technique, identically prepared GUV were measured with DODS and DW-RICM[17,44]. This microinterferometric technique can measure the height of a fluctuating membrane above a substrate with 4-nm axial resolution and 50-ms temporal resolution (as limited by the camera speed). The RICM image is formed from interfering rays being reflected at different optical layers in the sample. Depending on the difference of their optical path length, these rays interfere in a destructive or constructive manner. Knowing the refractive indices and thicknesses of the optical interfaces, the membrane-substrate height is calculated. For DW-RICM, two images (for $\lambda=546$ nm and 436 nm) are simultaneously recorded. This allows to unambiguously determine membrane-substrate heights up to several $\sim$100 nm. Images were acquired with a DW-RICM set-up described in detailed before[17,22,44]: an inverted microscope (Zeiss Axiovert 200, Carl Zeiss, Göttingen, Germany) equipped with a filter cube with crossed polarizers and a $\times 63$ Antiflex Plan-Neofluar oil objective with a numerical aperture of 1.25 and built in lambda quarter plate was used. Light emitted by a metal halogenide lamp (XCite, Exfo, Quebec, Canada) was filtered using a dual-interference filter ($\lambda=546\pm10$ and 436 ± 20 nm). The numerical aperture of illumination was set to 0.54. To achieve maximum contrast the antiflex technique was applied. To record two micrographs simultaneously, the reflected light was split according to its wavelength

(FT 460 nm, LP 470 nm (Carl Zeiss, Göttingen, Germany) and BP 436 ± 10 nm (AHF, Tübingen, Germany)) and focused on two separate digital CCD cameras (sensicam qe, PCO, Kehlheim, Germany). Image recording was controlled by the software OpenBox (version 1.77, Informationssysteme Schilling, Munich, Germany).

Images and data were analysed using the self-written routines in Matlab (version 3.0 (R2010b), The MathWorks, Inc. MA, USA) using the image processing toolbox and ImageJ (version 1.45 s, Rasband, W.S., NIH, Bethesda, MD, USA). Errors reported throughout are s.d.

Substrates. Thickness corrected glass coverslips (d = 170 ± 10 µm, Assistent, Karl Hecht KG, Sondheim, Germany) were cleaned by the following detergent treatment: ultrasonication in 2% Hellmanex solution (Hellma, Müllheim, Germany) for 10 min, flushing thoroughly with ultrapure water produced by a water purification system (Milli-Q Gradient A10, Millipore, San Francisco, CA) and again ultrasonication (2 × 10 min) in ultrapure water followed by repeated flushing with ultrapure water. To prevent unspecific interactions in GUV and RBC experiments, bare glass was passivated by incubation with 5 mg ml^{-1} bovine serum albumin (BSA, Sigma, Saint Louis, MO, USA) for 15 min. For macrophages, cell culture dishes (3-cm diameter, Greiner, Solingen, Germany) with thickness corrected glass coverslips were pre-coated with 10 µg ml^{-1} human fibronectin (BD Biosciences, Bedford, USA) in PBS for 30 min at 37 °C. In all cases, excess protein was removed by exchanging the buffer in a series of 10 washing steps.

Fluorophores. Fluorophores were purchased from Invitrogen (Eugene, OR, USA) as lipid conjugates. For GUVs, tetramethylrhodaminethiocarbamoyl conjugated to the lipid DHPE (*N*-(6-tetramethylrhodaminethiocarbamoyl)-1,2-dihexadecanoyl-sn-glycero-3-phosphoethanolamine, triethylammonium salt) was used at 1 mol% for DODS measurements. For cells, the fluorophore of choice was Texas Red, again conjugated to DHPE (Texas Red-1,2-dihexadecanoyl-sn-glycero-3-phosphoethanolamine, triethylammonium salt). The cell membrane was labelled as described below.

Lipids. SOPC (1-stearoyl-2-oleoyl-sn-glycero-3-phosphocholine), DOPE-PEG2000 (1,2-dioleoyl-sn-glycero-3-phosphoethanolamine-*N*-(methoxy (polyethyleneglycol)-2000)), DOPE-cap-biotin (1,2-dioleoyl-sn-glycero-3-phosphoethanolamine-*N*-(cap biotinyl)), DOPE (1,2-dioleoyl-sn-glycero-3-phosphoethanolamine) and DOTAP (1,2-dioleoyl-3-trime-thylammonium-propane, chloride salt) were purchased from Avanti Polar Lipids (Alabaster, AL, USA) and were used as it is.

Giant unilamellar vesicles. GUVs made of SOPC with 2 mol% DOPE-PEG2000, 5 mol% DOPE-cap-biotin and 0.001–1 mol% DHPE-tetramethylrhodaminethio carbamoyl were electro-swollen in 230 mOsm l^{-1} sucrose solution as reported in ref. 22. Therefore, 20 ml of a solution of the lipid dissolved in chloroform (2 mg ml^{-1}) was dispersed on glass slides coated with indium tin oxide (PGO, Iserlohn, Germany) and the solvent desiccated under vacuum overnight. Two lipid-coated glass slides were mounted in a teflon chamber filled with 230 mOsm l^{-1} sucrose solution, at a distance of 1 mm. An alternating voltage of 1.7 V and 10 Hz was applied for 1.5 h. This yielded GUVs of about 40-µm average diameter. The concentration of the fluorescent lipids depended on the experiment, 0.001% being appropriate for FCS and 1% for DODS. Observations were done in PBS buffer (10 mM Na_2HPO_4, 2 mM KH_2PO_4 and 3 mM KCl) at pH 7.2, with added NaCl to obtain the desired osmolarity (all salts were from Sigma, Germany). PBS (400 mOsm l^{-1}) was used for experiments with floppy GUVs and 250 mOsm l^{-1} for tense GUVs. In a typical experiment, vesicle solution in 1:50 dilution was added to the observation buffer in the experimental chamber, which was then covered with a glass slide to avoid osmolarity changes due to evaporation. DODS measurements were started 30 min later, to ensure full equilibration of the system. All measurements were undertaken at room temperature.

Preparation of RBCs. Human RBCs were freshly prepared before each experiment by pricking the finger of a healthy donor and then diluting 10 µl blood in 1 ml PBS (pH 7.4, 300 mOsm · l^{-1}, see above). RBCs were washed twice with PBS by centrifugation (1 min, 200*g*, Eppendorf Centrifuge 5804R, Hamburg, Germany) and aspiration of the supernatant. After fluorescent staining of the cell membrane (see below), cells were centrifuged again and the pellet was diluted 1:17 in the observation buffer (PBS + 0.1 mg ml^{-1} BSA for ATP depleted and PBS + 0.1 mg ml^{-1} BSA + 10 mM D-Glucose for ATP saturated cells). In case of ATP depletion, cells were kept in the observation buffer for 24 h before membrane staining and subsequent imaging.

Preparation of macrophages. Primary human macrophages were grown at 37 °C and 5% CO_2 in Roswell Park Memorial Institute Medium (RPMI 1640, Gibco, Karlsruhe, Germany), with 10% (v/v) fetal bovine serum (Sigma), 1:100 penicillin/streptomycin (10,000 U ml^{-1}, Sigma) and without phenol red, henceforth referred to as RPMI$^+$. Before measurements cells were washed with PBS to withdraw surplus organic compounds and medium. Subsequently, cells were incubated in 3-ml trypsin-EDTA solution (consisting of 0.5% trypsin and 0.2% EDTA, Sigma) for 3 min at 37 °C. This yielded cells in suspension, which were centrifuged (200*g*, 3 min), collected and resuspended in the experimental buffer (RPMI$^+$ for resting or RPMI$^+$ + 1,000 U · ml^{-1} IFNγ for primed cells). After seeding in the measurement chamber and incubation for ≥24 h the cell plasma membrane was stained as described below and imaging was started subsequently. During measurements a microscope with incubator at 37 °C and CO_2 supply was used.

Fluorescent labelling of cells. Fluorescent labelling of RBC or macrophage plasma membranes was carried out by a method developed by Csiszár *et al.*[50] Therefore, fusogenic liposomes consisting of ternary lipid mixtures, enabled highly efficient incorporation of fluorescent molecules into mammalian cell membranes. Small multilamellar liposomes were produced from a 1 mg ml^{-1} mixture of DOPE, DOTAP and Texas Red—DHPE in a 1:1:0.2 weight ratio. To do this, the lipid were first dissolved in chloroform and the solution was then dried under vacuum for 20 min. The lipids were resuspended in 20 mM 2-(4-(2-hydroxyethyl)-1-piperazinyl)-ethane-sulfonic acid (pH 7.5, HEPES, VWR) at 2.2 mg ml^{-1} final concentration. To produce multilamellar liposomes the suspension was stirred 1–2 min on a vortex-mixer followed by 10-min ultrasound bath treatment. The liposomes were stored at 4 °C. Cells were incubated with the liposome solution in a 1:100 dilution for 12 min at 37 °C. They were then washed and resuspended in fresh experiment buffer or medium, as appropriate.

References

1. Pierres, A., Benoliel, A.-M., Touchard, D. & Bongrand, P. How cells tiptoe on adhesive surfaces before sticking. *Biophys. J.* **94,** 4114–4122 (2008).
2. Perez, T. D., Tamada, M., Sheetz, M. P. & Nelson, W. J. Immediate-early signaling induced by E-cadherin engagement and adhesion. *J. Biol. Chem.* **283,** 5014–5022 (2008).
3. Zidovska, A. & Sackmann, E. Brownian motion of nucleated cell envelopes impedes adhesion. *Phys. Rev. Lett.* **96,** 048103 (2006).
4. Danuser, G., Allard, J. & Mogilner, A. Mathematical modeling of eukaryotic cell migration: insights beyond experiments. *Annu. Rev. Cell Dev. Biol.* **29,** 501–528 (2013).
5. Digman, M. A., Wiseman, P. W., Choi, C., Horwitz, A. R. & Gratton, E. Stoichiometry of molecular complexes at adhesions in living cells. *Proc. Natl Acad. Sci. USA* **106,** 2170–2175 (2009).
6. McMahon, H. T. & Gallop, J. L. Membrane curvature and mechanisms of dynamic cell membrane remodelling. *Nature* **438,** 590–596 (2005).
7. Ménard, L., Parker, P. J. & Kermorgant, S. Receptor tyrosine kinase c-Met controls the cytoskeleton from different endosomes via different pathways. *Nat. Commun.* **5,** 3907 (2014).
8. Park, Y. *et al.* Refractive index maps and membrane dynamics of human red blood cells parasitized by *Plasmodium falciparum*. *Proc. Natl Acad. Sci. USA* **105,** 13730–13735 (2008).
9. Jiang, W. G. Focus on science—membrane ruffling of cancer cells: a parameter of tumour cell motility and invasion. *Eur. J Surg. Oncol.* **21,** 307–309 (1995).
10. Cojoc, D. *et al.* Toward fast malaria detection by secondary speckle sensing microscopy. *Biomed. Opt. Express* **3,** 991–1005 (2012).
11. Partin, A. W., Schoeniger, J. S., Mohler, J. L. & Coffey, D. S. Fourier analysis of cell motility: correlation of motility with metastatic potential. *Proc. Natl Acad. Sci. USA* **86,** 1254–1258 (1989).
12. Hampoelz, B. *et al.* Microtubule-induced nuclear envelope fluctuations control chromatin dynamics in Drosophila embryos. *Development* **138,** 3377–3386 (2011).
13. Talwar, S., Kumar, A., Rao, M., Menon, G. I. & Shivashankar, G. V. Correlated spatio-temporal fluctuations in chromatin compaction states characterize stem cells. *Biophys. J.* **104,** 553–564 (2013).
14. Green, D. R. & Reed, J. C. Mitochondria and apoptosis. *Science* **281,** 1309–1312 (1998).
15. Frey, T. G., Renken, C. W. & Perkins, G. A. Insight into mitochondrial structure and function from electron tomography. *Biochim. Biophys. Acta.* **1555,** 196–203 (2002).
16. Mutz, M. & Helfrich, W. Bending rigidities of some biological model membranes as obtained from the Fourier analysis of contour sections. *J. Phys. (Paris)* **51,** 991–1001 (1990).
17. Monzel, C., Fenz, S., Merkel, R. & Sengupta, K. Probing biomembrane dynamics by dual-wavelength reflection interference contrast microscopy. *Chemphyschem* **10,** 2828–2838 (2009).
18. Rädler, J. O., Feder, T. J., Strey, H. H. & Sackmann, E. Fluctuation analysis of tension-controlled undulation forces between giant vesicles and solid substrates. *Phys. Rev. E* **51,** 4526–4536 (1995).
19. Faris, M. *et al.* Membrane tension lowering induced by protein activity. *Phys. Rev. Lett.* **102,** 038102 (2009).
20. Sengupta, K. & Limozin, L. Adhesion of soft membranes controlled by tension and interfacial polymers. *Phys. Rev. Lett.* **104,** 088101 (2010).
21. Döbereiner, H.-G. *et al.* Advanced flicker spectroscopy of fluid membranes. *Phys. Rev. Lett.* **91,** 048301 (2003).

22. Monzel, C., Fenz, S. F., Giesen, M., Merkel, R. & Sengupta, K. Mapping fluctuations in biomembranes adhered to micropatterns. *Soft Matter* **8,** 6128–6138 (2012).
23. Brochard-Wyart, F. & Lennon, J.-F. Frequency spectrum of the flicker phenomenon in erythrocyte. *J. Phys. (Paris)* **36,** 1035–1047 (1975).
24. Betz, Timo & Lenz Martin and Joanny, Jean-François and Sykes, Cécile, ATP-dependent mechanics of red blood cells. *Proc. Natl Acad. Sci. USA* **106,** 15320–15325 (2009).
25. Park, Y. *et al.* Metabolic remodeling of the human red blood cell membrane. *Proc. Natl Acad. Sci. USA* **107,** 1289–1294 (2010).
26. Gov, N. S. & Safran, S. A. Red blood cell membrane fluctuations and shape controlled by ATP-induced cytoskeletal defects. *Biophys. J.* **88,** 1859–1874 (2005).
27. Helfrich, W. Elastic properties of lipid bilayers: theory and possible experiments. *Z. Naturforsch. C* **28,** 693–703 (1973).
28. Lipowsky, R. & Sackmann, E. *Structure and Dynamics of Membranes: I. From Cells to Vesicles/II* (Generic and Specific Interactions, 1995).
29. Schmidt, D. *et al.* Signature of a nonharmonic potential as revealed from a consistent shape and fluctuation analysis of an adherent membrane. *Phys. Rev. X* **4,** 021023 (2014).
30. Smith, A.-S., Sengupta, K., Goennenwein, S., Seifert, U. & Sackmann, E. Force-induced growth of adhesion domains is controlled by receptor mobility. *Proc. Natl Acad. Sci. USA* **105,** 6906–6911 (2008).
31. Chiantia, S., Ries, J. & Schwille, P. Fluorescence correlation spectroscopy in membrane structure elucidation. *Biochim. Biophys. Acta* **1788,** 225–233 (2009).
32. Ries, J. *et al.* Modular scanning FCS quantifies receptor-ligand interactions in living multicellular organisms. *Nat. Methods* **6,** 643–645 (2009).
33. Humpolickova, J. *et al.* Probing Diffusion laws within cellular membranes by Z-Scan fluorescence correlation spectroscopy. *Biophys. J.* **91,** L23–L25 (2006).
34. Eggeling, C. *et al.* Direct observation of the nanoscale dynamics of membrane lipids in a living cell. *Nature* **457,** 1159–1162 (2009).
35. Wiseman, P. W. Image correlation spectroscopy: mapping correlations in space, time, and reciprocal space. *Methods Enzymol.* **518,** 245–267 (2013).
36. Digman, M. A., Wiseman, P. W., Horwitz, A. R. & Gratton, E. Detecting protein complexes in living cells from laser scanning confocal image sequences by the cross correlation raster image spectroscopy method. *Biophys. J.* **96,** 707–716 (2009).
37. Wohland, T., Shi, X., Sankaran, J. & Stelzer, E. H. K. Single plane illumination fluorescence correlation spectroscopy (SPIM-FCS) probes inhomogeneous three-dimensional environments. *Opt. Express* **18,** 10627–10641 (2010).
38. Hedde, P. N. *et al.* Stimulated emission depletion-based raster image correlation spectroscopy reveals biomolecular dynamics in live cells. *Nat. Commun.* **4,** 2093 (2013).
39. Weidemann, T., Mücksch, J. & Schwille, P. Fluorescence fluctuation microscopy: a diversified arsenal of methods to investigate molecular dynamics inside cells. *Curr. Opin. Struc. Biol* **28C,** 69–76 (2014).
40. Capoulade, J., Wachsmuth, M., Hufnagel, L. & Knop, M. Quantitative fluorescence imaging of protein diffusion and interaction in living cells. *Nat. Biotech.* **29,** 835–839 (2011).
41. Dertinger, T. *et al.* Two-focus fluorescence correlation spectroscopy: a new tool for accurate and absolute diffusion measurements. *ChemPhysChem* **8,** 433–443 (2007).
42. Baumgart, T., Hess, S. T. & Webb, W. W. Imaging coexisting fluid domains in biomembrane models coupling curvature and line tension. *Nature* **425,** 821–824 (2003).
43. Pedersen, S., Jorgensen, K., Baekmark, T. R. & Mouritsen, O. G. Indirect evidence for lipid-domain formation in the transition region of phospholipid bilayers by two-probe fluorescence energy transfer. *Biophys. J.* **71,** 554–560 (1996).
44. Limozin, L. & Sengupta, K. Quantitative reflection interference contrast microscopy (RICM) in soft matter and cell adhesion. *ChemPhysChem* **10,** 2752–2768 (2009).
45. Tuvia, S., Levin, S., Bitler, A. & Korenstein, R. Mechanical fluctuations of the membrane-skeleton are dependent on F-actin ATPase in human erythrocytes. *J. Cell Biol.* **141,** 1551–1561 (1998).
46. Schroder, K., Hertzog, P. J., Ravasi, T. & Hume, D. A. Interferon-gamma: an overview of signals, mechanisms and functions. *J. Leukoc. Biol.* **75,** 163–189 (2004).
47. Fradin, C., Abu-Arish, A., Granek, R. & Elbaum, M. Fluorescence correlation spectroscopy close to a fluctuating membrane. *Biophys. J.* **84,** 2005–2020 (2003).
48. Reister, E. & Seifert, U. Lateral diffusion of a protein on a fluctuating membrane. *Europhys. Lett.* **71,** 859–865 (2005).
49. Gauthier, N. C., Masters, T. A. & Sheetz, M. P. Mechanical feedback between membrane tension and dynamics. *Trends Cell Biol.* **22,** 527–535 (2012).
50. Csiszar, A. *et al.* Novel fusogenic liposomes for fluorescent cell labeling and membrane modification. *Bioconjugate Chem.* **21,** 537–543 (2010).

Acknowledgements

We thank Nils Hersch, Victor Messerschmidt and Tim Urbansky for providing macrophages. C.M. is grateful for the financial support by UFA and Cellnetworks. We thank David Gachet and Susanne Fenz for fruitful discussions and Laurent Limozin for careful reading of the manuscript. K.S. thanks European Research Council for funding via grant no. 307104 FP/2007-2013/ERC/SYNINTER and ASS for ERC/StG 337283.

Author contributions

The project was conceived by R.M., K.S. and C.M. The experimental set-up was established by C.M., D.K. and C.K.. Data analysis were performed by C.M. and D.S. supervised by R.M., K.S., A.S.S. and U.S. The article was written by C.M., K.S., A.S.S. and R.M.

Additional information

Supplementary Information accompanies this paper at http://www.nature.com/naturecommunications

Competing financial interests: The authors declare no competing financial interests.

Reprints and permission information is available online at http://npg.nature.com/reprintsandpermissions/

How to cite this article: Monzel, C. *et al.* Measuring fast stochastic displacements of bio-membranes with dynamic optical displacement spectroscopy. *Nat. Commun.* 6:8162 doi: 10.1038/ncomms9162 (2015).

Supplementary Figure 1: Confocal detection volume

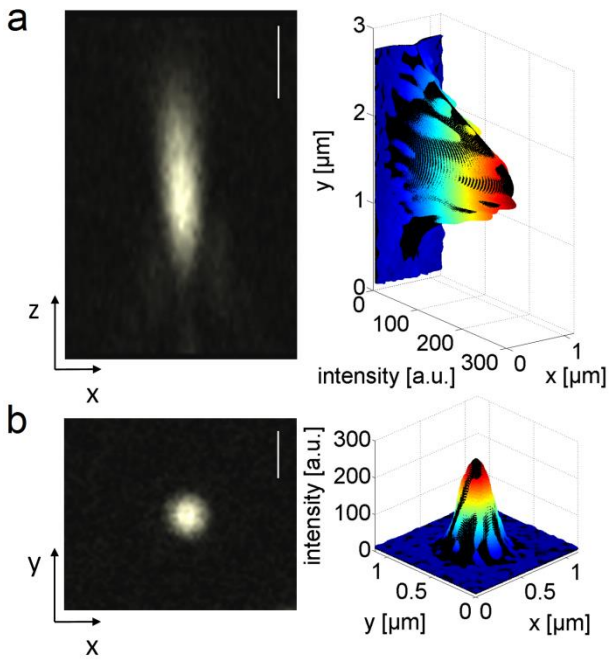

Knowledge about the intensity distribution in the confocal volume and its size is crucial for DODS measurements: To verify the near Gaussian shape in both axial as well as lateral direction, the confocal detection volume was measured for λ = 543 nm with beads of subresolution size. (a) Left: Axial (xz) view of measured bead intensity. Right: The intensity distribution is fitted with a 2D asymmetric Gaussian (rgb colour). (b) Left: Lateral (xy) view of measured bead intensity. Right: Fit of 2D symmetric Gaussian (rgb colour).
Scale bars: 1 µm (xz) and 0.5 µm (xy).

Supplementary Figure 2: Axial intensity scans and ACFs for GUVs

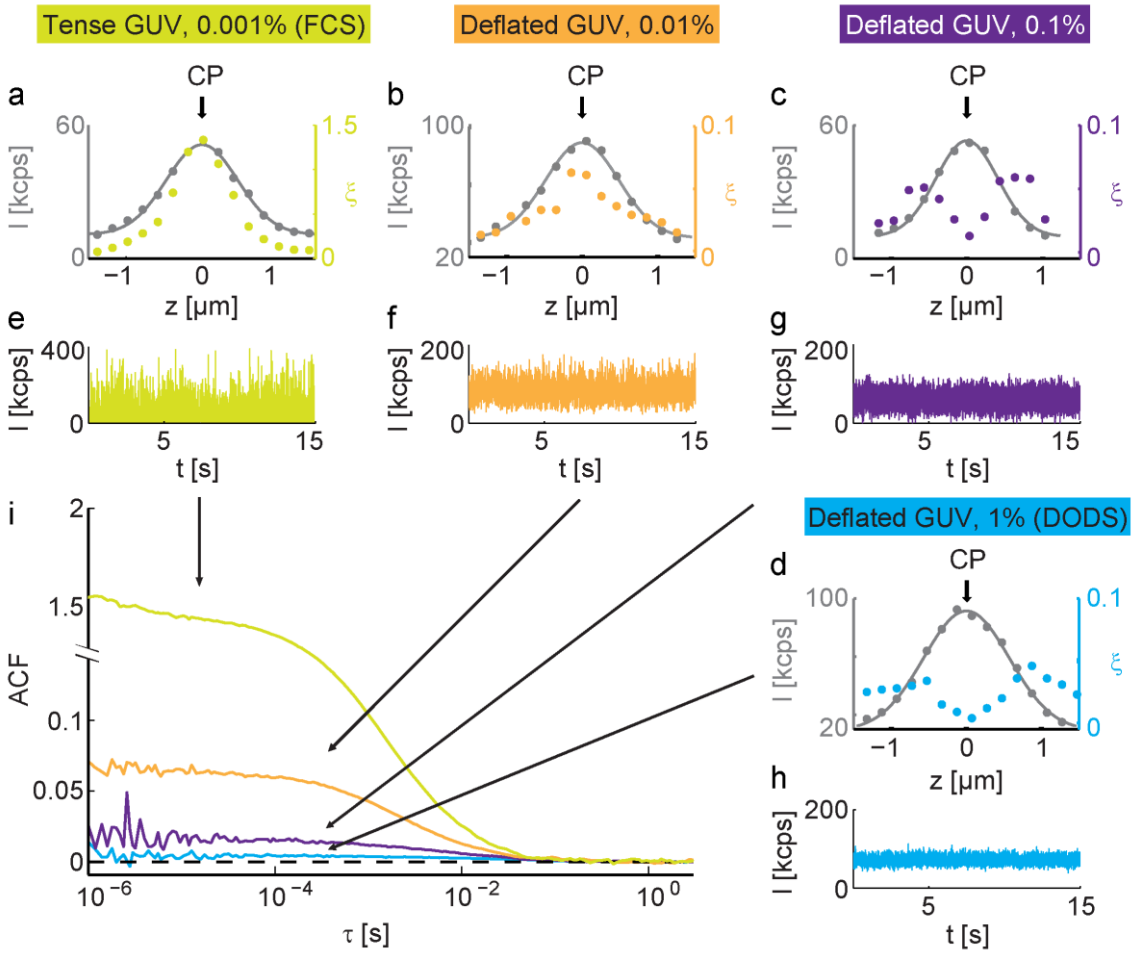

(a)-(d) Recorded axial scans of GUVs with different fluorophore concentrations. Average intensities (grey dots), Gaussian fit (grey line) and correlation amplitude ξ for fluorophore concentration 0.001% (yellow), 0.01% (orange), 0.1% (purple) and 1% (light blue) are shown. ξ changes from a single-peaked to a double-peaked shape when the GUV is deflated and the fluorophore concentration increased. (e)-(h) Intensity traces $I(h(t))$ were measured at the center CP of the confocal volume. (i) The ACF, defined as $\langle \delta I(\tau)\, \delta I(0) \rangle / \langle I(t) \rangle^2$, is calculated from these traces and exhibits a flattening of the amplitude.

Supplementary Figure 3: Axial intensity scans and ACFs for SLB

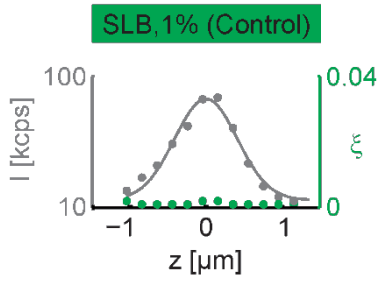

Recorded axial scan of a supported lipid bilayer (SLB) as control measurement. Average intensities (grey dots), Gaussian fit (grey line) and correlation amplitude ξ (green dots). ξ remains flat over the whole scan. Since a SLB cannot have spatial fluctuations, the maximal value, $\xi_{\mathrm{det}} = 0.0024$, marks the detection limit of our DODS setup.

Supplementary Figure 4: Influence of the signal-to-noise ratio on spatial resolution

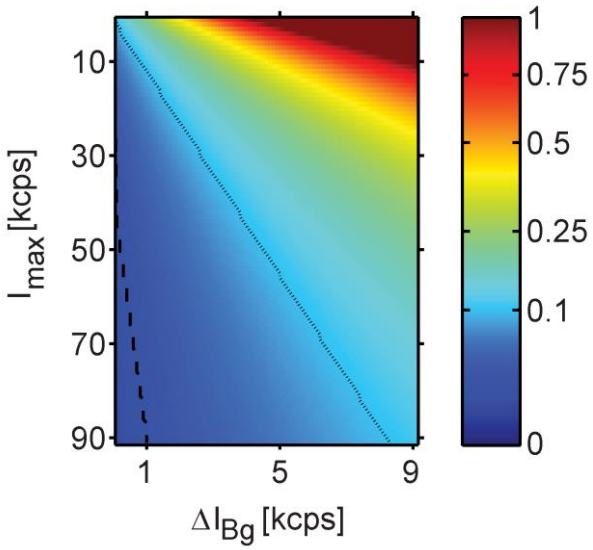

Illustration of typical signal intensity I_{max} vs. background intensity ΔI_{Bg}. The colour code indicates the corresponding spatial error Δh in µm, which is estimated analytically (see text for details). Black dashed line marks the $\Delta h = 20\,\mathrm{nm}$ and dotted black line the $\Delta h = 100$ nm error.

Supplementary Figure 5: Stationarity of measurement

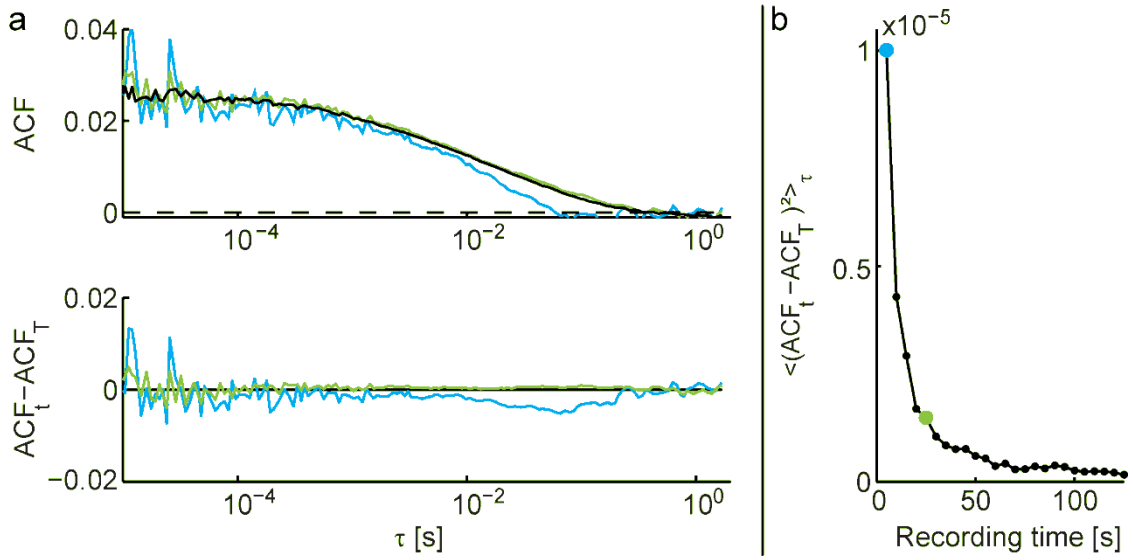

GUV membrane fluctuations are measured at the IP for a total recording time T = 3 min. The signal is subdivided into 5 s intervals, so-called repeats, and an ACF for each is calculated. (a) Top: Average ACF derived from all repeats (36×5 s = 3 min, black), in comparison to single repeat (5 s recording time, blue) and five repeat average (25 s recording time, green). Bottom: Deviation between the ACF of total recording time T = 3 min and the ACF for t = 5 s (blue) or t = 25 s (green). (b) Square deviation averaged over all lag times τ vs. recording time (5 s (blue) and 25 s (green) are indicated). With increasing recording time, the shape of the ACF stabilizes.

Supplementary Figure 6: Theoretical correlation amplitude

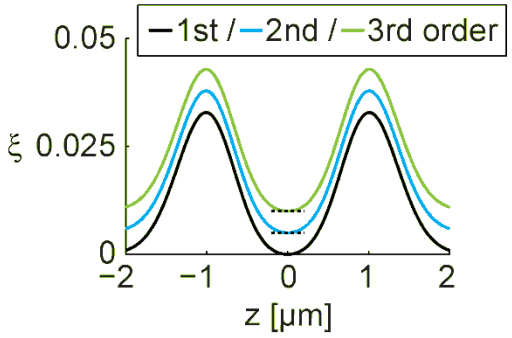

Here, ξ is shown for different orders of the approximation for small fluctuations $\delta h / z_0 << 1$. Parameters used to generate the curves are: $I_{max} = 60$ kcps, $\omega_0 = 0.281$ µm and $\omega_0 = 1.284$ µm and the membrane parameters (see also **Supplementary Note 3**) $\kappa = 20$ k_BT, $\sigma = 0.5$ µJm^{-2}. For visibility reasons, curves are shifted along the ξ-axis by 0.005. ξ is the same for all orders of approximation and exhibits the characteristic double-peaked shape, as observed in DODS experiments.

Supplementary Figure 7: Error in height conversion

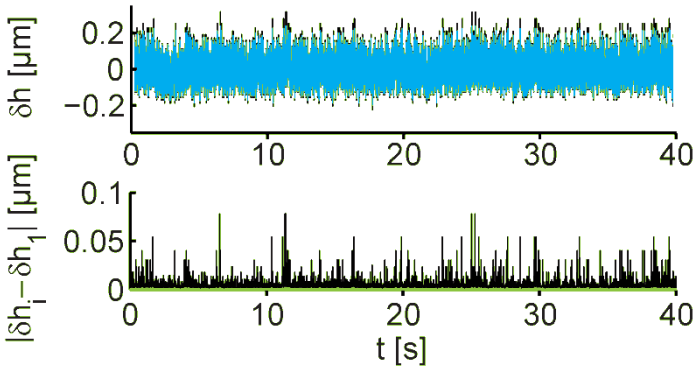

Top: displacement traces of a GUV membrane at the GUV distal site. Measurements were recorded at the inflection point of the confocal detection volume and converted via the linear intensity dependence (blue), for the 2nd (green) and 3rd (black) order expansion (see **Supplementary Eq. 2**). Bottom: absolute deviation between higher and first order conversion, $|\delta h_2 - \delta h_1|$ (green) and $|\delta h_3 - \delta h_1|$ (black). The average deviation $\langle |\delta h_3 - \delta h_1| \rangle_t$ amounted to 12 nm.

Supplementary Figure 8: Comparison of DODS and DW-RICM.

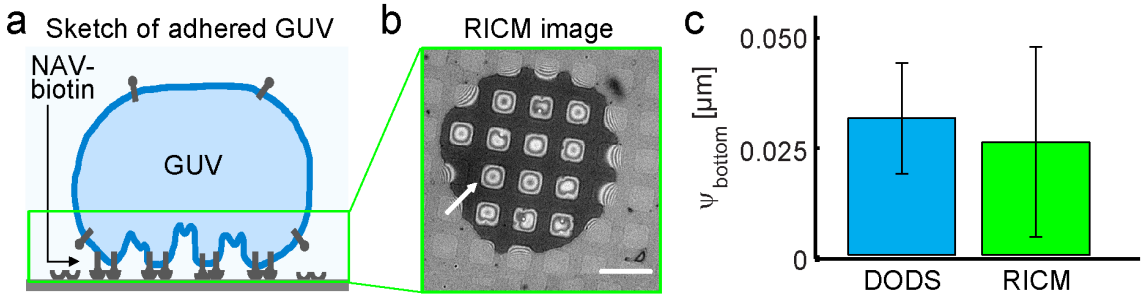

(a) Sketch of GUV adhered to protein grid with adhered and freely fluctuating membrane regions. Note, the sketch is not to scale. (b) One of the two RICM images recorded with DW-RICM showing the membrane bottom region. The arrow points to a square region where fluctuations where evaluated. Scale bar: 10 µm. (c) Average ψ and standard deviation as obtained from measurements at the vesicle bottom.

Supplementary Note 1: Converting intensity flickers to displacements

Here we derive the theoretical expressions linking first the measured intensity flickers $\delta I(t)$ to the real membrane displacements $\delta h(t)$, and second, the intensity autocorrelation function (ACF) to the displacement autocorrelation function (dACF). We assume that the signal from diffusion of fluorophores is negligible, and that the confocal volume has a Gaussian intensity distribution given by

$$I(z) = I_0 \frac{\pi c_0 \omega_0^2}{2} \exp\left[-2\frac{z^2}{z_0^2}\right] + I_{Bg} \quad . \tag{1}$$

Here, z is the average vertical position of the membrane within the confocal volume (see also **Fig. 2** for an explanation of coordinates and symbols), c_0 is the fluorophore concentration, I_{Bg} is the background intensity, and ω_0 and z_0 are the radial and axial dimensions of the confocal volume (ω_0 = 280 ± 5 nm (N = 10) and z_0 = 1285 ± 10 nm (N = 10)[1], as measured using fluorescent beads of sub-resolution size: data not shown). $I_{\max} = I_0 \pi c_0 \omega_0^2 / 2$ is the maximal intensity detected in a vertical scan through the confocal volume. For a fluctuating membrane, the vertical position z becomes time dependent $z \equiv h(t) = h_0 + \delta h(t)$ where $h_0 \equiv \langle h(t) \rangle$ is the mean membrane position and $\delta h(t)$ is the instantaneous membrane displacement (see **Fig. 2**).

Intensity-displacement relation: For membrane displacements that are small compared to the size of the confocal volume ($\delta h(t)/z_0 << 1$) the intensity fluctuation $\delta I(t)$ around the mean value $\langle I(t) \rangle$ is defined as $I(t) \equiv \langle I(t) \rangle + \delta I(t)$, where $I(t)$ is the instantaneous measured intensity. Using **Supplementary Eq. 1** and expanding $\delta I(t)$ around the mean position h_0,

$$\delta I(t) = -I_{\max} \exp\left[-2\frac{h_0^2}{z_0^2}\right]\left\{\frac{4h_0\,\delta h(t)}{z_0^2} + \frac{2}{z_0^2}\left(1 - \frac{4h_0^2}{z_0^2}\right)\left(\delta h^2(t) - \langle \delta h^2 \rangle\right) + \mathrm{O}(\delta h^3(t))\right\}. \tag{2}$$

If the membrane is placed at the inflection point of the intensity profile, as is the case with typical DODS measurements, the second order term vanishes and a first order approximation for $\delta I(t)$ is sufficient (see also **Supplementary Note 2** for validation of this approximation). **Supplementary Eq. 2** then reads

$$\delta I(t) = -I_{\max} \exp\left[-2\frac{h_0^2}{z_0^2}\right]\left\{\frac{4h_0\,\delta h(t)}{z_0^2}\right\} \equiv m \cdot \delta h(t)\,. \tag{3}$$

In a DODS experiment, the slope m is measured from axial scans in the vertical (z) direction as described in the main text. In the form $\delta I(t) = m \cdot \delta h(t)$ **Supplementary Eq. 3** can be used as long as the intensity distribution in the axial scan exhibits a well-defined inflection point.

[1] Error-bars are standard deviations. N is the number of measurements.

ACF-dACF relation: If the membrane fluctuates around a constant mean position (i.e. it has no net displacement over time), the system is amenable to correlation analysis. In general, the correlation amplitude and the autocorrelation function (ACF) of the intensity fluctuations are defined as

$$\xi \equiv \frac{\left\langle \delta I(t)^2 \right\rangle}{\left\langle I(t) \right\rangle^2} \quad \text{and} \quad ACF \equiv \frac{\left\langle \delta I(\tau)\, \delta I(0) \right\rangle}{\left\langle I(t) \right\rangle^2} \ . \tag{4}$$

Consequently, in the limit of small membrane fluctuations, the correlation amplitude and the ACF of the intensity fluctuations become (up to second order in $\delta h(t)$)

$$\xi = \frac{I_{\max}}{\left\langle I(t) \right\rangle^2} \exp\left[-4 \frac{h_0^2}{z_0^2} \right] \frac{16 h_0^2}{z_0^4} \psi^2 \equiv \frac{m^2}{\left\langle I(t) \right\rangle^2} \psi^2 \ , \tag{5}$$

$$ACF = \frac{\xi}{\psi^2} \left\langle \delta h(\tau)\, \delta h(0) \right\rangle \equiv \frac{m^2}{\left\langle I(t) \right\rangle^2} dACF \ , \tag{6}$$

defining the amplitude of fluctuations $\psi \equiv \sqrt{\left\langle \delta h^2 \right\rangle}$ and the displacement autocorrelation function $dACF \equiv \left\langle \delta h(t)\, \delta h(0) \right\rangle$. Note again that for DODS the membrane is placed at the inflection point of the Gaussian intensity profile. Here, the intensity profile is the steepest (the slope m is maximum) and thus, the correlation amplitude is the highest. Note, that the above conversion of intensity into heights has only a unique solution as long as fluctuations remain on one side of the Gaussian illumination profile. In all the cases considered here, this condition is easily fulfilled since the fluctuation amplitudes are much smaller than the axial confocal radius $z_0 \cong 1$ µm. The amplitude of the correlation function and hence the amplitude of fluctuations, as well as the relaxation time τ^* defined as the time-point where $dACF(\tau^*) \equiv dACF(0)/e$, is determined from the plot of the $dACF$.

Supplementary Note 2: Spatio-temporal resolution, recording time and validity of linear intensity/displacement relation

Temporal resolution: The raw data is recorded at rate of 200 ns. This is then averaged in the acquisition software (see Methods section) to 1 µs to build the intensity ACF. The absolute time resolution of the system is therefore 1 µs. However, for the systems studied here we found that the signal to noise ratio at such short times were unacceptably low. To determine the appropriate time cut-off, we examined dACF curves from optimal GUV data and chose the time point at which the value of the noise seen in the dACF data (defined as the standard deviation) exceeds 10% of dACF value. This corresponds to a lag time of 10 µs. Thus, 10 µs is the appropriate time resolution in the present set-up.

Spatial resolution: The spatial resolution is related to the shape of the confocal volume and the background noise. A rough estimate can be obtained by considering the traces from SLB presented in **Supplementary Fig. 2**. The maximum value of the correlation amplitude $\xi_{\text{det}} = 0.0024$, marks the detection limit. At the inflection point, for a typical slope of m =

130 kcps/µm, intensity of about 50 kcps, using **Supplementary Eq. 5**, a spatial resolution limit of $h_{\mathrm{det}} = \sqrt{(50\,kcps)^2 \cdot \xi_{\mathrm{det}} / m^2} = 20\,\mathrm{nm}$ is obtained. The influence of the signal-to-noise ratio on the spatial resolution can be estimated theoretically by calculating the error in displacement considering variable signal and background intensity. Here, a conversion of intensities into displacements at the inflection point of the Gaussian intensity profile (see **Supplementary Eq. 1**) is assumed, where $\delta h \propto \delta I$ holds. More specifically, as the background intensity increases by ΔI_{Bg} the error in the displacement Δh is given by the slope $m = 0.61 \cdot 2I_{\max} / z_0$, such that:

$$\Delta h = \frac{\Delta I_{Bg}}{m} = \frac{\Delta I_{Bg}\, z_0}{0.61 \cdot 2I_{\max}}$$

Supplementary Fig. 4 shows the result of this calculation for typical fluorescence intensity values $I_{\max} = 0 - 90\,\mathrm{kcps}$. Background intensities were varied between $I_{Bg} = 0 - 9$ kcps and z_0 = 1.285 µm is the measured axial radius of the confocal volume. A lower limit of ΔI_{Bg} is given by the dark current of the APDs amounting to 0.5 kcps. This is a common background intensity value for vesicle experiments in PBS buffer. It has to be noted, that other systems may exhibit higher ΔI_{Bg} values, resulting in a corresponding drastic increase in the spatial error. Clearly, only signal intensities of $70 - 100$ kcps and the usually measured background intensity of $\leq$ 1 kcps, allow for an accuracy of $\leq$ 20 nm. Note that utilization of phenol red containing medium raised ΔI_{Bg} to 2 kcps, its use was therefore avoided.

Stationarity and recording time: Stationarity of the signal and sufficient recording time are essential prerequisites for correlation analysis. To test their validity in DODS measurements, deflated GUVs of high fluorophor concentration were used and intensity traces of $\geq$ 180 s duration at the IP acquired. Each measurement was subdivided into $\geq$ 36 short intervals of 5 s duration, so-called repeats. The ACF of each repeat was calculated and, subsequently, average ACFs for an increasing number of repeats were generated. **Supplementary Fig. 5** illustrates examples of ACF, for a single repeat, an average of 5 repeats, as well as the total average ACF of all repeats after 3 min recording time. Stationarity of the signal is tested for by plotting the deviation between the total average ACF and an ACF of shorter recording time. While a symmetric variation around 0 indicates stationarity, the square of this deviation averaged over all τ specifies the shape stability of the ACF. In our setup, stationarity and a shape precision comparable to the experimental error is achieved in case of 5 repeats. Thus, the minimal recording time of DODS measurements is $5 \times 5 = 25\,\mathrm{s}$, which roughly amounts to 1000 correlation times (cf. **Supplementary Fig. 5a**).

Error introduced by linear approximation: The theoretical correlation amplitude, which is defined as the extrapolated ACF at zero lag time $\tau = 0$, is calculated to first order in $\langle \delta h(t)^2 \rangle$, see **Supplementary Eq. 5**. The theoretical correlation amplitude calculated up to different orders of approximation is shown in **Supplementary Fig. 6**. **Supplementary Fig. 7** depicts an example of intensity-displacement conversion via a Taylor expansion up to 1st, 2nd or 3rd order in $\delta h(t)$. The absolute deviation between higher and first order trace is calculated and averaged. Despite the obvious deviation in $|\delta h_3 - \delta h_1|$ the temporal average yields an error of 12 nm in lateral resolution.

Supplementary Note 3: Comparison of DODS and DW-RICM at the vesicle bottom

DODS was validated by comparing thermal fluctuations measured at the vesicle bottom with measurements obtained by Dual-wavelength Reflection Interference Contrast Microscopy (DW-RICM) [SI4, SI5]. This microinterferometric technique is an advanced setup of RICM where two interferograms for different wavelengths are recorded simultaneously. RICM is highly sensitive to membrane-substrate distances and allows reconstruction of membrane topographic shapes with 5 nm axial resolution and some ~ 10 ms temporal resolution (for further details see **Methods** and [SI4, SI5]). Here, this well established technique is used to compare DW-RICM with DODS using equally prepared GUV thus substantiating the DODS approach.
In order to perform experiments on a precisely studied system we monitored GUVs interacting with special substrates [SI6]. To prepare these, cleaned glass substrates were stamped with micro-scale grids of BSA-biotin which was further functionalized with neutravidin (NAV). The GUV membrane which exhibits biotin moieties, adheres to these grids but in-between the grids, the membrane continues to fluctuate (as shown in **Supplementary Fig. 8a and b**). This geometry ensures well defined measurement conditions without any lateral drift of the vesicles. Following reference [SI2], the DW-RICM data was theoretically corrected to account for the limited time resolution. Since both DW-RICM and DODS require dedicated microscopes, it was not possible to make one-to-one correspondence of the height traces. We therefore report the average and standard deviation of the fluctuation amplitude measured for 14 vesicles in each case. The two measurements were done successively on the same sample. The value extracted from DW-RICM data matches very well with DODS data.

Supplementary Note 4: Calculation of tension and dissipation from dACF

Accounting for system point spread function: The cross-section between the confocal volume and the membrane has a finite size, instead of being a single point $r=(x,y)$ on the membrane. In order to make quantitative comparison with theory, we account for blurring of the fluctuations by the point spread function $P(r)$ of the system

$$P(r)=\frac{2}{\pi\omega^2}\exp\left[-2\frac{r^2}{\omega^2}\right] \tag{7}$$

Here, ω is the radial radius of the laser beam at the axial position h_0 which increases with distance from the center of the point spread function (for definition of the coordinates see also **Fig. 2**) [SI1]

$$\omega^2=\omega_0^2\left(1+\frac{\lambda^2 h_0^2}{\pi^2 n^2 \omega_0^4}\right) \tag{8}$$

with the refractive index n of the bulk medium and the wavelength λ of the excitation light. Measured fluctuations are thus a convolution of the real membrane fluctuations and $P(r)$. For the general principle, see Schmidt et al. [SI2] and references therein. Here, $P(r)$ is used to deconvolve the dACF which is fitted with a theoretical expression to calculate the membrane

bending rigidity κ, membrane tension σ (see following subsection). Note that if the dACF is not deconvoluted, both κ and σ are underestimated by about 20% (Authors, in preparation).

Tension and dissipation from fluctuations: In a model membrane, the fluctuations are determined by the membrane bending elasticity, κ, membrane tension, σ, and a dissipation depending on the bulk liquid viscosity, η. The theoretical description of the dynamics of model membranes is well known in the literature (for a review see Seifert [SI3] and references therein), which combined with the deconvolution above yields

$$\left\langle \delta h(\tau)\, \delta h(0) \right\rangle = \frac{k_B T}{2\pi} \int_{q_{\min}}^{\infty} dq \frac{1}{\kappa q^3 + \sigma q} \exp\left[-\frac{1}{4} q^2 \omega^2 - \frac{(\kappa q^3 + \sigma q)\tau}{4\eta} \right] \qquad (9)$$

The integral runs over all modes that can be excited on the membrane, where the natural lower limit of the wave vector is given by the vesicle radius R and $q_{\min} = 1/R$. Note, that the Monge Gauge here assumes that on average the GUV membrane is flat (in fact, it is curved at large scale). Calculations in the quasi-spherical approximations yield values which can differ by up to 20% compared to an analysis performed in Monge Gauge. The systematic error can be reduced below 10% by choosing a slightly different lower cut off (Authors, in preparation). Here, for simplicity, we retain the flat membrane approximation and the conventionally used lower cut off. By using vesicles of typically 30 µm diameter and with a beam diameter of about 0.6 µm we ensured the validity of this approximation. For SOPC membrane, $\kappa = 20$ k_BT [6] is well known and was kept constant throughout the analyses. This strategy provides a way to sensitively determine σ and η. A typical fit is shown in **Fig. 3**. The corresponding tension is $0.23\,\mu J/m^2$ and the viscosity is 1.15 mPas. As mentioned in the main text, this is in very good agreement with expectations. Note, however, that a refinement in the theoretical description (see [SI2] and Authors, in preparation), accounting for the viscosity of the inner buffer, which is $\eta_i = 1.4$ mPas in the presented system and different from the outer buffer PBS with $\eta_0 = 1.0$ mPas, can further improve the agreement between the estimated value and the DODS measurements.

Supplementary Note 5: Axial scans for intensity gradient control

DODS can be used to measure membrane fluctuations at variable distances away from the substrate spanning 0-100 µm. This is demonstrated here for measurements at the rim and centre of erythrocytes, close to the cell body and in the lamellipodium of macrophages, at the distal surface of GUV and in control measurements with SLBs. This spatial flexibility is due to the fact that DODS requires only axial intensity gradient information around the membrane average position. This gradient intensity is measured by axial scans across the membrane, which –for the objects in this study- returned Gaussian intensity distributions. Measurements are performed at the inflection point of the Gaussian, where the highest intensity gradient is reached. Moreover, any systematic distortion of the confocal volume, asymmetric fluorophore distribution, etc. will directly be visible through changes in the Gaussian intensity distribution. Thus, performing axial scans prior to each measurement yields high control over the actual intensity variation for height fluctuation conversion.

Supplementary References

[1] Palmer, A. G. & Thompson, N. L., Optical spatial intensity profiles for high order autocorrelation in fluorescence spectroscopy, *Appl. Opt.*, **28**, 1214-1220 (1989).
[2] Schmidt, D. et al., Signature of a nonharmonic potential as revealed from a consistent shape and fluctuation analysis of an adherent membrane, *Phys. Rev. X*, **4**, 021023 (2014).
[3] Seifert, U., Configurations of fluid membranes and vesicles, *Advances in Physics*, **46**, 13-137 (1997).
[4] Monzel, C., Fenz, S., Merkel, R. & Sengupta, K. Probing biomembrane dynamics by dualwavelength reflection interference contrast microscopy. *Chemphyschem* **10**, 2828–2838 (2009).
[5] Limozin L., Sengupta K., Quantitative reflection interference contrast microscopy (RICM) in soft matter and cell adhesion. *Chemphyschem*, **10**, 2752-2768, (2009)
[6] Monzel, C., Fenz, S. F., Giesen, M., Merkel, R. & Sengupta, K. Mapping fluctuations in biomembranes adhered to micropatterns. *Soft Matter* **8**, 6128-6138 (2012).

P3

Nanometric thermal fluctuations of weakly confined bio-membranes measured with microsecond time-resolution

Nanometric thermal fluctuations of weakly confined bio-membranes measured with microsecond time-resolution

C. Monzel[1,2,†], D. Schmidt[3,4], U. Seifert[4], A.-S. Smith[3,5], R. Merkel[1], and K. Sengupta[2]

[1] Aix-Marseille Université, CNRS UMR 7325, Marseille Cedex 9, France
[2] ICS 7, Forschungszentrum Jülich, Jülich, Germany
[3] II. Institut für Theoretische Physik, Universität Stuttgart, Germany
[4] Institut für Theoretische Physik, Friedrich Alexander Universität Erlangen-Nürnberg, Germany
[†] Present addresses: Institut Curie, CNRS UMR 168, 75005 Paris Cedex 5, France

Soft Matter, 2016, Advance Article

DOI: 10.1039/C6SM00412A
http://pubs.rsc.org/en/content/articlelanding/2016/sm/c6sm00412a

ABSTRACT We probe bending fluctuations of bio-membranes using highly deflated giant unilamellar vesicles (GUVs) bound to a substrate by a weak potential arising from generic interactions. The substrate is either homogeneous, with GUVs bound only by the weak potential, or is chemically functionalized with a micro-pattern of very strong specific binders. In both cases, the weakly adhered membrane is seen to be confined at a well-defined distance above the surface while it continues to fluctuate strongly. We quantify the fluctuations of the weakly confined membrane at the substrate proximal surface as well as of the free membrane at the distal surface of the same GUV. This strategy enables us to probe in detail the damping of fluctuations in the presence of the substrate, and to independently measure the membrane tension and the strength of the generic interaction potential. Measurements were done using two complementary techniques – Dynamic Optical Displacement Spectroscopy (DODS, resolution: 20 nm, 10 μs), and Dual Wavelength Reflection Interference Contrast Microscopy (DW-RICM, resolution: 4 nm, 50 ms). After accounting for the spatio-temporal resolution of the techniques, excellent agreement between the two measurements was obtained. For both weakly confined systems we explore in detail the link between fluctuations on the one hand and membrane tension and the interaction potential on the other hand.

Soft Matter

PAPER

View Article Online
View Journal

Cite this: DOI: 10.1039/c6sm00412a

Nanometric thermal fluctuations of weakly confined biomembranes measured with microsecond time-resolution

Cornelia Monzel,†[ab] Daniel Schmidt,[cd] Udo Seifert,[c] Ana-Sunčana Smith,[de] Rudolf Merkel[b] and Kheya Sengupta*[a]

Received 17th February 2016,
Accepted 11th April 2016

DOI: 10.1039/c6sm00412a

www.rsc.org/softmatter

We probe the bending fluctuations of bio-membranes using highly deflated giant unilamellar vesicles (GUVs) bound to a substrate by a weak potential arising from generic interactions. The substrate is either homogeneous, with GUVs bound only by the weak potential, or is chemically functionalized with a micro-pattern of very strong specific binders. In both cases, the weakly adhered membrane is seen to be confined at a well-defined distance above the surface while it continues to fluctuate strongly. We quantify the fluctuations of the weakly confined membrane at the substrate proximal surface as well as of the free membrane at the distal surface of the same GUV. This strategy enables us to probe in detail the damping of fluctuations in the presence of the substrate, and to independently measure the membrane tension and the strength of the generic interaction potential. Measurements were done using two complementary techniques – dynamic optical displacement spectroscopy (DODS, resolution: 20 nm, 10 μs), and dual wavelength reflection interference contrast microscopy (DW-RICM, resolution: 4 nm, 50 ms). After accounting for the spatio-temporal resolution of the techniques, an excellent agreement between the two measurements was obtained. For both weakly confined systems we explore in detail the link between fluctuations on the one hand and membrane tension and the interaction potential on the other hand.

Introduction

In bio-membranes, spatial fluctuations, also called bending fluctuations, give rise to repulsive contributions and to inter-membrane interactions.[1–3] The physiological relevance of these fluctuations is highly debated, for example, in the case of erythrocyte membrane fluctuations and their ATP dependence.[4–7]

Thermally driven membrane fluctuations have been explored theoretically and experimentally since the 1970s,[1,3,8–10] starting with the pioneering studies by Helfrich[1,3] who introduced the concept of steric repulsion of bilayer membranes calculated from their bending rigidity. These studies stimulated a comprehensive theoretical description of membrane fluctuations,[11–16] accounting for the bilayer nature,[17,18] membrane tension,[19,20] molecular constituents[21] as well as the interaction with a substrate.[22,23]

To verify these concepts experimentally, membrane model systems were developed comprising solid supported lipid bilayers, membrane stacks, and giant unilamellar vesicles (GUVs) in a free,[24–26] micropipette aspirated[27] or adhered state.[28–33] Most of these experimental studies focused on a precise evaluation of the membrane physico-chemical properties.[34–36] Intriguingly, even for bending rigidity measurements, small-wavelength scattering experiments have identified anomalies,[36–38] which may be associated with the extreme sensitivity of fluctuations to the surrounding buffer conditions. The use of mixed membranes may of course introduce micro- or nano-scale phase-separation, which in turn may impact the measured membrane properties.[39]

Fluctuations were also used to analyse membrane adhesion dynamics and equilibrium states. For the latter, an initial bond density regime of $\sim 10^4\ \mu m^{-2}$ was mostly chosen, which largely exceeds the typical concentration of adhesion molecules on the cell surface of $\sim 10–100\ \mu m^{-2}$.[40] Adhesion in the limit of dilute bonds was investigated recently[41–43] and gained much attention as adhesion structures similar to those of cells were observed.[44] Still, data for weakly adhering membranes and the initial stages of adhesion are sparse and their properties are yet to be characterized in detail.

In addition, when studying the above models, a challenge arose whenever membrane properties were to be determined in

[a] Aix-Marseille Université, CNRS UMR 7325 (Centre Interdisciplinaire de Nanosciences de Marseille – CINaM), Marseille Cedex 9, France. E-mail: sengupta@cinam.univ-mrs.fr, cornelia.monzel@curie.fr
[b] Institute of Complex Systems 7 (ICS-7), Forschungszentrum Jülich, Jülich, Germany
[c] II. Institut für Theoretische Physik, Universität Stuttgart, Germany
[d] Institut für Theoretische Physik, Friedrich Alexander Universität Erlangen-Nürnberg, Germany
[e] Division of Physical Chemistry, Ruđer Bošković Institute, 10000 Zagreb, Croatia
† Present address: Institut Curie, CNRS UMR 168, 75005 Paris Cedex 5, France.

the vicinity of a substrate: herein, membrane fluctuations are sterically restricted as the thermally excited out-of-plane fluctuations repel the membrane from the hard wall – an interaction usually referred to as Helfrich repulsion. Conversely, biological membranes near a wall may encounter attractive interactions, which, for the systems discussed herein, comprise van der Waals interaction and gravity.[45] These generic interactions (likewise termed non-specific interactions) give rise to a total interaction potential of strength γ, which has the effect of rescaling membrane fluctuations.[46,47] In the past, several experimental and data analysis strategies have been developed to determine the interaction potential $V(h)$. Yet, most of these strategies are case specific. For example, in the limit of strong adhesion, the classical contact angle equation by Young–Dupré[48] can be used to determine the lateral membrane tension and the free energy of adhesion per unit area W, where $W \propto -V(h)$.[19,30,49–52] Another strategy in the case of ultra weak gravity dominated confinement is to use the overall shape deformation of the GUV.[52–54] Recently, we used the local equilibrium shape of the membrane to extract the detailed form of the interaction potential for the case of a membrane adhered to micropatterned substrates.[55] In the present study, a general, case-independent strategy is presented where γ is determined from the differences of fluctuations measured in the vicinity of the substrate and far away from it.

Finally, membrane fluctuations recorded with different techniques were hitherto difficult to compare since recordings are biased by the system resolution. Among the techniques predominately used to probe biomembranes shape fluctuations are flicker spectroscopy,[24,56] X-ray,[57,58] and neutron scattering.[59,60] Close to a wall, the technique of choice has been reflection interference contrast microscopy (RICM),[28,29,61–63] which is one of the techniques used in this work. RICM is limited to measurements in the substrate vicinity, due to the need for a reference beam for microinterferometry. Nevertheless, it is a label-free imaging technique which, in two wavelength implementation, probes membrane displacements in the normal direction with 4 nm resolution and with millisecond temporal precision.[28,64] The second technique used in this work is dynamic optical displacement spectroscopy (DODS),[7] which is complementary to RICM and based on a conventional fluorescence correlation spectroscopy (FCS) setup.[65,66] It records physical displacements of a fluorescent membrane with 10 μs temporal and 20 nm spatial resolution. In comparison to camera based techniques like RICM this is a temporal resolution enhancement by two to three orders of magnitude. Moreover, DODS can measure at both the top, *i.e.*, the distal surface of the GUV and in the vicinity of the substrate, *i.e.*, the proximal surface. A comparable technique to DODS was recently introduced,[67] which measures bending deformations in the lateral direction.

In order to compare data recorded using different techniques, we utilize an advanced theoretical framework which accounts for the spatio-temporal resolution of the setup.[55] This permits the simultaneous discussion of RICM and DODS data in this work.

Using RICM and DODS we investigate membrane fluctuations in two GUV/substrate based model systems (see Fig. 1). In the first model system the GUV hovers above a flat homogeneous substrate and the substrate proximal membrane is confined by a weak, generic potential. We call this the "weakly confined" case. In the second model system, the GUV is adhered to a chemical pattern exhibiting regions of strong adhesion and regions of weak, generic adhesion only. Within weakly adhesive regions, the membrane may fluctuate similarly to the weakly confined case. We call this the "structured adhered" case. Both systems represent membranes close to the adhesion–deadhesion transition,[68–70] as indicated by a circular shape of the GUV hemisphere. We trace membrane fluctuations over several orders of magnitude in space and time and, extract the tension, viscosity and the strength of the interaction potential from measurements at the distal and proximal surface. We propose an analysis protocol for compensating for finite resolution in experimental measurements, thus enabling us to

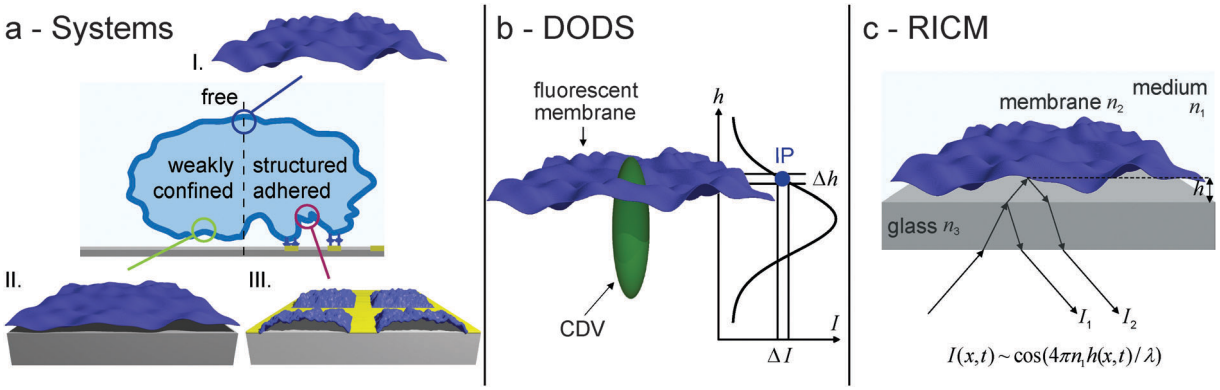

Fig. 1 (a) Sketch of systems investigated for nanometric membrane fluctuations: (I) free, unrestricted motion at the GUV distal side, (II) fluctuations of a weakly confined membrane near the substrate and (III) fluctuations of a structured adhered membrane. (b) Sketch of the DODS principle: a perpendicular intensity scan of the confocal detection volume (CDV) across the fluorescent membrane yields the inflection point (IP) of the intensity distribution. At this point physical displacements of the membrane, Δh, are most sensitively detected as intensity fluctuations, ΔI. (c) Sketch of the RICM principle: incident light of wavelength λ is reflected at interfaces of different refractive indices n_i, i = 1–3, near the substrate. Reflected rays (I_1, I_2) interfere with an intensity pattern $I(\mathbf{x}, t)$, from which the membrane height above the substrate, $h(\mathbf{x}, t)$, is determined.

compare and combine RICM and DODS data in a meaningful way. In doing so, we achieve a comprehensive description of two weakly confined GUV systems. We find that in each case, the data are consistent with the Helfrich description, while pointing to an interaction potential that holds the membrane highly above the substrate.

Experimental

Materials

Lipids. SOPC (1-stearoyl-2-oleoyl-*sn-glycero*-3-phosphocholine), DOPE-PEG 2000 (1,2-dioleoyl-*sn-glycero*-3-phosphoethanolamine-*N*-(methoxy(polyethyleneglycol)-2000)) and DOPE-cap-biotin (1,2-dioleoyl-*sn-glycero*-3-phosphoethanolamine-*N*-(cap biotinyl)) were purchased from Avanti Polar Lipids (Alabaster, AL, USA) and used without further purification. For DODS measurements, in addition, the fluorescently labelled lipid TRITC-DHPE (*N*-(6-tetramethylrhodaminethiocarbamoyl)-1,2-dihexadecanoyl-*sn-glycero*-3-phosphoethanolamine, triethylammonium salt) was purchased from Invitrogen (Eugene, OR, USA).

Proteins. Neutravidin covalently linked to the fluorescent label tetramethylrhodamine, henceforth called NAV-TMR, (Invitrogen) was reconstituted in PBS buffer (140 mM NaCl, 3 mM KCl, 10 mM Na_2HPO_4, 2 mM KH_2PO_4, pH 7.2) and ultracentrifuged at 137 000*g* and 4 °C for 2 hours to eliminate protein aggregates. Bovine serum albumin (BSA) and its covalently linked biotin conjugate (both: Sigma, Saint Louis, MO, USA) were dissolved in ultrapure water to a final concentration of 0.1 mg mL^{-1} and mixed in a 1 : 1 w/w ratio (BSA–biotin mix).

Ultrapure water (Milli-Q Gradient A10, Millipore, San Francisco, CA, USA) was used throughout. Thickness corrected glass coverslips (d = 170 ± 10 μm, Assistent, Karl Hecht KG, Sondheim, Germany) were cleaned by the following detergent treatment: ultrasonication in 2% Hellmanex solution (Hellma, Müllheim, Germany) for 10 minutes, flushing thoroughly with ultrapure water and again ultrasonication (2 × 15 minutes) in ultrapure water followed by repeated flushing with the same.

Substrate preparation

Substrates with patterned receptor distribution were prepared by the micro-contact printing technique (μCP).[71,72] For the preparation of microstamps see the detailed protocol published in Monzel *et al.*[28] In brief, polyolefin plastomer (POP) stamps were obtained by hot embossing the POP onto a silicon wafer with the desired structure. An inking pad, made from a silicone elastomer mixed with a crosslinker (Sylgard 184, Dow Corning, MI, USA), was incubated with 400 μl of the BSA–biotin mix, subsequently dried and used to ink the POP stamp. The latter was then pressed onto a cleaned coverslip thereby transferring the dried protein at the site of the pattern in a controlled manner. The patterned cover-slips, which served as substrates for GUV adhesion, were stored dry at 4–8 °C and used within 3 days. Prior to the experiment, the remaining regions of bare glass were passivated with 5 mg mL^{-1} BSA for 15 minutes, the stamped region was functionalized with NAV-TMR by incubation for 30 minutes at a final concentration of 100 μg mL^{-1}, and the passivation step with BSA was repeated. Homogeneous substrates for weakly confined GUV were prepared by passivating the glass with 5 mg mL^{-1} BSA for 15 minutes. In each case, excess protein was removed after each binding step by exchanging the buffer against protein free PBS.

GUV preparation

Giant unilamellar vesicles (GUVs) consisting of SOPC with 2 mol% DOPE–PEG 2000 and 5 mol% DOPE–cap-biotin (plus TRITC-DHPE at 1 mol% for DODS experiments) were prepared *via* electro-swelling in 230 mOsm L^{-1} sucrose (Sigma) solution.[45,73] For experiments, vesicles were immersed in PBS buffer of 400 mOsm L^{-1} (187 mM NaCl, 4 mM KCl, 13 mM Na_2HPO_4, 2.7 mM KH_2PO_4, pH 7.2) in a 1 : 50 dilution. The experimental chamber was then covered with a glass slide to avoid osmolarity changes due to evaporation. Measurements were started 30 min later to ensure full equilibration of the system. All measurements were carried out at room temperature.

Data acquisition and analysis

DODS

Previously, we used DODS to quantify membrane fluctuations in vesicles and cells. Herein, we summarize the basics of DODS which are relevant for the present study. A detailed description of the approach is given by Monzel *et al.*[7] The basic idea of this method is to record intensity variations which originate from the fluctuation of a fluorescent membrane in a confocal detection volume (CDV, see Fig. 1b). Such a signature of membrane fluctuations is known to be visible in diffusion measurements with FCS,[74] but hitherto the focus was on evaluating the diffusion rather than fluctuations. Quantification of fluctuations, on the other hand, can be achieved with DODS by doping the membrane with fluorophores in a 1 mol% concentration range whereby any signal fluctuation related to lipid diffusion is effectively suppressed. The following strategy then allows for an efficient detection of physical membrane displacements. First, an axial scan of the CDV at position $h_{CDV}(t)$ across the membrane located at the mean position $\langle h \rangle$ is applied and the intensity along the way is recorded. The intensity can be approximated by a Gaussian function (see Fig. 1b)

$$I(h_{CDV}(t)) = I_{max} \exp\left[-2\frac{\{h_{CDV}(t) - \langle h \rangle\}^2}{{z_0}^2}\right], \qquad (1)$$

where I_{max} denotes the maximally detected intensity and z_0 is the axial $1/e^2$ – radius of the CDV.[7] In a second step, the membrane is positioned at the inflection point (IP), of the CDV, given by $I(h_{CDV}^{IP}) = e^{-1/2} I_{max} \simeq 0.61\, I_{max}$. Here, the intensity gradient is maximal and, as a consequence, the sensitivity of fluctuation detection is the highest. This is the point where membrane displacements are recorded (Fig. 1b).

Fixing the CDV at the position of the IP, intensity fluctuations $\Delta I(h(t))$ arise from membrane fluctuations $\Delta h(t) \equiv h(t) - \langle h \rangle$, with the instantaneous membrane position $h(t)$.

Conversion from $\Delta I(h(t)) \rightarrow \Delta h(t)$ is realized *via* the slope m at the IP, as measured from the axial intensity scan:[7]

$$\Delta I(h(t)) \simeq m\Delta h(t). \quad (2)$$

In a similar manner, the intensity autocorrelation function (ACF) is related to the membrane displacement autocorrelation function (dACF $\equiv \langle \Delta h(\tau)\Delta h(0)\rangle$) *via*

$$\mathrm{ACF} \equiv \frac{\langle \Delta I(\tau)\Delta I(0)\rangle}{\langle I(\tau)\rangle^2} = \frac{m^2}{\langle I(\tau)\rangle^2}\mathrm{dACF}. \quad (3)$$

Intensity fluctuations are recorded for a specific time interval, typically 2–3 min, and the ACF is calculated.

DODS data were acquired with a FCS setup described in detail before:[7] a laser scanning microscope (LSM710, Carl Zeiss, Göttingen, Germany) equipped with an FCS accessory (Confocor 3, Zeiss) and a 40× water immersion objective (C-Apochromat, NA 1.2, Zeiss) was used. The sample was illuminated with a 5 mW HeNe laser (λ = 543 nm) and light was detected with 2 avalanche photodiodes (Perkin Elmer, Waltham, Ma, USA) for photon detection. The excitation laser was attenuated to a maximum count $I_{\max}$ of 70–100 kcps, which was well within the linear range of the detected fluorescence intensity. Appropriate filter sets were chosen (for the dye used here: beam splitter 488/543 nm for excitation and 580 nm long pass filter for emission, Zeiss) and the pinhole size was fixed to one Airy unit. Under these conditions the axial $1/e^2$-radius z_0 amounts to 1284 ± 11 nm (N = 10). Errors reported throughout are standard deviations and indicated by ±. Data acquisition and realtime autocorrelation were executed *via* the software ZEN (version 2008, Zeiss). Before the start of each DODS measurement, fluorescence and phase contrast images were acquired to determine the overall shape of the GUV and to choose the appropriate central position at the proximal or distal membrane.

RICM

For Dual Wavelength-RICM (DW-RICM)[64] an inverted microscope (Axiovert200, Carl Zeiss) was equipped with an oil immersion objective (Antiflex EC Plan-Neofluar Ph3 63x/1.25, Zeiss) containing a $\lambda/4$ plate. Light emitted by a metal halogenide lamp (X-Cite, Exfo, Quebec, Canada) was filtered using a dual-band interference filter (λ_g = 546 ± 10 nm and λ_b = 436 ± 20 nm). The numerical aperture of illumination was set to 0.54. In order to achieve maximum contrast the antiflex technique was applied.[75] Two micrographs were recorded simultaneously. For this purpose, the reflected light was split according to its wavelength (FT 460 nm, LP 470 nm (Zeiss) and BP 436 ± 10 nm (AHF, Tübingen, Germany)) and focused on two separate digital CCD cameras where one was triggered by the other (sensicam qe, PCO, Kehlheim, Germany). Image recording was controlled by the software OpenBox (version 1.77, Informationssysteme Schilling, Munich, Germany). 2000 consecutive micrographs with a frame rate of 20 Hz were recorded. Analysis was performed considering the interfaces of glass/outer buffer, outer buffer/membrane and membrane/inner buffer in the analysis within the square regions of the fluctuating membrane (for details see Monzel *et al.*[28]). Data were analyzed using self-written routines in Matlab (version 3.0 (R2010b), The MathWorks, Inc. MA, USA) utilizing the image processing toolbox and ImageJ (version 1.45s, Rasband, W.S., NIH, Bethesda, MD, USA).

Knowing the refractive indices and thicknesses of the different layers and using Fresnel's equations the detected intensity $I(h)$ is calculated. The theory of partial coherent light states that these data follow the intensity-height relation[52]

$$I(h) = \frac{S}{2} - D\frac{\sin(y)}{2y}\cos\left(2kn_1\left[h\cos^2\left(\frac{\alpha}{2}\right) - h_{\mathrm{off}}\right]\right) \quad (4)$$

and a fit with this equation gives the absolute membrane heights $h = h(\mathbf{x}, t)$. $y = 2kh\sin^2\left(\frac{\alpha}{2}\right)$ with the half angle $\alpha = 24^\circ$ of the cone of illumination being used to account for the illumination numerical aperture. The offset h_{off} = 35 nm[76] and S and D, the sum and difference of the maximal and minimal intensity, respectively, are determined from the fit. $k = 2\pi/\lambda$ is the wave vector and n_1 = 1.335 the refractive index of the outer buffer. The phase ambiguity arising from the cosine in eqn (4) is lifted using DW-RICM instead of conventional RICM. Here, two interferograms for wavelengths λ = 546 nm and 436 nm are recorded simultaneously and from the twofold intensity information a unique height of the object above the substrate can be derived.[64] A detailed description of this procedure can be found elsewhere.[28]

Correcting for finite resolution

Since the detected, apparent membrane heights $\bar{h}(\mathbf{x}, t)$ are always spatio-temporal averages of the instantaneous height $h(\mathbf{x}, t)$, the detected apparent fluctuations $\Delta\bar{h}(\mathbf{x}, t)$ and the dACF $\langle \Delta\bar{h}(\mathbf{x}, t)\Delta\bar{h}(\mathbf{x}, 0)\rangle$ were corrected to account for the resolution of the setup. In the following we describe the theoretical context relevant for this work and account for (i) the spatio-temporal resolution of the setup, (ii) the detection limits of the system, and (iii) the boundary conditions of the investigated membranes (see Fig. 1a).

In all cases, the correct form of the dACF is derived starting from the classical theory for membrane height fluctuations, which describes the membrane as a two-dimensional sheet with bending rigidity κ and membrane tension σ. In the vicinity of a wall an additional term accounts for the interaction potential $V(h)$ which in harmonic approximation has a minimum at h_0 and a curvature γ. The Hamiltonian is given by

$$\mathcal{H} = \int_{\mathcal{S}} \mathrm{d}\mathbf{x}\left[\frac{\kappa}{2}\left(\nabla^2 h\right)^2 + \frac{\sigma}{2}(\nabla h)^2 + \frac{\gamma}{2}(h - h_0)^2\right] \quad (5)$$

where $h = h(\mathbf{x})$, with $\mathbf{x} \equiv (x, y)$ the lateral position on the membrane, and $h_0 \equiv \langle h(\mathbf{x})\rangle$ in equilibrium. Far from the substrate at the distal membrane $\gamma \equiv 0$.

The true dACF without finite resolution effects is given by[14]

$$\langle \Delta h(\mathbf{x}, 0)\Delta h(\mathbf{x}, \tau)\rangle = \frac{k_{\mathrm{B}}T}{(2\pi)^2}\int \mathrm{d}q \frac{\mathrm{e}^{-\Gamma(q)\tau}}{\kappa q^3 + \sigma q + \gamma/q}. \quad (6)$$

At $\tau \equiv 0$ the dACF yields the root mean square fluctuation amplitude $\psi = \sqrt{\langle \Delta h(\mathbf{x},0)^2 \rangle}$. The coefficient $\Gamma(q)$ accounts for the hydrodynamic damping and relaxation of membrane fluctuations. At the distal membrane it takes the well known form $\Gamma(q) = (\kappa q^4 + \sigma q^2)/(4\eta q)$.[14] For the proximal membrane $\Gamma(q)$ is somewhat enhanced[55,77]

$$\Gamma(q) = \frac{(\kappa q^4 + \sigma q^2 + \gamma)}{4\eta q} \times \frac{2(\sinh^2(qh) - (qh)^2)}{\sinh^2(qh) - (qh)^2 + \sinh(qh)\cosh(qh) + (qh)}. \quad (7)$$

The bending rigidity for SOPC lipid membranes, used throughout here, is $\kappa = 20 k_B T$.[78] The viscosity η, is calculated as the arithmetic mean of the viscosity of the inner GUV buffer and outer buffer (see Appendix 1).

DODS. In the case of DODS the detection system is an avalanche photodiode which counts the photons originating from the fluorophores within the CDV. The CDV in turn has an intrinsic intensity distribution and only the integral value of intensities in the cross-section between the CDV and membrane are detected. Consequently, the true membrane fluctuations $\Delta h(\mathbf{x}, t)$ are smeared out to the apparent fluctuations $\Delta \bar{h}(\mathbf{x}, t)$, and these emerge from a convolution of the lateral point spread function $P(\mathbf{x}) = 2/(\pi\omega^2)\exp(-2\mathbf{x}^2/\omega^2)$ at $h(\mathbf{x}, t)$ and the fluctuations $\Delta h(\mathbf{x}, t)$. Note that, due to measurements at the IP the lateral $1/e^2$-radius ω_0 of the point spread function $P(\mathbf{x})$ increases to[79]

$$\omega^2 = {\omega_0}^2\left(1 + \frac{\lambda^2\left(h_{\mathrm{CDV}}^{\mathrm{IP}} - \langle h \rangle\right)^2}{\pi^2 {n_1}^2 {\omega_0}^4}\right).$$

n_1 is the refractive index of the bulk medium and λ the wavelength of the excitation light. For our measurement conditions $\omega_0 = 281 \pm 7$ nm ($N = 10$; standard deviation error). With these considerations and integrating over $\mathbf{x}$, the dACF in case of DODS reads

$$\langle \Delta\bar{h}(0)\Delta\bar{h}(\tau)\rangle^{\mathrm{DODS}} = \int_0^{\vartheta}\int_0^{\vartheta} \frac{\mathrm{d}t_1'\,\mathrm{d}t_2'}{\vartheta^2} \left\langle \Delta\bar{h}\left(t_1'\right)\Delta\bar{h}\left(\tau + t_2'\right)\right\rangle^{\mathrm{DODS}} = \frac{k_B T}{2\pi}\int_{q_{\min}}^{\infty} \mathrm{d}q \frac{q\mathrm{e}^{-\Gamma(q)\tau}}{\kappa q^4 + \sigma q^2 + \gamma} \mathrm{e}^{-\frac{1}{4}\omega^2 q^2} \psi_\vartheta(q), \quad (8)$$

where the averaged time component is given by

$$\psi_\vartheta(q) = \frac{\mathrm{e}^{-\Gamma(q)\vartheta} - 1 + \Gamma(q)\vartheta}{\Gamma^2(q)\vartheta^2}.$$

In comparison to the classical expression, the spatial averaging due to finite resolution only contributes an additional factor $\phi^{\mathrm{DODS}}(q) = \exp(-\omega^2 q^2/4)$ see eqn (8). This factor dampens the detection of high modes at the upper integral limit $q_{\max} = \infty$. At low frequencies the accessible modes are limited due to the finite size of the vesicle, *i.e.*, the wavelength spanning the whole vesicle $q_{\min} = \sqrt{3}/R$ (see Appendix 2). Note that in the limit of κ dominated fluctuations $\kappa q^2 \gg \sigma$, and in the limit of σ dominated fluctuations $\kappa q^2 \ll \sigma$. σ is typically of the order of 0.01–1 μJ m^{-2} and κq^2 runs from $\sim 10^{-5}$–1 μJ m^{-2}. Above the latter value the integrand is highly damped, wherefore small q values dominate the integral and $\sigma > \kappa q^2$ holds for the majority of investigated objects. Thus, in our case DODS is most sensitive to σ. A similar argument can be used to explain the sensitivity for γ.

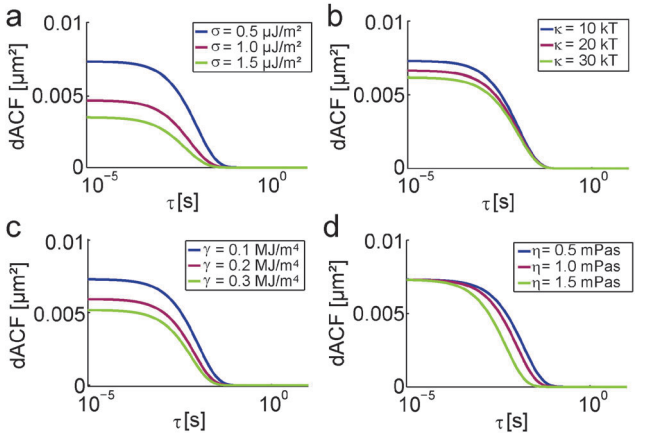

Fig. 2 Theoretical dACF variation with membrane/system parameters (eqn (8)): (a) membrane tension σ, (b) bending rigidity κ, (c) interaction potential strength γ, and (d) effective viscosity η. Default values are σ = 0.5 μJ m^{-2}, γ = 0.1 MJ m^{-4}, $\kappa = 10 k_B T$, η = 1.0 mPa s.

Using eqn (8), the theoretical shape of the dACF in case of DODS was calculated for typical system parameters and the results are illustrated in Fig. 2. The shape of the dACF is strongly influenced by changes in σ and somewhat less in γ, while κ and η have only little effect on the amplitude and relaxation of the function, respectively.

RICM. In case of RICM, true fluctuations are blurred to the apparent fluctuations in a similar manner. The camera based detection results in spatial averaging of the intensity over the, ideally resolution matched, pixel size A. The camera exposure time ϑ restricts the detected frequencies to values $< 1/(2\vartheta)$. Consequently, the apparent heights $\bar{h}(\mathbf{x}, t)$ follow

$$\bar{h}(\mathbf{x}, t) = \int_0^{\vartheta}\frac{\mathrm{d}t'}{\vartheta}\int_A \frac{\mathrm{d}\mathbf{x}'}{A} h(\mathbf{x} + \mathbf{x}', t + t'). \quad (9)$$

The apparent autocorrelation function emerges – similar to DODS – from a convolution of the true correlations (using eqn (6)) with the effects of the spatio-temporal averaging[55]

$$\langle \Delta\bar{h}(\mathbf{x},0)\Delta\bar{h}(\mathbf{x},\tau)\rangle^{\mathrm{RICM}} = \frac{k_B T}{(2\pi)^2}\int \mathrm{d}\mathbf{q} \frac{\mathrm{e}^{-\Gamma(q)\tau}}{\kappa q^4 + \sigma q^2 + \gamma} \phi^{\mathrm{RICM}}(\mathbf{q})\psi_\vartheta(\mathbf{q}), \quad (10)$$

where $\phi^{\mathrm{RICM}}(\mathbf{q})$ is a function of the spatial component

$$\phi^{\mathrm{RICM}}(\mathbf{q}) = \iint_A \frac{\mathrm{d}\mathbf{x}_1'\,\mathrm{d}\mathbf{x}_2'}{A^2} \mathrm{e}^{-i\mathbf{q}\left(\mathbf{x}_1' - \mathbf{x}_2'\right)}. \quad (11)$$

$\psi_\vartheta(\mathbf{q})$ accounts for the temporal averaging as given before.

The effect of finite resolution on the apparent mean square fluctuations $\langle \Delta\bar{h}^2 \rangle$ and their dependence on σ are illustrated in Fig. 3. For RICM compared to DODS $\langle \Delta\bar{h}^2 \rangle$ increases by more than a factor of 5 (see Fig. 3a). Thus, accounting for finite

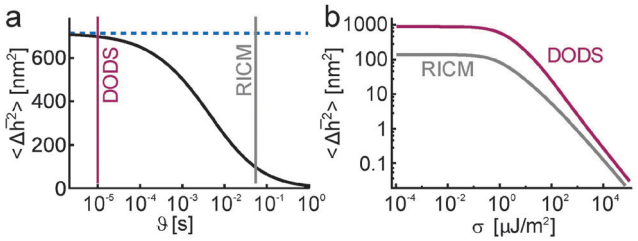

Fig. 3 (a) Calculated effect of temporal resolution ϑ on fluctuation amplitude $\langle\Delta\bar{h}^2\rangle$ for a weakly confined GUV at typical parameters σ = 0.5 μJ m^{-2}, γ = 4 MJ m^{-4} and h_0 = 600 nm (black line). Vertical lines indicate DODS and RICM temporal resolution, dashed line denotes infinite resolution. (b) $\langle\Delta\bar{h}^2\rangle$ calculated as a function of membrane tension σ, for the spatio-temporal resolution of RICM and DODS.

resolution enables us to correctly rescale the measured fluctuations, and permits quantitative comparison between different techniques.

Throughout, for both DODS and RICM, we correct the apparent fluctuations $\sqrt{\langle\Delta\bar{h}^2\rangle}$ and correlation functions $\langle\Delta\bar{h}(0)\Delta\bar{h}(\tau)\rangle$ to the instantaneous fluctuations $\psi = \sqrt{\langle\Delta h^2\rangle}$ and correlation functions $\langle\Delta h(0)\Delta h(\tau)\rangle$. Unless otherwise stated, all reported values are already corrected.

Results and discussion

Weakly confined membranes

In the experiment GUVs sedimented and hovered over the substrate, which was passivated to prevent strong attraction. The proximal membrane within the vesicle substrate contact zone was on average flat. Still, the membrane was highly fluctuating, indicating that it was confined in a generic potential. For measurements, vesicles with radii ≥10 μm were chosen to ensure membrane flatness within the detection volume.‡ When the vesicle has equilibrated to ambient conditions and no lateral drift on the timescales of the measurement (≃5 min) was detectable, the CDV was adjusted such that the membrane was vertically positioned at the IP before intensity fluctuations were recorded (see Fig. 4a).

First, we measured fluctuations at the distal surface of the GUV using DODS. Data were collected from the centre of the distal membrane of the vesicle. From these data the dACF was calculated using eqn (3). Fluctuation amplitudes were determined from the intercept of the dACF (*i.e.*, its value at $\tau \equiv 10^{-5}$ s), yielding an average value of $\psi^{\mathrm{DODS}}_{\mathrm{distal}} = 67 \pm 19$ nm ($N = 20$; standard deviation error). Values of $\psi_{\mathrm{distal}} \simeq 100$ nm are expected for GUVs that are freely fluctuating far from any surface. However, due to the lack of suitable techniques these were so far only measured using flicker spectroscopy at a spatio-temporal resolution of 30 Hz and 30 nm.[24,56,80,81]

Next, DODS data were collected at the proximal membrane of the vesicle. Here, membrane fluctuations are damped due to

‡ For vesicle radii ≥10 μm the spherical membrane shape deviates by less than 0.3 nm from a plane within the CDV.

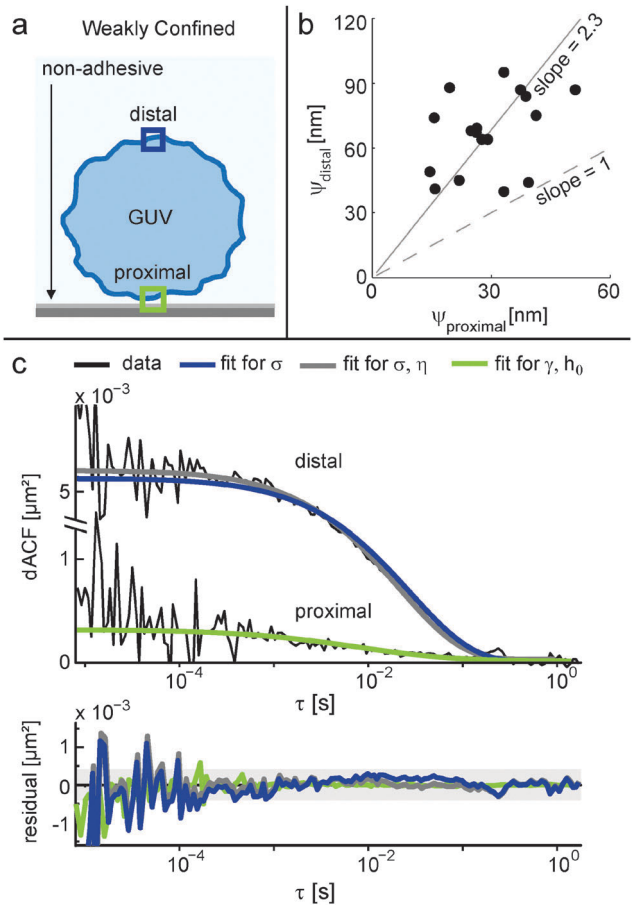

Fig. 4 GUV confined by a weak generic potential. (a) Sketch of the system. Colored boxes indicate measurement positions at distal (blue) and proximal (green) surfaces. (b) Relation between fluctuation amplitudes ψ at the distal and the proximal surface of each vesicle. Fluctuations at the distal surface are on average enhanced by a factor ×2.3 (solid line). (c) Typical dACFs. σ is obtained from a single parameter fit to the dACF at the distal surface (blue). A two parameter fit for σ and η (grey) is plotted for comparison. γ and h_0 are determined from a fit of the dACF at the proximal surface (green). Residuals remain mostly below the resolution limit (grey bar).

the presence of the substrate and consequently the average amplitude reduced to $\psi^{\mathrm{DODS}}_{\mathrm{proximal}} = 29 \pm 10$ nm ($N = 17$). This value can be compared to previous studies on weakly adhering vesicles, where amplitudes of 9 to 34 nm were detected using RICM (here we corrected the reported values to account for the spatio-temporal averaging inherent to RICM).[29,30,42] Note that in this study GUVs were prepared in such a way that they had higher osmotic deflation (osmotic difference: 170 mOsm L^{-1}) as compared to the studies cited here (20–100 mOsm L^{-1}).

Measurements at both distal and proximal surfaces of the same vesicle enable the direct assessment of the influence of the substrate on the fluctuation amplitude. Since the membrane tension is the same everywhere in the vesicle, changes in membrane fluctuation near the substrate directly reflect the changes due to the membrane–substrate interaction. Fig. 4b illustrates the attenuation of fluctuations from the distal to the proximal membrane, which on average amounts to ×2.3.

From the measurement at the distal membrane, and assuming a bending rigidity of $\kappa = 20k_BT$,[78] the membrane tension can be uniquely determined based on the mean square fluctuation amplitude (eqn (8) with τ and $\gamma \equiv 0$). Alternatively, it can be determined from the full ACF. Its decay is given by the classical expression for the damping coefficient $\Gamma(q)$, where in addition to σ, the buffer viscosity η is used as a fit parameter. The resulting fit shows convincing agreement with data and for correlation times $\tau > 10^{-4}$ s the residuals remain below the resolution limit (see Fig. 4c).

The membrane tension was found to be between 0.2–1.4 μJ m^{-2} and the average value of the viscosity was $\eta = 1.2 \pm 0.6$ mPa s ($N = 20$; standard deviation error). The latter accords with the expected value of $\eta = 1.2$ mPa s, which is the arithmetic mean of the outer buffer viscosity $\eta = 1.0$ mPa s and the viscosity of the sucrose solution inside the vesicle $\eta = 1.4$ mPa s (see Appendix 2). The same viscosity was also measured using FCS by Cha *et al.*[82] in a similar model system.

Having established that the viscosity is indeed as expected, we fixed its value to $\eta = 1.2$ mPa s and performed a one parameter fit with the tension as the only free parameter. Correspondence between data and the one-parameter fit remained high (see residuals in Fig. 4c) and changes in membrane tension values between two-parameter fit ($\sigma = 0.52 \pm 0.39$ μJ m^{-2}) and one-parameter fit (0.51 ± 0.37 μJ m^{-2}) were negligibly small. This analysis demonstrates the robustness of the determination of σ using this technique. Note that the observed variation in σ resulted from real tension variations between different GUVs. To test the influence of measurement uncertainty we undertook repeated DODS measurements on the same vesicle (Table 1). Performing one parameter fits the membrane tension was determined to an accuracy of ± 0.035 μJ m^{-2}.

Absolute tension values are in excellent agreement with results estimated from other fluctuation dominated systems, *e.g.*, unbound GUVs analyzed with flicker spectroscopy[24,56] and neutron scattering[83] or weakly adhered vesicles analyzed using RICM[30,84] where tensions were of the order of ~ 0.1 μJ m^{-2}. In more tightly adhered or micropipette aspirated GUVs membrane tensions are considerably larger and of the order of ~ 1 μJ m^{-2} and ~ 1 mJ m^{-2}, respectively.[29,67]

The dACFs of the proximal membrane were fitted using eqn (7) and (8), with fitting parameters γ and h_0, the latter being the equilibrium height above the substrate. σ was fixed to the value determined from the one-parameter fit at the distal side of the same vesicle. A typical example is depicted in Fig. 4c. The fit yielded high correspondence with data and residuals remained below the resolution limit for $\tau > 10^{-4}$ s, as before. Hence, this is the first time that σ and γ could be independently measured in direct experiments.

Table 1 Tension σ (in μJ m^{-2}) for two exemplary GUVs, (GUV1 and GUV2) and for repeated DODS measurements M1, M2 and M3 of the same vesicle

	M1	M2	M3
σ of GUV1	0.41	0.46	0.48
σ of GUV2	0.36	0.32	0.37

The interaction potential strength γ was between 0.7–20 $\times$ 10^6 J m^{-4} and h_0 between 150 and 654 nm. For the latter, the higher variation in the case of DODS arises from the limited sensitivity of this technique for h_0. The absolute values of γ were consistent with previously reported results for similar systems as measured with RICM.[29,30,85]

Structured adhered vesicles

GUVs were allowed to sediment and interact with the substrates bearing the adhesive grid patterns. They adhered to the substrate in a way that part of the proximal membrane became tightly bound while square-shaped patches (4×4 μm^2) remained free to fluctuate (see Fig. 5a). The selective pinning of the membrane to the substrate yields substantial control over absolute membrane heights and renders the system particularly amenable for RICM analyses. In our previous study we investigated similar systems with DW-RICM and demonstrated that the lipids on the membrane are free to diffuse across the adhered regions.[45] Therefore, the membrane within each square is expected to reach an equilibrium state.

DODS measurements were performed at the distal, and the fluctuating parts of the proximal membrane. Fig. 5b illustrates

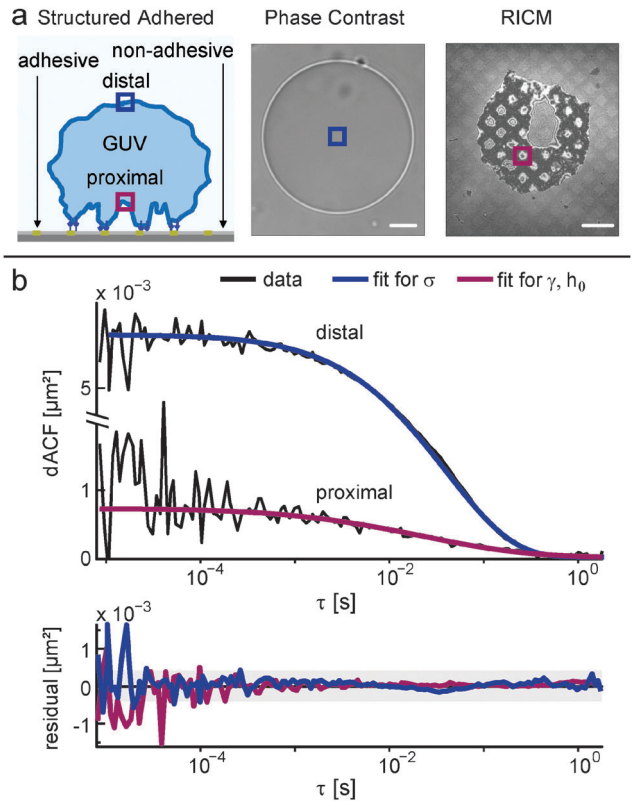

Fig. 5 Structured adhered GUV. (a) Sketch of the system (left), the phase contrast image of the vesicle (middle) and the RICM image of the vesicle–substrate contact zone (right). Colored boxes indicate measurement positions at the vesicle distal side and within fluctuation areas at the proximal side. Scale bar 10 μm. (b) Typical dACFs. σ is obtained from a single parameter fit to the dACF at the vesicle distal side (blue). γ and h_0 are determined from a fit to the dACF at the proximal side (purple). Residuals remain mostly below the resolution limit (grey area).

Table 2 DODS and RICM results: average and standard deviation of fluctuation amplitude, $\psi_{proximal}$, and membrane height, h_0 (N = 14 for DODS and RICM data)

Technique	$\psi_{proximal}$ [nm]	h_0 [nm]
DODS	31 ± 12	402 ± 252
RICM	26 ± 21	538 ± 56

a typical example of dACF measurements, along with the single-parameter fit for σ at the distal membrane and the simultaneous fit for γ and h_0 at the proximal membrane. Both fits yielded high correspondence with data and residuals remaining below the resolution limit for correlation times $\tau > 3 \times 10^{-5}$ s (grey area in Fig. 5b). The fluctuation amplitude at the distal membrane amounts to $\psi_{distal}^{DODS} = 82 \pm 23$ nm (N = 16) and is enhanced by a factor ×2.7 compared to their amplitudes measured at the proximal membrane. This is a similar enhancement as obtained for the weakly confined system. Parameters $\psi_{proximal}$, σ, γ, and h_0 as obtained from the fits are explicitly given in Tables 2 and 3, and discussed as follows.

For the structured adhered system RICM measurements at the proximal membrane were performed and compared to DODS data utilizing the theory accounting for finite resolution (see Fig. 3a). Results of both measurements are given in Table 2. Note that DODS is more suited for the determination of $\psi_{proximal}$ whereas RICM yields better results for h_0. Both of these values, $\psi_{proximal}^{DODS}$ and h_0^{RICM}, are slightly higher than their values obtained using other techniques but assessing the deviation *via* the Wilcoxon rank sum test yielded no statistical difference between data sets (significance level p = 0.27 for $\psi_{proximal}$, and p = 0.23 for h_0).

The standard deviation given in Table 2 represents the true distribution of fluctuation amplitudes GUVs exhibit. It cannot be solely attributed to measurement inaccuracy. This is different in the case of h_0 measured using DODS. Here, the large standard deviation compared to DW-RICM results from the lower sensitivity of DODS for h_0. Thus, for optimal results h_0 should be determined *via* RICM and σ *via* DODS measurements. So far we could not perform DODS and DW-RICM on the same setup and the same GUV, wherefore in the following we compare the average values over several GUVs.

Previous work on confined adhesion to substrate patterns used vesicles that were tenser than ours and reported fluctuation amplitudes of $\psi_{proximal}$ = 9–37 nm[29,30] (corrected for finite resolution) as well as equilibrium heights of h_0 = 31–49 nm.[29] Clearly, the differences to the present work arise from different membrane tension.

In the following text we present the results for the weakly confined and structured adhered system and compare them to

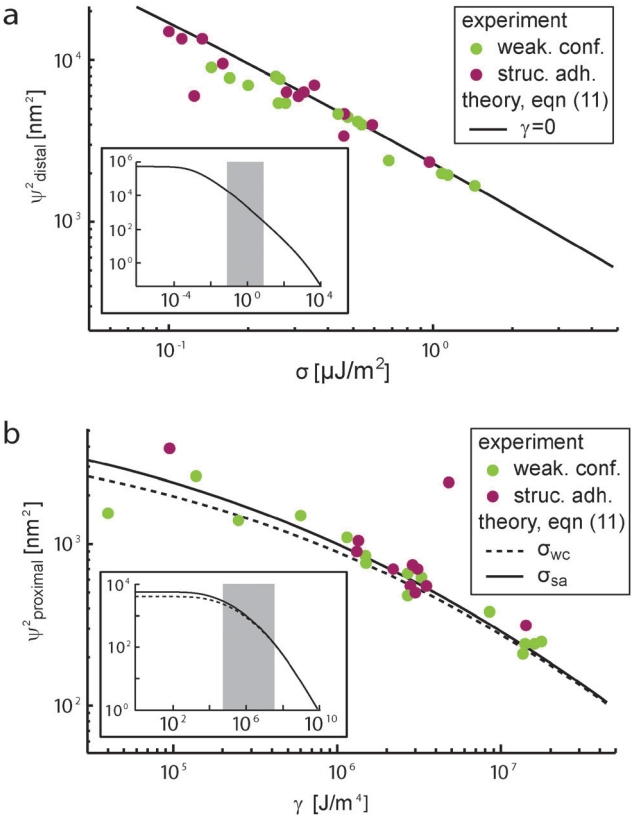

Fig. 6 Relation between fluctuation amplitude and membrane/system parameters: (a) ψ_{distal}^2 ($\equiv\langle\Delta h^2\rangle_{distal}$) *vs.* σ for weakly confined (green) and structured adhered values (purple). Data follow the theory, eqn (8). (b) $\psi_{proximal}^2$ ($\equiv\langle\Delta h^2\rangle_{proximal}$) *vs.* γ for weakly confined (wc, green) and structured adhered values (sa, purple). Data follow the theory for average σ_{wc} and σ_{sa}, respectively. The insets show the same theoretical fluctuation amplitude for the full parameter range, partially inaccessible to experiments. The grey shaded area illustrates the experimentally accessed parameter range.

theory (see Fig. 6). The fluctuations $\langle\Delta h^2\rangle_{distal}$ ($\equiv\psi^2$) as a function of membrane tension σ are very close to the theoretical curve described by eqn (8) for γ = 0 (Fig. 6a). For the fluctuations at the proximal position as a function of the potential strength γ, we find convincing agreement between experimental and theoretical data for both adhesion types (Fig. 6b). Here we used the averaged membrane tension, in the weakly confined (σ_{wc}) and structured adhered (σ_{sa}) case, though the membrane tension of individual vesicles could differ by more than 50%.

For all vesicles observed, Fig. 6a and b show that only part of the decay of the function is probed whereas the plateau region cannot be probed under the experimental conditions used (see insets of Fig. 6). Moreover, all parameters describing the vesicle membrane behaviour near the substrate, *i.e.*, $\psi_{proximal}$,

Table 3 Comparison of weakly confined and structured adhered systems: mean and standard deviation obtained using DODS (N = 17 for the weakly confined system, N = 14 for the struc. adh. system, unless otherwise stated)

System	ψ_{distal} [nm]	$\psi_{proximal}$ [nm]	h_0 [nm]	σ [μJ m^{-2}]	γ [MJ m^{-4}]
Weakly confined	67 ± 19 (N = 20)	29 ± 10	605 ± 428	0.51 ± 0.37	4 ± 5
Struc. adh.	82 ± 23 (N = 16)	31 ± 12	402 ± 252	0.35 ± 0.25	4 ± 3

γ, and h_0, exhibit similar values in both systems (see Table 3). This indicates that the presence of the substrate influences membrane fluctuations to a similar extent and that even in the structured adhered system the membrane is equilibrated since lipid molecules are free to diffuse over the adhered regions of the vesicle membrane.[45] In fact, as the substrate preparation within the square fluctuation regions of the structured adhered GUV and the weakly confined GUV was identical, the membrane should encounter similar membrane–substrate interaction if the influence of the pinned membrane sides is negligibly small – and this is observed indeed.

Moreover, in the structured adhered case it appears that the vesicle does not spread further on the patterned substrate. This behaviour is different from previous studies on GUVs adhering strongly to homogeneous substrates – as noticeable by the suppression of fluctuations within the adhesion zone and tension increase.[52,84] On homogeneous substrates fluctuations bring a new membrane area into contact with the substrate and cause growth of the adhesion zone. In the present case the non-adhesive square areas on the substrate are so large that fluctuations cannot reach to the other side to establish new contacts. Further adhesion is only possible along the adhesive grid, but this involves an increase in bending and vesicle deformation which does not occur. Thus, in the energetics of this system the energy costs due to bending exceed the gain in enthalpy arising from bond formation (and tension, for higher order deformations).

A direct overview of system parameters obtained in the weakly confined and structured adhered case is given in Table 3. Fluctuation amplitudes at the distal membrane yielded a difference of 20% with slightly larger amplitudes for structured adhered membranes; however, a Wilcoxon rank sum test clarifies the change as not statistically significant (significance level $p = 0.12$). The same holds for the membrane tension ($p = 0.15$), but here values for structured adhered membranes were slightly reduced.

Since within fluctuation regions the membrane exhibits the same equilibrium state as in the weakly confined case, the only difference between both systems is the formation of membrane bonds and suppressed fluctuations within adhered regions.[28] Here, the membrane is flattened and not free to explore all bending modes. Consequently, the membrane excess area within bound regions is smaller than within regions of the free membrane. It is indeed unevenly distributed already between the distal and proximal sides of the GUV as our observation of $\sim 2.5\times$ enhanced fluctuations at the distal GUV side demonstrates. In this sense the surface excess area is a fundamentally different quantity compared to the membrane tension, which assumes the same value all over the equilibrated fluid lipid membrane. In addition, the vesicle on the structured adhered substrate does not spread, wherefore it maintains its initial surface excess area. Upon adhesion the part of the surface excess area originating from the adhered zone must be redistributed within the GUV and may be shifted from the substrate contact zone to the vesicle hemisphere. We estimated this potential effect on fluctuation amplitudes on the distal side. For a typical vesicle of 15 μm radius, pinned over 67% of the area within the contact zone and by approximating fluctuations as paraboloid dents with 67 nm amplitude (see Table 3, weakly confined case), their flattening upon adhesion should result in a maximal increase of surface excess area in the vesicle hemisphere by 17%. This larger effective surface area would change the lower integral limit in eqn (8) resulting in fluctuation amplitudes of 81 nm. While such a slight enhancement of fluctuation in the GUV hemisphere upon adhesion is, in principle, possible, the estimated change is yet small enough to lie within the statistical spread of measured amplitudes (67 ± 19 nm for the weakly confined and 82 ± 23 nm for the structured adhered GUV). In the present case no significant effect is detectable, but changes in the fluctuation amplitude at the GUV distal site may be probed in more detail with a model system of larger adhesive area and with slowed adhesion kinetics. An interesting extension of our work to further characterize weakly adhering membranes concerns a systematic change of the ratio of non-adhesive/adhesive areas on the substrate.

Comparison

Here we have quantified the fluctuation of membranes confined in a weak generic potential using DODS which was cross-checked using RICM wherever possible. When a membrane is close to another surface, fluctuations contribute to the interaction potential. At the same time, fluctuations are a means to measure material properties of the membrane as well as the interaction potential itself.[16,30,36,85] Hitherto, RICM was the tool of choice for measuring the interaction potential since other techniques, such as flicker spectroscopy, do not give access to the membrane fluctuations near a surface.[25,34,86] However, the tensions inferred from RICM measurements are usually over-estimated because of the limited resolution in time and in the lateral spatial direction.[29,52] Furthermore, working solely with fluctuations at the substrate proximal surface, the tension and the potential needs to be determined together in a self-consistent manner.[23,87]

DODS[7] enabled us to measure at the upper surface of a vesicle to determine the tension independently of the potential, and then use this value to determine the strength of the potential from data gathered at the lower surface of the same vesicle. A key step towards establishing the validity of DODS was its cross-comparison with RICM. This became possible by accounting theoretically for the finite resolution of the two techniques.[55] We also showed that since our system is in the tension dominated regime, the measurements are highly sensitive to changes in tension, but are not robust against changes in the bending rigidity. For this reason we are not sensitive to complications arising from recent suggestions that the bending rigidity may be different, for example, with small changes in buffer composition.[36–38] Since small changes are not expected to impact our results, the value available in the literature was used throughout.

In the past, most studies investigated model systems with high ligand numbers, and consequently a state of firm adhesion and tense membrane.[30,84,85,88] Weak or structured adhesion was

much less studied. Theoretical work predicts interesting phenomena, for example, geometrically structured/rough substrates result in a decrease of the substrate's attractiveness compared to homogeneous adhesive surfaces and lead to a drop in adhesion energy.[89,90]

We addressed this gap by analysing membrane fluctuations in two different systems – structured adhered or weakly bound, where GUVs were either partially adhered or confined solely by a generic interaction with a substrate. We worked with highly deflated GUVs and therefore, in both cases, the tension primarily acts to reduce thermally-driven membrane undulations. In both cases, the tension was determined to be about $\sigma \sim 0.5\ \mu J\ m^{-2}$, the strength of the interaction potential to be $\gamma \sim 4\ MJ\ m^{-4}$ – values that are reasonable in light of prior studies.[24,29,30,42,80,81,84,85] The measured viscosity matched very well with theoretical predictions (see Appendix 1). Similar values for all the measured quantities in the two systems show that in the partially adhered system, though the membrane is selectively bound to the substrate, the non-adhered part of the membrane behaves like its weakly confined counterpart. We can conclude that at least when the tension is low, non-adhered parts of a partly adhered cell or vesicle can be treated independently of the adhered parts.

We found that both our systems are well-described within the Helfrich framework, which then allowed us to measure the strength of the effective interaction potential. In earlier work we showed that this potential is highly non-linear,[91] and that with decreasing membrane tension, effected *via* osmotic deflation of GUVs, the minimum of the potential gets further from the substrate and the shape gets broader.[45] Here we explored the highly deflated case where the membrane is held at the considerable height of ~540 nm, while fluctuating with an amplitude of only 30 nm. These numbers – as well as those reported before – for the membrane height and fluctuation amplitude are difficult to reconcile with the classical idea of extracting the effective potential from a superposition of relevant individual contribution, which typically include gravity, van der Waal's and Helfrich potentials.[29,30,52] We conclude that the physical origin of the effective potential in eqn (5), is still to be fully understood. However, with the fine description offered by us here and elsewhere,[55] the measured potential can be used as such as a basis for further studies.

Conclusions

Two weakly adhered model systems were studied using the techniques DW-RICM and DODS, and the results obtained largely validated the current consensus on membrane dynamics. Let us consider each relevant parameter: at the relatively long wavelengths probed here, the dissipation is expected to come from the viscous damping in the buffer and not from internal membrane friction. Indeed, this is reflected in our experimentally measured values. The membrane tension, σ, is measured independently of other parameters and is in the expected range. For the bending rigidity the value available in the literature has been used, since our system is in the tension dominated regime and as such is not sensitive to small changes in this parameter. Our major contribution here has been to shed light on the generic interaction between the substrate and the membrane. The potential is a major player in determining the dynamics of the eventual specific adhesion of the membrane to the substrate, and to our knowledge, this is the first time that the strength of the potential, γ, was measured from fluctuations, but independently of the tension. Such measurement was realized utilizing the two complementary techniques of DODS – which features high temporal resolution and enabled the decoupling of σ and γ – and RICM – which features high accuracy in membrane–substrate distance measurements.

In the context of specific ligand–receptor mediated adhesion, the interaction potential plays a dual role – it contributes to defining the membrane–surface distance and its strength, given by the curvature at the minimum, dictates the extent of stochastic exploration by the membrane, ultimately enabling the nucleation of an adhesive patch that may grow.[52] Fluctuations of weakly adhered systems may be used to probe specific interactions, assessing the change with adhesion bond density,[32,42,43] for heterogeneous bond distribution,[92] or during osmolarity changes.[45] Other potential applications include exploring on-off dynamics of bonds, and weakly confined vesicles subjected to thermal gradients or external shear.

Appendix 1: effective viscosity for a planar membrane surrounded by two different fluids

The fluctuations of a membrane decay due to the dissipation of energy in the surrounding fluids. In this paragraph, we will calculate the damping coefficients of a membrane surrounded by two different fluids following Seifert.[77] The membrane is described by the Helfrich Hamiltonian, eqn (5) in the main text. The coordinate system is such that the membrane is on average in the xy plane ($z = 0$) with z perpendicular to the membrane plane. Imposing translational invariance, we reduce the calculation to two dimensions (x and z, without loss of generality). The viscosity of the fluids above and below the membrane are denoted by η^+ and η^-, respectively (see Fig. 7). Stokes equations for the hydrodynamics of the fluids around the membrane are

$$\nabla \cdot \mathbf{v}^i = 0 \tag{12}$$

$$\eta^i \nabla^2 \mathbf{v}^i = \nabla p^i, \tag{13}$$

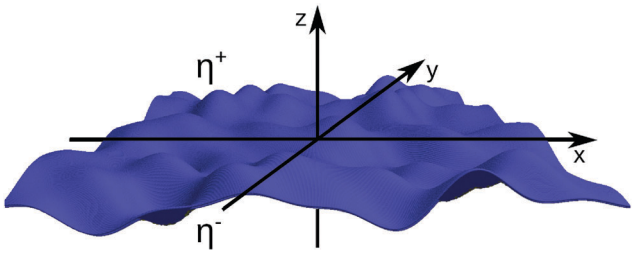

Fig. 7 Sketch of the system introducing the parameters with a membrane at the average position $z = 0$.

with $i = \mathrm{sgn}(z)$. Thereby, $\mathbf{v}^i$ is the velocity field $\mathbf{v}^i \equiv (v_x^i(x, z), v_z^i(x, z))$ of the fluids and p^i is the pressure field $p^i = p^i(x, z)$.

The ansatz for the z-component of $\mathbf{v}$ imposing a planar incoming wave is given by

$$v_z^{\pm} = [C^{\pm} + D^{\pm} qz]\mathrm{e}^{\mp qz}\mathrm{e}^{iqx - \Gamma(q)t} \tag{14}$$

with constraints $\mathbf{v}(z \to \pm\infty) = \mathbf{0}$. Using eqn (12), we find the x-component of the velocity field $v_x^{\pm}$. Moreover, the velocity field has to be continuous at $z = 0$ and the in-plane divergence of v_x has to vanish at $z = 0$, *i.e.*, $\partial_x v_x(x, z = 0) = 0$. All together, we find after some algebra $C^{\pm} = \pm D^{\pm}$. Now, we calculate the pressure field $p^{\pm}(x, z)$ with eqn (13) and finally use force balance at $z = 0$,

$$-T^{+}_{zz|z=0} + T^{-}_{zz|z=0} = -\frac{\delta \mathcal{H}}{\delta h_{\mathbf{q}|z=0}} \tag{15}$$

with the liquid-stress-tensor $T^{\pm}_{kl} = -p^{\pm}\delta_{kl} + \eta^{\pm}(\partial_k v_l^{\pm} + \partial_l v_k^{\pm})$. Combining the results for the pressure fields and the velocity fields, we finally resolve the damping coefficients

$$\Gamma(q) = \frac{\kappa q^3 + \sigma q}{2(\eta^{+} + \eta^{-})} \equiv \frac{\kappa q^3 + \sigma q}{4\eta_{\mathrm{eff}}}, \tag{16}$$

with $\eta_{\mathrm{eff}} \equiv (\eta^{+} + \eta^{-})/2$. Thus, the effective viscosity for a membrane surrounded by different fluids is given by the arithmetic mean of both viscosities.

Appendix 2: spectral boundaries for a quasi-planar membrane

Over the years, the membrane was described in various approximations. A first approximation was the quasi-spherical geometry for the vesicle shape and, for adhesion to a flat substrate, a quasi-planar membrane was considered. Both representations provide fluctuation amplitudes from theoretical modelling. Here, we will compare both fluctuation amplitudes, in the quasi-spherical and in the quasi-planar geometry, and consequently determine the spectral boundaries in the planar geometry.

In quasi-planar geometry, the fluctuation amplitude for a membrane far away from the substrate (*i.e.*, without the interaction potential term) is known to be

$$\langle \Delta h^2 \rangle = \frac{k_{\mathrm{B}}T}{2\pi}\int_{q_{\min}}^{q_{\max}} \mathrm{d}q \frac{1}{\kappa q^3 + \sigma q}. \tag{17}$$

Therefore, the upper integration limit is given by $q_{\max} = 2\pi/d$ with d being the size of a lipid. The lower integration limit is not known in detail; however, it is of the order of $1/R$, where R is the radius of the vesicle.

In the following we will derive a more accurate estimate for $q_{\min}$. In quasi-spherical geometry, we expand the membrane shape

$$R(\Omega, t) = R(1 + u(\Omega, t)), \tag{18}$$

around its mean spherical shape with radius R and fluctuations $u(\Omega,t)$ at the angle Ω. Following the calculation shown in Milner and Safran,[13] the fluctuation amplitude $\langle u^2 \rangle$ in quasi-spherical geometry is given by

$$\langle u^2 \rangle = R^2 \sum_{l=2}^{l_{\max}} \left\langle |u_{lm}|^2 \right\rangle \frac{2l+1}{4\pi}, \tag{19}$$

with

$$\left\langle |u_{lm}|^2 \right\rangle = \frac{k_{\mathrm{B}}T}{(l+2)(l-1)[\kappa(l+1)l + \sigma R^2]}. \tag{20}$$

Therefore, the maximal order of spherical harmonics $l_{\max}$ is the order R/d.

The limits for $\sigma \to 0$ are found in both geometries as

$$\langle \Delta h^2 \rangle_{\sigma\to 0} \simeq \frac{k_{\mathrm{B}}T}{4\pi\kappa}\frac{1}{(q^0_{\min})^2}, \tag{21}$$

$$\langle u^2 \rangle_{\sigma\to 0} \simeq \frac{k_{\mathrm{B}}T}{4\pi\kappa}\frac{R^2}{3}. \tag{22}$$

The relative errors due to various approximations is below 1% for $q_{\max} > 10q_{\min}$ in eqn (21) and below 1% for $l_{\max} \geq 17$ in eqn (22). Finally, from this we find the correct lower integration limit for the fluctuation amplitude in quasi-planar geometry as

$$q^0_{\min} = \frac{\sqrt{3}}{R}. \tag{23}$$

Including membrane tension, the lower integration limit $q_{\min}$ is found numerically from eqn (17) and (18) and we show $q_{\min}$ in Fig. 8 for typical values of a vesicle (κ = 2, 20, 200$k_{\mathrm{B}}T$, and R = 10 μm). We find $q_{\min}$ to remain close to $q^0_{\min}$ for a broad range of membrane tensions. However, for typical membrane tensions of a vesicle we determine $q_{\min} \simeq 0.81q^0_{\min}$. Only for large membrane tensions, $\sigma \gg \kappa/d^2 \simeq 0.1\ \mathrm{J\ m^{-2}}$, which are far beyond the lysis tension of biomembranes, we find prominent deviations from $q^0_{\min}$ which saturate at $q_{\min} \simeq 5.09q^0_{\min}$ for $\sigma \to \infty$.

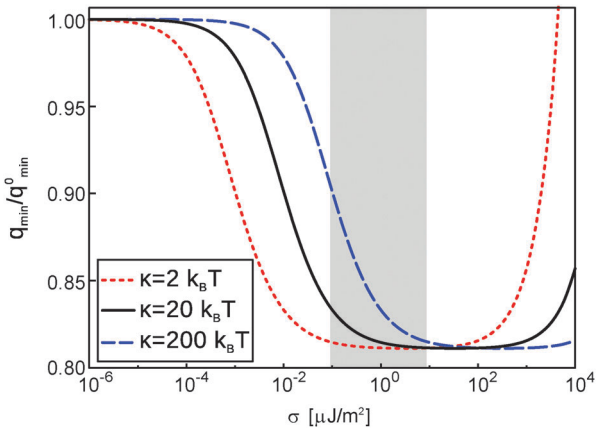

Fig. 8 Lower integration limit $q_{\min}$ as a function of the membrane tension σ. The vesicle radius was kept constant at R = 10 μm while the grey shaded area illustrates the experimentally accessible parameter range.

Conflict of interest

The authors declare no competing financial interests.

Acknowledgements

C. M. is grateful for the financial support by DAAD and Fonds der Chemischen Industrie. A.-S. S. and D. S. received funding from the European Research Council (starting grant 2013-337283), the Cluster of Excellence: "Engineering of Advanced Materials", and the Research Training Group 1962 of the Friedrich-Alexander Universität Erlangen-Nürnberg. K. S. thanks the European Research Council for funding *via* grant no. 307104 FP/2007-2013/ERC/SYNINTER and AMIDEX grant Affinity.

References

1 W. Helfrich, Elastic properties of lipid bilayers: theory and possible experiments, *Z. Naturforsch., C: Biochem., Biophys., Biol., Virol.*, 1973, **28**, 693–703.
2 C. Monzel and K. Sengupta, Measuring shape fluctuations in biological membranes, *J. Phys. D: Appl. Physics*, 2016, **49**, 107791.
3 R. M. Servuss and W. Helfrich, Mutual Adhesion of Lecithin Membranes at Ultralow Tensions, *J. Phys.*, 1989, **50**, 809–827.
4 Y. Park, M. Diez-Silva, G. Popescu, G. Lykotrafitis, W. Choi, M. S. Feld and S. Suresh, Refractive index maps and membrane dynamics of human red blood cells parasitized by Plasmodium falciparum, *Proc. Natl. Acad. Sci. U. S. A.*, 2008, **105**, 13730–13735.
5 T. Betz, M. Lenz, J.-F. Joanny and C. Sykes, ATP-dependent mechanics of red blood cells, *Proc. Natl. Acad. Sci. U. S. A.*, 2009, **106**, 15320–15325.
6 D. Cojoc, S. Finaurini, P. Livshits, E. Gur, A. Shapira, V. Mico and Z. Zalevsky, Toward fast malaria detection by secondary speckle sensing microscopy, *Biomed. Opt. Express*, 2012, **3**, 991–1005.
7 C. Monzel, D. Schmidt, C. Kleusch, D. Kirchenbüchler, U. Seifert, A.-S. Smith, K. Sengupta and R. Merkel, Measuring fast stochastic displacements of bio-membranes with dynamic optical displacement spectroscopy, *Nat. Commun.*, 2015, **6**, 8162.
8 E. A. Evans and V. A. Parsegian, Thermal-mechanical fluctuations enhance repulsion between bimolecular layers, *Proc. Natl. Acad. Sci. U. S. A.*, 1986, **83**, 7132–7136.
9 R. Podgornik and V. Parsegian, Thermal-Mechanical Fluctuations of Fluid Membranes in Confined Geometries: The Case of Soft Confinement, *Langmuir*, 1992, **8**, 557–562.
10 L. B. Freund, Entropic pressure between biomembranes in a periodic stack due to thermal fluctuations, *Proc. Natl. Acad. Sci. U. S. A.*, 2013, **110**, 2047–2051.
11 E. Evans and W. Rawicz, Entropy-Driven Tension and Bending Elasticity in Condensed-Fluid Membranes, *Phys. Rev. Lett.*, 1990, **64**, 2094–2097.
12 J. F. Faucon, M. D. Mitov, P. Méléard, I. Bivas and P. Bothorel, Bending elasticity and thermal fluctuations of lipid membranes. Theoretical and experimental requirements, *J. Phys.*, 1989, **50**, 2389–2414.
13 S. T. Milner and S. A. Safran, Dynamical fluctuations of droplet microemulsions and vesicles, *Phys. Rev. A: At., Mol., Opt. Phys.*, 1987, **36**, 4371–4379.
14 U. Seifert, Configurations of fluid membranes and vesicles, *Adv. Phys.*, 1997, **46**, 13–137.
15 R. Lipowsky and E. Sackmann, *Structure and Dynamics of Membranes: I. From Cells to Vesicles/II. Generic and Specific Interactions*, North Holland, Amsterdam, 1995.
16 F. Ahmadpoor and P. Sharma, Thermal fluctuations of vesicles and nonlinear curvature elasticity-implications for size-dependent renormalized bending rigidity and vesicle size distribution, *Soft Matter*, 2016, **12**, 2523–2536.
17 U. Seifert and S. A. Langer, Viscous modes of fluid bilayer membranes, *Europhys. Lett.*, 1993, **23**, 71–76.
18 E. Evans and A. Yeung, Hidden dynamics in rapid changes of bilayer shape, *Chem. Phys. Lipids*, 1994, **73**, 39–56.
19 E. Evans, Bending resistance and chemically-induced moments in membrane bilayers, *Biophys. J.*, 1974, **14**, 923–931.
20 J.-B. Fournier and C. Barbetta, Direct Calculation from the Stress Tensor of the Lateral Surface Tension of Fluctuating Fluid Membranes, *Phys. Rev. Lett.*, 2008, **100**, 078103.
21 P. Girard, J. Prost and P. Bassereau, Passive or active fluctuations in membranes containing proteins, *Phys. Rev. Lett.*, 2005, **94**, 088102.
22 O. Farago, Membrane fluctuations near a plane rigid surface, *Phys. Rev. E: Stat., Nonlinear, Soft Matter Phys.*, 2008, **78**, 051919.
23 T. R. Weikl, M. Asfaw, H. Krobath, B. Rozycki and R. Lipowsky, Adhesion of membranes *via* receptor–ligand complexes: Domain formation, binding cooperativity, and active processes, *Soft Matter*, 2009, **5**, 13.
24 J. Pécréaux, H.-G. Döbereiner, J. Prost, J.-F. Joanny and P. Bassereau, Refined contour analysis of giant unilamellar vesicles, *Eur. Phys. J. E: Soft Matter Biol. Phys.*, 2004, **13**, 277–290.
25 H.-G. Döbereiner, G. Gompper, C. Haluska, D. Kroll, P. Petrov and K. Riske, Advanced Flicker Spectroscopy of Fluid Membranes, *Phys. Rev. Lett.*, 2003, **91**, 048301.
26 R. Hirn, T. M. Bayerl, J. O. Rädler and E. Sackmann, Collective membrane motions of high and low amplitude, studied by dynamic light scattering and micro-interferometry, *Faraday Discuss.*, 1998, **111**, 17–30.
27 J.-B. Manneville, P. Bassereau, S. Ramaswamy and J. Prost, Active membrane fluctuations studied by micropipet aspiration, *Phys. Rev. E: Stat., Nonlinear, Soft Matter Phys.*, 2001, **64**, 021908.
28 C. Monzel, S. Fenz, R. Merkel and K. Sengupta, Probing biomembrane dynamics by dual-wavelength reflection interference contrast microscopy, *ChemPhysChem*, 2009, **10**, 2828–2838.
29 J. O. Rädler, T. J. Feder, H. H. Strey and E. Sackmann, Fluctuation analysis of tension-controlled undulation forces between giant vesicles and solid substrates, *Phys. Rev. E: Stat. Phys., Plasmas, Fluids, Relat. Interdiscip. Top.*, 1995, **51**, 4526–4536.
30 R. Bruinsma, A. Behrisch and E. Sackmann, Adhesive switching of membranes: experiment and theory, *Phys. Rev. E: Stat. Phys., Plasmas, Fluids, Relat. Interdiscip. Top.*, 2000, **61**, 4253–4267.
31 D. Cuvelier and P. Nassoy, Hidden dynamics of vesicle adhesion induced by specific stickers, *Phys. Rev. Lett.*, 2004, **93**, 228101.

32 A.-S. Smith, K. Sengupta, S. Goennenwein, U. Seifert and E. Sackmann, Force-induced growth of adhesion domains is controlled by receptor mobility, *Proc. Natl. Acad. Sci. U. S. A.*, 2008, **105**, 6906–6911.
33 A.-S. Smith, S.-F. Fenz and K. Sengupta, Interferring spatial organization of bonds within adhesion clusters by exploiting fluctuations of soft interfaces, *Europhys. Lett.*, 2010, **89**, 28003.
34 F. Brochard-Wyart and J.-F. Lennon, Frequency spectrum of the flicker phenomenon in erythrocyte, *J. Phys.*, 1975, **36**, 1035–1047.
35 J. Evans, W. Gratzer, N. Mohandas, K. Parker and J. Sleep, Fluctuations of the red blood cell membrane: relation to mechanical properties and lack of ATP dependence, *Biophys. J.*, 2008, **94**, 4134–4144.
36 R. Dimova, Recent developments in the field of bending rigidity measurements on membranes, *Adv. Colloid Interface Sci.*, 2014, **208**, 225–234.
37 J. F. Nagle, M. S. Jablin, S. Tristram-Nagle and K. Akabori, What are the true values of the bending modulus of simple lipid bilayers?, *Chem. Phys. Lipids*, 2015, **185**, 3–10.
38 R. M. Venable, F. L. Brown and R. W. Pastor, Mechanical properties of lipid bilayers from molecular dynamics simulation, *Chem. Phys. Lipids*, 2015, **192**, 60–74.
39 C. L. Armstrong, W. Häußler, T. Seydel, J. Katsaras and M. C. Rheinstädter, Nanosecond lipid dynamics in membranes containing cholesterol, *Soft Matter*, 2014, **10**, 2600–2611.
40 M. Arnold, E. A. Cavalcanti-Adam, R. Glass, J. Blümmel, W. Eck, M. Kantlehner, H. Kessler and J. P. Spatz, Activation of integrin function by nanopatterned adhesive interfaces, *ChemPhysChem*, 2004, **5**, 383–388.
41 Z.-H. Huang, G. Massiera, L. Limozin, P. Boullanger, M.-P. Valignat and A. Viallat, Sensitive detection of ultra-weak adhesion states of vesicles by interferometric microscopy, *Soft Matter*, 2010, **6**, 1948.
42 S. F. Fenz, T. Bihr, R. Merkel, U. Seifert, K. Sengupta and A.-S. Smith, Switching from ultraweak to strong Adhesion, *Adv. Mater.*, 2011, **23**, 2622–2626.
43 S. F. Fenz, A.-S. Smith, R. Merkel and K. Sengupta, Intermembrane adhesion mediated by mobile linkers: Effect of receptor shortage, *Soft Matter*, 2011, **7**, 952.
44 K. H. Biswas, K. L. Hartman, C.-h. Yu, O. J. Harrison, H. Song, A. W. Smith, W. Y. C. Huang, W.-C. Lin, Z. Guo and A. Padmanabhan, *et al.*, E-cadherin junction formation involves an active kinetic nucleation process, *Proc. Natl. Acad. Sci. U. S. A.*, 2015, **112**, 10932–10937.
45 C. Monzel, S. F. Fenz, M. Giesen, R. Merkel and K. Sengupta, Mapping fluctuations in biomembranes adhered to micropatterns, *Soft Matter*, 2012, **8**, 6128.
46 U. Seifert, Self-Consistent Theory of Bound Vesicles, *Phys. Rev. Lett.*, 2002, **74**, 5060.
47 K. Mecke, T. Charitat and F. Graner, Fluctuating Lipid Bilayer in an Arbitrary Potential: Theory and Experimental Determination of Bending Rigidity, *Langmuir*, 2003, **19**, 2080.
48 U. Seifert and R. Lipowsky, Adhesion of vesicles, *Phys. Rev. A: At., Mol., Opt. Phys.*, 1990, **42**, 4768–4771.
49 E. Sackmann and R. F. Bruinsma, Cell adhesion as wetting transition?, *ChemPhysChem*, 2002, **3**, 262–269.
50 S. Goennenwein, M. Tanaka, B. Hu, L. Moroder and E. Sackmann, Functional Incorporation of Intergins into Solid Supported Membrane on Ultrathin Films of Cellulose: Impact on Adhesion, *Biophys. J.*, 2003, **85**, 646–655.
51 G. Bell, M. Dembo and P. Bongrand, Competition between nonspecific repulsion and specific bonding, *Biophys. J.*, 1984, **45**, 1051–1064.
52 K. Sengupta and L. Limozin, Adhesion of soft membranes controlled by tension and interfacial polymers, *Phys. Rev. Lett.*, 2010, **104**, 088101.
53 M. Kraus and U. Seifert, Relaxation modes of an adhering bilayer membrane, *J. Phys. II*, 1994, **4**, 1117–1134.
54 P.-H. Puech, V. Askovic, P.-G. De Gennes and F. Brochard-Wyart, Dynamics of Vesicle Adhesion: Spreading Versus Dewetting Coupled to Binder Diffusion, *Biophys. Rev. Lett.*, 2006, **1**, 85–95.
55 D. Schmidt, C. Monzel, T. Bihr, R. Merkel, U. Seifert, K. Sengupta and A.-S. Smith, Signature of a Nonharmonic Potential as Revealed from a Consistent Shape and Fluctuation Analysis of an Adherent Membrane, *Phys. Rev. X*, 2014, **4**, 021023.
56 M. Schneider, J. Jenkins and W. Webb, Thermal fluctuations of large quasi-spherical bimolecular phospholipid vesicles, *J. Phys.*, 1984, **45**, 1457–1472.
57 N. Kučerka, Y. Liu, N. Chu, H. I. Petrache, S. Tristram-Nagle and J. Nagle, Structure of fully hydrated fluid phase DMPC and DLPC lipid bilayers using X-ray scattering from oriented multilamellar arrays and from unilamellar vesicles, *Biophys. J.*, 2005, **88**, 2626–2637.
58 Y. Lyatskaya, Y. Liu, S. Tristram-Nagle, J. Katsaras and J. Nagle, Method for obtaining structure and interactions from oriented lipid bilayers, *Phys. Rev. E: Stat. Phys., Plasmas, Fluids, Relat. Interdiscip. Top.*, 2001, **63**, 011907.
59 M. C. Rheinstädter, W. Häußler and T. Salditt, Dispersion Relation of Lipid Membrane Shape Fluctuations by Neutron Spin-Echo Spectrometry, *Phys. Rev. Lett.*, 2006, **97**, 048103.
60 B.-A. Brüning, S. Prévost, R. Stehle, R. Steitz, P. Falus, B. Farago and T. Hellweg, Bilayer undulation dynamics in unilamellar phospholipid vesicles: effect of temperature, cholesterol and trehalose, *Biochim. Biophys. Acta*, 2014, **1838**, 2412–2419.
61 L. Limozin and K. Sengupta, Quantitative reflection interference contrast microscopy (RICM) in soft matter and cell adhesion, *ChemPhysChem*, 2009, **10**, 2752–2768.
62 S. Marx, J. Schilling, E. Sackmann and R. Bruinsma, Helfrich Repulsion and Dynamical Phase Separation of Multicomponent Lipid Bilayers, *Phys. Rev. Lett.*, 2002, **88**, 138102.
63 A. Zidovska and E. Sackmann, Brownian motion of nucleated cell envelopes impedes adhesion, *Phys. Rev. Lett.*, 2006, **96**, 048103.
64 J. Schilling, K. Sengupta, S. Goennenwein, A. R. Bausch and E. Sackmann, Absolute interfacial distance measurements

by dual-wavelength reflection interference contrast microscopy, *Phys. Rev. E: Stat., Nonlinear, Soft Matter Phys.*, 2004, **69**, 021901.

65 S. A. Kim, K. G. Heinze and P. Schwille, Fluorescence correlation spectroscopy in living cells, *Nat. Methods*, 2007, **4**, 963–973.

66 J. Enderlein, I. Gregor, D. Patra, T. Dertinger and U. B. Kaupp, Performance of fluorescence correlation spectroscopy for measuring diffusion and concentration, *ChemPhysChem*, 2005, **6**, 2324–2336.

67 T. Betz and C. Sykes, Time resolved membrane fluctuation spectroscopy, *Soft Matter*, 2012, **8**, 5317.

68 A.-S. Smith, B. G. Lorz, U. Seifert and E. Sackmann, Antagonist-induced deadhesion of specifically adhered vesicles, *Biophys. J.*, 2006, **90**, 1064–1080.

69 R. R. Netz, Complete Unbinding of Fluid Membranes in the Presence of short-ranged forces, *Phys. Rev. E: Stat. Phys., Plasmas, Fluids, Relat. Interdiscip. Top.*, 1995, **51**, 2286–2294.

70 R. Lipowsky and B. Zielinska, Binding and unbinding of lipid membranes: A Monte Carlo study, *Phys. Rev. Lett.*, 1989, **62**, 1572–1575.

71 A. Kumar and G. M. Whitesides, Features of gold having micrometer to centimeter dimensions can be formed through a combination of stamping with an elastomeric stamp and an alkanethiol ink followed by chemical etching, *Appl. Phys. Lett.*, 1993, **63**, 2002–2004.

72 A. P. Quist, E. Pavlovic and S. Oscarsson, Recent advances in microcontact printing, *Anal. Bioanal. Chem.*, 2005, **381**, 591–600.

73 D. S. Dimitrov and M. I. Angelova, Lipid swelling and liposome formation mediated by electric fields, *Bioelectrochem. Bioenerg.*, 1988, **19**, 323–336.

74 E. P. Petrov and P. Schwille, Chapter State of the Art and Novel Trends in Fluorescence Correlation Spectroscopy, in *Springer Series on Fluorescence*, ed. U. Resch-Genger, Springer, New York, 2008, vol. 6, pp. 145–197.

75 J. S. Ploem, *Mononuclear Phagocytes in Immunity, Infection and Pathology*, Blackwell Scientific, Oxford, 1975.

76 L. Limozin and K. Sengupta, Modulation of vesicle adhesion and spreading kinetics by hyaluronan cushions, *Biophys. J.*, 2007, **93**, 3300–3313.

77 U. Seifert, Dynamics of a bound membrane, *Phys. Rev. E: Stat. Phys., Plasmas, Fluids, Relat. Interdiscip. Top.*, 1994, **46**, 3124–3127.

78 Y. Zhou and R. M. Raphael, Effect of salicylate on the elasticity, bending stiffness, and strength of SOPC membranes, *Biophys. J.*, 2005, **89**, 1789–1801.

79 J. Humpolíčková, E. Gielen, A. Benda, V. Fagulova, J. Vercammen, M. VandeVen, M. Hof, M. Ameloot and Y. Engelborghs, Probing diffusion laws within cellular membranes by Z-scan fluorescence correlation spectroscopy, *Biophys. J.*, 2006, **91**, L23–L25.

80 W. Häckl, U. Seifert and E. Sackmann, Effects of Fully and Partially Solubilized Amphiphiles on Bilayer Bending Stiffness and Temperature Dependence of the Effective Tension of Giant Vesicles, *J. Phys. II*, 1997, **7**, 1141–1157.

81 H. Engelhardt, H. Duwe and E. Sackmann, Bilayer bending elasticity measured by Fourier analysis of thermally excited surface undulations of flaccid vesicles, *J. Phys., Lett.*, 1985, **46**, 395–400.

82 S. Cha, S. H. Kim and D. Kim, Viscosity of Sucrose Aqueous Solutions Measured by Using Fluorescence Correlation Spectroscopy, *J. Korean Phys. Soc.*, 2010, **56**, 1315–1318.

83 M. Mell, L. H. Moleiro, Y. Hertle, I. López-Montero, F. J. Cao, P. Fouquet, T. Hellweg and F. Monroy, Fluctuation dynamics of bilayer vesicles with intermonolayer sliding: experiment and theory, *Chem. Phys. Lipids*, 2015, **185**, 61–77.

84 A. Albersdörfer, T. Feder and E. Sackmann, Adhesion-induced domain formation by interplay of long-range repulsion and short-range attraction force: A model membrane study, *Biophys. J.*, 1997, **73**, 245–257.

85 E. Sackmann and A.-S. Smith, Physics of cell adhesion: some lessons from cell-mimetic systems, *Soft Matter*, 2014, **10**, 1644–1659.

86 K. Fricke, K. Wirthensohn, R. Laxhuber and E. Sackmann, Flicker spectroscopy of erythrocytes. A sensitive method to study subtle changes of membrane bending stiffness, *Eur. Biophys. J.*, 1986, **14**, 67–81.

87 A.-S. Smith and U. Seifert, Vesicles as a model for controlled (de-)adhesion of cells: a thermodynamic approach, *Soft Matter*, 2007, **3**, 275–289.

88 S. F. Fenz, R. Merkel and K. Sengupta, Diffusion and intermembrane distance: case study of avidin and E-cadherin mediated adhesion, *Langmuir*, 2009, **25**, 1074–1085.

89 P. S. Swain and D. Andelman, The Influence of Substrate Structure on Membrane Adhesion, *Langmuir*, 1999, **15**, 8902–8914.

90 P. S. Swain and D. Andelman, Supported membranes on chemically structured and rough surfaces, *Phys. Rev. E: Stat., Nonlinear, Soft Matter Phys.*, 2001, **63**, 051911.

91 T. Bihr, S. Fenz, E. Sackmann, R. Merkel, U. Seifert, K. Sengupta and A.-S. Smith, Association rates of membrane-coupled cell adhesion molecules, *Biophys. J.*, 2014, **107**, L33–L36.

92 V. D. Gordon, T. J. O'Halloran and O. Shindell, Membrane adhesion and the formation of heterogeneities: biology, biophysics, and biotechnology, *Phys. Chem. Chem. Phys.*, 2015, **17**, 15522–15533.

P4

Coexistence of dilute and densly packed domains of ligand-receptor bonds in membrane adhesion

Coexistence of dilute and densely packed domains of ligand-receptor bonds in membrane adhesion

D. Schmidt[1], T. Bihr[1], U. Seifert[1], and A.-S. Smith[2]

[1] II. Institut für Theoretische Physik, Universität Stuttgart, Germany
[2] Institut für Theoretische Physik and Excellence Cluster: Engineering of Advanced Materials, Universität Erlangen-Nürnberg, Germany

EPL, **99** (2012) 38003

DOI: 10.1209/0295-5075/99/38003
http://iopscience.iop.org/article/10.1209/0295-5075/99/38003

ABSTRACT We analyze the stability of micro-domains of ligand-receptor bonds that mediate the adhesion of biological model membranes. After evaluating the effects of membrane fluctuations on the binding affinity of a single bond, we characterize the organization of bonds within the domains by theoretical means. In a large range of parameters, we find the commonly suggested dense packing to be separated by a free energy barrier from a regime in which bonds are sparsely distributed. If bonds are mobile, a coexistence of the two regimes should emerge, which agrees with recent experimental observations.

A Letters Journal Exploring the Frontiers of Physics

August 2012

EPL, **99** (2012) 38003
doi: 10.1209/0295-5075/99/38003

www.epljournal.org

Coexistence of dilute and densely packed domains of ligand-receptor bonds in membrane adhesion

Daniel Schmidt[1], Timo Bihr[1], Udo Seifert[1] and Ana-Sunčana Smith[2]

[1] *II. Institut für Theoretische Physik, Universität Stuttgart - Stuttgart, Germany, EU*
[2] *Institut für Theoretische Physik and Excellence Cluster: Engineering of Advanced Materials, Universität Erlangen-Nürnberg - Erlangen, Germany, EU*

received 10 February 2012; accepted in final form 9 July 2012
published online 7 August 2012

PACS 87.16.dj – Dynamics and fluctuations
PACS 87.16.dt – Structure, static correlations, domains, and rafts
PACS 87.17.Rt – Cell adhesion and cell mechanics

Abstract – We analyze the stability of micro-domains of ligand-receptor bonds that mediate the adhesion of biological model membranes. After evaluating the effects of membrane fluctuations on the binding affinity of a single bond, we characterize the organization of bonds within the domains by theoretical means. In a large range of parameters, we find the commonly suggested dense packing to be separated by a free energy barrier from a regime in which bonds are sparsely distributed. If bonds are mobile, a coexistence of the two regimes should emerge, which agrees with recent experimental observations.

The key step in the recognition process of living cells is the establishment of adhesive contacts either between opposing membranes of two cells or between the membrane of a cell and the extracellular matrix (ECM). It has been shown previously that the organization of bonds within domains has strong effects on the adhesion of cells and the consequent active response [1]. Most insightful were the experiments with cells binding to substrates containing ligands organized on a hexagonal lattice of a characteristic length between 40 and 150 nm. A length of 58 to 73 nm distance between bonds was shown necessary for a successful formation of domains [2], and at distances larger then 90 nm, domains would not form [3].

Instead of using living cells, the so-called bottom up approach [4] has been successfully used to elucidate various elements relevant to cell membranes and adhesion [5]. The main protagonists of this research are giant unilamellar vesicles that are functionalized with ligands to interact with receptors immobilized on the surface [6]. Depending on the density of binders on the substrate and in the vesicle, as well as on the intrinsic binding affinity of the binding pair, either domains with densely packed bonds have been observed to grow radially from a nucleation center, or no specific adhesion was reported. In the context of the formation of these densely packed domains, valuable information on their nucleation and the growth [7], equilibrium [8], cooperative effects [9–11], and membrane roughness [12–14] have been discussed over the years from both the experimental and the theoretical points of view.

With the development of experimental methods [15], more detailed imaging of the distribution of bonds within the adhesion domains became possible. Consequently, large domains consisting of sparsely distributed bonds have been identified in coexistence with densely packed domains [16,17]. It was reported that sparse domains may become densely packed by a gradual increase of density of ligand-receptor bonds within an area of the domain of several square micrometers. However, some sparse domains were also found stable on time scales of the experiment (several hours) [17].

The coexistence between the sparse and dense domains driven by membrane-mediated interactions was first shown within an effective model [18]. At about the same time, an adhesion stabilized phase separation induced by attractive interactions of binders within the same membrane, was suggested [19]. A somewhat similar phase diagram emerged from considering the interplay of a binding bond potential and a nonspecific repulsion [20], but in the absence of membrane transmitted correlations. More recently, a complex phase behavior was suggested for active binders and binders of different length coexisting within the same membrane [11,21]. Here we show, that the stability of sparse domains and their coexistence

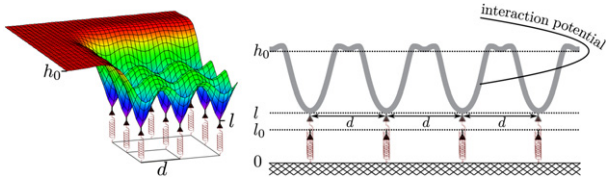

Fig. 1: (Colour on-line) The system under investigation: a large patch of a bonded membrane that deforms and fluctuates in a harmonic potential. Bonds are separated by a distance d.

with dense domains emerges from basic principles, at low membrane tension. Thereby, the cost of deforming the membrane in an effective nonspecific potential is balanced with the energy gain associated with the formation of bonds.

The model. – We consider bonds placed on a regular square (sq) or central hexagonal (ch) lattice. Thereby, we assume that the lateral size of the membrane adhesion domain is significantly larger than the size of a lattice unit cell (fig. 1). We model the total free energy of a domain (containing N bonds) and investigate its dependence on the distance d between the bonds.

The membrane deformation energy (in units of $k_{\rm B}T$, where $k_{\rm B}$ is the Boltzmann constant and T the temperature) is described by the Helfrich Hamiltonian [18,20,22]

$$\mathcal{H}_0 = \int\limits_A {\rm d}\mathbf{r}\left[\frac{\kappa}{2}\left(\nabla^2 h(\mathbf{r})\right)^2 + \frac{\sigma}{2}(\nabla h(\mathbf{r}))^2 + \frac{\gamma}{2}\left(h(\mathbf{r})-h_0\right)^2\right]. \quad (1)$$

Thereby, the Monge parametrization is used to represent the membrane of a bending stiffness κ as a surface of projected area A placed above the substrate at the height $h(\mathbf{r})$, $\mathbf{r}=(x,y)$ being the in-plane position vector. The first term is the bending energy, whereas the second term accounts for the tension σ in the membrane. In a simplistic manner, the last term models the generic membrane-substrate interaction potential with the harmonic potential of a strength γ with a minimum at the height h_0. In the context of mimetic systems, this interaction potential encompasses for a number of contributions such as the van der Waals attraction, or the steric repulsion emerging from both repeller and membrane shape fluctuations [22]. In the case of cells, numerous other factors associated with actin (de)polymerization, active forces, the glycocalix and the ECM, may all contribute to this potential depending on the cell type and the treatment of the substrate.

The receptors are modeled as thermalized harmonic springs of rest length l_0 and spring constant λ, fixed for all bonds on the lattice. When the receptor is relatively stiff such as a bulky protein, it is modeled with a very large spring constant ($\lambda\to\infty$). If the receptor is a soft polymer, deforming to form a bond, λ is set finite.

Ligands and receptors interact through a square-well potential [20,23], of a very short range α and depth ϵ_b ($1-35\,k_{\rm B}T$), the latter associated with the intrinsic binding affinity. Thus, the total Hamiltonian $\mathcal{H}$ of a domain with N bonds situated at position $\mathbf{r}_b^j$ reads

$$\mathcal{H} = \mathcal{H}_0 + \frac{\lambda}{2}\sum_{j=1}^{N}(l(\mathbf{r}_b^j)-l_0)^2 + N\epsilon_b \equiv N\mathcal{H}_d + N\epsilon_b. \quad (2)$$

Here, $l(\mathbf{r}_b^j)$ is the extension of the j-th spring. When $\alpha\to 0$, obviously $h(\mathbf{r}_b^j)\to l(\mathbf{r}_b^j)$. Furthermore, $\mathcal{H}_d$ denotes the deformation energy per bond stored in the membrane and all receptors. The last term is the binding enthalpy.

Free energy. – The stability of the domain is determined from the difference $\Delta\mathcal{F}^N$ between the free energy of the domain with N formed bonds $\mathcal{F}_b^N$, and the free energy of the reference state in which receptors and the membrane fluctuate freely $\mathcal{F}_{ub}^N$. Both $\mathcal{F}_b^N$ and $\mathcal{F}_{ub}^N$ are calculated from the partition function $\mathcal{Z}$, comprising all possible conformations of N receptors and the membrane. Thereby, the partition functions of the reference and the bound state ($\mathcal{Z}_{ub}$ and $\mathcal{Z}_b$), and hence $\mathcal{F}_{ub}^N\equiv\ln\mathcal{Z}_{ub}$ and $\mathcal{F}_b^N\equiv\ln\mathcal{Z}_b$, are associated with the conformations in which the membrane is outside or within the range α of the square potential at the position of all receptors, respectively. The domain is stable if $\Delta\mathcal{F}^N=\mathcal{F}_b^N-\mathcal{F}_{ub}^N<0$.

Here we have clearly omitted the change in the mixing entropy of binders that could, in principle, affect the results. However, we assume the adhesion to be mediated by large domains of bonds. Such domains typically form when the concentration of the mobile ligands is significantly larger than the concentration of the immobilized receptors [8]. In the context of the free energy of the system, in this regime the mixing entropy will provide a constant, proportional to the number of bonds and to the chemical potential of the free ligands, but independent of the distance between bonds. Consequently, in this regime, the mixing entropy will act to re-scale the effective binding affinity of a single bond [18], without affecting the general phase behavior of the domains.

The reference state for N receptors. The partition function for the free membrane and N unbound fluctuating receptors is, up to the normalization,

$$\mathcal{Z}_{ub} = \prod_{j=1}^{N}\left(\int {\rm d}l(\mathbf{r}_b^j)\exp\left[-\frac{\lambda}{2}(l(\mathbf{r}_b^j)-l_0)^2\right]\right) \times\left(\int\mathcal{D}\left[h'(\mathbf{r})\right]{\rm e}^{-\mathcal{H}_0[h'(\mathbf{r})]}\right)\equiv\mathcal{C}\left(\frac{2\pi}{\lambda}\right)^{N/2}, \quad (3)$$

where $\mathcal{C}$ is denoting the result of the functional integral $\mathcal{D}[h'_{\mathbf{q}}]$.

In this state, the membrane is free, on average flat, and positioned in the minimum of the nonspecific potential $\langle h(\mathbf{r})\rangle = h_0$. The fluctuation amplitude is that of a membrane under tension [24]

$$\Sigma_0^2 \equiv \frac{1}{A}\sum_{\mathbf{q}}\frac{1}{\kappa q^4+\sigma q^2+\gamma} = \frac{\arctan(\sqrt{4\kappa\gamma-\sigma^2}/\sigma)}{2\pi\sqrt{4\kappa\gamma-\sigma^2}}, \quad (4)$$

where the sum runs over all possible wave vectors $\mathbf{q}$ with $q \equiv |\mathbf{q}|$, set by the system size. The spatial correlation function [24,25] is simply given by

$$G(\mathbf{r}_0 - \mathbf{r}) \equiv \frac{1}{A} \sum_{\mathbf{q}} \frac{\cos\left(\mathbf{q} \cdot (\mathbf{r}_0 - \mathbf{r})\right)}{\kappa q^4 + \sigma q^2 + \gamma}, \tag{5}$$

where $\mathbf{r}_0$ and $\mathbf{r}$ are arbitrary positions on the membrane. In the tensionless limit, $\Sigma_0^2 = 1/(8\sqrt{\kappa\gamma})$ and $G(r) \approx -4\pi^{-1}\xi_\perp^2 \mathrm{kei}(r/\xi_\parallel)$, with kei signifying the Kelvin function. Thereby, $\xi_\perp^2 \equiv 1/(8\sqrt{\kappa\gamma})$ and $\xi_\parallel \equiv \sqrt[4]{\kappa/\gamma}$ are the vertical roughness and the lateral correlation length of a tensionless unbound membrane, respectively [22,24,25], setting the length and other scales of the system.

An isolated bond —$N = 1$. The shape of the membrane bound to the substrate by one bond is typified by the Kelvin function [25]. The associated membrane deformation energy $\mathcal{U}(\sigma) = (h_0 - h(\mathbf{r}_b))^2/(2\Sigma_0^2)$ is quadratic with respect to the offset from the minimum of the nonspecific potential. When $\lambda \to \infty$ the entire deformation is stored in the membrane. If, furthermore, $\sigma = 0$, one finds $\mathcal{U}_0 = (h_0 - l_0)^2/2\xi_\perp^2$, as previously determined [18].

Because both the membrane and the receptor deformations are quadratic with the elongation, we map the problem of forming one bond to a problem of two one-dimensional (1D) thermalized springs of stiffness k_1 and k_2 (fig. 2). The springs are said to interact if their relative distance falls within a square-well potential of a (short) range α and depth V_0. The free energy difference between the bound and the unbound state

$$\Delta\mathcal{F}^{sp} = \frac{1}{2}\frac{k_1 k_2 L^2}{k_1 + k_2} - V_0 + \frac{1}{2}\ln\left[\frac{2\pi(k_1 + k_2)}{k_1 k_2}\frac{1}{\alpha^2}\right] \tag{6}$$

is calculated as described previously, by subdividing the configurational space of the receptor and the membrane. The first term on the right side is identified with the deformation energy of the two springs, characterized by a reduced spring constant of the coupled system consisting of two springs in series $k_1 k_2/(k_1 + k_2)$ elongated to meet the system size L. The second and the third terms are the enthalpy gain and the entropy loss due to the formation of a bond. Thereby, the last contribution only affects the depth of the potential.

By analogy (fig. 2), for a membrane binding to a single receptor (indicated by the superscript 1)

$$\Delta\mathcal{F}^1 = \frac{1}{2}\frac{(h_0 - l_0)^2}{\Sigma_0^2 + 1/\lambda} - \bar{\epsilon_b} \equiv \mathcal{H}_d^1 - \bar{\epsilon_b}. \tag{7}$$

Thereby, $\mathcal{H}_d^1$ is the total deformation energy associated with an isolated bond and sets the energy scale of the problem. For $\sigma = 0$ and $\lambda \to \infty$, $\mathcal{H}_d^1 = \mathcal{U}_0$. Furthermore, $\bar{\epsilon_b}$ is the effective binding affinity

$$\bar{\epsilon_b} \equiv \epsilon_b - \frac{1}{2}\ln\left[\frac{2\pi}{\alpha^2}\left(\frac{1}{\lambda} + \Sigma_0^2\right)\right], \tag{8}$$

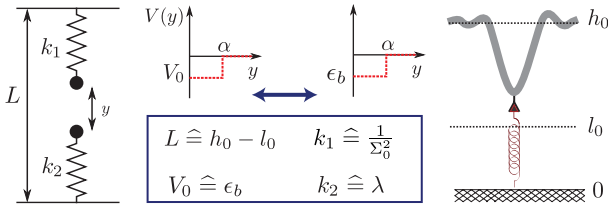

Fig. 2: (Colour on-line) Mapping of the model for two fluctuating interacting springs to the membrane-bond model.

which is the contribution of a single bond to the free energy. In essence, it is the intrinsic binding affinity decreased by the entropic cost related to the change in the fluctuations of the membrane and the receptor upon binding. At room temperature and typical parameters this cost amounts to several $k_\mathrm{B}T$. If mixing entropy of the binders is considered in the regime of large domains, the chemical potential of free ligands would need to be subtracted on the right-hand side of eq. (8).

A domain with N bonds. The free energy of an arbitrary bond configuration of N bonds emerges from the partition function for the bound system $\mathcal{Z}_b$

$$\mathcal{Z}_b = \int \mathcal{D}\left[h'(\mathbf{r})\right] \prod_j^N \int_{h'(\mathbf{r}_b^j)-\alpha}^{h'(\mathbf{r}_b^j)} \mathrm{d}l(\mathbf{r}_b^j) \mathrm{e}^{-\mathcal{H}[h'(\mathbf{r}),\{l(\mathbf{r}_b^j)\}]}, \tag{9}$$

that accounts for all conformations in which all receptors and the membrane are simultaneously within the bond potential range α. With the Hamiltonian from eq. (2), one gets

$$\mathcal{Z}_b = \frac{\mathcal{C}\alpha^N \exp\left[-\left(\mathcal{H}_d^1 \sum_{i,j=1}^N M_{ij}^{-1} - N\epsilon_b\right)\right]}{\sqrt{(1 + \lambda\Sigma_0^2)^N \det M}}, \tag{10}$$

with $M_{ij} \equiv (\delta_{ij} + \lambda G(\mathbf{r}_b^i - \mathbf{r}_b^j))/(1 + \lambda\Sigma_0^2)$ accounting for the membrane-coupled deformations of bound receptors on positions $\mathbf{r}_b^i$ and $\mathbf{r}_b^j$. The free energy difference becomes

$$\Delta\mathcal{F}^N = \mathcal{H}_d^1 \sum_{i,j=1}^N M_{ij}^{-1} - N\bar{\epsilon_b} + \frac{1}{2}\ln\left(\det M\right). \tag{11}$$

Similarly to eq. (7), the first term in eq. (11) is the total deformation energy of the receptors and the membrane. The second term is proportional to the effective binding affinity of a single bond and to the total number of bonds within the domain. The last term calculates the fluctuation-induced interactions between the bonds, which interestingly, can be fully decoupled from other contributions. At large bond separations, $d \gg \xi_\parallel$, $\mathcal{H}_d \approx \mathcal{H}_d^1$ and $\Delta\mathcal{F}^N/N \approx \Delta\mathcal{F}^1$.

Phase diagram. To compare domains with the same number of bonds that due to packing, cover different area, we analyze the free energy density $\Delta f \equiv \Delta\mathcal{F}^N/A$ that if negative, signifies stable domains (fig. 3). Three distinct regimes are apparent even though a global minimum is

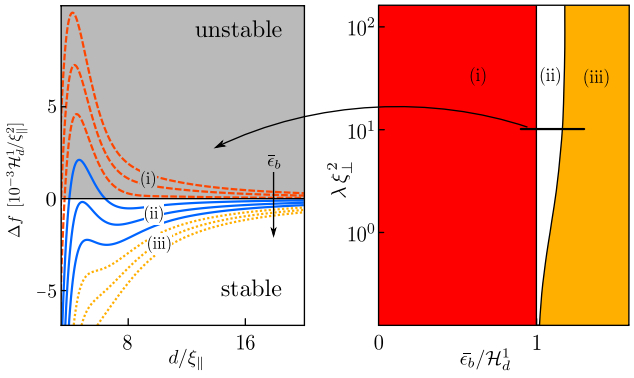

Fig. 3: (Colour on-line) Free energy density as a function of the distance between the bonds for the ch lattice (left), and the respective phase diagram (right). All variables are rendered dimensionless. $\sigma = 0$. For a detailed discussion, see the main text.

found in all cases. This minimum, however, appears at such small d that it could be rendered inaccessible by the finite size of the binders.

In the limit when $d \to \infty$, the $\Delta f \to 0$ limit is approached either from positive values (fig. 3, red dashed lines) or negative values (blue solid and yellow dotted lines), signifying unstable and stable binding, respectively. In the former case (regime (i) in the phase diagram), by a maximum at intermediate distances precedes either stable (regime (ii)) or unstable domains at large distances between the bonds (regime (i)), in which case the domains are stable only close to the boundary minimum. The phase transition line separating the regimes (i) and (ii) is found in the limit of $d \to \infty$ as $\bar{\epsilon_b} = \mathcal{H}_d^1$.

Following the maximum, Δf curves of the region (ii) possess a shallow secondary minimum that is always negative, with locally stable domains. The maximum, on the other hand, penetrates toward positive values of Δf for smaller values of $\bar{\epsilon_b}$, making the domains unstable at intermediate bond separations. At larger values of $\bar{\epsilon_b}$, the maximum may remain with fully negative free energies, hence stable domains can take place for any distances between bonds. This is also true for the regime (iii) in which Δf remains negative, despite its monotonous increase. The border between the regimes (ii) and (iii) is given by the (dis)appearance of a root in the second derivative of the free energy density with respect to the bond distance, and has to be determined numerically.

This phase diagram should be applicable to the situation in which the distance between the bonds is predefined, such as when one of the binder type is immobilized on the substrate [3,6]. The domains should be observable for any distance in which the total free energy density is smaller than zero. Consequently, the commonly observed densely packed domains [16] can be found within our model at low free energies. However, when both receptors and ligands are mobile, the distance between the bonds within the domain becomes a free parameter. In this case, domains should be found only at the distances at which the minima in the total energy density appear. More specifically, apart from the densely packed agglomerates, domains associated with the minimum in the region (ii) at intermediate distances between the bonds, should be seen. Indeed, coexistence between densely packed domains and domains with a sparse distribution of bonds has been observed recently in experiments with mobile ligand-receptor pairs [17,26].

Optimum deformation. – The understanding of the above phase diagram evolves from the analysis of the mean membrane shape and the fluctuations amplitude. They emerge as moments of the height probability distribution $p(h(\mathbf{r}))$ of the membrane within the domain with a fixed bond configuration. The latter is a functional integral over all appropriately weighed realizations of the membrane profile

$$p\left(h(\mathbf{r})\right) \sim \int \mathcal{D}[h'(\mathbf{r})] \exp(-\mathcal{H}[h'(\mathbf{r})])\delta(h'(\mathbf{r}) - h(\mathbf{r})) \sim \exp\left(-\frac{1}{2}\frac{(h(\mathbf{r}) - \langle h(\mathbf{r})\rangle)^2}{\Sigma^2(\mathbf{r})}\right). \tag{12}$$

Because of the quadratic form of eq. (2), $p(h(\mathbf{r}))$ is a Gaussian distribution with the expectation value giving the equilibrium shape

$$\langle h(\mathbf{r})\rangle \equiv h_0 - \frac{(h_0 - l_0)}{\Sigma_0^2/\Sigma^2(\mathbf{r})} \sum_{ij} G(\mathbf{r}_b^i - \mathbf{r}) L_{ij}^{-1}, \tag{13}$$

and variance $\Sigma^2(\mathbf{r})$

$$\Sigma^2(\mathbf{r}) \equiv \frac{\Sigma_0^4}{\Sigma_0^2 + \sum_{ij} G(\mathbf{r}_b^i - \mathbf{r}) L_{ij}^{-1} G(\mathbf{r}_b^j - \mathbf{r})}, \tag{14}$$

being the fluctuation amplitude. Thereby

$$L_{ij} \equiv \frac{\delta_{i,j}}{\lambda} + G(\mathbf{r}_b^i - \mathbf{r}_b^j) - \frac{G(\mathbf{r}_b^i - \mathbf{r}) G(\mathbf{r}_b^j - \mathbf{r})}{\Sigma_0^2}. \tag{15}$$

By setting $N = 0$ and $N = 1$ one recovers the results presented in the previous sections.

The equilibrium shape can be also determined by direct minimization of $\mathcal{H}$ from eq. (2), with constrained extension of bonds, and periodic boundary conditions. Consequently, the effect of the lattice is explicit, and one obtains

$$\langle h(\mathbf{r})\rangle = h_0 - \frac{g(\mathbf{r})}{\phi + 1/\lambda}(h_0 - l_0). \tag{16}$$

Here $\phi \equiv a^{-1} \sum_{\mathbf{q}} (\kappa q^4 + \sigma q^2 + \gamma)^{-1}$ and $g(\mathbf{r}) \equiv a^{-1} \sum_{\mathbf{q}} \cos(\mathbf{qr})(\kappa q^4 + \sigma q^2 + \gamma)^{-1}$, with a being the area of a unit cell. For the squared lattice, the sums run over wave vectors $\mathbf{q} \equiv (q_1, q_2) = (2\pi z_1/d, 2\pi z_2/d)$, with z_1, z_2 being integers, while for the hexagonal lattice, $q_1 = 2\pi(2z_1 + z_2)/(\sqrt{3}d)$ and $q_2 = 2\pi z_2/d$.

Combining the total Hamiltonian, eq. (2), and the equilibrium shape of the membrane, eq. (16), results in the total membrane and spring deformation energy per bond

$$\mathcal{H}_d[\langle h(\mathbf{r})\rangle] = \frac{(h_0 - l_0)^2}{2\left[\phi + 1/\lambda\right]}. \tag{17}$$

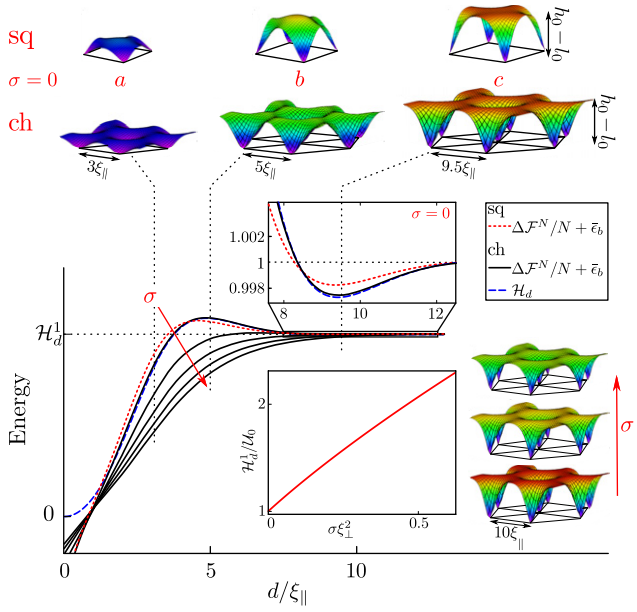

Fig. 4: (Colour on-line) For $\sigma = 0$, stiff bonds, and $\mathcal{H}_d^1(\sigma = 0) = 5.6\ k_BT$, shapes and the free energy per bond $\Delta\mathcal{F}^N/N + \bar{\epsilon_b}$ for the ch and the sq lattice (black solid line and red dotted line, respectively) are displayed. The deformation energy per bond $\mathcal{H}_d$ on the ch lattice is presented with the blue dashed line. Upper inset highlights the minimum at $d = 9.5\xi_\parallel$. For tensions $\sigma = (0.125, 0.25, 0.375, 0.5)\xi_\perp^{-2}$, shapes (ch lattice, $d = 10\xi_\parallel$) and the free energy are shown. All curves are scaled by $\mathcal{H}_d^1$ that depends on the tension as shown in the lower inset.

Thereby, all bonds have the same extension and the membrane is at $h(\mathbf{r}_b^i) = h_b$, for all $\mathbf{r}_b^i$. This result is consistent with the first term in eq. (11) as well as with the 1D energy profile found for a membrane deformed by two infinite cylinders [27], and the potential calculated for the interaction between two bonds [18].

It is instructive to first analyze the case of stiff bonds when $\lambda(h(\mathbf{r}_b) - l_0)^2 \to 0$, and $\mathcal{H}_d$, eq. (17), depends only on the lattice type and d (fig. 4). The optimum deformation energy has a shallow minimum at intermediate distances between the bonds, causing the minimum in the free energy density. This minimum can be understood by analyzing the shape of the membrane. Namely, when the bonds are far apart, they act as isolated bonds producing a local deformation in which the membrane, prior to flattening into the minimum of the nonspecific potential at h_0, overshoots h_0 (fig. 4). As the bonds come closer, the overshoots become shared by neighboring bonds, decreasing the overall cost in bending. When the overshoots fully overlap, the shallow minimum appears in Δf (shapes c in fig. 4). Bringing the bonds even closer, again increases the bending energy providing an energy barrier (shapes b). When the overshoots disappear the membrane starts to flatten between the bonds. Consequently, the energy slides towards a boundary minimum $\mathcal{H}_d \to 0$, as $d \to 0$. With the increasing tension (at constant γ) the overshoots in the shape become less pronounced, but the cost for deforming the membrane rise (fig. 4). The secondary minimum

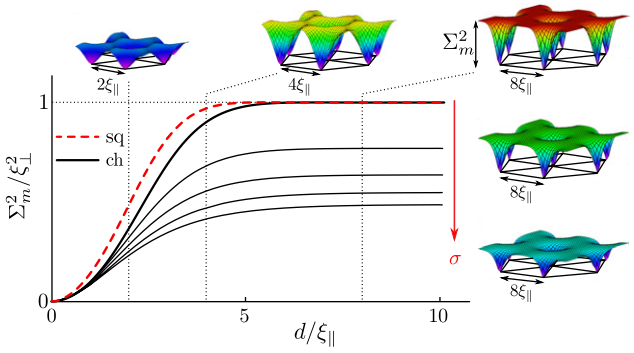

Fig. 5: (Colour on-line) Maximal fluctuation amplitude for the ch and sq lattice (black solid line and red dashed lines, respectively). Fluctuation maps at $\sigma = 0$ (horizontal array), and finite tensions at $d = 8\xi_\parallel$ (vertical array) are also shown. Parameters as in fig. 4.

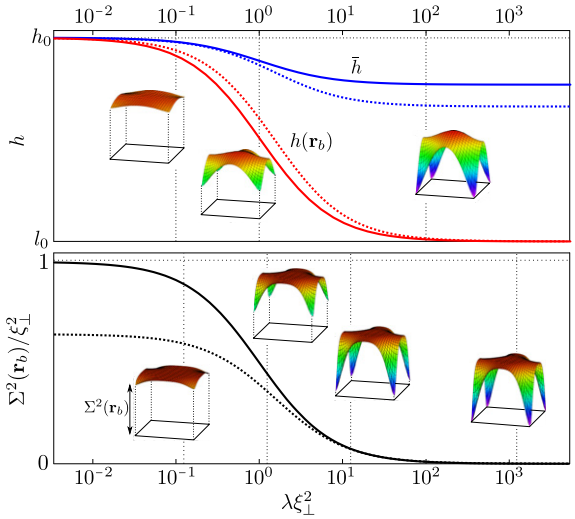

Fig. 6: (Colour on-line) Top: average height of the membrane $\bar{h}$ (blue) and the extension of the bonds (red) as a function of λ and the corresponding shapes at $d = 6\xi_\parallel$. Bottom: the fluctuation amplitude of a bond as a function of λ. Full and dotted lines are obtained with $\sigma = 0$ and $\sigma = 1/(4\xi_\perp^2)$, respectively.

becomes shallower and appears at larger d, shrinking the parameter space for the phase (ii).

In the limit of $d \to 0$, flattening of the membrane caused by the large density of bonds makes both the deformation energy and fluctuations insensitive to the tension (fig. 5). If, on the other hand, $d \to \infty$, bonds on any lattice become independent of one another and the maximal fluctuation amplitude Σ_m^2 of the domain fluctuation profile $\Sigma(\mathbf{r})^2$, takes the limit $\Sigma_m^2 \to \Sigma_0^2$.

Decreasing the spring constant λ transmits the deformation from the membrane to the receptors, again affecting the size of the region (ii) in the phase diagram. For very soft bonds ($\lambda \to 0$), the entire deformation is stored in the springs and ($h(\mathbf{r}_b) \to h_0$). In this case, the membrane is in average flat as evidenced by the mean membrane height $\bar{h}$ within the domain and the bond extensions (fig. 6).

Furthermore, in this regime, the membrane fluctuates as an unbound one, irrespectively of d.

Conclusions. – We analyzed the properties of large adhesion domains forming between a membrane and a flat substrate, when the ligand-receptor adhesion competes with the nonspecific adhesion. While some aspects of our model have been investigated previously [18,20], our work provides a unifying framework within which the stability of the domains can be fully explored. Our first conclusion is that the energetics of the domains forming on different lattices including the simple hexagonal one (data not shown) is qualitatively the same. This suggests that the modeling on commonly used sq lattices [24,28] will well reproduce the behavior of domains that most likely form on the ch lattice. This result emerges from the decoupling of the entropic free energy contributions associated with the correlations between bonds and contributions of individual bonds. At room temperatures, the correlation contributions seem to be small and have no qualitative effects on the phase diagram. However, on a level of individual bonds, the effect of fluctuations may be significant resulting in considerable differences between the intrinsic and the effective binding affinity. Furthermore, another important result is the evaluation of several regimes in which domains are stable. Consequently, our model provides a physical explanation for the recently observed coexistence of densely packed and sparse domains of bonds.

While we have demonstrated the power of our approach with a very simple model of receptors and of the bond potential, the quadratic nature of the membrane deformation energy allows for stability analysis of domains formed from bonds with a very wide range of potentials. Such extensions of the model may be important for quantitative comparison with measured data, which is a task that may be challenging, both from experimental and theoretical points of view. However, in order to fully comprehend the stability of adhesion domains, this comparison needs to be performed. In this light, the current work could become the necessary foundation for the understanding of the stability of domains in cellular and mimetic systems.

* * *

We thank K. Sengupta and S. Fenz for helpful discussions. US, A-SS and TB acknowledge the support from DFG-SE 1119/2-1.

REFERENCES

[1] Geiger B., Spatz J. P. and Bershadsky A. D., *Nat. Rev. Mol. Cell Biol.*, **10** (2009) 21.
[2] Ranzinger J. *et al.*, *Nano Lett.*, **9** (2009) 4240.
[3] Deeg J. A. *et al.*, *Nano Lett.*, **11** (2011) 1469.
[4] Liu A. P. and Fletcher D. A., *Nat. Rev. Mol. Cell Biol.*, **10** (2009) 644.
[5] Smith A.-S. and Sackmann E., *ChemPhysChem*, **10** (2009) 66.
[6] Sackmann E. and Bruinsma R. F., *ChemPhysChem*, **3** (2002) 262; Lorz B. *et al.*, *Langmuir*, **23** (2007) 12293.
[7] Raudino A. and Pannuzzo M., *J. Chem. Phys.*, **132** (2010) 045103.
[8] Smith A.-S. and Seifert U., *Soft Matter*, **3** (2007) 275.
[9] Speck T., Reister E. and Seifert U., *Phys. Rev. E*, **82** (2010) 021923; Farago O., *Phys. Rev. E*, **78** (2008) 051919.
[10] Reister E. *et al.*, *New J. Phys.*, **13** (2011) 025003.
[11] Krobath H., Rozycki B., Lipowsky R. and Weikl T. R., *PLoS One*, **6** (2011) 23284.
[12] Krobath H., Schütz G. J., Lipowsky R. and Weikl T. R., *EPL*, **78** (2007) 38003.
[13] Fenz S. F. *et al.*, *Adv. Mater.*, **23** (2011) 2622.
[14] Lin L. C.-L., Groves J. T. and Brown F. L. H., *Biophys. J.*, **91** (2006) 3600.
[15] Limozin L. and Sengupta K., *ChemPhysChem*, **10** (2009) 2752; Monzel C., Fenz S. F., Merkel R. and Sengupta K., *ChemPhysChem*, **10** (2009) 2828.
[16] Smith A.-S., Fenz S. F. and Sengupta K., *EPL*, **89** (2010) 28003.
[17] Smith A.-S. *et al.*, *Proc. Natl. Acad. Sci. U.S.A.*, **105** (2008) 6906.
[18] Bruinsma R., Behrisch A. and Sackmann E., *Phys. Rev. E*, **61** (2000) 4253.
[19] Komura S. and Andelman D., *Eur. Phys. J. E*, **3** (2000) 259.
[20] Weikl T. R., Andelman D., Komura S. and Lipowsky R., *Eur. Phys. J. B*, **8** (2002) 59.
[21] Weikl T. R. *et al.*, *Soft Matter*, **5** (2009) 3273.
[22] Raedler J. O., Feder T. J., Strey H. H. and Sackmann E., *Phys. Rev. E*, **51** (1995) 4523.
[23] Breidenich M., Netz R. R. and Lipowsky R., *Eur. Phys. J. E*, **5** (2001) 403.
[24] Lipowsky R., in *Structure and Dynamics of Membranes*, edited by Lipowsky R. and Sackmann E. (Elsevier) 1995, Chapt. 11.
[25] Bruinsma R., Goulian M. and Pincus P., *Biophys. J.*, **67** (1994) 746.
[26] Fenz S. F., Smith A.-S., Merkel R. and Sengupta K., *Soft Matter*, **7** (2011) 952.
[27] Weikl T. R., *Eur. Phys. J. E*, **12** (2003) 265.
[28] Merath R.-J. and Seifert U., *Phys. Rev. E*, **73** (2006) 010401.

P5

A model for spectral properties of a pinned membrane

A model for spectral properties of a pinned membrane

D. Schmidt[1,2], U. Seifert[2], and A.-S. Smith[1,3]

[1] Institut für Theoretische Physik, Department für Physik, and the Excellence Cluster: Engineering of Advanced Materials, Friedrich Alexander Universität Erlangen-Nürnberg, 91058 Erlangen, Germany
[2] II. Institut für Theoretische Physik, Fakultät 8: Mathematik und Physik, Universität Stuttgart, 70550 Stuttgart, Germany
[3] Division of Physical Chemsitry, Ruđer Bošković Institute, 10000 Zagreb, Croatia

in preparation (2016)

ABSTRACT Biological membranes connect to adjacent cells or the extra-cellular matrix with the help of adhesion proteins forming bonds. These bonds transmit stresses across cell boundaries and pin the membrane locally which affects the mechanics of the thermally excited membrane. Here, we investigate the static and dynamic mechanical properties of a membrane upon formation of a single bond in a minimal model system by theoretical means and compare our results to detailed simulations of the fluctuating membrane. We calculate the eigenmodes of the pinned membrane to determine its static properties and show that the pinning can be treated by an effective potential . For the membrane dynamics, we introduce for the pinned membrane a first order correction to the damping coefficients of the unbound membrane and obtain membrane dynamics that match the simulations. As a third result, we show that membrane transmitted correlations between different bonds can be fully treated in a local description. With the results for the static and dynamic properties of a pinned membrane, the effect of the membrane-anchored adhesion protein on the mechanics of the membrane is fully understood.

A model for spectral properties of a pinned membrane

Daniel Schmidt,[1,2] Udo Seifert,[2] and Ana-Sunčana Smith[1,3,*]

[1] *Institut für Theoretische Physik and Cluster of Excellence: Engineering of Advanced Materials, Friedrich Alexander Universität Erlangen-Nürnberg, 91052 Erlangen, Germany*

[2] *II. Institut für Theoretische Physik, Universität Stuttgart, 70569 Stuttgart, Germany*

[3] *Institut Ruđer Bošković, 10000 Zagreb, Croatia*

(Dated: April 11, 2016)

Biological membranes connect to adjacent cells or the extra-cellular matrix with the help of adhesion proteins forming bonds. These bonds transmit stresses across cell boundaries and pin the membrane locally which affects the mechanics of the thermally excited membrane. Here, we investigate the static and dynamic mechanical properties of a membrane upon formation of a single bond in a minimal model system by theoretical means and compare our results to detailed simulations of the fluctuating membrane. We calculate the eigenmodes of the pinned membrane to determine its static properties and show that the pinning can be treated by an effective potential . For the membrane dynamics, we introduce for the pinned membrane a first order correction to the damping coefficients of the unbound membrane and obtain membrane dynamics that match the simulations. As a third result, we show that membrane transmitted correlations between different bonds can be fully treated in a local description. With the results for the static and dynamic properties of a pinned membrane, the effect of the membrane-anchored adhesion protein on the mechanics of the membrane is fully understood.

I. INTRODUCTION

Membrane-anchored proteins play a crucial role in biological processes transmitting information or small molecules between different membrane-separated compartments or cells [1]. Some membrane-anchored proteins such as integrins or cadherins transfer mechanical stresses [2, 3]. These proteins are involved in interconnecting cells and the formation of tissue and were commonly used in cell mimetic models [4–6]. Mechanical stresses are also found at the red blood cell plasma membrane that is connected to the underlying spectrin cytoskeleton by ankyrin linkers to stabilize the cell membrane and which then provides interesting mechanical interplay [7]. Many of these membrane-anchored proteins are studied intensively on a molecular level, however, how their function couples to the membrane fluctuations and how their activity in turn affects the membrane is poorly understood.

Recently, the first issue how the membrane affects binding equilibrium and kinetics of a bond was addressed from various angles. With respect to binding equilibrium, it was shown that unstable individual bonds can be stabilized by membrane transmitted correlations between neighbouring bonds and, for biological relevant parameters, few bonds packed closely together form a stable nucleation seed [8]. Binding kinetics of membrane-anchored proteins, confined to two dimensions, were shown to behave substantially different compared to the same protein in solution [9–11]. Additionally, reaction rates of membrane-anchored proteins depend sensitively on, e.g., the local separation and roughness of the membranes [8, 12–14]. On the one hand a closer membrane distance enhances binding kinetics of a bond, suppression of membrane fluctuations, on the other hand, decrease the probability of bond formation. Thus, formation of a bond in the vicinity of an existing bond can either be increased or decreased depending on the actual system. Consequently, growth of adhesion domains from a stable nucleation seed depends not only on protein parameters but also on properties of the membrane [15]. However, a microscopic minimal model capturing mechanic properties of the bond and resembling correct binding equilibrium and kinetics is still missing.

From the membrane point of view, it was shown that the mean membrane shape and roughness depend on the bond density [16–19]. However, understanding of dynamics of pinned membranes is not yet achieved due to a sophisticated hydrodynamic interplay between the membrane, the bond and the surrounding fluid. First steps to understanding this hydrodynamic interplay were made for pinned but discretized membranes by simulations [20, 21] and by numerically calculating the fluctuation spectrum [22–24]. On the other hand, analytically modelling revealed the dynamics for unbound membranes by solving the hydrodynamic interactions for each fluctuation modes individually [25]. However, pinning the membrane by a bond couples all fluctuation modes making the analytical modelling excessively difficult.

In this paper, we calculate the eigenmodes of the pinned membrane and first recover the known static properties [19, 24, 26–28] of the fluctuating membrane. We show that these results can be resembled in a homogenized system, where the pinning is treated by an effective potential. For the dynamics we show that pinning has significant effects in the low frequency regime where hydrodynamic interactions dependent on the properties of the pinning. To account for this effect, we introduce a

* author to whom correspondence should be addressed: smith@physik.uni-erlangen.de

first order correction to the damping coefficients. With this improvement, we obtain a power spectral density that matches the simulations. In combination, the results for the statics and dynamics of the pinned membrane unveil a complete picture of the effect of the membrane-anchored protein on the mechanics of the membrane.

II. MODEL

Our minimal model for studying the effect of a bond on the membrane consists of a permanent bond and a membrane in continuum description, omitting the molecular complexity of both the adhesion protein and the biological membrane (for a sketch see Fig. 1). We describe the membrane profile mathematically in Monge gauge, i.e., by a fluctuating surface with height $h(\mathbf{x})$ above a solid scaffold at lateral position $\mathbf{x}$. The membrane is fully characterised by two mechanical parameters, the bending rigidity κ and the tension σ, and fluctuates in a harmonic membrane-scaffold interaction potential with strength γ centred at height h_0. The adhesion protein, from now on called receptor and fixed at lateral position $\mathbf{x}_0$, is modelled by a harmonic spring with elastic constant λ and rest length l_0. In the biological reference system, the bond can form and break, however, to study the effect of a bond on mechanic properties of the membrane the bond is permanently formed.

For our minimal model of a pinned membrane, the Hamiltonian is build by the sum of the Helfrich-Hamiltonian for the membrane in Monge gauge and a harmonic spring for the receptor

$$\mathcal{H} = \int_A \mathrm{d}\mathbf{x} \left[\frac{\kappa}{2}\left(\nabla^2 h(\mathbf{x})\right)^2 + \frac{\sigma}{2}\left(\nabla h(\mathbf{x})\right)^2 + \frac{\gamma}{2}\left(h(\mathbf{x}) - h_0\right)^2\right] + \frac{\lambda}{2}\left(h(\mathbf{x}_0) - l_0\right)^2 + \epsilon_b^0, \quad (1)$$

where we use the intrinsic binding affinity ϵ_b^0 for formation of the bond. The pinning implies for the receptor synchronized fluctuations with the membrane, i.e., the elongation of the receptor coincides with the instantaneous membrane height h at the receptor position $\mathbf{x}_0$. Here and throughout the paper, we set the energy scale $k_\mathrm{B}T \equiv 1$, with Boltzmann constant k_B and absolute temperature T. From the Hamiltonian and its variations, we find all mechanic properties of the pinned membrane imposing analytical and numerical methods as well as simulations. In the simulations, the membrane profile follows Langevin dynamics by numerical integration of all systematic and stochastic forces, as described previously in great detail [12].

The Hamiltonian is also suitable for studying a domain of N bonds placed at lateral positions $\mathbf{x}_1, ..., \mathbf{x}_N$ by adding to the Hamiltonian a harmonic spring term for each bond and N times the intrinsic binding affinity ϵ_b^0. It is worth noting that the harmonic type of the Hamiltonian reaches its limits if the membrane comes close to the substrate [19].

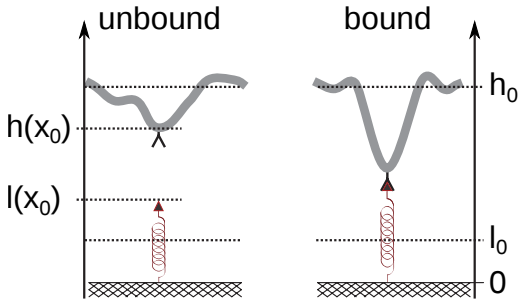

Figure 1. Sketch of the model system in the unbound state (left) and in the bound state (right) introducing the relevant heights. For more details see explanations in the main text.

III. A PINNED MEMBRANE WITHOUT MEAN MEMBRANE DEFORMATIONS

In this section, we pin the membrane by a receptor with a rest length $l_0 = h_0$ (see fig. 2a), such that the mean membrane profile is unaffected by the receptor, $\langle h(\mathbf{x})\rangle = h_0$. Nonetheless, fluctuations and correlation functions are altered by the pinning. Here, we first establish eigenmodes of the pinned membrane which we then use to calculate static and dynamic properties of the membrane.

A. Eigenmodes of a pinned membrane

In order to calculate the membrane fluctuations and the correlation functions, the membrane is expanded in eigenmodes, which are, for an unbound membrane, plane waves. However, pinning the membrane by a bond couples all Fourier modes. To keep the modes decoupled, we expand the instantaneous membrane profile

$$h(\mathbf{x}) = \sum_{q,m} h_{q,m}\psi_{q,m}(\mathbf{x}) \quad (2)$$

in a basis set which is constructed from eigenmodes $\psi_{q,m}(\mathbf{x})$ to the eigenvalue equation

$$\left[\kappa\nabla^4 - \sigma\nabla^2 + \gamma + \lambda\delta(\mathbf{x})\right]\psi_{q,m}(\mathbf{x}) = E_{q,m}\psi_{q,m}(\mathbf{x}), \quad (3)$$

derived from the Hamiltonian, eq. (1). Here we use the Dirac $\delta(\mathbf{x})$-function to pin the receptor at position $\mathbf{x}_0$.

The system obeys radial symmetry with respect to the pinning site. Thus, we write the eigenmodes as a product of axial and radial terms,

$$\psi_{q,m}(\mathbf{x}) = R_{q,m}(r)\mathrm{e}^{im\phi}, \quad (4)$$

with radial coordinates (r, ϕ) for the lateral position $\mathbf{x}$.

We solve the eigenvalue equations by imposing the following boundary conditions: the integral of the eigenvalue equation vanishes over an infinitesimal small circle centred at the receptor position and $R_{q,m}(r)$ stays finite for the limits $r \to 0$ and $r \to \infty$. solutions to the eigenvalue equation are found analytically for a tensionless membrane with the help of Bessel functions. Thus, we will restrict the section of the pinned membrane to a tensionless membrane and extend our model in the next section to tense membranes. We find the eigenmodes of a tensionless membrane

$$R_{q,0}(r) = \mathcal{N}_{q,0}\left[J_0(qr) + \frac{\lambda}{8\kappa q^2}\left\{Y_0(qr) + \frac{2}{\pi}K_0(qr)\right\}\right], \tag{5}$$

and

$$R_{q,m}(r) = \mathcal{N}_{q,m}J_m(qr) \qquad \text{for } m \neq 0, \tag{6}$$

using the Bessel functions J_m and Y_0 of the first and second kind, respectively, and the modified Bessel function K_0 of the second kind. The normalisation $\mathcal{N}_{q,m}$ is given in the supporting information for each m. The stiffness λ affects only the eigenmode $m = 0$. For vanishing λ the pinned membrane becomes unbound and all the eigenmodes are given by the Bessel functions $J_m(r)$ for all m. The latter is, basically, the equivalent to a basis set constructed from plane waves in radial geometry.

With full knowledge of the basis set $\{\psi_{q,m}(\mathbf{r})\}$ for a pinned membrane and the energy of each mode,

$$E_{q,m} = \kappa q^4 + \gamma, \tag{7}$$

we find easily the fluctuation amplitude as well as lateral correlation functions.

B. Fluctuation amplitude

According to the equipartition theorem, each mode q, m of the membrane profile is associated with a mean thermal energy $k_BT/2$. Thus, the fluctuation amplitude $\langle\Delta h^2(\mathbf{x})\rangle_\lambda$ at position $\mathbf{x}$ for the membrane pinned by a receptor of stiffness λ is given by

$$\langle\Delta h^2(\mathbf{x})\rangle_\lambda = \sum_{q,m}\frac{1}{E_{q,m}}|\psi_{q,m}(\mathbf{x})|^2. \tag{8}$$

Imposing $E_{q,m}$ and the eigenmodes $\psi_{q,m}(\mathbf{x})$ of the pinned membrane, we find numerically the fluctuation amplitude of a pinned membrane (see Fig. 2b).

At the position of the pinning site, all Bessel functions for $m \neq 0$ vanish and, thus, the fluctuation amplitude is recovered analytically

$$\begin{aligned}\langle\Delta h^2(\mathbf{0})\rangle_\lambda &= \frac{1}{2\pi}\int_0^\infty \mathrm{d}q\ \frac{q}{\kappa q^4 + \gamma}\left[1 + \left(\frac{\lambda}{8\kappa q^2}\right)^2\right]^{-1} \\ &= \frac{1}{8\sqrt{\kappa\gamma} + \lambda} \equiv \frac{1}{\lambda_m + \lambda}.\end{aligned} \tag{9}$$

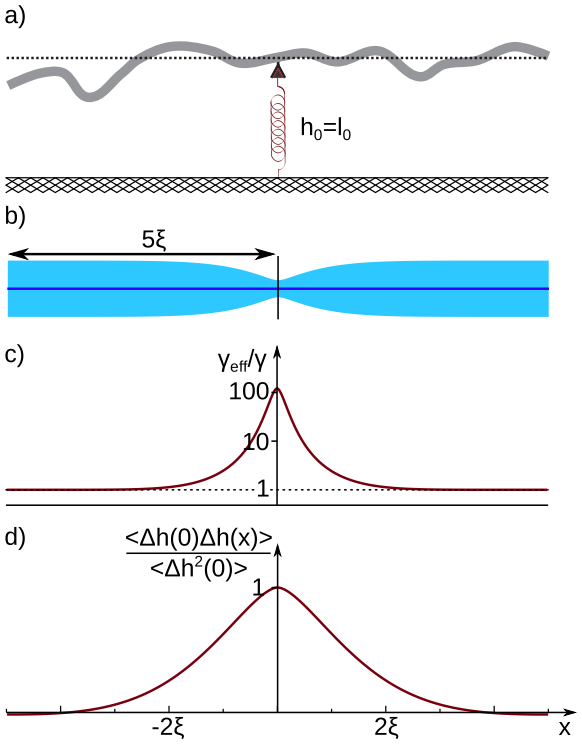

Figure 2. a) Sketch of the membrane fluctuating around its potential minimum (dashed line) being pinned at the lateral position of the receptor to the height of the potential minimum. b) Profile (thick blue line) and fluctuation amplitude (light blue area) for a tensionless membrane pinned with stiffness $\lambda = 10\lambda_m$. c) For the membrane shown in b) the effective potential γ_{eff} is shown as a function of the position. d) The lateral correlation function measured from the pinning site for the same membrane. The lateral correlation length is given by $\xi_\parallel \equiv \sqrt[4]{\kappa/\gamma}$.

Here, we transformed the remaining sum of eq. (8) into an integral. Interestingly, the fluctuation amplitude at the pinning site is given by the inverse of the sum of the elastic constants of the membrane $\lambda_m \equiv 8\sqrt{\kappa\gamma}$ and the receptor λ which is in an homogenized description recognized as the fluctuation amplitude of two parallel springs with elastic constants λ_m and λ.

The fluctuation amplitude of the pinned membrane agrees numerically with previous results [8, 19] and analytical agreement is found, after some algebra, for the position of the pinning site.

C. Effective potential of the homogenized system

In the spirit of an effective spring constant for combining two harmonic springs, we introduce an effective interaction potential γ_{eff} including the effect of the receptor onto the membrane fluctuation amplitude. The fluctuation amplitude for a pinned membrane depends of the distance to the receptor and, thus, the effective in-

teraction potential is a function of the distance to the receptor, too. We define the strength of the effective interaction potential $\gamma_{\text{eff}}(\mathbf{x})$ such that the fluctuation amplitude in the effective description coincides with the fluctuation amplitude for the pinned membrane. Solving for γ_{eff} yields

$$\gamma_{\text{eff}}(\mathbf{x}) = \frac{1}{\kappa}\left(\frac{1}{8\langle\Delta h^2(\mathbf{x})\rangle_\lambda}\right)^2 = \gamma\left(\frac{\langle\Delta h^2\rangle}{\langle\Delta h^2(\mathbf{x})\rangle_\lambda}\right)^2, \quad (10)$$

using the fluctuation amplitude $\langle\Delta h^2\rangle \equiv 1/8\sqrt{\kappa\gamma}$ of the unbound membrane. In Fig. 2c, we show the effective potential strength as a function of the distance from the pinning site, eq. (10). We find the strength of the effective interaction potential

$$\gamma^0_{\text{eff}} = \gamma\left(1 + \frac{\lambda}{\lambda_m}\right)^2. \quad (11)$$

analytically for restraining for the pinning site.

D. Lateral correlation function

The lateral correlation function for the unbound membrane has been discussed in eq. (SI-2) in the supporting information to this article. For a pinned membrane, the lateral correlation function is calculated straightforward from the eigenmodes and the energy per mode,

$$\langle\Delta h(\mathbf{x}_1)\Delta h(\mathbf{x}_2)\rangle = \sum_{q,m}\frac{1}{E_{q,m}}|\psi_{q,m}(\mathbf{x}_1)\psi_{q,m}(\mathbf{x}_2)|. \quad (12)$$

For the special case of $\mathbf{x}_1 = \mathbf{x}_0$, we show the lateral correlation function in Fig. 2d. We find, numerically, the lateral correlation length of the pinned membrane identical to the correlation length of the unbound membrane, given by $\xi = \sqrt[4]{\kappa/\gamma}$ in the tensionless membrane [29]. However, the amplitude of the lateral correlation function changes due to pinning to the value of the fluctuation amplitude, eq. (9). With the results for the lateral correlation function, all static mechanic properties of the pinned membrane have been obtained with results identical to previous findings.

E. Temporal auto-correlation function and power spectral density

For the unbound membrane, the temporal correlations are found by explicitly solving Stokes equations for the dynamics of the membrane's surrounding fluids. Adding a pinning site to the system breaks translational symmetry and a rigorous derivation of the temporal correlations by determining the damping coefficients via Stokes equations is inaccessible. We address the issue with the help of Langevin simulations of the membrane-receptor system, using a simulation scheme described previously in great detail [12]. From the simulation, we obtain the instantaneous membrane height at the position of the receptor and use the height trajectory to calculate the power spectral density. We find the general form of the power spectral density preserved for the pinned membrane compared to the unbound membrane. In detail, the power spectral density of the pinned membrane is a λ-dependent constant in the low frequency regime and decays algebraically with $\omega^{-5/3}$ in the high frequency regime (see Fig. 3). While the high frequency regime is completely independent of λ, the constant in the low frequency regime decreases monotonically with λ (see Fig. 4). Moreover, the low frequency limit of the power spectral density simulated for three orders of magnitude in γ fall on a single master curve. Thereby, we rescale both, the power spectral density by the respective power spectral density of the unbound membrane and the receptor stiffness λ with the elastic constant λ_m of the membrane (see Fig. 4). This points towards a systematic effect of the pinning.

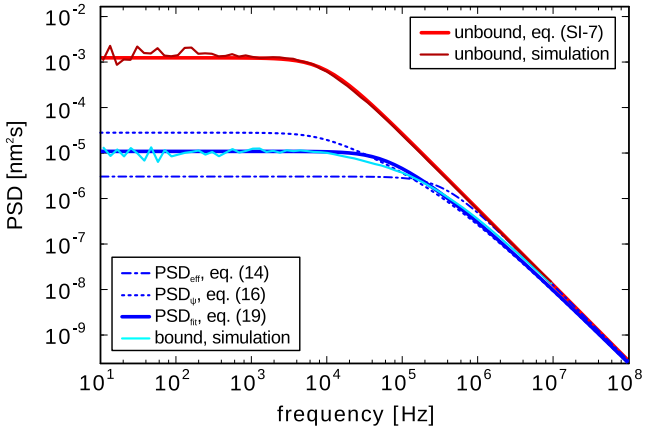

Figure 3. Power spectral density of an unbound membrane (red) and a bound membrane (blue) measured at the position of the bond. The solid, thin curves show simulations, agreeing with the analytical approximations (solid, thick curves). The dashed curve shows the power spectral density accordingly to eq. (**??**) with clear deviations from the simulations. Parameters used are $\kappa = 20\,\text{k}_\text{B}\text{T}$, $\sigma = 0$, $\gamma = 1.29 \cdot 10^9\,\text{J/m}^4$, $\lambda = 8.28 \cdot 10^{-4}\,\text{J/m}^2$, and $\eta = 1\,\text{mPas}$.

In the following, we will present three different approaches to find an effective description of the spectral properties for the receptor pinned to the membrane.

In the first approach, we expand the instantaneous membrane profile in plane waves, $h(\mathbf{x}) = \sum_\mathbf{k}\tilde{h}_\mathbf{k}\text{e}^{i\mathbf{kr}}$, and assume that all effects of the pinned membrane are described by a single parameter, the effective interaction potential γ_{eff} which we identified in eq. (11). Consequently, the Langevin equation for the membrane dynamics is given by [**?**]

$$\partial_t\tilde{h}_\mathbf{k}(t) = -\Lambda_\mathbf{k}(\kappa k^4 + \gamma_{\text{eff}})\tilde{h}_\mathbf{k}(t) + \xi_\mathbf{k}. \quad (13)$$

Here, we use the Oseen tensor $\Lambda_\mathbf{k}$ and the stochastic

noise $\xi_{\mathbf{k}}$. By the fluctuation-dissipation theorem, the noise correlations $\langle \xi_{\mathbf{k}} \xi_{\mathbf{k}'} \rangle$ are related to the Oseen tensor, while we assume the latter unaffected by the pinning, i. e. $\Lambda_{\mathbf{k}} = (4\eta k)^{-1}$ [**?**]. Form the Langevin equation, we find the effective power spectral density $\langle |h(\omega)|^2 \rangle_{\text{eff}}$ analytically yielding

$$\langle |h(\omega)|^2 \rangle_{\text{eff}} = \frac{4\eta}{\pi} \int_0^\infty \mathrm{d}k \; \frac{k^2}{(4\eta k \omega)^2 + (\kappa k^4 + \gamma_{\text{eff}})^2}. \quad (14)$$

Comparing $\langle |h(\omega)|^2 \rangle_{\text{eff}}$ with simulation results shows an excellent agreement in the high frequency regime and the low frequency limit $\langle |h(0)|^2 \rangle_{\text{eff}}$ decreases monotonically with λ. However, the effect of the receptor stiffness λ in the low frequency regime is over-estimated (see dash-dotted curves in Figs. 3 and 4). Thus, the effective description of the receptor by γ_{eff} captures the main characteristics but is insufficient for an effective description of the pinning on temporal correlations.

In a second approach, we apply the basis set $\{\psi_{q,m}(\mathbf{r})\}$ and solve the corresponding Langevin equation for the fluctuating membrane profile $h(\mathbf{r},t) = \sum_{q,m} h_{q,m}(t)\psi_{q,m}(\mathbf{r})$. However, the Langevin equation for the expansion coefficients $h_{q,m}(t)$ is coupled due to the membrane pinning, making it impossible to recall to power spectral density. We overcome this hurdle by approximating the off-diagonal elements of the Oseen tensor $\Lambda_{q,m}$ to be negligible which decouples the Langevin equation yielding

$$\partial_t h_{q,m}(t) = -\Lambda_{q,m}(\kappa q^4 + \gamma) h_{q,m}(t) + \xi_{q,m}. \quad (15)$$

We approximate the Oseen tensor $\Lambda_{q,m}$ with the Oseen tensor of the unbound membrane $\Lambda_{\mathbf{k}}$, replacing $|\mathbf{k}|$ with q. We solve eq. (15) analytically and obtain for the power spectral density

$$\langle |h(\omega)|^2 \rangle_{\psi} = \sum_{q,m} \frac{2\Lambda_{q,m}}{\omega^2 + \Lambda_{q,m}^2(\kappa q^4 + \gamma)^2} |\psi_{q,m}(\mathbf{r})|^2 \quad (16)$$

$$= \frac{4\eta}{\pi} \int_0^\infty \mathrm{d}q \; \frac{q^2}{(4\eta q \omega)^2 + (\kappa q^4 + \gamma)^2} \frac{1}{1 + \left(\frac{\lambda}{8\kappa q^2}\right)^2}.$$

Comparing the so harsh approximated power spectral density with the power spectral density obtained from simulations reveals some remarkable successes. First, the high frequency regime of eq. (16) agrees perfectly with both, the simulations and the analytical results for the unbound membrane (Fig. 3) and, second, the low frequency limit of the power spectral density decreases monotonically with λ. However, the approximations made in eq. (16) under-estimate the effect of the receptor (see dashed, blue curves in Figs. 3 and 4). Consequently, the harsh approximation neglecting all off-diagonal term in the Oseen tensor is overstretched.

In our third approach, we build on the previous attempt and expand the membrane again in the basis set

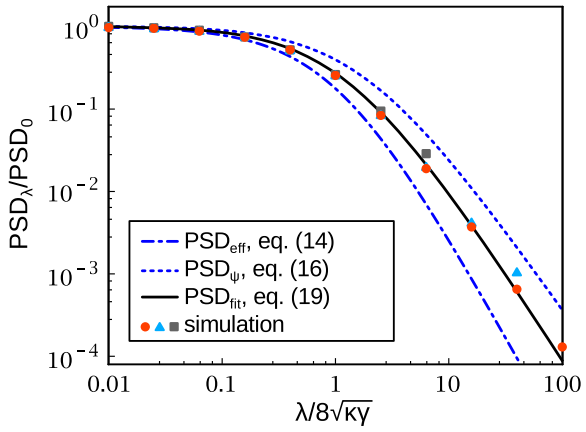

Figure 4. Power spectral density in the low frequency limit as a function of the receptor stiffness λ. Simulations for three different interaction potentials $\gamma = 1.29{\cdot}10^9 \,..1.29{\cdot}10^{11}$ J/m^4 are shown as red, blue and grey dots. The power spectral density is rescaled with the low frequency limit of the power spectral density of an unbound membrane, eq. (**??**), for the respective interaction potential. The solid curve shows the empirically motivated power spectral density whereas the dashed and dash-dotted curves are related to the local friction regime and the naïve approach, respectively (see main text for more details).

of eigenmodes. We improve the approximations of the second approach by replacing the Oseen tensor $\Lambda_{q,m}$ in eq. (15) with a diagonal Oseen tensor $\tilde{\Lambda}_{q,m}$ that accounts effectively for all off-diagonal elements. To maintain the excellent agreement with simulations of the second approach in the high-frequency regime, we introduce in $\tilde{\Lambda}_{q,m}$ corrections of the form λ/λ_m compared to the Oseen tensor $\Lambda_{q,m}$ of the unbound membrane. Each mode q,m of the corrections in $\tilde{\Lambda}_{q,m}$ is weighed with the respective energy $E_{q,m}$ (normalized by γ). In total, the corrections to the Oseen tensor result in

$$\tilde{\Lambda}_{q,m} = \frac{1}{4\eta q}\left(1 + \frac{\lambda}{\lambda_m}\frac{\gamma}{\kappa q^4 + \gamma}\right). \quad (17)$$

With this Oseen tensor, the power spectral density is found analytically and resembles the form of eq. (16) but replaces $\Lambda_{q,m}$ with $\tilde{\Lambda}_{q,m}$. After some re-arranging and introducing the notation

$$\chi = \gamma\left(1 + \frac{\lambda}{\lambda_m}\right) \quad (18)$$

the power spectral density becomes

$$\langle |h(\omega)|^2 \rangle_{\text{fit}} = \quad (19)$$

$$= \frac{4\eta}{\pi} \int_0^\infty \mathrm{d}q \; \frac{\kappa q^4 + \chi}{\kappa q^4 + \gamma} \frac{q^2}{(4\eta q \omega)^2 + (\kappa q^4 + \chi)^2} \frac{1}{1 + \left(\frac{\lambda}{8\kappa q^2}\right)^2}.$$

The power spectral density has an excellent agreement with simulation results in the high frequency regime by

construction. In the low frequency limit, we find a convincing agreement with the simulations over more than four orders of magnitude in λ/λ_m and for three orders of magnitude in γ, displayed in Fig. 4. The few points of the simulation deviating from eq. (19) arise from very stiff receptors causing extremely small fluctuations of the membrane that reached the numerical resolution limit in the simulation.

For eq. (19), we built on the findings of the second approach expanding the membrane in eigenmodes. Alternatively, we could expand the membrane in plane waves and impose the effective potential strength γ_{eff}. With the modified Oseen tensor in eq. (17), the power spectral density becomes by expanding in plane waves and replacing γ by γ_{eff}

$$\langle |h(\omega)|^2 \rangle_{\text{fit2}} = \tag{20}$$
$$= \frac{4\eta}{\pi} \int_0^\infty \mathrm{d}q \, \frac{\kappa q^4 + \chi}{\kappa q^4 + \gamma_{\text{eff}}} \frac{q^2}{(4\eta q \omega)^2 + (\kappa q^4 + \chi)^2}.$$

The agreement with the simulation is, again, very convincing and numerically very close to eq. (19). However, despite the persuasive numerical evidence, analytical agreement between eqs. (19) and (20) is not achieved.

Describing the power spectral density of the pinned membrane in the form of eq. (19) is a phenomenological finding with quantitative justification due to comparison with simulations. A calculation of the power spectral density for the membrane including the receptor based on fundamental grounds is, to our knowledge, not feasible. However, with the finding of an effective Oseen tensor eq. (17) a hint towards a possibly more stringent determination of the temporal correlations is given.

IV. PERMANENT BOND

In this section, we will extend our knowledge of the pinned membrane to effects arising due to a receptor deforming the mean membrane profile (for a sketch see Fig. 5). Thereby, the bond is, again, permanently bound to the membrane and fluctuations of the membrane have to coincide with fluctuations of the receptor. We will focus on the effect of a single receptor attached to the membrane, adjusting membrane measures as mean membrane profile, fluctuation map, and correlation functions.

A. Mode coupling for expansion in plane waves

The permanent bond deforms the mean membrane profile. However, the membrane fluctuations and correlation functions depend on the second variation of the Hamiltonian, eq. (1), which is independent of the mean membrane profile. Thus, the fluctuations and correlation functions of the deformed membrane stay identical compared to the undeformed membrane.

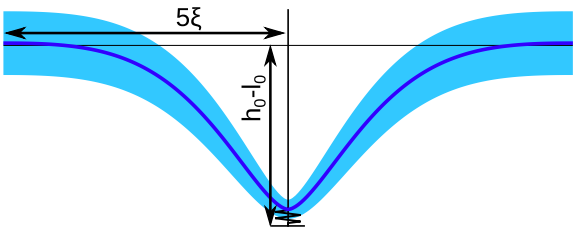

Figure 5. Profile (thick blue line) and fluctuation amplitude (light blue area) for a membrane pinned to a stiff bond with $h_0 - l_0 = 50\,\text{nm}$. Membrane parameters are $\kappa = 20\,\text{kT}$, $\sigma = 0$ and $\gamma = 10^9\,\text{J/m}^4$.

Here, we introduce a complementary method to expansion in a basis set of eigenfunctions, shown in the previous chapter. Now, we expand the membrane profile in plane waves around the mean of the unbound membrane

$$h(\mathbf{x}) = \sum_{\mathbf{k}} h_{\mathbf{k}} \mathrm{e}^{i\mathbf{k}\mathbf{x}} + h_0 \tag{21}$$

and account for mode coupling by explicitly calculating the functional integrals for $\langle h_{\mathbf{k}} \rangle$ and $\langle h_{\mathbf{k}} h_{\mathbf{k}'} \rangle$ defined by

$$\langle h_{\mathbf{k}} \rangle \equiv \frac{1}{\mathcal{Z}} \int \mathcal{D}\bar{h}_{\mathbf{k}} \; h_{\mathbf{k}} \exp\left[-\mathcal{H}\right],$$
$$\langle h_{\mathbf{k}} h_{\mathbf{k}'} \rangle \equiv \frac{1}{\mathcal{Z}} \int \mathcal{D}\bar{h}_{\mathbf{k}} \; h_{\mathbf{k}} h_{\mathbf{k}'} \exp\left[-\mathcal{H}\right], \tag{22}$$

using the partition function

$$\mathcal{Z} = \int \mathcal{D}h_{\mathbf{k}} \; \exp\left[-\mathcal{H}\right]. \tag{23}$$

For a permanent bond at lateral position $\mathbf{x}_0 = \mathbf{0}$, the solutions to eq. (22) are found after some algebra as

$$\langle h_{\mathbf{k}} \rangle = -\frac{\lambda\lambda_m}{\lambda + \lambda_m} \frac{1}{A} \frac{(h_0 - l_0)}{\kappa k^4 + \sigma k^2 + \gamma}, \tag{24}$$
$$\langle h_{\mathbf{k}} h_{\mathbf{k}'} \rangle = \frac{1}{A} \frac{\delta(\mathbf{k} + \mathbf{k}')}{\kappa k^4 + \sigma k^2 + \gamma} + \langle h_{\mathbf{k}} \rangle \langle h_{\mathbf{k}'} \rangle -$$
$$- \frac{\lambda\lambda_m}{\lambda + \lambda_m} \frac{1}{A^2} \frac{1}{\kappa k^4 + \sigma k^2 + \gamma} \frac{1}{\kappa k'^4 + \sigma k'^2 + \gamma}.$$

Equipped with eqs. (21) and (24), we easily find the mean membrane profile, the fluctuation amplitude and the correlation functions.

B. Mean membrane profile

We identified $\langle h_{\mathbf{k}} \rangle$ as a function of the absolute value of the mode, $k \equiv |\mathbf{k}|$. Thus, the mean membrane profile is radially symmetric to the position of the receptor. Using the distance $r \equiv |\mathbf{x}|$ from the receptor, the mean membrane height is given by

$$\langle h(r) \rangle = \sum_q \langle h_q \rangle \mathrm{e}^{iqr} + h_0$$
$$= h_0 - \frac{\lambda\lambda_m}{\lambda + \lambda_m} (h_0 - l_0) G(r). \tag{25}$$

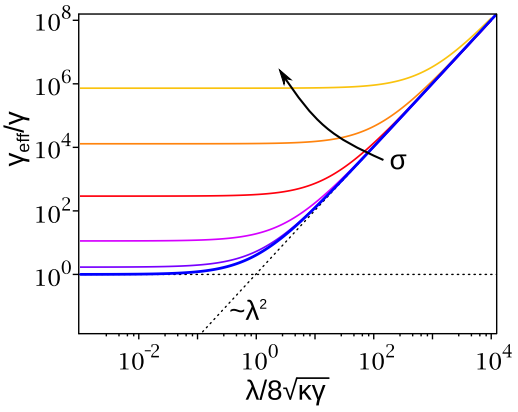

Figure 6. Effective potential strength $\gamma_{\rm eff}$ as a function of the normalized bond stiffness. The respective curves for different membrane tensions, $\sigma/\sqrt{\kappa\gamma} = 0, 1, 10, 100, 1000, 10000$, are shown in colors, with the arrow pointing in direction of increasing σ.

Here, we use the lateral correlation function $G(r)$ of the unbound membrane, given in eq. (SI-2) in the supporting information, after transforming the sum of eq. (25) into an integral. In Fig. 5, we show the mean membrane profile for a permanently bound receptor deforming the membrane profile (system parameters given in the figure caption). For special cases of weak and strong receptors, the membrane profile at the position of the receptor emerges naturally: for a weak receptor, $\lambda \ll \lambda_m$, the mean membrane position stays $h(\mathbf{x}_0) = h_0$ whereas for a stiff receptor, $\lambda \gg \lambda_m$, the membrane at the position of the receptor is pulled to the rest length of the receptor, $h(\mathbf{x}_0) = l_0$. Deformations of the mean membrane profile relax on the scale of the lateral correlation ξ of the unbound membrane to the mean membrane profile of the unbound membrane at h_0.

C. Deformation energy

The deformation energy of the membrane and the receptor upon forming a bond is found by applying the mean membrane profile to the Hamiltonian. We find

$$\mathcal{H}[\langle h(\mathbf{x})\rangle] \equiv \mathcal{H}_d = \frac{1}{2}\frac{\lambda\lambda_m}{\lambda+\lambda_m}(h_0 - l_0)^2. \qquad (26)$$

Obviously, for $h_0 = l_0$ the mean membrane profile is flat and the deformation energy vanishes. However, in any other case, the deformation energy increases quadratically with the height difference of membrane and receptor mean positions which was described previously [30].

The deformation energy of the particular set of system parameters for the membrane depicted in Fig. 5 is $\mathcal{H}_d \simeq 22\,\mathrm{k_B T}$.

D. Fluctuation map

The fluctuation amplitude at lateral position $\mathbf{x}$, i. e. the fluctuation map, is found easily with the help of eq. (24) using

$$\langle \Delta h^2(\mathbf{x})\rangle \equiv \langle h^2(\mathbf{x})\rangle - \langle h(\mathbf{x})\rangle^2 \qquad (27)$$
$$= \sum_{\mathbf{k},\mathbf{k}'} \langle h_{\mathbf{k}} h_{\mathbf{k}'}\rangle e^{i(\mathbf{k}+\mathbf{k}')\mathbf{x}} - \left(\sum_{\mathbf{k}} \langle h_{\mathbf{k}}\rangle e^{i\mathbf{k}\mathbf{x}}\right)^2.$$

Evaluating the sums, we find, after some re-arranging, the fluctuation map as a function of the distance r from the receptor

$$\langle \Delta h^2(r)\rangle_\lambda = \langle \Delta h^2\rangle - \frac{\lambda\lambda_m}{\lambda+\lambda_m} G^2(r), \qquad (28)$$

with the fluctuation amplitude $\langle \Delta h^2\rangle$ and the lateral correlation function $G(r)$ of the unbound membrane, introduced in eqs. (SI-1) and (SI-2) in the supporting information, respectively. For a tensionless membrane, we obtain for the fluctuation amplitude at $r = 0$ the analytical form

$$\langle \Delta h^2(0)\rangle_\lambda = \frac{1}{\lambda+\lambda_m},$$

i. e. the same expression as for the undeformed membrane obtained from expanding in the basis set $\{\psi_{q,m}(\mathbf{x})\}$, eq. (8). For the fluctuation map of a tensionless membrane, we find numerically the same result as depicted in Fig. 2b found for a pinned membrane.

The fluctuation map of the permanently bound membrane, eq. (28), is unaffected by a mean membrane deformation. Thus, the effective interaction potential $\gamma_{\rm eff}$, identified in eq.(10), holds for a permanent bond deforming the membrane, too. In the case of a tense membrane, we show the effective interaction potential $\gamma^0_{\rm eff}$ at the position of the receptor in Fig. 6 for five orders of magnitude in membrane tension σ and seven orders of magnitude in receptor stiffness λ. In the case of a tensionless membrane, $\gamma^0_{\rm eff}(\lambda = 0) = \gamma$, otherwise, the effective potential accounts for the effect of membrane tension on the fluctuation amplitude, too.

E. Lateral correlation function

For calculating the lateral correlation function of a permanently bound membrane, we apply again eq. (24). We find the lateral correlation function, measured between positions $\mathbf{x}_1$ and $\mathbf{x}_2$, as

$$\langle \Delta h(\mathbf{x}_1)\Delta h(\mathbf{x}_2)\rangle = \sum_{\mathbf{k},\mathbf{k}'} \langle h_{\mathbf{k}} h_{\mathbf{k}'}\rangle e^{i\mathbf{k}\mathbf{x}_1} e^{i\mathbf{k}'\mathbf{x}_2}$$
$$- \sum_{\mathbf{k}} \langle h_{\mathbf{k}}\rangle e^{i\mathbf{k}\mathbf{x}_1} \sum_{\mathbf{k}'} \langle h_{\mathbf{k}'}\rangle e^{i\mathbf{k}'\mathbf{x}_2}. \qquad (29)$$

The lateral correlation function accounts for the effect of the permanent bond in a non-trivial way. However, if

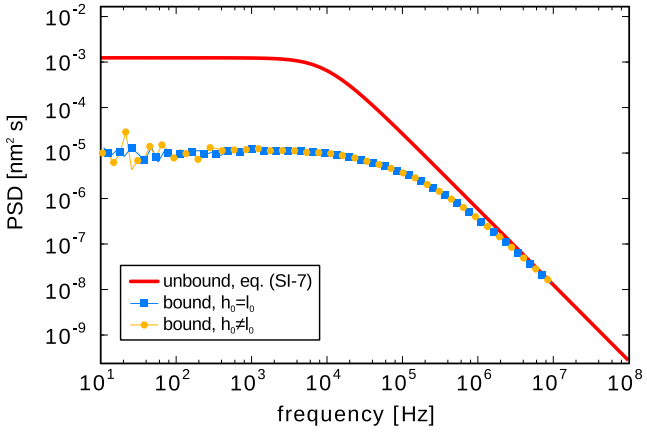

Figure 7. Simulation results for the power spectral density of a permanently bound membrane with receptor rest length $l_0 = h_0$ (blue squares) and $l_0 \neq h_0$ (green circles). Both curves match very well with small deviations for low frequencies emerging from weak statistical data. The system parameters are identical to those of Fig. 2.

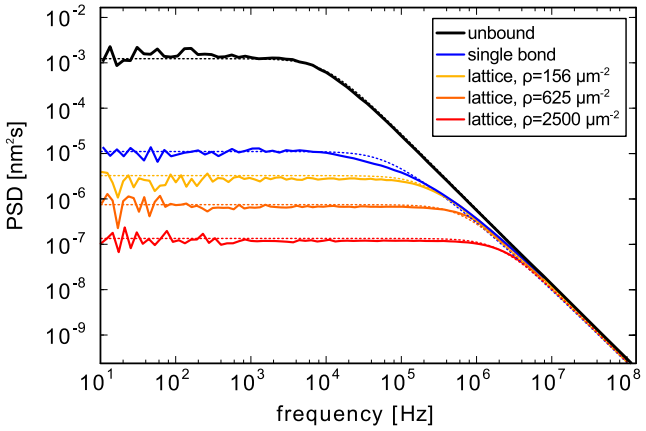

Figure 8. Simulation results for the power spectral density of membrane bound permanently to a square lattice. With increasing bond density, the low frequency regime of the power spectral density decreases. The system parameters are identical to those of Fig. 2.

the receptor lies on the straight line of $\mathbf{x}_1\mathbf{x}_2$, the lateral correlation function reduces to

$$\langle \Delta h(\mathbf{x}_1)\Delta h(\mathbf{x}_2)\rangle = \tag{30}$$
$$= G(|\mathbf{x}_1 - \mathbf{x}_2|) - \frac{\lambda\lambda_m}{\lambda+\lambda_m} G(|\mathbf{x}_1|)G(|\mathbf{x}_2|),$$

being independent of mean membrane deformations. If $\mathbf{x}_1 = \mathbf{0}$, i. e. measuring the lateral correlation function from the position of the receptor, it reduces to a rescaled lateral correlation function of an unbound membrane,

$$\langle \Delta h(\mathbf{0})\Delta h(\mathbf{x}_2)\rangle = \frac{\lambda_m}{\lambda+\lambda_m} G(|\mathbf{x}_2|). \tag{31}$$

In the limit of $\mathbf{x}_2 = \mathbf{0}$ we resemble the fluctuation amplitude at the position of the receptor, eq. (28). Numerically, the lateral correlation function eq. (31) in the tensionless limit is identical to the lateral correlation function calculated for the pinned membrane and shown in Fig. 2c.

F. Temporal correlations

Encouraged by the finding for the fluctuation map and the lateral correlation function, we simulate the membrane with a permanent bond, imposing $h_0 \neq l_0$. We find strong numerical evidence that the power spectral density evaluated at the receptor position is identical to the power spectral density of the pinned membrane with $h_0 = l_0$ (see Fig. 7). Consequently, we will describe the power spectral density of a permanent bond at the position of the receptor by eq. (19).

V. MEMBRANE-TRANSMITTED CORRELATIONS BETWEEN BONDS

The fluctuation amplitude of the membrane is reduced in the presence of other bonds, i.e., the local membrane stiffness $\lambda_m(\mathbf{x})$ is increased (see, e.g., Fig. 2c). How the fluctuation map and the local membrane stiffness is affected by an arbitrary bond configuration was calculated previously by solving functional integrals [8, 19].

Placing a new bond of stiffness λ in the presence of other bonds changes the fluctuation amplitude of the membrane at the position of the newly formed bond to $1/(\lambda + \lambda_m(\mathbf{x}))$ as suggested by eq. (9). For static membrane properties is it clear that membrane transmitted correlations between bonds can be summed up to a local description where the only parameter is the local membrane stiffness $\lambda_m(\mathbf{x})$. However, how the membrane dynamics are affected at the position of a bond in the presence of other bonds is unclear.

In the following, we simulate the membrane dynamics of bond lattices with different bond densities and extract the membrane height trajectory at the position of one of the bonds to calculate the power spectral density. To achieve comparable results for different bond densities, we impose periodic boundary conditions, i.e., deal in all cases with infinite lattices. For the power spectral density, we find again the high frequency regime unaffected by the pinning, whereas the power spectral density in the low frequency regime decreases monotonically with increasing bond density (see Fig. 8). We compare the simulations to calculations of the power spectral density following our effective description of eq. (19). However, to account for the neighbouring bonds, we change the membrane stiffness and the corresponding interaction potential strength γ to the local membrane stiffness $\lambda_m(\mathbf{x})$ for the given bond configuration and the corresponding

effective interaction potential strength $\gamma_{\text{eff}}(\mathbf{x})$. The so obtained power spectral density is overlaid with the simulation curves (dotted curves in Fig. 8) and both curves agree very well without any further information than the bond density. Consequently, this numerical agreements hints towards the fact that membrane transmitted correlations between bonds can be summed up by local membrane stiffnesses for static and dynamic mechanical properties of the membrane.

VI. CONCLUSION

Binding of a generic type of adhesion protein to a model of a cellular membrane reveals interesting effects on static measures and spectral properties of the membrane. With a minimal model of a pinned membrane consisting of a two dimensional surface equipped with two mechanic parameters, the bending rigidity and the membrane tension, fluctuating in a harmonic potential and bound to a harmonic spring, we were able to finally determine the effect of a bond on all static and dynamic mechanic properties of the membrane. First, we determined the eigenmodes which granted access to calculate all static measures of a pinned membrane. As a complementary method to the eigenvalue description, we describe the membrane profile in plane waves and calculate analytically the first and second moment of the membrane height in Fourier space. Equipped with those two powerful methods, we calculated whenever possible analytically and otherwise numerically the mean membrane shape, the fluctuation map, and the lateral correlation function for a pinned membrane. For membrane dynamics, we found a first order correction to the damping coefficients which reproduce simulation results obtained for five orders of magnitude in the bond stiffness and three orders of magnitude in the interaction potential strength.

In our membrane model, the Hamiltonian is always quadratic in the membrane profile. The fluctuations and correlations functions depend on the second variation of the Hamiltonian which render independent of the actual mean membrane shape. Consequently, the fluctuations and lateral and temporal correlation functions stay unaffected by a receptor deforming the membrane.

We learnt that within the questions addressed in this work, the membrane can be described as a harmonic spring of stiffness λ_m. For a lattice of receptors, the fluctuation amplitude at the position of a receptor can be calculated [19] and with the help of eq. (9) the stiffness of the "membrane spring" is found. Going all the way to the power spectral density within the two spring picture, using either eq. (19) or eq. (20), the simulations and the predictions from the effective description show solid agreement.

[1] B. Alberts, A. Johnson, J. Lewis, M. Raff, K. Roberts, and P. Walter, *Molecular Biology of the Cell*, 5th ed. (Garland Science, Taylor & Francis Group, LLC, 2007).

[2] N. Wang, J. P. Butler, and D. E. Ingber, "Mechanotransduction across the cell surface and through the cytoskeleton," Science **260**, 1124–1127 (1993).

[3] B. Geiger, J. P. Spatz, and A. D. Bershadsky, "Environmental sensing through focal adhesion," Nat. Rev. Mol. Cell Biol. **10**, 21 (2009).

[4] S. Goennenwein, M. Tanaka, B. Hu, L. Moroder, and E. Sackmann, "Functional incorporation of integrins into solid supported membranes on ultrathin films of cellulose: impact on adhesion," Biophys J. **85**, 646–655 (2003).

[5] J. P. Frohnmayer, D. Brüggemann, C. Eberhard, S. Neubauer, C. Mollenhauer, H. Böhm, H. Kessler, B. Geiger, and J. P. Spatz, "Minimal synthetic cells to study integrin-mediated adhesion," Angew. Chem. Int. Ed. **54**, 12472–12478 (2015).

[6] K. H. Biswas, K. L. Hartman, C. Yu, O. J. Harrison, H. Song, A. W. Smith, W. Y. C. Huang, W. Lin, Z. Guo, A. Padmanabhan, S. M. Troyanovsky, M. L. Dustin, L. Shapiro, B. Honig, R. Zaidel-Bara, and J. T. Groves, "E-cadherin junction formation involves an active kinetic nucleation process," Proc. Natl. Acad. Sci. U. S. A. **112**, 10932–10937 (2015).

[7] S.-C. Liu and J. Palek, "Spectrin tetramer–dimer equilibrium and the stability of erythrocyte membrane skeletons," Nature (1980), 10.1038/285586a0.

[8] T. Bihr, U. Seifert, and A.-S. Smith, "Nucleation of ligand-receptor domains in membrane adhesion," Phys. Rev. Lett. **109**, 258101 (2012).

[9] Y. Wu, J. Vendome, L. Shapiro, A. Ben-Shaul, and B. Honig, "Transforming binding affinities from three dimensions to two with application to cadherin clustering," Nature **475**, 510–513 (2011).

[10] T. Bihr, S. Fenz, E. Sackmann, R. Merkel, U. Seifert, K. Sengupta, and A.-S. Smith, "Association rates of membrane-coupled cell adhesion molecules," Biophys. J. **107**, L33–L36 (2014).

[11] L. Ju, J. Qian, and C. Zhu, "Transport regulation of two-dimensional receptor-ligand association," Biophys. J. **108**, 1773–1784 (2015).

[12] T. Bihr, U. Seifert, and A.-S. Smith, "Multiscale approaches to protein-mediated interactions between membranes—relating microscopic and macroscopic dynamics in radially growing adhesions," New J. Phys. **17**, 083016 (2015).

[13] J. Hu, R. Lipowsky, and T. R. Weikl, "Binding constants of membrane-anchored receptors and ligands depend strongly on the nanoscale roughness of membranes," Proc. Natl. Acad. Sci. U. S. A. **110**, 15283–15288 (2013).

[14] J. Hu, G.-K. Xu, R. Lipowsky, and T. R. Weikl, "Binding kinetics of membrane-anchored receptors and ligands: Molecular dynamics simulations and theory," J. Chem. Phys. **143**, 243137 (2015).

[15] D. Schmidt, T. Bihr, S. Fenz, R. Merkel, U. Seifert, K. Sengupta, and A.-S. Smith, "Crowding of receptors induces ring-like adhesions in model membranes," BBA-Mol. Cell Res. **1853**, 2984–2991 (2015).

[16] H. Krobath, G. J. Schütz, R. Lipowsky, and T. R. Weikl,

"Lateral diffusion of receptor-ligand bonds in membrane adhesion zones: Effect of thermal membrane roughness," Europhys. Lett. **78**, 38003 (2007).

[17] E. Reister, T. Bihr, U. Seifert, and A.-S. Smith, "Two intertwined facets of adherent membranes: membrane roughness and correlations between ligand–receptors bonds," New J. Phys. **13**, 025003:1–15 (2011).

[18] S. F. Fenz, T. Bihr, R. Merkel, U. Seifert, K. Sengupta, and A.-S. Smith, "Switching from ultraweak to strong adhesion," Adv. Mater. **XX**, 1–5 (2011).

[19] D. Schmidt, T. Bihr, U. Seifert, and A.-S. Smith, "Coexistence of dilute and densely packed domains of ligand-receptor bonds in membrane adhesion," Europhys. Lett. **99**, 38003 (2012).

[20] N. S. Gov and S. A. Safran, "Red blood cell membrane fluctuations and shape controlled by atp-induced cytoskeletal defects," Biophys. J. **88**, 1859–1874 (2005).

[21] L. C.-L. Lin and F. L. H. Brown, "Dynamic simulations of membranes with cytoskeletal interactions," Phys. Rev. E **72**, 011910 (2005).

[22] J.-B. Fournier, D. Lacoste, and E. Raphaël, "Fluctuation spectrum of fluid membranes coupled to an elastic meshwork: jump of the effective surface tension at the mesh size," Phys. Rev. Lett. **92**, 018102 (2004).

[23] T. Auth and G. Gompper, "Fluctuation spectrum of membranes with anchored linear and star polymers," Phys. Rev. E **72**, 031904 (2005).

[24] R.-J. Merath and U. Seifert, "Nonmonotonic fluctuation spectra of membranes pinned or tethered discretely to a substrate," Phys. Rev. E **73**, 010401 (2006).

[25] U. Seifert, "Dynamics of a bound membrane," Phys. Rev. E **49**, 3124–3127 (1994).

[26] M. Breidenich, R. R. Netz, and R. Lipowsky, "The shape of polymer-decorated membranes," Europhys. Lett. **49**, 431–437 (2000).

[27] O. Farago, "Membrane fluctuations near a plane rigid surface," Phys. Rev. E **78**, 051919 (2008).

[28] T. Speck, E. Reister, and U. Seifert, "Specific adhesion of membranes: Mapping to an effective bond lattice gas," Phys. Rev. E **82**, 021923 (2010).

[29] J. O. Rädler, T. J. Feder, H. H. Strey, and E. Sackmann, "Fluctuation analysis of tension-controlled undulation forces between giant vesicles and solid substrates," Phys. Rev. E **51**, 4526–4536 (1995).

[30] R. Bruinsma, A. Behrisch, and E. Sackmann, "Adhesive switching of membranes: Experiment and theory," Phys. Rev. E **61**, 4253–4267 (2000).

A model for spectral properties of a pinned membrane

Daniel Schmidt,[1,2] Udo Seifert,[2] and Ana-Sunčana Smith[1,3,*]

[1] *Institut für Theoretische Physik and Cluster of Excellence: Engineering of Advanced Materials, Friedrich Alexander Universität Erlangen-Nürnberg, 91052 Erlangen, Germany*

[2] *II. Institut für Theoretische Physik, Universität Stuttgart, 70569 Stuttgart, Germany*

[3] *Insitut Ruđer Bošković, 10000 Zagreb, Croatia*

(Dated: February 11, 2016)

THE UNBOUND MEMBRANE REVISITED

The unbound membrane ($b = 0$) described by the Helrich Hamiltonian is well understood. In this case, the receptor has no effect on the membrane. The mean membrane profile is flat with $\langle h(\mathbf{x})\rangle = h_0$ minimizing the Hamiltonian. The fluctuation amplitude was determined for the unbound membrane in early studies in the 1990s, finding [1, 2]

$$\langle \Delta h^2\rangle = \frac{1}{2\pi}\frac{\arctan(\sqrt{4\kappa\gamma-\sigma^2}/\sigma)}{\sqrt{4\kappa\gamma-\sigma^2}}. \tag{SI-1}$$

For a tensionless membrane, $\sigma = 0$, the fluctuation amplitude becomes $\langle \Delta h^2\rangle = 1/(8\sqrt{\kappa\gamma})$. The height probability distribution of a membrane is Gaussian [3, 4] which gives rise to model the membrane by a harmonic spring of stiffness $\lambda_m = 1/\langle \Delta h^2\rangle$ and rest length h_0.

In the unbound case, the membrane is homogeneous and isotropic such that the lateral correlation function $G(r)$ is a function of the distance $r \equiv |\mathbf{x}_1 - \mathbf{x}_2|$ between positions $\mathbf{x}_1$ and $\mathbf{x}_2$. The lateral correlation function is identified with [5, 6]

$$G(r) = \frac{1}{2\pi}\int_0^\infty \mathrm{d}q \frac{qJ_0(qr)}{\kappa q^4+\sigma q^2+\gamma}, \tag{SI-2}$$

using the Bessel function J_0 of the first kind. The lateral correlation function at $r = 0$ is equivalent to the fluctuation amplitude of an unbound membrane. For a tensionless membrane $\sigma = 0$, the integral in the lateral correlation function is solved analytically yielding

$$G(r)_{|\sigma=0} = -\frac{1}{2\pi\sqrt{\kappa\gamma}}\mathrm{kei}_0\left(\frac{r}{\xi}\right). \tag{SI-3}$$

Here we use the Kelvin function kei_0 and the lateral correlation length $\xi \equiv \sqrt[4]{\kappa/\gamma}$.

The temporal auto-correlation function $\langle \Delta h(t)\Delta h(0)\rangle$ describes how a perturbation at time $t = 0$ dissipates into the surrounding fluid of viscosity η and for the unbound membrane it is given by [7]

$$\langle \Delta h(t)\Delta h(0)\rangle = \int_0^\infty \mathrm{d}q \frac{q\mathrm{e}^{-\Gamma(q)t}}{\kappa q^4+\sigma q^2+\gamma} \tag{SI-4}$$

with damping coefficients

$$\Gamma(q) = \frac{\kappa q^4+\sigma q^2+\gamma}{4\eta q}. \tag{SI-5}$$

The damping coefficients $\Gamma(q)$ are found from analytically solving Stokes equations for the membrane fluctuating in the surrounding fluid [1, 8, 9]. If the unbound membrane is surrounded by two different fluids with viscosities η_1 and η_2, the viscosity η in the damping coefficients is replaced by the arithmetic mean of the viscosities of the surrounding fluids, $\eta = (\eta_1+\eta_2)/2$ [**?**]. The damping coefficients in eq. (5) account for a permeable wall. However, if the membrane is in presence of a hard, impermeable wall, solving the Stokes equations reveals modified damping coefficients [8].

Another measure for temporal correlations of the membrane is the power spectral density, defined as the Fourier transform of the auto correlation function. For the unbound membrane, the power spectral density is given by

$$\langle |h(\omega)|^2\rangle_u = \frac{1}{\pi}\int_0^\infty \mathrm{d}t \int_0^\infty \mathrm{d}q \frac{q\mathrm{e}^{-\Gamma(q)t}}{\kappa q^4+\sigma q^2+\gamma}\mathrm{e}^{i\omega t}. \tag{SI-6}$$

Performing the time integral reveals the integrand of the power spectral density $\langle |h(\omega)|^2\rangle_u$ as a Lorentzian in the frequency ω (algebraic decay with exponent -2 in the high frequency regime),

$$\langle |h(\omega)|^2\rangle_u = \frac{4\eta}{\pi}\int_0^\infty \mathrm{d}q \frac{q^2}{(\kappa q^4+\sigma q^2+\gamma)^2+(4\eta q\omega)^2} \tag{SI-7}$$

However, after integrating over all modes q, we find in limits of small and large frequencies

$$\langle |h(\omega)|^2\rangle_u = \begin{cases} \frac{\eta}{\sqrt{4\kappa\gamma^2(2\sqrt{\kappa\gamma}+\sigma)}}, & \omega \ll \omega_0 \\ \frac{1}{6\sqrt[3]{2\eta^2\kappa}}\omega^{-5/3}, & \omega \gg \omega_0. \end{cases} \tag{SI-8}$$

Here, we use the characteristic frequency $\omega_0 \equiv \sqrt[4]{\kappa\gamma^3}/\eta$. We find the power spectral density constant in the low frequency regime and algebraically decaying with exponent $-5/3$ for the high frequency regime. For a tensionless membrane, the power spectral density reduces in the low frequency limit to $\langle |h(0)|^2\rangle_u = \eta/(\sqrt{8}\sqrt[4]{\kappa^3\gamma^5})$.

[1] R. Lipowsky, "Generic interactions of flexible membranes," in *Structure and dynamics of membranes*, edited by R. Lipowsky and E. Sackmann (Elsevier, 1995) Chap. 11, pp. 521–602.

[2] J. O. Rädler, T. J. Feder, H. H. Strey, and E. Sackmann, "Fluctuation analysis of tension-controlled undulation forces between giant vesicles and solid substrates," Phys. Rev. E **51**, 4526–4536 (1995).

[3] D. Schmidt, T. Bihr, U. Seifert, and A.-S. Smith, "Coexistence of dilute and densely packed domains of ligand-receptor bonds in membrane adhesion," Europhys. Lett. **99**, 38003 (2012).

[4] T. Bihr, U. Seifert, and A.-S. Smith, "Nucleation of ligand-receptor domains in membrane adhesion," Phys. Rev. Lett. **109**, 258101 (2012).

[5] K. R. Mecke, T. Charitat, and F. Graner, "Fluctuating lipid bilayer in an arbitrary potential: theory and experimental determination of bending rigidity," Langmuir **19**, 2080–2087 (2003).

[6] T. Speck, E. Reister, and U. Seifert, "Specific adhesion of membranes: Mapping to an effective bond lattice gas," Phys. Rev. E **82**, 021923 (2010).

[7] U. Seifert, "Configuratios of fluid membranes and vesicles," Adv. Phys. **46**, 13–137 (1997).

[8] U. Seifert, "Dynamics of a bound membrane," Phys. Rev. E **49**, 3124–3127 (1994).

[9] U. Seifert and S. A. Langer, "Hydrodynamics of membranes: the bilayer aspect and adhesion," Biophys. Chem. **49**, 13–22 (1994).

* author to whom correspondence should be addressed: smith@physik.uni-erlangen.de

P6

Spectral properties of a stochastically bound membrane

Spectral properties of a stochastically bound membrane

D. Schmidt[1,2], U. Seifert[2], and A.-S. Smith[1,3]

[1] Institut für Theoretische Physik, Department für Physik, and the Excellence Cluster: Engineering of Advanced Materials, Friedrich Alexander Universität Erlangen-Nürnberg, 91058 Erlangen, Germany
[2] II. Institut für Theoretische Physik, Fakultät 8: Mathematik und Physik, Universität Stuttgart, 70550 Stuttgart, Germany
[3] Division of Physical Chemsitry, Ruđer Bošković Institute, 10000 Zagreb, Croatia

in preparation (2016)

ABSTRACT Association and dissociation of individual membrane-anchored adhesion proteins is the basis of inter-cellular adhesion. In the biological world, the adhesion process is controlled by the cell; however, it is subject to physical bounds on the binding equilibrium and kinetics. By proposing a minimal model for membrane-anchored adhesion proteins, we explore these physical bounds and determine by theoretical means the binding affinity and reaction rates for a single adhesion protein embedded in the membrane. We find effective reaction rates that take membrane and protein fluctuations into account and react strongly on variations in membrane position and fluctuations. With this fundament in binding kinetics, we predict non-trivial effects of the membrane fluctuations and temporal correlations in the case of stochastic association and dissociation of the adhesion protein.

Spectral properties of a stochastically bound membrane

Daniel Schmidt,[1,2] Udo Seifert,[2] and Ana-Sunčana Smith[1,3,*]

[1] *Institut für Theoretische Physik and Cluster of Excellence: Engineering of Advanced Materials, Friedrich Alexander Universität Erlangen-Nürnberg, 91052 Erlangen, Germany*

[2] *II. Institut für Theoretische Physik, Universität Stuttgart, 70569 Stuttgart, Germany*

[3] *Insitut Ruđer Bošković, 10000 Zagreb, Croatia*

(Dated: May 6, 2016)

Association and dissociation of individual membrane-anchored adhesion proteins is the basis of inter-cellular adhesion. In the biological world, the adhesion process is controlled by the cell; however, it is subject to physical bounds on the binding equilibrium and kinetics. By proposing a minimal model for membrane-anchored adhesion proteins, we explore these physical bounds and determine by theoretical means the binding affinity and reaction rates for a single adhesion protein embedded in the membrane. We find effective reaction rates that take membrane and protein fluctuations into account and react strongly on variations in membrane position and fluctuations. With this fundament in binding kinetics, we predict non-trivial effects of the membrane fluctuations and temporal correlations in the case of stochastic association and dissociation of the adhesion protein.

I. INTRODUCTION

Dynamic temporary binding between cells is essential for several biological processes like embryogenesis, maturation of lymphoid cells and for metastatic spreading of cancer cells. On the molecular level, dynamic and temporary binding requires the association and dissociation of adhesive interactions typically mediated by highly specific membrane-anchored bonds [1]. First models for the binding kinetics in terms of reaction rates were phenomenologically proposed by Bell [2] and Dembo [3] and provide force dependent dissociation rates, which were confirmed by single molecule experiments [4–7]. In addition to the properties of the protein, the binding equilibrium and kinetics of membrane-anchored adhesion proteins were recently shown to depend strongly on the mechanical properties of the membrane [8–10]. While the binding of proteins and the membrane mechanics are studied separately to great extend, their mutual interplay in stochastic binding and unbinding is poorly understood.

First insights into the mutual interplay between membrane and bond are achieved by analysing the effect of a permanent bond on the membrane mechanics. It is known that the static membrane properties as, e.g., mean membrane shape and its roughness depend on the bond density and the membrane properties [11–14][SingleBond1]. Much more challenging are calculations for the dynamics of a permanently bound membrane. The membrane dynamics is determined by an elaborated hydrodynamic interplay between the membrane, the surrounding fluids and the bond, where the latter couples all fluctuation modes. First steps to understanding the membrane dynamics involve discretized membranes in simulations [15, 16] and numerical calculations of the fluctuation spectrum [17–19]. Recently, we introduced to the analytical description a first order correction to the damping coefficients and found for the power spectral density convincing agreement with results from simulations [SingleBond1]. In summary, the static and dynamic mechanical properties of a permanently bound membrane are, at least numerically, understood.

The issue how the membrane affects binding equilibrium and kinetics of a bond was addressed from various angles. With respect to binding equilibrium, it was shown that unstable individual bonds can be stabilized by membrane transmitted correlations between neighbouring bonds and, for biological relevant parameters, few bonds packed closely together form a stable nucleation seed [20]. Recently, the binding kinetics of membrane-anchored proteins were shown to depend sensitively on, e.g., the local separation and roughness of the membranes [20–23]. Consequently, growth of adhesion domains from a stable nucleation seed depends not only on protein parameters but on properties of the membrane, too [24]. However, a minimal model system capturing mechanic properties of a membrane-anchored adhesion protein and resembling correct binding equilibrium and kinetics is still missing.

In this paper, we propose a minimal model system for the binding process that allows us to first calculate the binding affinity of a membrane-anchored adhesion protein including contributions from membrane deformation and suppression of fluctuations. In a second step, we obtain within the minimal model thermodynamic consistent reaction rates for the formation of a bond. By integrating fluctuations of the bond, we find reaction rates that resemble the core characteristic of the phenomenologically proposed reaction rates by Bell [2] and Dembo [3]. Integrating additionally the membrane fluctuation leads to effective rates that depend only on system parameters and, thus, allow for efficient simulations of the adhesion process on the scale of a cell [23]. In the last part of this work, we predict the manifestations of a stochastically bound membrane in experimental observables as,

* author to whom correspondence should be addressed: smith@physik.uni-erlangen.de

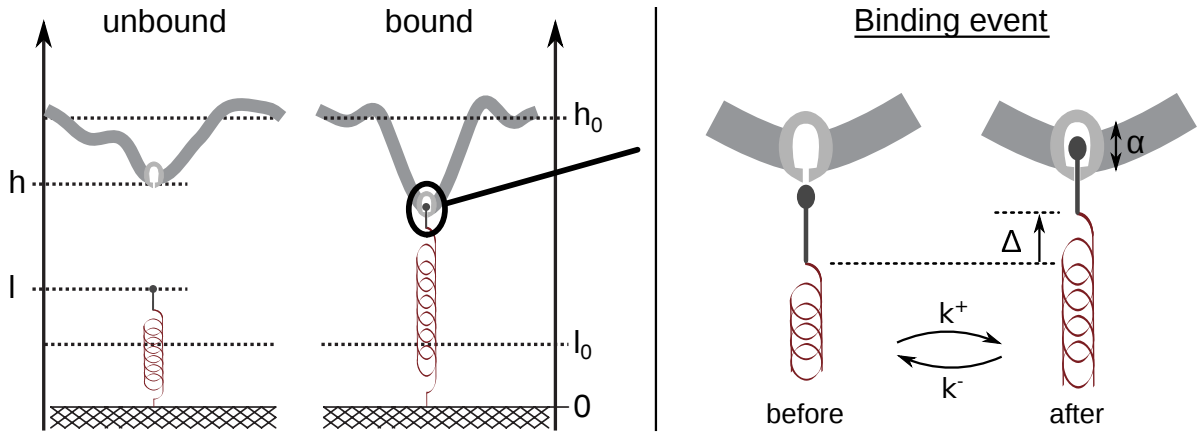

Figure 1. Left: Sketch of the system illustrating the flexible membrane (grey) and the binder (red spring). Right: Sketch of the binding event. Before binding, the ligand on the membrane and the receptor are in close proximity while, immediately after binding, the binder is transferred to the binding pocket of size α. The position of the binding pocket in the sketch, shifted by Δ from the membrane position, is associated with a normal bond.

e.g., membrane fluctuations and temporal correlations. In combination, the results for the binding affinity, reaction rates, and mechanical membrane properties of a single stochastic bond developed from a minimal model system for the bond display a full picture of the mutual interplay between membrane and membrane-anchored adhesion proteins.

II. MODEL

The biological system consists of a membrane that adheres with the help of a membrane-anchored adhesion protein to another adhesion protein positioned on the rigid scaffold by establishing a bond. The membrane is described in a continuum picture by a fluctuating surface with height $h(\mathbf{x})$ above the scaffold at lateral position $\mathbf{x}$. The mechanics of the membrane are determined by the parameters bending rigidity κ and tension σ while fluctuating in a harmonic membrane-scaffold interaction potential of stiffness γ positioned at height h_0 above the scaffold. We model the extensible parts of the two adhesion proteins by a single harmonic spring with stiffness λ and rest length l_0. The harmonic spring is placed on the scaffold at position $\mathbf{x}_0$ and its tip has height l above the scaffold. To clarify the notation, the harmonic spring will be referred to as receptor. As in the biological system, a bond connecting the membrane with the scaffold can be established if the binding sites of the adhesion proteins come into contact that is in our minimal model if the tip of the receptor spring comes close to the membrane position, $h(\mathbf{x}_0) = l$ (Fig. 1).

We describe the minimal model by a Hamiltonian consisting of the Helfrich Hamiltonian for the membrane and a term for the harmonic receptor spring,

$$\mathcal{H} = \int_A \mathrm{d}\mathbf{x} \left[\frac{\kappa}{2} \left(\nabla^2 h(\mathbf{x}) \right)^2 + \frac{\sigma}{2} \left(\nabla h(\mathbf{x}) \right)^2 + \frac{\gamma}{2} \left(h(\mathbf{x}) - h_0 \right)^2 \right] + \frac{\lambda}{2} \left(l(\mathbf{x}_0) - l_0 \right)^2 - b\epsilon_b^0 \,, \quad (1)$$

where the association of the bond is linked to an intrinsic binding affinity ϵ_b^0 and the parameter b describes the binding state (unbound: $b = 0$, bound: $b = 1$). Here and throughout the paper, we set the energy scale $k_\mathrm{B}T \equiv 1$, with Boltzmann constant k_B and absolute temperature T.

The binding pocket is of size α and shifted by the length Δ with respect to the instantaneous membrane position $h(\mathbf{x}_0)$ which opens a way to account for various types of adhesion proteins. In particular, for normal or slip bonds $\Delta > 0$ and for catch bonds $\Delta < 0$. In the unbound case, $b = 0$, the fluctuations of the membrane and the receptor spring are independent of each other. If the membrane and the tip of the receptor are in close distance, $l(\mathbf{x}_0) = h(\mathbf{x}_0)$, an association event can occur with a microscopic reaction rate k^+ which transfers the tip of the receptor immediately to a random position within the binding pocket. For a bound receptor, the fluctuations of the receptor relative to the membrane are confined to the binding pocket. The dissociation event can occur for any receptor position within the binding pocket with microscopic rate k^- and transfers the receptor immediately to the position of the membrane $l(\mathbf{x}_0) = h(\mathbf{x}_0)$.

III. 2D BINDING AFFINITY

In the binding process, the system gains the intrinsic binding affinity ϵ_b^0 for association of the bond. However, the total binding affinity is given by all energetic and

entropic contributions comparing the unbound with the bound state. For instance, in the bound state the membrane and the receptor are deformed compared to the equilibrium state, which is associated with a deformation energy. Moreover, due to bond association the system loses conformational degrees of freedom related to an entropic term. In the following, we will determine all energetic and entropic terms which occur in the binding process. We address this issue by calculating the partition functions for the bound and the unbound states and obtain the free energy difference between bound and unbound states, i.e., the 2D binding affinity.

The partition functions $\mathcal{Z}_b$ for the bound state and $\mathcal{Z}_u$ for the unbound state contain all information necessary to calculate the 2D binding affinity given by

$$\Delta\mathcal{F} \equiv \ln\left(\frac{\mathcal{Z}_u}{\mathcal{Z}_b}\right). \tag{2}$$

We find both partition functions in a straightforward manner from the microscopic model (see. Fig. 1). In general, a partition function is found by integrating the exponential of the system's Hamiltonian over the accessible phase space. In order to calculate the partition functions, we impose the spring representation of the membrane where we model the membrane by a harmonic spring of stiffness $\lambda_m \equiv 1/\langle\Delta h^2\rangle$ and rest length h_0 [singlebond1]. We find for the partition function $\mathcal{Z}_u$ of the unbound state

$$\mathcal{Z}_u = \tag{3}$$
$$= \int_{-\infty}^{\infty}\frac{\mathrm{d}h}{L_m}\int_{-\infty}^{h}\frac{\mathrm{d}l}{L_s}\,\exp\left[-\frac{\lambda_m}{2}(h-h_0)^2-\frac{\lambda}{2}(l-l_0)^2\right],$$

where each degree of freedom h and l is assigned with a characteristic length L_m and L_s, respectively. In the limit

$$h_0 - l_0 \gg \sqrt{2(\lambda+\lambda_m)/(\lambda\lambda_m)},$$

the membrane and the receptor fluctuate independent of each other and the partition function becomes a product of the partition functions for two independent springs that evaluate to

$$\mathcal{Z}_u \approx \sqrt{\frac{2\pi}{\lambda_m L_m^2}}\sqrt{\frac{2\pi}{\lambda L_s^2}}. \tag{4}$$

For the bound state, the position of the receptor spring is confined to the binding pocket given by the interval $l \in [h+\Delta-\alpha/2, h+\Delta+\alpha/2]$. Consequently, the partition function for the bound membrane becomes

$$\mathcal{Z}_b = \int_{-\infty}^{\infty}\frac{\mathrm{d}h}{L_m}\int_{h+\Delta-\alpha/2}^{h+\Delta+\alpha/2}\frac{\mathrm{d}l}{L_s}\times \tag{5}$$
$$\times\exp\left[-\frac{\lambda_m}{2}(h-h_0)^2-\frac{\lambda}{2}(l-l_0)^2+\epsilon_b^0\right].$$

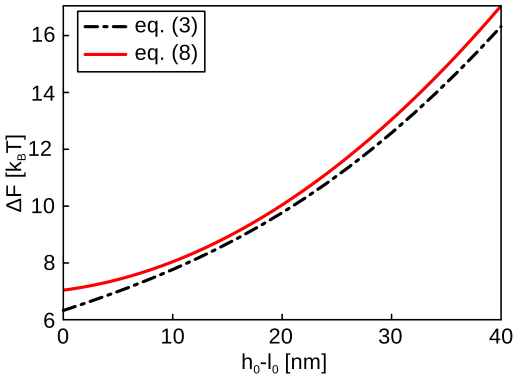

Figure 2. 2D binding affinity as a function of the height difference between potential minimum h_0 and est length l_0. The exact curve of $\Delta\mathcal{F}$ is shown as a black dash-dotted curve whereas the approximated 2D binding affinity, eq. (7), is shown as a solid red curve. The parameters chosen for this particular example are $\lambda = \lambda_m \simeq 83\,\mu\mathrm{J/m^2}$, $\epsilon_b^0 = 6\,\mathrm{k_BT}$, $\Delta = 5\,\mathrm{nm}$ and $\alpha = 10\,\mathrm{nm}$. Typically, the binding pocket is smaller in size and was enlarged to demonstrate the effects of the various approximations.

Solving the integrals in $\mathcal{Z}_b$ gives rise to error functions which we approximate in the limit

$$\alpha \ll \sqrt{2(\lambda+\lambda_m)/(\lambda\lambda_m)}$$

in first order in α to

$$\mathcal{Z}_b \approx \tag{6}$$
$$\approx \sqrt{\frac{2\pi}{\lambda_m+\lambda}}\frac{\alpha}{L_m L_s}\exp\left[-\frac{1}{2}\frac{\lambda\lambda_m}{\lambda+\lambda_m}(h_0+\Delta-l_0)^2+\epsilon_b^0\right].$$

With eqs. (4) and (6), we have found two analytical approximations for the partition functions in the unbound and bound state, respectively.

With the given approximations of the partition functions, we find the 2D binding affinity

$$\Delta\mathcal{F} \approx \frac{1}{2}\frac{\lambda\lambda_m}{\lambda+\lambda_m}(h_0+\Delta-l_0)^2 \tag{7}$$
$$-\epsilon_b^0+\frac{1}{2}\ln\left(\frac{2\pi}{\alpha^2}\frac{\lambda+\lambda_m}{\lambda\lambda_m}\right).$$

The first term is identified with the deformation energy of a series of harmonic springs with elastic constants λ and λ_m to overcome a separation of $h_0+\Delta-l_0$. The second term is given by the intrinsic binding affinity ϵ_b^0 while the third term accounts for the entropic cost due to loss of fluctuation modes of the membrane and the receptor upon confining the relative distance between both degrees of freedom, h and l, to the binding pocket.

The necessary approximations for eqs. (4) and (6), a large separation between the equilibrium positions of the membrane and the receptor and a small binding pocket α might not be fulfilled for all systems. In this case, we solve the integrals of the partition functions numerically.

For a set of parameters, we show in Fig. 2 the possible errors for overstretching the approximations for the error functions.

IV. THERMODYNAMICALLY CONSISTENT REACTION RATES

The binding kinetics of association and dissociation of the bond are modelled by reaction rates. To assure thermodynamically consistent reaction rates, the rates in our minimal model will obey a local detailed balance condition. These microscopic rates depend on the instantaneous membrane and receptor position. Assuming the receptor dynamics much faster than the membrane dynamics, we integrate the receptor fluctuations into the microscopic reaction rates and obtain reaction rates depending only on the membrane position. We show that the h-dependent reaction rates follow the characteristics phenomenologically proposed by Bell [2] and Dembo [3]. In a next step, we assume the membrane dynamics much faster than the (un-)binding of the bond which allows for another level of coarse-graining. Here, we obtain effective reaction rates that depend only on system parameters.

A. Microscopic reaction rates

To maintain thermodynamically consistent reaction rates $k^{\pm}$ on the microscopic level, we account for all energetic terms involved in the binding process and impose local detailed balance between the association and the dissociation rates. A binding event can occur if the membrane and the unbound receptor are at the same vertical position $l = h$. In our model, we fix the membrane height for the binding event and transfer the receptor from the membrane position h to a random position l^* in the binding pocket with $l^* \in [h + \Delta - \alpha/2, h + \Delta + \alpha/2]$. Besides an instantaneous elongation of the receptor spring, the intrinsic binding ϵ_b^0 is emitted. Consequently, the local detailed balance condition for the microscopic rates is given by

$$\frac{k^+}{k^-} = \exp\left[-\frac{\lambda}{2}\left\{(l^* - l_0)^2 - (h - l_0)^2\right\} + \epsilon_b^0\right], \qquad (8)$$

where the term in the exponential is just the negative energy difference gained in the association process.

For two microscopic rates only one constraint exists and, to maintain the individual rates, we introduce a load sharing factor θ as a free parameter [29, 30] that would be accessible, in a higher-level, molecular analysis of the particular adhesion protein forming the ligand-receptor complex. With the load sharing factor the individual microscopic rates become

$$k^+ = k_0 \exp\left[-\theta\frac{\lambda}{2}\left\{(l^* - l_0)^2 - (h - l_0)^2\right\}\right], \qquad (9)$$

$$k^- = k_0 \exp\left[(1-\theta)\frac{\lambda}{2}\left\{(l^* - l_0)^2 - (h - l_0)^2\right\} - \epsilon_b^0\right]. \qquad (10)$$

Here, k_0 describes the intrinsic rate if $l^* = h$. The microscopic rates account for the specific bond type implicitly due to the shift Δ of the binding pocket relative to the instantaneous membrane position h. For positive Δ the receptor spring is elongated during the binding process describing a normal bond and for negative Δ the receptor spring is compressed in the binding event which describes a catch bond.

The binding kinetics for association and dissociation events of, e.g., chemical reactions are typically described by Arrhenius rates which describe the temperature dependence of reaction rates and have the general form $k_A = A\exp[-E_a]$ [31]. Here, we use the non-exponential prefactor A and the activation energy E_a. Our microscopic reaction rates, eqs. (9) and (10), can be understood in the picture of Arrhenius rates by identifying $A = k_0$ and the activation energy E_a by the negative exponent of the respective rate k_{on} or k_{off}.

B. h-dependent reaction rates

If the receptor dynamics is much faster than the membrane dynamics, we apply our first level of coarse-graining. In this case, the receptor has probed its entire phase space before the membrane moves and, consequently, the membrane position can be regarded as fixed and the receptor is described by its height probability distribution. Therefore, we determine the reaction rates that depend on the membrane position h and integrate the receptor degree of freedom into the reaction rates.

Between an association and a dissociation event, the system equilibrates and, thus, the height probability distribution of the receptor height is Gaussian at the time of an event,

$$p_u^{\mathrm{rec}}(l) = \frac{1}{\mathcal{Z}}\exp\left[-\frac{\lambda}{2}(l - l_0)^2\right],$$

$$p_b^{\mathrm{rec}}(l) = \frac{1}{\mathcal{Z}}\exp\left[-\frac{\lambda}{2}(l - l_0)^2 + \epsilon_b^0\right], \qquad (11)$$

with height probability distributions $p_u^{\mathrm{rec}}(l)$ and $p_b^{\mathrm{rec}}(l)$ for the unbound and bound state, respectively. The par-

tition function $\mathcal{Z}$ of the total system is given by

$$\mathcal{Z} = \int_{-\infty}^{h} \mathrm{d}l \ \exp\left[-\frac{\lambda}{2}(l-l_0)^2\right] + \\ + \int_{h+\Delta-\alpha/2}^{h+\Delta+\alpha/2} \mathrm{d}l \ \exp\left[-\frac{\lambda}{2}(l-l_0)^2 + \epsilon_b^0\right], \qquad (12)$$

integrating all possible receptor positions of both, the unbound and the bound state.

Assuming equilibrium for the system implies balancing currents j^+ and j^- for transitions from unbound to bound states and vice versa, respectively. In other words, in a given and sufficiently long time interval, the number of association events balance the number of dissociation events. Both requirements, the height probability distribution and the balanced transition currents, allow for determining the h-dependent reaction rates $k_{\mathrm{on}}(h)$ and $k_{\mathrm{off}}(h)$ defined by

$$k_{\mathrm{on}}(h) = \frac{j^+(h)}{P_u} \qquad \text{and} \qquad k_{\mathrm{off}}(h) = \frac{j^-(h)}{P_b}, \qquad (13)$$

respectively. The probabilities P_u and P_b for being in unbound and bound state, respectively, are given by the respective height probability distribution $p_u^{\mathrm{rec}}(l)$ and $p_b^{\mathrm{rec}}(l)$ integrated over the available space in the unbound and bound state. The currents $j^+(h)$ and $j^-(h)$ equal and follow the form

$$j^+(h) \equiv \int_{h+\Delta-\alpha/2}^{h+\Delta+\alpha/2} \mathrm{d}l^* \ p_u^{\mathrm{rec}}(h) k^+(l^*, h) = j^-(h). \qquad (14)$$

With the microscopic reaction rate in eq. (9) and the height probability distribution in eq. (11) both currents $j^\pm$ are determined. In the limits $\alpha \ll \sqrt{2/\lambda} \ll h - l_0$, we solve the integral analytically and find the explicit form of the current

$$j^+(h) \approx \frac{k_0 \alpha}{\mathcal{Z}} \exp\left[\frac{\lambda}{2}(h-l_0)^2 - \theta\lambda\Delta\left(h - l_0 + \frac{\Delta}{2}\right)\right]. \qquad (15)$$

By imposing the same approximations for calculating the probabilities P_u and P_b, we determine the h-dependent reaction rates to be

$$k_{\mathrm{on}}(h) \approx \\ \approx k_0 \sqrt{\frac{\lambda\alpha^2}{2\pi}} \exp\left[-\frac{\lambda}{2}(h-l_0)^2 - \theta\lambda\Delta\left(h - l_0 + \frac{\Delta}{2}\right)\right], \\ k_{\mathrm{off}}(h) \approx \qquad (16) \\ \approx k_0 \exp\left[-\epsilon_b^0 + (1-\theta)\lambda\Delta\left(h - l_0 + \frac{\Delta}{2}\right)\right].$$

These h-dependent rates have the receptor dynamics integrated and can be, to some extend, understood intuitively. For instance, the pre-factor $\sqrt{\lambda\alpha^2/2\pi}$ in the k_{on}-rate accounts for the entropic effect of confining the receptor fluctuations to the binding pocket of size α.

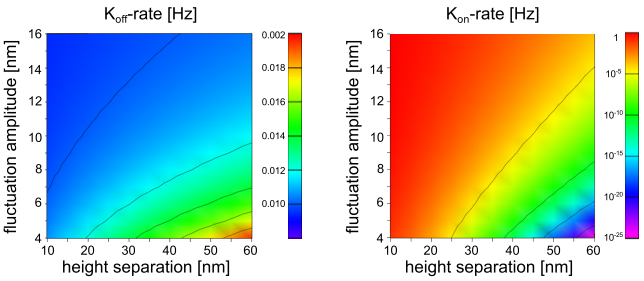

Figure 3. Illustration of the effective reaction rates K_{off} (left) and K_{on} (right) as a function of the mean membrane separation and the fluctuation amplitude displayed in a color code. The respective colouring is different for both rates, shown by a color bar next to the graph. The parameters are $\epsilon_b^0 = 7\,\mathrm{k_B T}$, $\lambda = 0.05\,\mathrm{k_B T/nm^2}$, $\theta = 0.5$, and $k_0 = 1\,\mathrm{Hz}$.

It is worth noting that the h-dependent association rate k_{on} resembles a harmonic term in the membrane position h which was phenomenologically introduced by Dembo et al. [3]. Comparable to Dembo's work, the dissociation rate k_{off} is fully determined by the association rate k_{on} and the detailed balance condition, eq. (8). Moreover, for $\theta \neq 1$ and $\Delta \neq 0$, the dissociation rate k_{off} has a linear term in h which can be understood as the exponential force dependence claimed by Bell [2]. At this stage it becomes obvious to characterize the bond type, whether it is a slip bond or a catch bond, by the parameter Δ determining the force dependence of the dissociation rate k_{off}.

Interestingly, the h-dependent reaction rates obtain local detail balance for a fluctuating receptor and a binding pocket of size α at fixed position $h + \Delta$. The 2D binding affinity $\Delta\tilde{\mathcal{F}}(h)$ between the unbound and the bound state for a fixed membrane position at $h + \Delta$ is determined in a calculation comparable to eq. (7), yielding

$$\Delta\tilde{\mathcal{F}}(h) \approx \frac{\lambda}{2}(h - l_0 + \Delta)^2 - \epsilon_b^0 + \frac{1}{2}\ln\left(\frac{2\pi}{\lambda\alpha^2}\right), \qquad (17)$$

under the assumption $\alpha \ll \sqrt{2/\lambda} \ll h - l_0$. The local detailed balance condition connects the association and the dissociation rates to the 2D binding affinity $\Delta\tilde{\mathcal{F}}(h)$ by

$$\frac{k_{\mathrm{on}}(h)}{k_{\mathrm{off}}(h)} = \exp\left[-\Delta\tilde{\mathcal{F}}(h)\right]. \qquad (18)$$

Determining the left-hand side of eq. (18) with the h-dependent reaction rates, eq. (16) and comparing to the right-hand side of the detailed balance condition reveals the equality.

C. Effective reaction rates

The previously determined h-dependent reaction rates, eq. (16), have a functional dependence on the instantaneous membrane position h. However, the membrane

fluctuations live on a much shorter time scale than the association and dissociation events such that the membrane fluctuations equilibrate in the respective state. Thus, the height probability distributions for the membrane position in the respective states become

$$p_u^{\rm mem}(h) = \sqrt{\frac{\lambda_m}{2\pi}} \exp\left[-\frac{\lambda_m}{2}(h-h_0)^2\right],$$
$$p_b^{\rm mem}(h) = \sqrt{\frac{\lambda+\lambda_m}{2\pi}} \exp\left[-\frac{\lambda+\lambda_m}{2}(h-h_b)^2\right]. \quad (19)$$

Here, we use the elastic constant of the membrane λ_m and the mean membrane positions h_0 and h_b for the unbound and the bound state, respectively. The mean membrane position in the bound state,

$$h_b = \frac{\lambda_m h_0 + \lambda l_0}{\lambda_m + \lambda}, \quad (20)$$

is found by a force balance between the membrane and the receptor spring.

The aim of effective rates is to integrate the membrane fluctuations. The concept of effective reaction rates was proven recently [23], by directly comparing the adhesion dynamics and the domain growth of specific membrane adhesion in an effective simulation scheme with the results of a higher level simulation scheme that explicitly simulates the membrane fluctuations. We obtain the effective rates by convoluting the h-dependent reaction rates with the respective height probability distribution,

$$K_{\rm on} = \int_{-\infty}^{\infty} {\rm d}h\ k_{\rm on}(h) p_u^{\rm mem}(h),$$
$$K_{\rm off} = \int_{-\infty}^{\infty} {\rm d}h\ k_{\rm off}(h) p_b^{\rm mem}(h). \quad (21)$$

The effective association and dissociation rates are shown in Fig. 3 as a function of the mean height separation $\Delta h = h_0 - l_0$ and the fluctuation amplitude. The system parameters used to obtain the graphs are given in the figure caption. Independent of the particular form of the system parameters, we find systematically the association rate $K_{\rm on}$ is increased by either declining the height separation or by enhancing the membrane fluctuations. The opposite trend holds for the dissociation rate that is increased by either raising the height separation or by reducing the membrane fluctuations. Interestingly, the dissociation rate changes for the given height separations and fluctuation amplitudes by a factor of two, while the association rate changes for the same parameter ranges by more the 20 orders of magnitude. For all biological relevant parameter ranges the association rate is much more sensitive to variations in the membrane than the dissociation rate.

The effective reaction rates $K_{\rm on}$ and $K_{\rm off}$ depend only on system parameters and allow for an a priori calculation of the probability that the system is in the bound or the unbound state. The probability $\mathcal{P}_b$ to be in the bound state is given by

$$\mathcal{P}_b = \frac{K_{\rm on}}{K_{\rm on} + K_{\rm off}}, \quad (22)$$

and the probability for being in the unbound state is given by $\mathcal{P}_u = 1 - \mathcal{P}_b$.

The h-dependent reaction rates as well as the effective reaction rates contain various parameters unidentifiable in experimental systems. Some system parameters as, e.g., the height difference $h_0 - l_0$ between bound and unbound system and the elastic constants λ and λ_m can be determined in independent experiments. Others, e.g., the size of the binding pocket α can be estimated from molecular considerations. However, the load sharing factor θ and the depth of the binding pocket Δ are challenging to measure and both of them have great impact on the reaction rates in all levels of coarse-graining.

V. NON-TRIVIAL EFFECTS OF A STOCHASTIC BOND

A stochastic bond combines the unbound and the bound state of a membrane-bond system, coupling the properties of both states. Membrane quantities as, e.g., fluctuation amplitude or correlation functions, are measured with respect to the mean membrane height during the entire measurement. In a stochastic bond, jumping between states with possibly different mean membrane heights renders, for instance, the fluctuation amplitude not by the mean of the fluctuation amplitudes of the individual states. The stochastic process on its own is associated with a fluctuation amplitude and temporal correlations, too.

For all considerations concerning the stochastic bond, we impose the reaction rates deduced in the previous sections. To apply the effective rates, we assume first the time for transitions between states substantially small compared to the time in a state and, second, the effective reaction rates are independent of the membrane trajectory. Thus, the main property of the system describing the stochastic nature of the bond is given by the probability being in the bound or the unbound state, $\mathcal{P}_b$ and $\mathcal{P}_u = 1 - \mathcal{P}_b$, respectively. Our minimal model exhibits three processes, namely the fluctuations of an unbound membrane, the fluctuations of a bound membrane and a stochastic two-state process for jumping between the unbound and bound state. The latter is commonly described in a Bernoulli distribution of a stochastic two-state trajectory [33].

The mean membrane height at the position of a stochastic bond is given by the mean of the unbound and the bound membrane heights while each height is weighted with the probability being in the respective state. The mean membrane height in the unbound and the bound state is given by $h_u = h_0$ and h_b, respectively.

Consequently, the mean membrane height of the stochastic bond is

$$\langle h\rangle_{\rm tot} = (1-\mathcal{P}_b)h_0 + \mathcal{P}_b\frac{\lambda_m h_0 + \lambda l_0}{\lambda_m+\lambda}, \qquad (23)$$

where we used h_b from eq. (20).

A. Fluctuation amplitude

Experiments measuring the fluctuation amplitude of a membrane that adheres specifically to a rigid substrate from the unbound state to a permanently bound state show a non-monotonic fluctuation amplitude in the binding process [13]. In the first stage of the adhesion process establishing at the adhesion spot few bonds that form and break constantly, the fluctuation amplitude of the membrane increases. As soon as the adhesion spot is stabilized, the fluctuation amplitude decreases until, finally, the fluctuation amplitude of the bound state is reached. In our minimal model, we recover the main characteristics of this adhesion process.

The duration of the transition process between the unbound and the bound state are negligible and, thus, the fluctuation amplitude of the stochastic bond is given by the sum of three individual terms. The first and the second term are given by the fluctuation amplitude in the unbound and bound state of the membrane,

$$\langle \Delta h^2\rangle_u \equiv \langle (h(t)-h_0)^2\rangle = \frac{1}{\lambda_m} \qquad (24)$$

$$\langle \Delta h^2\rangle_b \equiv \langle (h(t)-h_b)^2\rangle = \frac{1}{\lambda_m+\lambda}, \qquad (25)$$

respectively. The third term $\langle\Delta h^2\rangle_{u\leftrightarrow b}$ is given by the fluctuation amplitude of the Bernoulli distribution convoluted with the squared height difference between the states, i.e.,

$$\langle \Delta h^2\rangle_{u\leftrightarrow b} = \mathcal{P}_b(1-\mathcal{P}_b)\left(\frac{\lambda}{\lambda_m+\lambda}\right)^2 (h_0-l_0)^2. \qquad (26)$$

Combining all three terms for the fluctuation amplitude of the stochastic bond results in

$$\begin{aligned}\langle \Delta h^2\rangle_{\rm tot} =& (1-\mathcal{P}_b)\langle\Delta h^2\rangle_u + \mathcal{P}_b\langle\Delta h^2\rangle_b + \langle\Delta h^2\rangle_{u\leftrightarrow b} \qquad (27)\\ =& \frac{1}{K_{\rm on}+K_{\rm off}}\left(\frac{K_{\rm off}}{\lambda_m}+\frac{K_{\rm on}}{\lambda_m+\lambda}\right)\\ &+\frac{K_{\rm on}K_{\rm off}}{(K_{\rm on}+K_{\rm off})^2}\frac{\lambda^2}{(\lambda_m+\lambda)^2}(h_0-l_0)^2.\end{aligned}$$

For $\mathcal{P}_b = 0$ and $\mathcal{P}_b = 1$, i.e., for the unbound and bound states, respectively, the fluctuation amplitudes of the stochastic two-state trajectory vanishes and the fluctuation amplitude of the respective pure states is recovered.

The fluctuation amplitude for the stochastic bond can easily exceed the maximal fluctuation amplitude of the pure states. The amplitude of the third term in eq. (27) is independent of the fluctuation amplitudes in the unbound and bound state and, thus, by tuning the mean height difference between the unbound and the bound membrane, $\langle\Delta h^2\rangle_{\rm stoch}$ could become large for $0 < \mathcal{P}_b < 1$. However, the probability $\mathcal{P}_b$ is directly connected to the effective reaction rates such that, for a dominant term $\langle\Delta h^2\rangle_{u\leftrightarrow b}$ in $\langle\Delta h^2\rangle_{\rm tot}$, the squared height difference between the unbound and the bound membrane has to exceed $1/\lambda_m$ significantly, which decreases the effective rates $K_{\rm on}$ and $K_{\rm off}$ to a minimum and transitions between the states become absent. Consequently, the system remains in either the unbound or the bound state and $\langle\Delta h^2\rangle_{u\leftrightarrow b}$, the fluctuation amplitude for transitions between the states, vanishes. Thus, the fluctuation amplitude of the stochastic bond exceeds the fluctuation amplitude of the unbound membrane typically only by little (see Fig. 4). For the parameters chosen, the fluctuation amplitude of the stochastic bond exceeds the fluctuation amplitude of the unbound membrane by about 10% for $\mathcal{P}_b \simeq 0.25$. Simulating the membrane by a time-discretized Langevin equation and imposing h-dependent reaction rates shows excellent agreement with the predicted fluctuation amplitude.

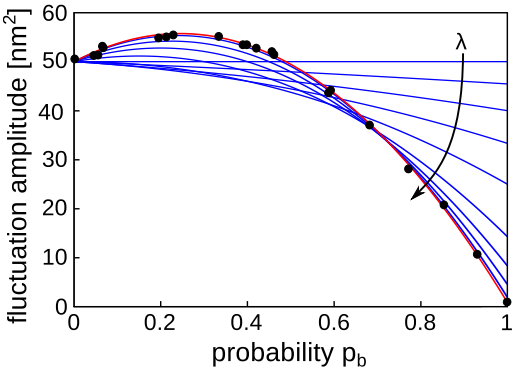

Figure 4. Fluctuation amplitude of a stochastic bond as a function of the probability $\mathcal{P}_b$ to find the system in bound state. For $\mathcal{P}_b = 0$ and $\mathcal{P}_b = 1$, the fluctuation amplitudes in the unbound and bound state are recovered, respectively. The membrane parameters are assigned with $\kappa = 20\,\mathrm{kT}$ and $\gamma = 1.29{\cdot}10^9\ \mathrm{J/m^4}$ and we use $h_0 - l_0 = 10\,\mathrm{nm}$. The stiffness of the bond is $\lambda/\lambda_m = 0, 0.1, 0.25, 0.5, 1, 2.5, 5, 10, 25$, increasing in the direction of the arrow. The red curve has $\lambda/\lambda_m = 50$ and shows excellent agreement with simulation data for the same parameters (black dots).

B. Spectral properties

After dealing with the fluctuation amplitude of a stochastic bond, we address temporal correlations in the height displacements of the membrane. We treat again the membrane height trajectory at the position of the bond for which we expect, motivated by the findings for the fluctuation amplitude, characteristic signs of the

stochastic association and dissociation in the temporal correlations.

The quantity of choice for measuring temporal correlations is the power spectral density, i.e., the Fourier transform of the temporal auto-correlation function into the frequency regime. For the unbound state, the power spectral density is well known [34],

$$\langle |h(\omega)|^2 \rangle_{\mathrm{u}} = \frac{4\eta}{\pi} \int_0^\infty \mathrm{d}q \, \frac{q^2}{(4\eta q \omega)^2 + (\kappa q^4 + \gamma)^2}. \tag{28}$$

$$\approx \begin{cases} \frac{\eta}{\sqrt{8}\sqrt[4]{\kappa^3\gamma^5}}, & \omega \ll \frac{\sqrt[4]{\kappa\gamma^3}}{\eta}, \\ \frac{1}{6\sqrt[3]{2\eta^2\kappa}}\omega^{-5/3}, & \omega \gg \frac{\sqrt[4]{\kappa\gamma^3}}{\eta}. \end{cases} \tag{29}$$

For a permanently bound membrane, we quantified the influence of the bond onto the membrane's power spectral density and introduced a first order correction [single-bond1]. According to this correction, the power spectral density of the bound state is

$$\langle |h(\omega)|^2 \rangle_{\mathrm{b}} = \tag{30}$$
$$= \frac{4\eta}{\pi} \int_0^\infty \mathrm{d}q \, \frac{\kappa q^4 + \chi}{\kappa q^4 + \gamma} \frac{q^2}{(4\eta q\omega)^2 + (\kappa q^4 + \chi)^2} \frac{1}{1 + \left(\frac{\lambda}{8\kappa q^2}\right)^2},$$

using the notation

$$\chi = \gamma \left(1 + \frac{\lambda}{\lambda_m}\right). \tag{31}$$

For both, the unbound and the permanently bound membrane the power spectral densities follow the same qualitative form and obey characteristic frequencies ω_u and ω_b, respectively, which separate the low frequency from the high frequency regime. In the low frequency regime, the power spectral density is a constant, while for the high frequency regime, the power spectral density decays algebraically with $\omega^{-5/3}$.

In our minimal model for the stochastic bond, the power spectral density is given by the sum of the power spectral densities in the unbound and the bound state, both weighted with the respective probability $\mathcal{P}_u$ and $\mathcal{P}_b$, and the power spectral density of the two-state trajectory. The latter is obtained by a Fourier transform of the auto-correlation function of the two-state trajectory that is proportional to an exponential decay with characteristic time scale $(K_{\mathrm{on}} + K_{\mathrm{off}})^{-1}$. The amplitude of the auto-correlation function is given by the fluctuation amplitude of the Bernoulli process, eq. (26). A Fourier transform reveals the power spectral density of the two-state trajectory

$$\langle |h(\omega)|^2 \rangle_{u\leftrightarrow b} = \tag{32}$$
$$= \frac{K_{\mathrm{on}} K_{\mathrm{off}}}{K_{\mathrm{on}} + K_{\mathrm{off}}} \frac{\lambda^2 (h_0 - l_0)^2}{(\lambda_m + \lambda)^2} \frac{1}{(K_{\mathrm{on}} + K_{\mathrm{off}})^2 + \omega^2},$$

which is a Lorentzian, i.e., a constant in the low frequency regime below the characteristic frequency $\omega_{u\leftrightarrow b} = K_{\mathrm{on}} + K_{\mathrm{off}}$ and decays algebraically with ω^{-2} in the high frequency regime. Consequently, we find the power spectral density of the stochastic bond as

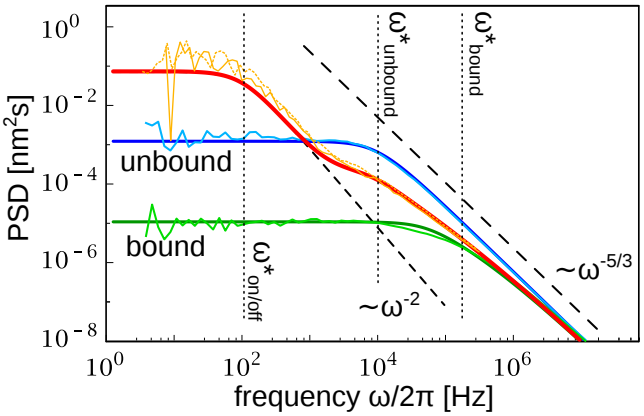

Figure 5. Power spectral densities for the unbound (blue), permanently bound (green) and stochastically bound (red) membrane. The thick curves show the analytical curves, whereas the thin curves show simulation results from 10^9 Langevin simulation steps with a single time step $t_s = 10^{-9}s$. Other parameters are $h_0 - l_0 = 10\,\mathrm{nm}$, $\eta = 1\,\mathrm{mPas}$, $\epsilon_b = 4.61\ kT$, $k_0 = 5000\,\mathrm{Hz}$, $K = 20\,\mathrm{kT/a^2}$, $\kappa = 20kT$ and $\gamma = 1.29 \cdot 10^9\ \mathrm{J/m^4}$

$$\langle |h(\omega)|^2 \rangle_{\mathrm{tot}}(\omega) = \tag{33}$$
$$= \mathcal{P}_u \langle |h(\omega)|^2 \rangle_u + \mathcal{P}_b \langle |h(\omega)|^2 \rangle_b + \langle |h(\omega)|^2 \rangle_{u\leftrightarrow b}.$$

In other words, it is characterized by a constant for the low frequency regime below the smallest characteristic frequency and decays with $\omega^{-5/3}$ in the high frequency regime above the largest characteristic frequency. The intermediate regime shows three characteristic frequencies, ω_u for the unbound membrane, ω_b for the permanently bound membrane and $\omega_{u\leftrightarrow b}$ for the Bernoulli process. In Fig. 5, the theoretical curve of the power spectral density for a stochastic bond follows closely the curves obtained from detailed dynamic simulations of the membrane (thin curves). Intriguingly, the theoretical curves were obtained by applying the effective reaction rates whereas the simulations use the h-dependent reaction rates for form and break a bond. Thus, this convincing agreement does not only confirm the considerations for the power spectral density but it is another independent validation of the concept of effective reaction rates.

The power spectral density of the stochastic bond depends critically on the probability $\mathcal{P}_b$ to be in the bound state. By varying the intrinsic binding affinity of the receptor, $\mathcal{P}_b$ changes and so does the power spectral density (Fig. 6). The most prominent variations arise from the power spectral density of the stochastic two-state trajectory, eq. (32), altering both, the characteristic frequency and the low frequency limit.

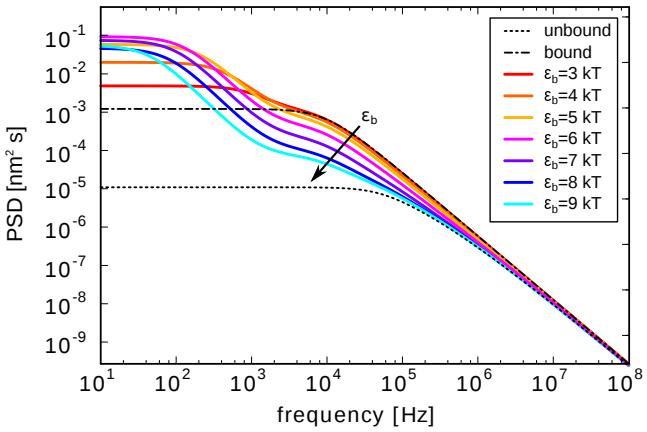

Figure 6. Power spectral densities of a stochastically bound membrane measured at the position of the bond for various binding affinities ϵ_b, as given in eq. (33). In the direction of the arrow, the binding affinity increases, transforming the power spectral density from the form of the unbound membrane (dash-dotted curve) towards the permanently bound membrane (dotted curve).

VI. CONCLUSION

Stochastic association and dissociation of a membrane-anchored adhesion protein is key to successful cell adhesion. In our microscopic model presented herein, we mapped a generic adhesion protein onto a harmonic spring omitting all molecular details and reduced the molecular complexity of a cell membrane to its main mechanical characteristics. By specifying the key-lock mechanism of the adhesion protein, we gained access to the 2D binding affinity and microscopic reaction rates for the binding events. Our microscopic model for the binding mechanism requires three additional parameters, namely the intrinsic binding affinity, the size of the binding pocket, and the shift in positions of the binding pocket to the first ligand-receptor encounter. Now, the full range of different types of adhesion proteins, from slip bonds to catch bonds, is within reach of our microscopic model.

With the given microscopic model of the binding event, we calculated the 2D binding affinity from the system's partition function. In the approximation of small binding pockets and a large difference between the minimum of the membrane-scaffold interaction potential and the mean position of the unbound adhesion protein, we found the 2D binding affinity built of three terms. The first term accounts for the static deformation of the adhesion protein and the membrane. The second term is the intrinsic binding affinity while the third term accounts for an entropic effect due to suppression of fluctuations modes in the membrane and the adhesion protein upon bond formation. However, without any approximations, the 2D binding affinity is inseparable into individual terms. For system parameters at the edge of biologically motivated parameters, the difference in the 2D binding affinity determined with and without approximations might sum up to few kT.

The stochastic bond lives for formation and rupture of the ligand-receptor bond. In our microscopic model, we have the possibility to calculate microscopic reaction rates which were obtained by freezing the membrane profile. In a biological system, the time scales of fluctuations of an adhesion protein are typically much faster than the fluctuations of the membrane. Thus, with the time scale separation, we average the receptor fluctuations and find h-dependent reaction rates. This first level of coarse-graining of the microscopic rates resembled the functional forms of Bell's and Dembo's rates. In a further level of coarse-graining, the membrane fluctuations were integrated into effective rates describing the transition rates of a two-state process from bound to unbound and vice versa.

Equipped with different levels of coarse-grained reaction rates, we addressed non-trivial effects of a stochastic bond. While the mean membrane position is given by the mean position of the bound and the unbound state, the fluctuation amplitude and the spectral properties show interesting effects. For instance, the fluctuation amplitude of a stochastic bonds may exceed the fluctuation amplitude of the unbound state. The additional fluctuation amplitude arises from the stochastic two-state trajectory. While this effect seems to be of only academic interest, first hints have been measured already in the formation of an adhesion cluster [25]. Other signs of a stochastic bond possibly detectable in experiments are three different time scales characterizing the power spectral density. Here, each of the processes, dynamics in the bound and the unbound state as well as the two-state process, add an individual term to the total power spectral density. In principal, from the decay of the power spectral density ($\sim \omega^{-2}$ for the stochastic two-state process and $\sim \omega^{-5/3}$ for the bound and unbound membrane) one could determine the dominant term unambiguously. However, experimental resolution limits set bounds and may change the high frequency decay of the power spectral densities [34]. Nevertheless, measuring the power spectral density of a stochastic bond offers beneficial insights into stochastic nature of an adhesion protein bound the a cell membrane.

[1] B. Alberts, A. Johnson, J. Lewis, M. Raff, K. Roberts, and P. Walter, *Molecular Biology of the Cell*, 5th ed. (Garland Science, Taylor & Francis Group, LLC, 2007).
[2] G.I. Bell, "Models for the specific adhesion of cells to

cells," Science **200**, 618–627 (1978).
[3] M. Dembo, D.C. Torney, K. Saxman, and D. Hammer, "The reaction-limited kinetics of membrane-to-surface adhesion and detachment," P. Roy. Soc. Lond. B Bio. **234**, 55–83 (1988).
[4] R. Alón, D. A. Hammer, and T. A. Springer, "Lifetime of the p-selectin-carbohydrate bond and its response to tensile force in hydrodynamic flow," Nature **374**, 539–542 (1995).
[5] R. Merkel, P. Nassoy, A. Leung, K. Ritchie, and E. Evans, "Energy landscapes of receptor–ligand bonds explored with dynamic force spectroscopy," Nature **397**, 50–53 (1999).
[6] S. Chen and T. A. Springer, "Selectin receptor–ligand bonds: Formation limited by shear rate and dissociation governed by the bell model," Proc. Natl. Acad. Sci. U. S. A. **98**, 950–955 (2001).
[7] B. T. Marshall, M. Long, J. W. Piper, T. Yago, R. P. McEver, and C. Zhu, "Direct observation of catch bonds involving cell-adhesion molecules," Nature **423**, 190–193 (2003).
[8] Y. Wu, J. Vendome, L. Shapiro, A. Ben-Shaul, and B. Honig, "Transforming binding affinities from three dimensions to two with application to cadherin clustering," Nature **475**, 510–513 (2011).
[9] T. Bihr, S. Fenz, E. Sackmann, R. Merkel, U. Seifert, K. Sengupta, and A.-S. Smith, "Association rates of membrane-coupled cell adhesion molecules," Biophys. J. **107**, L33–L36 (2014).
[10] L. Ju, J. Qian, and C. Zhu, "Transport regulation of two-dimensional receptor-ligand association," Biophys. J. **108**, 1773–1784 (2015).
[11] H. Krobath, G. J. Schütz, R. Lipowsky, and T. R. Weikl, "Lateral diffusion of receptor-ligand bonds in membrane adhesion zones: Effect of thermal membrane roughness," Europhys. Lett. **78**, 38003 (2007).
[12] E. Reister, T. Bihr, U. Seifert, and A.-S. Smith, "Two intertwined facets of adherent membranes: membrane roughness and correlations between ligand–receptors bonds," New J. Phys. **13**, 025003:1–15 (2011).
[13] S. F. Fenz, T. Bihr, R. Merkel, U. Seifert, K. Sengupta, and A.-S. Smith, "Switching from ultraweak to strong adhesion," Adv. Mater. **XX**, 1–5 (2011).
[14] D. Schmidt, T. Bihr, U. Seifert, and A.-S. Smith, "Coexistence of dilute and densely packed domains of ligand-receptor bonds in membrane adhesion," Europhys. Lett. **99**, 38003 (2012).
[15] N. S. Gov and S. A. Safran, "Red blood cell membrane fluctuations and shape controlled by atp-induced cytoskeletal defects," Biophys. J. **88**, 1859–1874 (2005).
[16] L. C.-L. Lin and F. L. H. Brown, "Dynamic simulations of membranes with cytoskeletal interactions," Phys. Rev. E **72**, 011910 (2005).
[17] J.-B. Fournier, D. Lacoste, and E. Raphaël, "Fluctuation spectrum of fluid membranes coupled to an elastic meshwork: jump of the effective surface tension at the mesh size," Phys. Rev. Lett. **92**, 018102 (2004).
[18] T. Auth and G. Gompper, "Fluctuation spectrum of membranes with anchored linear and star polymers," Phys. Rev. E **72**, 031904 (2005).
[19] R.-J. Merath and U. Seifert, "Nonmonotonic fluctuation spectra of membranes pinned or tethered discretely to a substrate," Phys. Rev. E **73**, 010401 (2006).
[20] T. Bihr, U. Seifert, and A.-S. Smith, "Nucleation of ligand-receptor domains in membrane adhesion," Phys. Rev. Lett. **109**, 258101 (2012).
[21] J. Hu, R. Lipowsky, and T. R. Weikl, "Binding constants of membrane-anchored receptors and ligands depend strongly on the nanoscale roughness of membranes," Proc. Natl. Acad. Sci. U. S. A. **110**, 15283–15288 (2013).
[22] J. Hu, G.-K. Xu, R. Lipowsky, and T. R. Weikl, "Binding kinetics of membrane-anchored receptors and ligands: Molecular dynamics simulations and theory," J. Chem. Phys. **143**, 243137 (2015).
[23] T. Bihr, U. Seifert, and A.-S. Smith, "Multiscale approaches to protein-mediated interactions between membranes—relating microscopic and macroscopic dynamics in radially growing adhesions," New J. Phys. **17**, 083016 (2015).
[24] D. Schmidt, T. Bihr, S. Fenz, R. Merkel, U. Seifert, K. Sengupta, and A.-S. Smith, "Crowding of receptors induces ring-like adhesions in model membranes," BBA-Mol. Cell Res. **1853**, 2984–2991 (2015).
[25] S. F. Fenz, A.-S. Smith, R. Merkel, and K. Sengupta, "Inter-membrane adhesion mediated by mobile linkers: Effect of receptor shortage," Soft Matter **7**, 952–962 (2011).
[26] J. O. Rädler, T. J. Feder, H. H. Strey, and E. Sackmann, "Fluctuation analysis of tension-controlled undulation forces between giant vesicles and solid substrates," Phys. Rev. E **51**, 4526–4536 (1995).
[27] R. Lipowsky, "Generic interactions of flexible membranes," in *Structure and dynamics of membranes*, edited by R. Lipowsky and E. Sackmann (Elsevier, 1995) Chap. 11, pp. 521–602.
[28] U. Seifert, "Configuratios of fluid membranes and vesicles," Adv. Phys. **46**, 13–137 (1997).
[29] M. E. Fisher and A. B. Kolomeisky, "The force exerted by a molecular motor," Proc. Natl. Acad. Sci. U.S.A. **96**, 6597–6602 (1999).
[30] A. B. Kolomeisky and M. E. Fisher, "Molecular motors: a theorist's perspective," Annu. Rev. Phys. Chem. **58**, 675–695 (2007).
[31] P. Atkins and J. De Paula, *Physical chemistry for the life sciences* (Oxford University Press, USA, 2011).
[32] E. Reister-Gottfried, S.M. Leitenberger, and U. Seifert, "Diffusing proteins on a fluctuating membrane: Analytical theory and simulations," Phys. Rev. E **81**, 031903 (2010).
[33] M. Evans, N. Hastings, and B. Peacock, *Statistical distributions* (IOP Publishing, 2001).
[34] T. Betz and C. Sykes, "Time resolved membrane fluctuation spectroscopy," Soft Matter **8**, 5317–5326 (2012).

P7

Crowding of receptors induces ring-like adhesions in model membranes

Crowding of receptors induces ring-like adhesions in model membranes

D. Schmidt[1,2], T. Bihr[1,2], S. Fenz[3,4], R. Merkel[3], U. Seifert[2], K. Sengupta[5], and A.-S. Smith[1,6]

[1] Institut für Theoretische Physik and Cluster of Excellence: Engineering of Advanced Materials, Friedrich Alexander Universität Erlangen-Nürnberg, 91052 Erlangen, Germany
[2] II. Institut für Theoretische Physik, Universität Stuttgart, 70569 Stuttgart, Germany
[3] Institute of Complex Systems 7: Biomechanics, Forschungszentrum Jülich GmbH, 52425 Jülich, Germany
[4] Lehrstuhl für Zell- und Entwicklungsbiologie (Zoologie I), Biozentrum der Universität Würzburg, 97074 Würzburg, Germany
[5] Aix-Marseille Université, CNRS, CINaM UMR 7325, 13288 Marseille, France
[6] Insitut Ruđer Bošković, 10000 Zagreb, Croatia

Biochim. Biophys. Acta (2015)

DOI: 10.1016/j.bbamcr.2015.05.025
http://www.sciencedirect.com/science/article/pii/S0167488915001792

ABSTRACT The dynamics of formation of macromolecular structures in adherent membranes is key to a number of cellular processes. However, the interplay between protein reaction kinetics, diffusion and the morphology of the growing domains, governed by membrane mediated interactions, is still poorly understood. Here we show, experimentally and in simulations, that a rich phase diagram emerges from the competition between binding, cooperativity, molecular crowding and membrane spreading. In the cellular context, the spontaneously-occurring organization of adhesion domains in ring-like morphologies is particularly interesting. These are stabilized by the crowding of bulky proteins, and the membrane-transmitted correlations between bonds. Depending on the density of the receptors, this phase may be circumvented, and instead, the adhesions may grow homogeneously in the contact zone between two membranes. If the development of adhesion occurs simultaneously with membrane spreading, much higher accumulation of binders can be achieved depending on the velocity of spreading. The mechanisms identified here, in the context of our mimetic model, may shed light on the structuring of adhesions in the contact zones between two living cells.

Biochimica et Biophysica Acta 1853 (2015) 2984–2991

Contents lists available at ScienceDirect

Biochimica et Biophysica Acta

journal homepage: www.elsevier.com/locate/bbamcr

Crowding of receptors induces ring-like adhesions in model membranes☆

Daniel Schmidt [a,b], Timo Bihr [a,b], Susanne Fenz [c,d], Rudolf Merkel [c], Udo Seifert [b], Kheya Sengupta [e], Ana-Sunčana Smith [a,f,*]

[a] Institut für Theoretische Physik and Cluster of Excellence: Engineering of Advanced Materials, Friedrich Alexander Universität Erlangen–Nürnberg, 91052 Erlangen, Germany
[b] II. Institut für Theoretische Physik, Universität Stuttgart, 70569 Stuttgart, Germany
[c] Institute of Complex Systems 7: Biomechanics, Forschungszentrum Jülich GmbH, 52425 Jülich, Germany
[d] Lehrstuhl für Zell- und Entwicklungsbiologie (Zoologie I), Biozentrum der Universität Würzburg, 97074 Würzburg, Germany
[e] Aix-Marseille Université, CNRS, CINaM UMR 7325, 13288 Marseille, France
[f] Insitut Ruđer Bošković, 10000 Zagreb, Croatia

ARTICLE INFO

Article history:
Received 9 March 2015
Received in revised form 21 May 2015
Accepted 22 May 2015
Available online 28 May 2015

Keywords:
Cell adhesion
Immunological synapse
Adhesion dynamics
Membrane transmitted correlations
Ligand-receptor bonds
Crowding effects
Membrane fluctuations
Diffusion–reaction systems

ABSTRACT

The dynamics of formation of macromolecular structures in adherent membranes is a key to a number of cellular processes. However, the interplay between protein reaction kinetics, diffusion and the morphology of the growing domains, governed by membrane mediated interactions, is still poorly understood. Here we show, experimentally and in simulations, that a rich phase diagram emerges from the competition between binding, cooperativity, molecular crowding and membrane spreading. In the cellular context, the spontaneously-occurring organization of adhesion domains in ring-like morphologies is particularly interesting. These are stabilized by the crowding of bulky proteins, and the membrane-transmitted correlations between bonds. Depending on the density of the receptors, this phase may be circumvented, and instead, the adhesions may grow homogeneously in the contact zone between two membranes. If the development of adhesion occurs simultaneously with membrane spreading, much higher accumulation of binders can be achieved depending on the velocity of spreading. The mechanisms identified here, in the context of our mimetic model, may shed light on the structuring of adhesions in the contact zones between two living cells. This article is part of a Special Issue entitled: Mechanobiology.

1. Introduction

Reorganization of cell surface molecules at the adhesive interface is recognized as an essential feature of cell adhesion and has been extensively studied in the context of integrins, cadherins, and many other cell adhesion molecules [1–6]. A particularly intriguing example is the drastic molecular rearrangement at the interface between a T lymphocyte and an antigen presenting cell, leading to the formation of concentric rings, each enriched in certain specific cell surface molecules [1]. Interestingly, T cells interacting with supported lipid bilayers (SLBs) carrying mobile ligands reproduce this phenomenon [2], and studies on such hybrid systems have revealed the detailed structure and dynamics of formation of these so called SMACs (Supra Molecular Adhesion Structures) [4,3] and elucidated the connection to receptor mobility [5]. From a theoretical perspective, several groups have proposed different effects as the possible driving mechanism for ring-like SMAC formation. These include differences in binding affinity and stiffness [7,8], biased diffusion of antigen complexes towards the interior of the synapse [9] and membrane driven interaction between binding pairs of different lengths [10–15]. The current consensus in the immunology community, based on seemingly decisive experiments with size modified binders [16,17], is that if two types of binders are not of different length the segregation is disrupted. In this context, theoretical considerations suggest that even with two binders, ring-like SMACs are unstable [12].

However, recent experiments showed that the T cell receptor is actually driven by actin, obviating the need to invoke the difference in length between the receptors to explain segregation [4].

Very recently, a ring like structure was also found during the formation of tight junctions in spreading epithelial cells [6]. While the late stage of spreading, which takes place after the ring is formed, is clearly driven by actin, the mechanism for the initial structuring of cadherin adhesions into a ring like structure is not yet understood [6].

Adhesion experiments with model membranes, where the cell in hybrid systems described above is replaced by a giant unilamellar vesicle (GUV, for a sketch of the model see Fig. 1), have furthered our understanding of membrane adhesion, and have vastly aided theoretical

☆ This article is part of a Special Issue entitled: Mechanobiology.

* Corresponding author at: Institut für Theoretische Physik and Cluster of Excellence: Engineering of Advanced Materials, Friedrich Alexander Universität Erlangen–Nürnberg, 91052 Erlangen, Germany and Insitut Ruđer Bošković, 10000 Zagreb, Croatia.
E-mail address: smith@physik.uni-erlangen.de (A.-S. Smith).

http://dx.doi.org/10.1016/j.bbamcr.2015.05.025
0167-4889/

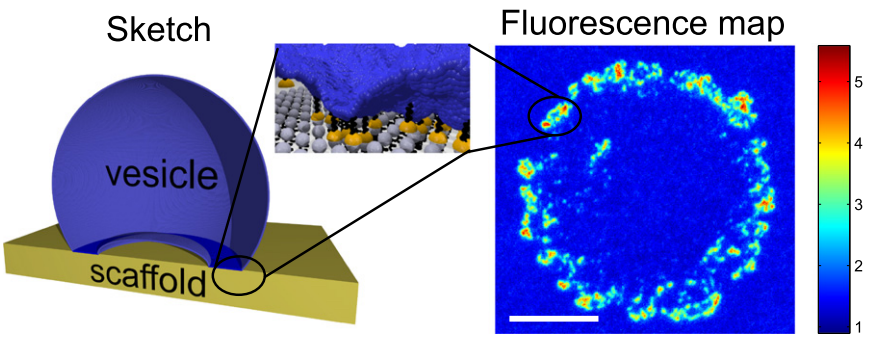

Fig. 1. Left: Cartoon of the system involving a vesicle (blue) which adheres to a scaffold (yellow). The specific adhesion domain (dark-blue and zoom-in on right side) forms a ring. For better visibility, a cut through the vesicle is shown. The inset visualizes a typical microscopic membrane profile. Vertical and lateral dimensions are not to scale. Right: Fluorescence map of a vesicle showing the accumulated receptors in a color code (units in 10^3 μm^{-2}). The scale bar is 10 μm.

modeling [18–20]. In many cases, especially if the GUV is floppy, a ring like domain was seen [21]. However, in most of these cases, the ring, observed in reflection interference contrast microscopy (RICM) images as a dark domain, is transient [21]. One notable exception was reported recently where biotin carrying GUVs adhering to neutravidin carrying SLBs gave rise to SMAC like rings of fluorescent labeled receptors [22]. These rings, formed under conditions of receptor shortage, were reported to be long lived and seemingly stable.

From a theoretical point of view, a thermodynamically stable ring-like domain should be associated with a global minimum of the free energy of adhesion. The latter can be calculated for a fixed number of bonds confined to a particular configuration (see Fig. 2). In this case, the free energy of an adhesion domain emerges as a sum over all bonds for the gain in binding enthalpy and the cost for deforming both the flexible membrane and the adhesion proteins. Additional entropic costs emerge from confining the diffusive binders upon the formation of the bond [23–25] and for suppressing membrane fluctuations. Such a free energy possesses a global minimum for a topologically circular domain where the bond density is not maximal, but is determined by balance of energetic terms that favor maximal bond density and the entropic terms that push the bonds apart. However, we find that in addition to the global minimum, a local minimum exists for a ring-like topology. Since the free energy difference between the global and the meta-stable ring configuration is of several k_BT per bond (see Fig. 2), it is not clear, even for model membranes, what leads to the formation of adhesions in a ring configuration. In the cellular context, coupling to the actin was found to play a major role at longer time scales, but the mechanism for the selective binding at the edge of the contact zone has not been clearly identified yet.

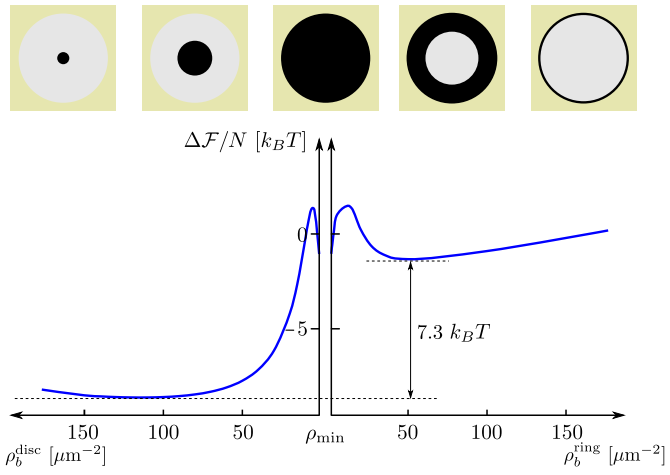

Fig. 2. Free energy per bond $\Delta\mathcal{F}/N$ for a bond domain with a circular (left) and ring like (right) shape. The sketches in the top row illustrate the domain area (black) in the contact zone (gray) accordingly to the axis in the graph. For the circular domain the bond density decreases from left to right while for the ring-like domain it increases. The number of bonds is fixed to $N_b = 200$ for all bond densities with $\rho_{\min} \approx 1.4$ μm^{-2}. All other parameters are chosen according to Table 1.

The aim of our current work is to deepen the understanding of the physical mechanisms that determine the number of adhesion domains, their growth patterns and final morphology. The goal is to identify physical mechanisms that drive the formation of ring-like adhesions, which were experimentally observed in model systems but also in the cellular context. In the latter case, this work may shed light on the role of active processes (not considered here explicitly), which can be used to control the dynamics and the emergent structure of adhesions, including the ring-shaped domains. We achieve this goal by performing an extensive theoretical analysis of the experimentally observed phenomena. We show that ring like structures appear spontaneously in vesicular systems due to the interplay of slow protein diffusion and fast binding kinetics, which results in the formation of bonds at the periphery of the vesicle-substrate contact zone. Furthermore, we find that the necessary conditions for the formation of stabilized rings are (i) the mobility of both binding partners, (ii) membrane transmitted correlations, (iii) bulkiness of binders which allows for crowding and (iv) a significant slowing down of bulky receptors upon binding.

Following this introduction, we first present details of the experimental and simulation procedures. We proceed with constructing the phase diagrams of adhesion for mobile and immobile receptors on the supported bilayer. We analyze and analytically model the identified regimes of growth, and study the stability of ring-like structures. We compare our theoretical framework to the experimental result, and find excellent agreement between the two approaches.

2. Experimental methods

Giant unilamellar vesicles (GUVs) containing a specified amount (0.1 to 5%) of DOPE-cap-biotin (1,2-dioleoyl-sn-glycero-3-phosphoethanolamine-N-(cap biotinyl)) and 2% DOPE-PEG2000 (1,2-dioleoyl-sn-glycero-3-phosphoethanolamine-N-(methoxy (polyethyleneglycol)-2000)), dispersed in a matrix of SOPC (1-stearoyl-2-oleoyl-sn-glycero-3-phosphocholine) (all from Avanti Polar Lipids, Alabaster), are prepared by electro-swelling [26]. Supported lipid bilayers (SLBs) of equivalent composition are prepared by the Langmuir–Blodgett/Langmuir–Schäfer technique and are functionalized with neutravidin covalently linked to the fluorescent label Oregon Green or tetra-methylrhodamine (neutravidin-fl, both Invitrogen, Eugene, OR) and suitable passivated with bovine serum albumin (BSA, 98% purity, Sigma, Saint Louis, MO) (both reconstituted in PBS buffer and ultracentrifugated to eliminate protein aggregates) [26]. The experimental design ensures that both ligands (biotins) and receptors (neutravidins) are mobile [26]. The amount of biotinylated lipids in the GUV and SLB determines the density of ligands and receptors,

respectively. In a typical experiment, 10 μl of the vesicle solution is added to the SLB in a total volume of 1 ml PBS buffer.

Vesicles adhering in steady state are identified by imaging with reflection interference contrast microscopy (RICM) [27,28]. The corresponding receptor distribution of neutravidin-fl is recorded with epifluorescence microscopy using a 63× Antiflex Plan-Neofluar 1.25 oil objective.

The enrichment factor of the receptors, which reflects how much receptors are accumulated in the contact zone, relative to the bulk density, is calculated as described earlier [22]. The diameters of GUVs are determined from phase contrast microscopy in the final state and typically range from 20 to 30 μm.

3. Simulation method

To simulate the process of domain formation we use our recently developed Monte Carlo approach [29]. In this scheme, the vesicle membranes and the SLB membranes are represented by rectangular superimposed grids (lateral size of 40.96 μm), functionalized with ligands and receptors, respectively. To account for different sizes of ligands and receptors, the two lattices have different lattice constants (the lattice constant of the ligand grid is 8 times smaller (4096×4096 lattice nodes) than that of the receptor grid).

A circular region is selected on each membrane to represent a contact zone. Both the vesicle membrane and the SLB are treated as reservoirs with a constant number of binders. In both cases periodic boundary conditions for binder diffusion are imposed at the edge of the system. Diffusion is simulated by a simple random walk (diffusion constant D) of particles that mutually interact in the plane of the membrane by hard core repulsion.

To simulate creation and disruption of bonds, we use effective binding and unbinding rates [30], which are sensitive to the local configuration of bonds [31], and integrate the local shape and fluctuations of the vesicle membrane [29]. Binding attempts take place when a free ligand and a free receptor find each other at the same lateral position. Motivated by experimental findings [32,26] which suggest a drastic decline of the mobility of a ligand-receptor complex compared to the diffusion of the unbound species, the formation of a bond is associated with the immobilization of the involved ligand and receptor. If a bond breaks, the ligand and the receptor regain their initial mobility.

The simulation starts by randomly placing ligands on their lattice (lattice constant a) such that the desired ligand density ρ_l^0 is obtained. Furthermore, if the receptors are deemed immobile, they are regularly spaced on their lattice at separations of $\bar{r} = 1/\sqrt{\rho_r^0}$. Alternatively, when simulating mobile receptors, a randomly distributed starting configuration is generated, with the appropriate density ρ_r^0. The simulation is executed until the number of bonds saturates for a significant amount of time.

To be able to compare with experiments, in the simulation we choose the membrane bending rigidity to be $\kappa = 20\ k_BT$ [33], the strength of the interaction potential $\gamma = 6.5\ \mathrm{J/cm^2}$ [34]. The difference between the equilibrium position of the unbound vesicle membrane and the height for specific adhesion to the substrate is set to $\Delta h = 45$ nm and the vesicle radius is $R = 11.6$ μm with a volume fraction of 97.5% (standard average conditions in the experiments). The binding enthalpy of the biotin–neutravidin bond is taken to be $\epsilon_b \approx 10\ k_BT$ in accordance with previous estimates [22] for the enthalpy of membrane bound biotin–neutravidin bonds, which is considerably weakened because of the coupling of the ligands and receptors to the membrane. All parameters are summed up in Table 1.

Table 1
Parameters used in the simulations.

	Meaning	Value
a	Lattice constant	10 nm
k_BT	Thermal energy at 300 K	$4.14 \cdot 10^{-21}$ J
κ	bending rigidity [33]	20 k_BT
γ	Curvature of the interac. pot.†	6.5 J/cm^4
Δh	Distance between equilibrium Positions of membr. and bond†	45 nm
λ	Stiffness of the bond/receptor*	0.21 mJ/m^2
ϵ_b	Binding enthalpy [22]	9.55 k_BT
D	Diffusion constant [26]	5.0 μm^2/s
R_c	Radius of contact zone†	6.81 μm
d	Lateral size of simulation box (size of the vesicle)†	40.96 μm

† Measured.
* Typical value from literature.

4. Morphological phase diagram

The analysis of simulation and experimental data shows that there are, in principle, four regimes of adhesion processes, mainly determined by the initial ligand and receptor density (Fig. 3). The first is the regime of unstable adhesion at low ligand and receptor densities. Increasing the density of at least one of the binders enables adhesion. Several morphologically different processes ensue. If the density of ligands is larger than the receptor density, numerous randomly distributed nucleation seeds form within the contact zone. The domains grow independently of each other until they come in direct contact and merge, developing further as a large, single domain. We denote this as the regime of multiple nucleation (first row in Fig. 3C). At higher densities of immobile receptors we find a transient ring regime (second row in Fig. 3C). It occurs because ligands diffuse from the bulk of the vesicle into the contact zone, where they bind to the surplus of receptors close to the edge of the contact zone, forming a ring. However, due to the small size of ligands, they are able to diffuse through a bond domain restoring the ligand density in the interior of the ring and continue thickening the ring. Furthermore, upon unbinding from the inner edge of the ring, the ligands move deeper into the contact zone, making the ring morphology only transient. At low densities of mobile receptors, the ring morphology is stabilized by the inability of bulky receptors to penetrate the contact zone (stable ring shown in the third row in Fig. 3C). The large packing density of receptors stabilizes the morphology on time scales that are significantly longer than those accessible in an experiment (stable ring regime).

4.1. Unstable adhesion

For very small ligand and receptor densities, only single bonds opening and closing over the whole contact zone could be observed without ever forming a stable nucleus. We also find that for the current choice of the binding affinity, temperature and membrane bending stiffness, enthalpic arguments [30] predict the critical size of the seed to be two or more bonds. Actually, for immobile receptors, the critical size of the nucleus diverges if the density of bonds (receptors) or ligands becomes too low (dashed line in Fig. 3). For mobile ligands, the density of bonds is self-regulated and typically sufficiently large, such that the adhesion should never be impeded. Indeed, the unstable regime occurs at significantly lower densities than for immobile receptors. However, eventually the domains no longer appear even if receptors are mobile, which suggests that the nucleation process is diffusion limited at very low binder densities. Namely, while the ligands and receptors form occasionally one bond, the time necessary for another pair of binders to diffuse and form the second bond is longer than the life time of the first bond. This, in effect, impedes nucleation.

4.2. Multiple nucleation

This growth regime is reaction limited (initial receptor density ρ_r^0 smaller than initial ligand density ρ_l^0) and it occurs because the nucleation rate is large (the full lines indicate the cross-over from diffusion to reaction limited regimes in Fig. 3A and B). However, the multiple

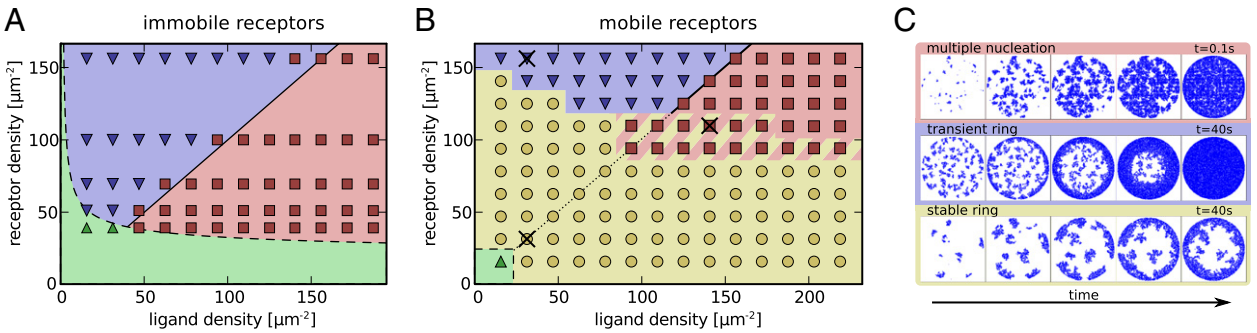

Fig. 3. Phase diagrams for immobile (A) and mobile receptors (B), showing the four regimes of growth: (i) unstable adhesion (green) (ii) regime of multiple nucleation (red) characterized by the formation of small domains all over the contact zone, (iii) transient rings (blue), (iv) stable rings (yellow). (C) Time evolution of adhesions in the contact zone for the three adhesive regimes. The particular parameters are marked in (B) with crosses. Growth dynamics of adhesion obtained in simulations is provided in supplementary material in a form of a movie for each phase.

nucleation regimes are not always accessible in the phase space. For example, a smaller binding affinity leads to a coarsening of the adhesion process, i. e. larger individual adhesion domains and fewer nucleation seeds, and ultimately to radial growth [35]. While having immobile receptors, we find this regime to overlap with the reaction limited part of the phase space, for mobile receptors multiple nucleation occurs at high binder densities where diffusion into the contact zone plays no role and the receptors are almost immobile due to crowding. On the other hand, the surplus of ligands keeps the nucleation rate constant.

This situation is well accounted by the Johnson–Mehl—Avrami–Kolmogorov-theory (JMAK) [36,37] describing the growth dynamics of domains that nucleate at constant nucleation rate Γ and grow with a radial velocity v, independent of time. Under these conditions the number of bonds as a function of time is given by [37]

$$N_b(t) = N_{\mathrm{eq}}\left(1-\exp\left[-\frac{\pi}{3}\Gamma v^2 t^3\right]\right) \tag{1}$$

where N_{eq} denotes the number of bonds in equilibrium and the growth curve has a cubic time dependence in the exponent.

A comparison of this theory with exemplary simulation data with mobile (Fig. 4, yellow diamonds) and immobile receptors (red squares and blue circles) shows reasonable agreement. Small deviations in the growth law arise because the domains do not grow independently due to the relatively small area they are confined to. Furthermore, the vesicle reservoir of ligands becomes depleted over time, affecting both the nucleation rate and the growth velocity. Ultimately, the simulation growth curve saturates and the equilibrium state is achieved.

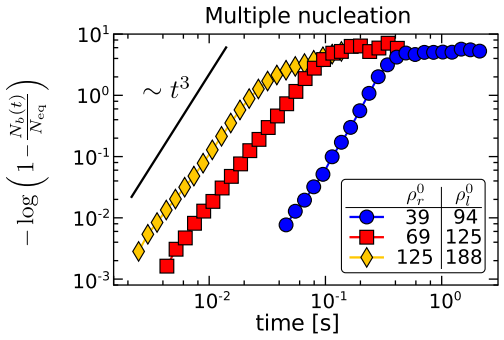

Fig. 4. Avrami plot for three exemplary curves of domain growth in the multiple nucleation regime. The solid black line is a cubic function for comparison with analytical prediction, Eq. (1). Yellow diamonds originate from mobile receptors whereas red squares and blue circles belong to immobile receptors. The densities in the legend are in units of μm^{-2}.

4.3. Transient ring

The formation of a transient ring morphology (blue shaded regions in Fig. 3 A and B) is driven by the diffusion of ligands into the contact zone, where an enthalpy gain is induced upon binding. The formation of transient rings occurs if the initial density of receptors is larger than the initial density of ligands, and if the diffusion of receptors plays no role (immobile receptors or high density of mobile receptors). Because of the relatively large binding affinity, and the surplus of receptors, the ligands bind relatively fast after penetrating the contact zone. This promotes nucleation and a faster growth of domains at the periphery of the contact zone. Eventually, these domains merge and form a ring (identified as an enhancement in the radially averaged bond density close to the edge of the contact zone, relative to the density at the center). However, because of their small size, ligands can move between bonds in the ring. If not bound in the ring, the ligands may penetrate through the ring and bind to free receptors in the interior of the contact zone. This leads to thickening of the ring until it is completely transformed to a disk and the entire contact zone is filled with bonds (second row in Fig. 3C).

As the limiting time scale of the ring closure is determined by diffusion dynamics, the reaction kinetics, earlier important in the regime of multiple nucleation, do not need to be considered. Hence, the dynamics ensuing the establishment of the ring can be modeled by the radially symmetric diffusion equation for the ligand density $\rho_l(r, t)$ [38–41]

$$\frac{\partial \rho_l(r,t)}{\partial t} = D\left(\frac{\partial^2 \rho_l(r,t)}{\partial r^2} + \frac{1}{r}\frac{\partial \rho_l(r,t)}{\partial r}\right). \tag{2}$$

Here D is the diffusion constant of ligands, the radial distance r is measured from the center of the contact zone, and the bond density within the ring will be denoted by ρ_b. This equation is accompanied with a moving boundary condition for the inner radius $R(t)$ of the ring

$$\frac{\partial R(t)}{\partial t} = -\frac{D}{\rho_b}\frac{\partial \rho_l(r,t)}{\partial r}\bigg|_{r=R(t)}, \tag{3}$$

and the density of ligands at the inner interface

$$\rho_l(R(t),t) = \rho_l^e. \tag{4}$$

Initial conditions intuitively set the density of ligands and the thickness of the ring at $t = 0$ to be

$$\rho_l(r,0) = \rho_l^0, \quad \text{and} \quad R(0) = R_c. \tag{5}$$

Since no full analytic solution is available for this moving boundary problem, Eqs. (2) to (5) are solved numerically for $\rho_l^e = 0$ and ρ_b is extracted from simulations. The solution is compared with the results of

the simulation in Fig. 5A. Without any fit parameters, we find excellent agreement between the two approaches confirming that the closure of the ring is mainly driven by the diffusion of ligands from the bulk of the vesicle into the contact zone.

Interestingly, the dynamics of the ring closure is stable with respect to the shape of the inner interface. This is unusual behavior for diffusion limited growth processes where typically dendritic or even fractal patterns evolve in time [42,43]. However, this can be understood from the ligand density profile around a ring domain with shape perturbations at the inner interface (Fig. 5B). Because the flux of ligands from the outside is larger at trailing parts of the interface than at the leading parts, the shape instability is suppressed and the inner shape of the ring is stabilized.

4.4. Stable rings

Formation of the stable ring morphology (yellow shaded regions in Fig. 3B) is driven by the diffusion of receptors into the contact zone. It occurs at densities where the receptor mobility is not significantly impeded by crowding effects (low receptor densities), but is sufficiently large for stable nucleation to take place. For this reason, the stable ring regime strongly relies on the membrane-transmitted cooperative effects between bonds.

The importance of cooperativity is clearly demonstrated in Fig. 6A, where we show snapshots from a simulation without (left) and with (right) the membrane implicitly resolved. In the first case the formation of bonds does not affect the shape and the fluctuations of the membrane (no cooperativity), hence, the ligand-receptor reaction rates are constant. In the second case, the reaction rate is coupled to the membrane as discussed in the method section. Due to this cooperativity, the bonds organize into domains, and the number of bonds is an order of magnitude larger compared to the case without the membrane transmitted interactions between bonds. In the latter case, the bonds are randomly distributed over the contact zone. In fact, without correlations, nucleation is suppressed, and stable adhesion may not take place. If this occurs, the formation of the ring is significantly delayed. Yet, in the latter case, the closing of the ring occurs on significantly shorter time scales than for stable rings, suggesting a transient ring regime.

The stability of the ring is hence promoted by the cooperative effects which promote binding in the vicinity of already existing bonds. However, because of their size, bulky bound receptors become obstacles for diffusing receptors, which slow down their transport toward the center of the contact zone, and further promote their binding at the edge. This induces crowding of receptors and seals the interior of the contact zone from the outer reservoir of binders. Another consequence of cooperativity is the significantly diminished unbinding rate. Hence, even receptors at the inner edge unbind extremely rarely, which suppresses further thickening of the ring on experimentally accessible time scales.

In very long simulations (Fig. 6B), however, we observe the increase of the ring thickness of about 50% after extending the simulation to an order of magnitude longer than time necessary for the formation of the ring. This suggest, that ultimately, even “stable” ring-like domains are, in essence, transient even though not on accessible time scales. However, as the ring growth depends solely on the unbinding and rebinding of bonds at the inner edge of the ring domain, increasing the effective binding affinity drastically decreases the growth of the ring.

Last but not least, the stability of the phase diagram depends on the system size. For example, decreasing the number of available ligands by keeping the same concentration but decreasing the size of the vesicles, at some point induces a shortage of ligands. Hence, the small domains may not merge to cover the entire contact zone or to close the rings. On the other hand, quadrupling the area of the vesicle (ligand reservoir of 8192×8192 lattice points for a vesicle of a radius $R = 23.1$ μm) induced no changes in the phase diagram.

Additional effects arise from the finite size of the contact zone. It does not affect the regimes of transient ring formation and multiple nucleation. However, for smaller radii of the contact zone, the phase space for the formation of stable rings shrinks because the ring thickness depends only on the concentrations of binders and not on their absolute number. The thickness of the ring is related to the length of the mean free path of a receptor coming from the bulk into the contact zone before forming a bond. If the contact zone is smaller than this mean free path, the receptor can explore the surface entirely, and the contact zone will be filled up with bonds. Conversely, increasing the size of the contact zone increases the phase space associated with stable rings.

5. Comparison with the experiments

5.1. Steady state morphology and size of adhesions

To study the interplay between protein diffusion, binding kinetics, and membrane transmitted correlations in an experimental system, we construct the experimental phase diagram for adhesion of a biotin decorated vesicle that binds to SLB with mobile neutravidins. We systematically change the concentration of neutravidin and of biotin and image the distribution of neutravidin in the steady state in 44 vesicles (Fig. 7A).

In previous work [28], we showed that within biotin–neutravidin adhesions the membrane is nearly flat, very close to the SLB, and fluctuations are completely suppressed (< 1 nm). This suggests that the affinity for biotin–neutravidin binding is very high, and that each neutravidin in the contact zone is bound to its ligand [25]. This is confirmed by simulations where we find that the number of bonds is at least 95% of the number of available receptors, even though the binding affinity used in simulations is smaller than the binding affinity of a biotin–neutravidin

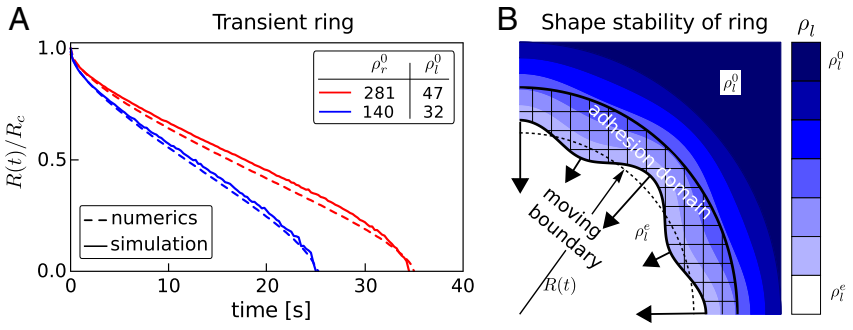

Fig. 5. A) Dynamics of the ring closure from simulations (solid lines) and the numerical model (dashed lines). B) Ligand density profile around a perturbed inner edge of the ring-like domain (shaded with squares). Arrows represent the magnitude and the directions of the flux of ligands towards the interior. The unperturbed interior edge is shown with a dotted line.

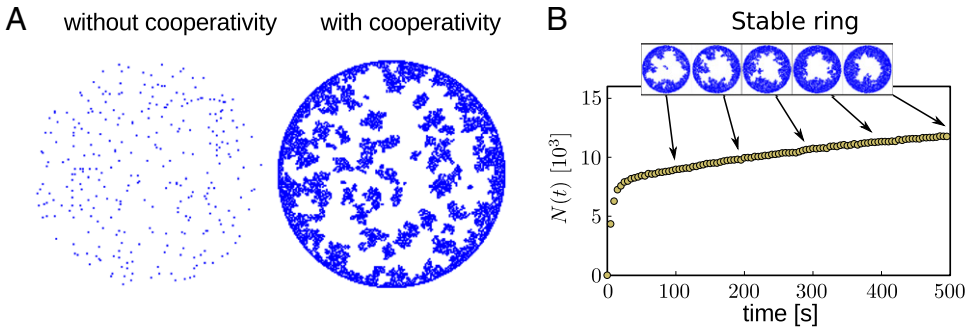

Fig. 6. A) Snapshots of the contact zone in steady state. A snapshot of the contact zone for a system without cooperativity (left), is compared to the contact zone from the full simulation including membrane induced cooperative effects between bonds (right). Both simulations are performed with identical parameters as stated in the simulation method section, except for the effective binding affinity which was increased to 15 k_BT. The binder densities are set to $\rho_l^0 = \rho_r^0 = 31\ \mu m^{-2}$. B) A very long simulation in the stable ring regime with an effective binding affinity of 10 k_BT shows slow thickening of the ring. Increasing the binding affinity slows down the thickening of the ring (data not shown).

pair within adhesions. The same result can be visualized by comparison of the bond and receptor distributions (Fig. 7B and C).

Compared to biotin ligands, neutravidin receptors are very large, and are expected to crowd when penetrating the contact zone, and hence, induce stable rings. Indeed, as in simulations, at high concentrations of receptors the contact zone is uniformly filled with bonds, but decreasing the receptor concentration results in the appearance of ring-like adhesions.

If the concentration of receptors is low, increasing the ligand density for a fixed receptor density, decreases the average area of adhesions (Fig. 7B, bottom rows) and, moreover, the ring thickness d decreases, too (Fig. 8A). For example, for vesicles shown in Fig. 7A, increasing the ligand density by factor of 10 from $\rho_l^0 = 1.4 \cdot 10^3\ \mu m^{-2}$, induces a decrease of the adhesion area from 51% to 35% of the contact zone, and the ring thickness from 3.6 to 2.4 μm (Fig. 8A inset). On the other hand, increasing the receptor density from $\rho_b^0 = 1.4 \cdot 10^3$ to $3.5 \cdot 10^3\ \mu m^{-2}$ for a constant ligand density of $\rho_l^0 = 14 \cdot 10^3\ \mu m^{-2}$, results in the increase of the adhesion area from 35% to 76%. This trend is confirmed in simulations which show that not only the thickness of the ring is smaller, but also the actual number of bonds becomes smaller at larger concentrations of ligands. More specifically, the thickness of the ring drops by a factor about 3 over the entire range of ligand surface coverage.

The reason for the density dependency lies in the dynamics of ring formation. For high ligand densities, the ring closes faster than for low ligand densities. Consequently, the number of receptors diffusing into the contact zone, before crowding, is smaller for the high ligand densities than for low ligand densities allowing only for a thin ring and therefore a smaller number of bonds.

5.2. Enrichment factor

In simulations, we find that the final number of bonds is almost equal to the initial receptor density ρ_r^0 (see Fig. 8B), and only at low receptor concentrations, it is affected by the initial ligand density ρ_l^0 (see Fig. 8B inset). Such a trend emerges because the receptor density shows only little enrichment of the initial receptor density in the contact zone. This is due to the fact that at large receptor densities, bonds form over the entire contact zone which prevents further accumulation of binders. The significantly smaller ligands, in contrast, diffuse through a bond domain restoring the ligand density in the contact zone at every stage of domain formation, until the growth process is stopped by the lack of receptors.

This result agrees well with experimental observations of the enrichment factor at low temperatures (small diffusion constants). However, at high temperatures (fast diffusion) very high enrichment factors (see Fig. 9), maximizing the packing of neutravidin in the contact zone (blue doted line) are observed, even at low initial receptor densities. It was previously argued [26], that such high enrichments occur because the accumulation of receptors takes place during the spreading of the vesicle, and not after the contact zone is formed.

To confirm this hypothesis, we perform a set of simulations where the vesicle falls onto the substrate with a constant velocity v_s, i.e. the contact area changes linearly in time. Moreover, in these simulations the nucleation time is fast.

In such a scenario, the bonds start to form in a very small contact zone, and the binders accumulate in the contact zone while it is spreading. As a result, the enrichment factor becomes a function of the velocity v_s (in units of μm/s). To compare different initial ligand and receptor

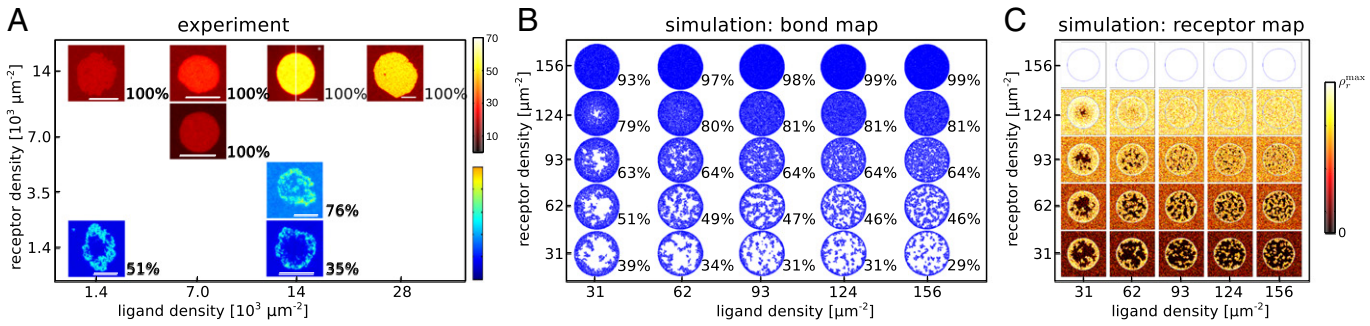

Fig. 7. Comparison of the measured (A) and simulated phase diagrams (B, C). Epifluorescent images of neutravidins in the steady state as a function of ligand and receptor coverage is shown in A. The increase in bulk concentration of receptors is seen by the change of color outside of the contact zone. The number indicates the fraction of the contact zone occupied by adhesions. The scale bar shows 10 μm and the color code in units of 10^3 μm. (B) Contact zones in the steady state obtained from simulations as a function of ligand and receptor bulk density. Bonds are marked with blue, and the respective receptors distributions are shown in (C).

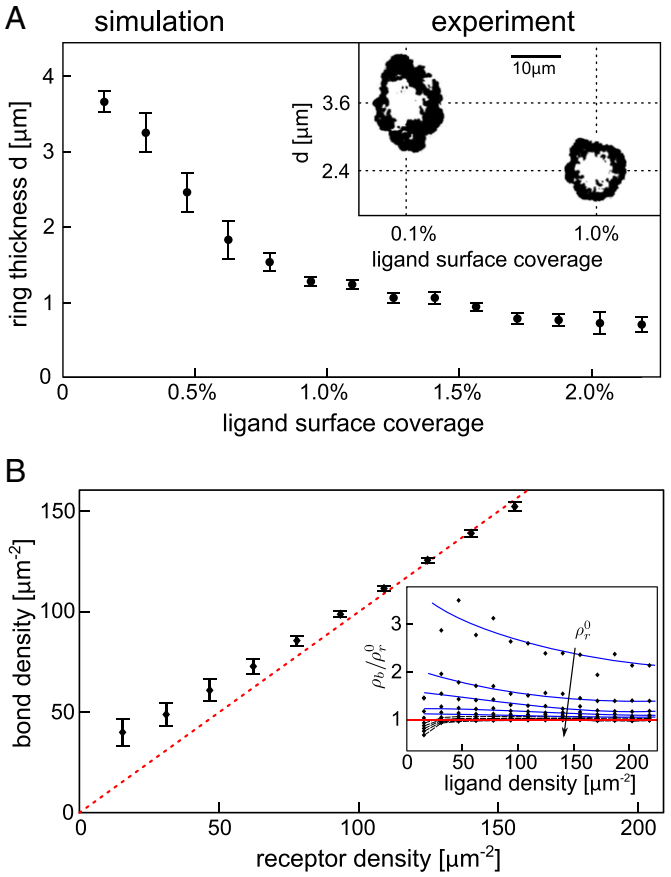

Fig. 8. (A) Ring thickness as a function of the ligand density for the simulation and the experiment (inset). Error bars mark the standard deviation for various receptor densities. Inset: Snapshots of the bond domain from the experiment (black area) for two different ligand densities. (B) Accumulated bond density ρ_b in the contact zone as a function of the initial receptor density ρ_r^0. The inset shows the normalized bond density ρ_b/ρ_r^0 as a function of the initial ligand density ρ_l^0.

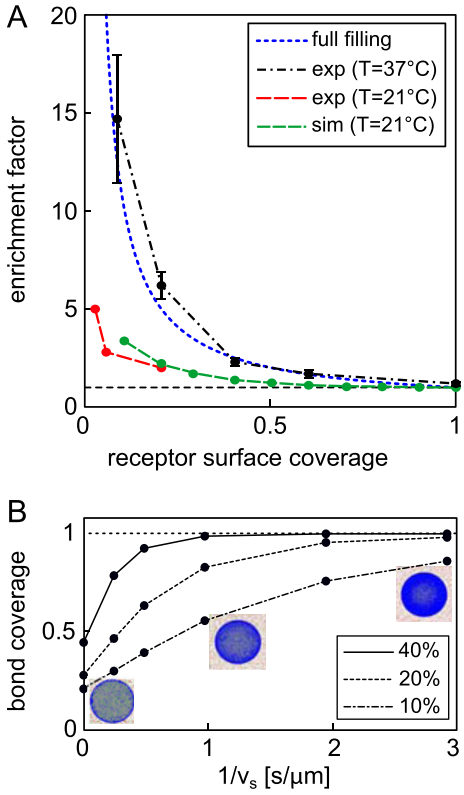

Fig. 9. (A) Enrichment factor observed experimentally at different temperatures and in simulations. The experiments presented in this work are performed at $T = 21$ °C. The enrichment factors at high temperature ($T = 37$ °C) was taken from Fenz et al. [26] (B) Simulated steady state bond coverages for vesicles spreading as the bonds are being formed. The vesicles sediment to the substrate with constant velocity v_s ($\rho_l^0 = \rho_r^0$, indicated in the legend).

densities, we show in Fig. 9 (bottom) the bond coverage in steady state. We find that as the inverse of v_s increases the thickness of the ring of crowded receptors also increases up to full packing above a critical value.

The actual value of the critical velocity depends sensitively on the concentration of both, receptors and ligands. At low ligand and high receptors densities, the reservoir of ligands may be fully depleted before the spreading is completed which results in densely packed domains in the center of the contact zone and the edge free of bonds.

6. Discussion and conclusions

In this work, we studied the interplay between the capacity of binders to diffuse through growing structures in the membrane and the morphology of these structures. We find that the initial density of bulky binders plays a major role as a control parameter for the final organization of adhesions. Furthermore, a rich phase space of growth patterns was identified, showing very similar features in simulations and experiments.

Particularly interesting are spontaneously forming ring-like structures, which arise due to the recruitment of binders into the contact zone of two membranes. If the ring is created as a consequence of accumulation of small binders (ligands), the ring structure is transient. On the other hand, if it is caused by crowding of bulky binders (receptors), the ring becomes significantly more stable, due to the inability of the large proteins to diffuse through the already established structure. Such a ring naturally creates a coral in the membrane, isolating the interior of the ring from the outside. In the cellular context, our results suggest that the formation of the ring may be passive, but the transport through the ring should involve active mechanisms. The latter seems to be the case for the T cell receptors that are transported, by coupling to the actin retrograde flow [4].

The formation of rings may be preceded by a formation of numerous small domains within the entire contact zone. This result is in agreement with recent observations of the formation of cadherin rings in the contact zone between two epithelial cells [6], where in the initial stage, multiple nucleation is promoted by homogeneous fluctuations of the composite cell membrane. However, a ring forms within a minute, at the edge of the contact zone by nucleations of small adhesions, which grow both by accumulation of cadherin from the bulk, as well as from cadherins within the emergent coral. The closure of the ring seems to provide a signal to the actin–myosin apparatus to actively exert contractile forces on the cadherin junctions, expanding the ring and increasing the contact zone. This scenario of ring-closure agrees very well with the simulations presented in this study (Fig. 7), suggesting that the initial stage of the cell–cell recognition process may rely on cadherin binding, regulated by their density and the physical properties of the cell envelope. Furthermore, our results suggest that active actin driven cell spreading couples to the development of adhesion in a highly regulated fashion, an idea which could be explored beyond the current manuscript.

Another interesting observation is the increase of the enrichment factor with the speed of the spreading of the contact zone. While this effect was demonstrated on a relatively large scale, the mechanism applies also for small contact areas. This would allow cells to regulate the density of binders in the forming of adhesions by controlling the speed of protruding lamellipodia and filopodia from the cell surface.

In conclusion, we established a Monte Carlo scheme with which we are able to understand the details of experimental observations, from the stability of bonds to the organization into macromolecular structures. Intriguingly, the micro-domain bond structures described here closely resemble those reported since more than a decade ago for integrin/TCR mediated adhesion in immune cells [1–3,5], as well as more recent reports on cadherin mediated adhesion in epithelial carcinoma cells [6]. The insights gained from the dual simulation and experimental model system can potentially identify regulating mechanisms, that can then be tested in a cellular system. Receptor crowding, arising from steric hindrance or lateral interactions, as well as ring closure, which itself is determined by molecular concentrations, interactions, and transport, have been identified here as potential important players in cell adhesion.

Acknowledgments

We thank Michael Dustin and Virgile Viasnoff for insightful discussions. A.S.S., D.S., and T.B. received funding from the European Research Council (starting grant 2013-337283), Research Training Group 1962 at Friedrich-Alexander-Universität Erlangen–Nürnberg and were supported by the Excellence Cluster: Engineering of Advanced Materials at Friedrich-Alexander-Universität Erlangen–Nürnberg. K.S. received funding from the European Research Council (307104FP/2007–2013/ERC).

Appendix A. Supplementary data

Supplementary data to this article can be found online at http://dx.doi.org/10.1016/j.bbamcr.2015.05.025.

References

[1] C. Monks, B. Freiberg, H. Kupfer, N. Sciaky, A. Kupfer, Nature 395 (1998) 82–86.
[2] A. Grakoui, S.K. Bromley, C. Sumen, M.M. Davis, A.S. Shaw, P.M. Allen, M.L. Dustin, Science 285 (1999) 221–227.
[3] Y. Kaizuka, A.D. Douglass, R. Varma, M.L. Dustin, R.D. Vale, Proc. Natl. Acad. Sci. U. S. A. 104 (2007) 20296–20301.
[4] M.L. Dustin, J.T. Groves, Annu. Rev. Biophys. 41 (2012) 543–556.
[5] P. Dillard, R. Varma, K. Sengupta, L. Limozin, Biophys. J. 107 (2014) 2629–2638.
[6] W. Engl, B. Arasi, L.L. Yap, J.P. Thiery, V. Viasnoff, Nat. Cell Biol. 16 (2014) 584–591.
[7] P.K. Tsourkas, N. Baumgarth, S.I. Simon, S. Raychaudhuri, Biophys. J. 92 (2007) 4196–4208.
[8] P.K. Tsourkas, M.L. Longo, S. Raychaudhuri, Biophys. J. 95 (2008) 1118–1125.
[9] P.K. Tsourkas, S. Raychaudhuri, Cell. Mol. Bioeng. 3 (2010) 256–268.
[10] S.Y. Qi, J.T. Groves, A.K. Chakraborty, Proc. Natl. Acad. Sci. U. S. A. 98 (2001) 6548–6553.
[11] N.J. Burroughs, C. Wülfing, Biophys. J. 83 (2002) 1784–1796.
[12] T.R. Weikl, J.T. Groves, R. Lipowsky, EPL (Europhysics Letters) 59 (2002) 916.
[13] T.R. Weikl, R. Lipowsky, Biophys. J. 87 (2004) 3665–3678.
[14] D. Coombs, M. Dembo, C. Wofsy, B. Goldstein, Biophys. J. 86 (2004) 1408–1423.
[15] H. Krobath, B. Rozycki, R. Lipowsky, T.R. Weikl, PLoS One 6 (2011) e23284.
[16] J. Brzostek, J.-G. Chai, F. Gebhardt, D.H. Busch, R. Zhao, P.A. van der Merwe, K.G. Gould, Eur. J. Immunol. 40 (2010) 2050–2059.
[17] O. Milstein, S.-Y. Tseng, T. Starr, J. Llodra, A. Nans, M. Liu, M.K. Wild, P.A. van der Merwe, D.L. Stokes, Y. Reisner, M.L. Dustin, J. Biol. Chem. 283 (2008) 34414–34422.
[18] A.-S. Smith, E. Sackmann, ChemPhysChem 10 (2009) 66–78.
[19] S.F. Fenz, K. Sengupta, Integr. Biol. 4 (2012) 982–995.
[20] E. Sackmann, A.-S. Smith, Soft Matter 10 (2014) 1644–1659.
[21] P. Streicher, P. Nassoy, M. Barmann, A. Dif, V. Marchi-Artznerm, F. Brochard-Wyart, J. Spatz, P. Bassereau, Biochim. Biophys. Acta Biomembr. 1788 (2009) 2291–2300.
[22] S.F. Fenz, A.-S. Smith, R. Merkel, K. Sengupta, Soft Matter 7 (2011) 952–962.
[23] G.I. Bell, M. Dembo, P. Bongrand, Biophys. J. 45 (1984) 1051.
[24] A.-S. Smith, U. Seifert, Soft Matter 3 (2007) 275–289.
[25] D. Schmidt, T. Bihr, U. Seifert, A.-S. Smith, EPL (Europhysics Letters) 99 (2012) 38003.
[26] S.F. Fenz, R. Merkel, K. Sengupta, Langmuir 25 (2009) 1074–1085.
[27] L. Limozin, K. Sengupta, ChemPhysChem 10 (2009) 2752–2768.
[28] A.-S. Smith, S.F. Fenz, K. Sengupta, EPL (Europhysics Letters) 89 (2010) 28003.
[29] T. Bihr, U. Seifert, A.-S. Smith, arXiv arXiv:1503.017182015.
[30] T. Bihr, U. Seifert, A.-S. Smith, Phys. Rev. Lett. 109 (2012) 258101.
[31] J. Hu, R. Lipowsky, T.R. Weikl, Proc. Natl. Acad. Sci. U. S. A. 110 (2013) 15283–15288.
[32] A.-S. Smith, K. Sengupta, S. Goennenwein, U. Seifert, E. Sackmann, Proc. Natl. Acad. Sci. U. S. A. 105 (2008) 6906–6911.
[33] E. Evans, W. Rawicz, Phys. Rev. Lett. 64 (1990) 2094–2097.
[34] S.F. Fenz, T. Bihr, R. Merkel, U. Seifert, K. Sengupta, A.-S. Smith, Adv. Mater. 23 (2011) 2622–2626.
[35] T. Bihr, S. F. Fenz, D. Schmidt, R. Merkel, K. Sengupta, U. Seifert and A.-S. Smith, in preparation.
[36] M. Avrami, J. Chem. Phys. 8 (1940) 212–224.
[37] P.L. Krapivsky, S. Redner, E. Ben-Naim, A Kinetic View of Statistical Physics, Cambridge University Press, 2010.
[38] A. Boulbitch, Z. Guttenberg, E. Sackmann, Biophys. J. 81 (2001) 2743–2751.
[39] V.B. Shenoy, L.B. Freund, Proc. Natl. Acad. Sci. U. S. A. 102 (2005) 3213–3218.
[40] H. Gao, W. Shi, L.B. Freund, Proc. Natl. Acad. Sci. U. S. A. 102 (2005) 9469–9474.
[41] T. Bihr, S. Fenz, E. Sackmann, R. Merkel, U. Seifert, K. Sengupta, A.-S. Smith, Biophys. J. 107 (2014) L33–L36.
[42] W.W. Mullins, R.F. Sekerka, J. Appl. Phys. 34 (1963) 323–329.
[43] T.A. Witten, L.M. Sander, Phys. Rev. Lett. 47 (1981) 1400–1403.

P8

Membrane fluctuations mediate lateral interactions between bonds

Membrane fluctuations mediate lateral interactions between bonds

T. Bihr[1,2], S. Fenz[3,4], D. Schmidt[1,2], R. Merkel[4], K. Sengupta[5], U. Seifert[2], and A.-S. Smith[1,6]

[1] Institut für Theoretische Physik and Cluster of Excellence: Engineering of Advanced Materials, Friedrich Alexander Universität Erlangen-Nürnberg, 91052 Erlangen, Germany
[2] II. Institut für Theoretische Physik, Universität Stuttgart, 70569 Stuttgart, Germany
[3] Lehrstuhl für Zell- und Entwicklungsbiologie (Zoologie I), Biozentrum der Universität Würzburg, 97074 Würzburg, Germany
[4] Institute of Complex Systems 7: Biomechanics, Forschungszentrum Jülich GmbH, 52425 Jülich, Germany
[5] Aix-Marseille Université, CNRS, CINaM UMR 7325, 13288 Marseille, France
[6] Insitut Ruđer Bošković, 10000 Zagreb, Croatia

in preparation (2016)

ABSTRACT The integrity of living tissues is maintained by domains of *trans*-dimer bridges formed between cadherins on neighbouring cells. There is clear evidence that the domains are stabilized by lateral *cis*-interactions between cadherins on the same membrane; however no *cis* dimer has ever been detected in solution. Here we introduce suppression of membrane fluctuations as a source of generic lateral interactions between bonds and show, using analytical, experimental and computational approaches that this regulatory role of the membrane is particularly relevant for Cadherins. Membrane fluctuations introduce complex cooperative effects that modulate the rates of binding and unbinding of the *trans*-dimers, which in turn impact the nucleation and growth of adhesion domains. Importantly, small changes in initial height and fluctuation amplitude, which impact cooperative effects, can change the rates by up to a couple of orders of magnitude. The regulatory activity of the membrane, quantified here in the context of cadherins, relies on physical principles and therefore may be a generic player in the context of formation of any adhesion structures on the plasma membrane and in the cell interior.

Membrane fluctuations mediate lateral interaction between bonds

Timo Bihr*,[1,2] Susanne Fenz*,[3,4] Daniel Schmidt,[1,2] Rudolf Merkel,[4] Kheya Sengupta,[5] Udo Seifert,[2] and Ana-Sunčana Smith[1,6]

[1] *PULS Group, Institut für Theoretische Physik and the Excellence Cluster: Engineering of Advanced Materials, Universität Erlangen-Nürnberg, Nägelsbachstrasse 49b, 91052 Erlangen, Germany*
[2] *II. Institut für Theoretische Physik, Universität Stuttgart, Pfaffenwaldring 57, 70550 Stuttgart, Germany*
[3] *Department of Cell and Developmental Biology, Universität Würzburg, Am Hubland, 97074 Würzburg, Germany*
[4] *Institute of Complex Systems 7: Biomechanics Forschungszentrum Jülich GmbH, 52425 Jülich, Germany*
[5] *CNRS UPR 3118, Centre Interdisciplinaire de Nanosciences de Marseille, Aix-Marseille Université Campus de Luminy, 13288 Marseille cedex 9, France*
[6] *Institute Ruđer Bošković, Division of Physical Chemistry, Bijenička cesta 54, 10000 Zagreb, Croatia*

(Dated: May 11, 2016)

The integrity of living tissues is maintained by domains of *trans*-dimer bridges formed between cadherins on neighbouring cells. There is clear evidence that the domains are stabilized by lateral *cis*-interactions between cadherins on the same membrane; however no *cis* dimer has ever been detected in solution. Here we introduce suppression of membrane fluctuations as a source of generic lateral interactions between bonds and show, using analytical, experimental and computational approaches that this regulatory role of the membrane is particularly relevant for Cadherins. Membrane fluctuations introduce complex cooperative effects that modulate the rates of binding and unbinding of the *trans*-dimers, which in turn impact the nucleation and growth of adhesion domains. Importantly, small changes in initial height and fluctuation amplitude, which impact cooperative effects, can change the rates by up to a couple of orders of magnitude. The regulatory activity of the membrane, quantified here in the context of cadherins, relies on physical principles and therefore may be a generic player in the context of formation of any adhesion structures on the plasma membrane and in the cell interior.

Cadherins are a family of trans-membrane proteins responsible for cohesion of cells [1, 2]. Following a nucleation process [3], they assemble into domains called adherens junctions, forming bridges between the actin-cytoskeletons of neighbouring cells [4, 5]. The *trans*-dimers aggregate in the plane of the cell-cell interface, presumably due to lateral *cis*-interations [6], which however have never been detected in solution. Cells containing a specific cadherin subtype cluster together to the exclusion of other types, both in cell culture and during embryo development [7]. This selectivity is promoted by small variations in the two-dimensional binding affinity (2D-K_a) for *trans*-dimerization [6, 8], and allows proteins of the cadherin family to have a structural and regulatory role in tissue morphogenesis and homeostasis [9]. This family of proteins is an important determinant of tumour progression, and in particular, E-cadherins serve as suppressors of cancer invasion and metastasis [10, 11].

Cadherins exhibit a considerable level of complexity even at the level of single-bonds [12], and exhibit metastable, low-affinity *tras*-bonds [13, 14], prior to the assembly of the high-affinity *trans*-dimer linking the two outer-most domains [15–17]. *Trans*-interactions have been studied in detail, and recently, electrostatic, hydrophobic and entropic contributions were identified to play an important role in the stability of the complex [17]. Unlike *trans*-bonds, *cis*-interactions have been detected only in membrane bound cadherins [], and the origin of *cis*-interactions remains elusive. Based on computational studies, it has been suggested that the origin of cis- interactions resides in entropic reasons related to mechanics of the monomeric and dimmeric states [6, 18] but this is not sufficient to explain the exquisite sensitivity of the cadherin system to membrane parameters that are hinted at in cell experiments [] and which we demonstrate here in cell free model membranes. Our analytical calculations pinpoint membrane-fluctuation transmitted cooperativity as not only a significant modulator of 2D-K_a for both *trans*and *cis*-dimerization, but also capable of by itself promoting *cis* interactions.

Our work was motivated by experiments on cells showing that [19, 21–24] that the formation and renewal of oligomers occurs in three steps: (i) spontaneous cadherin recruitment to the domain, (ii) lateral growth and (iii) active release from the resulting cluster. Furthermore, later stages may involve the actin driven formation of super-structures of junctions organizing in a ring at the periphery of the contact zone [20]. As shown in Fig. 1, we can capture the first two of these steps in an experimental model system consisting of giant unilamellar vesicles (GUVs) functionalized with E-cadherin extracellular domains, which interact with supported lipid bilayers (SLBs), which are similarly functionalized ([25] and section I in Supplementary Information). The dynamics of adhesion is recorded and quantified in terms of the evolving membrane substrate distance (h) as well as the amplitude of membrane-fluctuations (ψ) using Reflection Interference Contrast Microscopy (RICM) ([26, 43] and

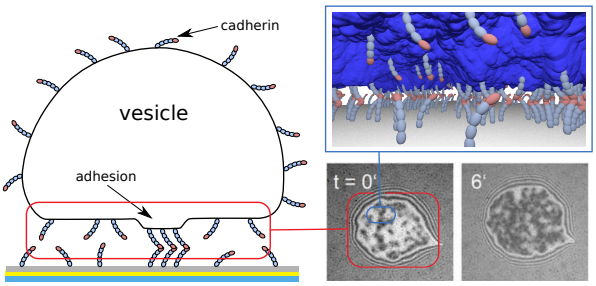

Figure 1: Schematic representation of the model system consisting of a giant unilamellar vesicle (GUV) and a supported lipid bilayer (SLB), both decorated with diffusing cadherin fragments (left panel). The formation of adhesions was recorded by reflection interference contrast microscopy (RICM). Examples of snapshots of the contact zone are shown in the lower right panels. The dark spots in the micrographs are associated with *trans*-cadherin domains, the formation of which can be simulated with excellent accuracy. Top right panel shows the key players in the adhesion process including the fluctuating membrane (blue) and the substrate (gray), enriched with cadherin fragments (gray-orange beads).

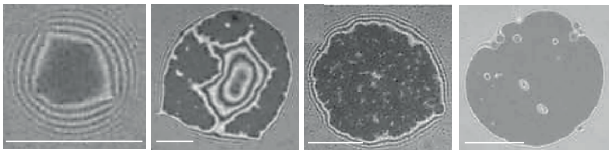

Figure 2: Steady state contact zones with model junctions (dark areas) formed between E-cadherin motifs in the supported lipid bilayer binding identical motifs in giant unilamellar vesicles. Despite identical preparation, a large variability of the morphology of adhesions is observed. Scale bars are 10 μm.

SI). In RICM, the zone of GUV-SLB contact is seen as an area of flickering dark and bright pixels, distinct from the uniformly grey background. The instantaneous value of intensity in a given pixel is related to h and the dynamic change of the pixel intensity can be directly related to membrane fluctuations.

At time zero, the membrane fluctuates, with a typical amplitude of 5 to 20 nm, around an average separation of about $80 - 100$ nm (Fig. 1). After some time, model adhesions spontaneously form within the contact zone. We find that a variety of growth scenarios are possible, leading to different final states (Fig. 2). Detailed analysis shows small differences the initial h and ψ lead to these very different outcomes. These variations are found to be smaller than 10 nm, and yet lead to an enormous difference in the outcome.

Specifically, we systematically find that increased fluctuations of even a couple of nanometres, drive the system from forming one large radially growing domain to a regime where numerous very small domains are formed simultaneously. Furthermore, nanometric increase in the separation between membranes results in less numerous adhesion domains which become larger in time (Fig. 2 CAN WE PUT A,B,C etc and say which case is which?).

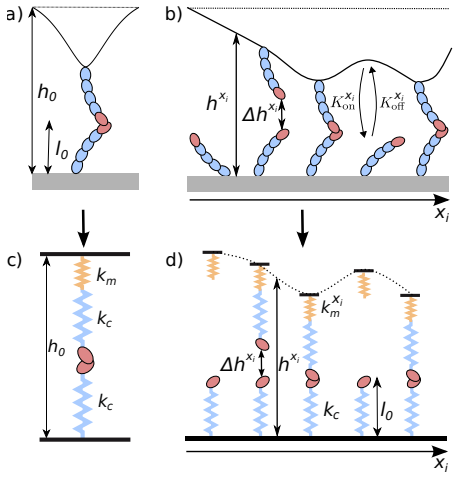

Figure 3: a) Calculated average shape of a membrane deformed by an isolated cadherin *trans*-dimer. b) An example of a calculated profile of a membrane connecting several cadherin *trans*-dimers. Bonds are formed with a rate $K_{\rm on}^{x_i}$ and broken with a rate $K_{\rm off}^{x_i}$ depending on the local separation between cadherins Δh^{x_i}, at the position of a bond x_i. c) Mapping of the system of a single bond into coupled thermalized springs, with stiffnesses relating to fluctuations in the system. The yellow (k_m) and the blue springs (k_c) represent the membrane and the cadherins, respectively. d) In the case of several bonds, the membrane is parametrized by a set of spatially and temporally variable spring constants $k_m^{x_i}$, and separations Δh^{x_i}.

This sensitive dependence of the entire adhesion process on initial h and ψ points to a regulatory role of the membrane in determining the *tras* and *cis* dimerization. To understand this, we consider a model where the formation of a *trans*-dimer induces local deformations (Fig. 3a) and the suppression of membrane fluctuations. We hypothesize that this local change in the membrane promotes *trans*-bonds between cadherins in the vicinity of the already formed *trans*-dimers, resulting in an effective *cis*-interaction and aggregation of the laterally mobile cadherins into domains (Fig. 3b).

To verify this hypothesis analytically, we construct a mechanistic model (Fig. 3c), where the cadherins are represented by harmonic, thermalized springs (elastic constant k_c, length l_0), attached either to a flat, or to a fluctuating deformable membrane (SLB and GUV respectively). The GUV-membrane itself is represented by an elastic degree of freedom with a local effective elastic con-

stant $k_m^{x_i} = k_B T(\xi_\perp^{x_i})^{-2}$, with $\xi_\perp^{x_i}$ being the fluctuation amplitude of the membrane at the binding site x_i [34]. In the absence of any bonds $k_m^{x_i} = k_m$. In cells, the fluctuations may be driven by the polymerization and depolymerization of actin [3]. In vesicles, the fluctuation amplitude k_m is associated with the thermally induced roughness of the unbound membrane. It naturally depends on the membrane bending rigidity, tension and a potential which prevents the nonspecific binding between the GUV and the SLB [32, 34, 35]. The interplay between these contributions sets the initial separation between the membranes.

In our model, the *trans* interaction is represented by a potential well, of range α and depth equal to the 3D binding affinity $\epsilon_b = 7\ k_B T$ [6]. No direct *cis*-interactions are introduced. Such a description (section II in SI) yields the local free energy gain $E_b^{x_i}$ for forming a *trans*-dimer (in units of $k_B T$ with k_B being the Boltzmann constant, and T the temperature)

$$E_b^{x_i} = \frac{1}{2}\Omega_u^{x_i}(\Delta h^{x_i})^2 + \frac{1}{2}\ln\left[\frac{2\pi}{\Omega_u^{x_i}\alpha^2}\right] - \epsilon_b. \qquad (1)$$

The first term on the right hand side is the deformation energy stored in the *trans*-dimer and membrane as shown in Fig. 3c. It is proportional to the effective spring constant $\Omega_u^{x_i}$ of a construct consisting of two cadherins and the membrane (i.e. three springs in series). Obviously, it is also proportional to the square of separation between outer cadherin domains $\Delta h^{x_i} \equiv h_0^{x_i} - 2l_0$, that has to be overcome to bring the two cadherins into the binding range. Here, $h_0^{x_i}$ is the vertical distance between the two membranes before the bond is formed and l_0 is the typical size of a the cadherin (see Fig. 3d). The second term on the right hand side of eq. (1) is the entropic penalty associated with the suppression of the membrane as well as cadherin conformational fluctuations. An estimation of the value of the two terms (ADD TO SI) shows that they can be comparable.

The membrane deformation field around an already existing trans-dimer extends laterally up to 500 nm, affecting both the height and the membrane fluctuations. Therefore, the formation and the stability of any trans-dimer in this range is impacted, and many body effects emerge. We recognize this as membrane-mediated correlations between trans-dimers. If membrane-transmitted correlations are weak (WITH respect to what?), then $\Omega_u^{x_i}$ and Δh^{x_i} do not depend on the position x_i and formation of each *trans*-dimer is an independent event. However, when these correlations are strong (Fig. 3d), as is the case in the current experiments and in typical cellular systems [3, 20], the free energy gain for the formation of the *trans*-dimer $\tilde{E}_b^d$, i. e. 2D binding affinity, becomes

$$\tilde{E}_b^d = \frac{1}{N_b}\sum_{i=1}^{N_b}\left(E_b^{x_i} + \frac{1}{2}\ln\frac{k_m + k_c}{k_m^{x_i} + k_c}\right), \qquad (2)$$

where N_b is the number of formed bonds. The second term arises from non-local entropic costs for suppressing the fluctuations in the entire system.

While these static arguments quantify the effective affinity, understanding the dynamics of junction formation requires modelling the binding and unbinding rates $k_{\rm on}(h)$ and $k_{\rm off}(h)$ [37–39]. These rates depend on the instantaneous separation h between the cadherins, which obviously do not interact at separations beyond the binding range. For cadherins embedded into simple, static interfaces, $k_{\rm on}(h)$ and $k_{\rm off}(h)$ are expected to obey local detailed balance [39]. However, the membrane performs complex stochastic motions, which can be characterised by a Gaussian height distribution function $p^{x_i}(h)$, with the first and the second moments being the average height Δh^{x_i} and the fluctuation amplitude $1/k_m^{x_i}$ (see SI). The AMPLITUDE of these fluctuations determines how often the cadherins get into binding range, and how strong are the stochastic forces that act on a bond. Therefore, in order to obtain the actual effective rates for the trans-dimerization $K_{\rm on}^{x_i}$, $K_{\rm off}^{x_i}$, the height-dependent rates are weighed by the membrane height distribution function $p^{x_i}(h)$

$$K_{\rm offon}^{x_i} \equiv \int {\rm d}h\, p^{x_i}(h) k_{\rm off} on(h), \qquad (3)$$

FIX THE EQ. Consequently, the effective reaction rates ($K_{\rm on}^{x_i}$, $K_{\rm off}^{x_i}$) depend directly on Δh^{x_i} and $k_m^{x_i}$ at a given position in the membrane (see SI for details and Fig. 4). The clear separation in time scales between the membrane fluctuations and the binding kinetics ensures that $p^{x_i}(h)$ is fully sampled and that the averaging is appropriately performed.

Note that, membrane fluctuations promote the binding rate because the probability for the encounter between the two cadherins is increased. Likewise, the unbinding rate of a *trans*-dimer increases because stronger fluctuations exert stronger stochastic forces inducing unbinding. However, the effect of fluctuations on $K_{\rm on}^{x_i}$ is larger than on $K_{\rm off}^{x_i}$, which suggests that membrane fluctuations stabilize *trans*-dimers. Importantly, small changes in initial height and fluctuation amplitude, as well as cooperative effects can affect the rates for up to a couple of orders of magnitude (Fig. 4),

The effect of membrane-mediated correlations is reflected in the spatial variability of the effective rates which themselves become sensitive to the local distribution of bonds (Fig. 4). For example, deep within the model junction, where each cadherin complex is surrounded by other *trans*-dimers, the unbinding rate is small. On the other hand, bonds at the smooth edge of the model junction unbind with a probability that is several times larger, while fully exposed, or isolated trans-dimers are even more unstable. Similarly, compared to cadherins far away from the cluster, where the binding probability is very low, free cadherins at the edge of the

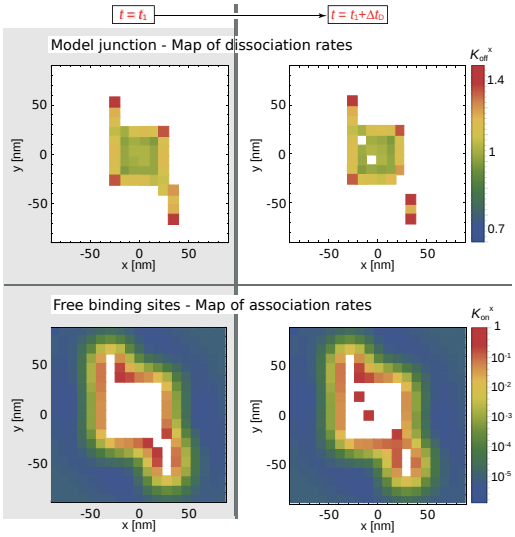

Figure 4: A model adhesions junction at $t = t_0$ (left panels) and $t = t_0 + \Delta t_D$ (right panels). Top: Each bond is represented by a square of a color that represents the effective bond dissociation rate $K_{\text{off}}^{x_i}$, sensitive to the instantaneous configuration of bonds. Bottom: The color of the square now represents the effective association rate $K_{\text{on}}^{x_i}$ which depends on the position of the free receptor relative to the cluster. All rates are given in units of the intrinsic reaction rate k_0. The rates were calculated for a membrane with a bending rigidity $\kappa = 20\,k_BT$, fluctuating with an amplitude of 10 nm, at a distance of $h_0 = 40$ nm above the receptors. The latter are modeled as harmonic springs with a stiffness $k_c = 5 \times 10^{-2}\,\mathrm{k_BT/nm^2}$. These rates account for effects of the membrane in the Monte Carlo simulations of a cadherin-mediated formation of junctions.

cluster have an up to five times larger probability to form a bond, which again points to a subtle interplay of *trans* and membrane-mediated *cis* interactions.

It is natural to expect that the susceptibility of the reaction rates to the membrane parameters is reflected in the nucleation dynamics of adhesions. The process of nucleation is characterized by two parameters - the number of *trans*-dimers forming the smallest stable adhesions junction N_c, and its characteristic formation time $\bar{\tau}$. N_c is calculated within the capillary approximation [33] as: $N_c \simeq 1 + \frac{(\Delta h)^4 k_m^2}{4\pi\rho_b \xi_{||}^2 \left(\tilde{E}_b^d\right)^2}$, where $\xi_{||}$ is the lateral extension of the membrane deformation around a *trans*-dimer, and ρ_b is the bond density within the adhesions junction. PUTTING TYPICAL VALUES(?) shows that the minimal number of *trans*-dimers within a stable junction is typically small. It increases with the fourth power of the separation between the unbound cadherins, and decreases with the fourth power of the membrane fluctuation amplitude.

The average nucleation time $\bar{\tau}$ is directly related to effective rates for the association and dissociation of the first and the second bond PUT BACK EQ IN LINE From the dependence on the effective reaction rates (see SI), one sees that in the regime of moderate fluctuations, the nucleation time is a decreasing exponential function of the square of the fluctuation amplitude. On the other hand $\bar{\tau}$ is an increasing exponential function of the square of the initial separation between cadherins.

This extreme sensitivity of both the critical size and the characteristic nucleation time obtained in the model clearly demonstrates the importance of the membrane parameters for the formation of model junctions. Furthermore, it is fully consistent with the experimentally observed variability of the number and size of growing adhesions junctions due to very small variations in the GUV membrane fluctuation amplitude, as well as in the initial height separation between the GUV and the SLB (Fig. 2).

To verify this analytic theory, and to reproduce experimental conditions, we take advantage of a recently developed coarse-grained Monte Carlo (MC) simulation frame-work that allows us to access experimental length and time-scales [39]. We simulate an entire GUV binding to an SLB (both $1000\,\mu\mathrm{m}^2$), with the spatial and time resolutions of 40 nm and 5×10^{-6} s for about 100 s or until equilibrium is reached. Free cadherins, at experimental concentrations, are allowed to diffuse and form *trans*-dimers following the rates introduced in Eq. (3). While no explicit *cis*-interactions are introduced, membrane-mediated effects should give rise to clearly identifiable lateral interactions. We systematically investigate the affinity of *trans*-dimers, the morphology of adhesions, the minimal size of the stable adhesions junction and the nucleation time. We map the results into two phase diagrams (Fig. 5b and c) spanned by the initial separation between cadherins and the fluctuation amplitude of the membrane.

Direct comparison of the simulations with the experiments became possible since we could access similar time and length scales. As is clear from Fig. 5a (experiments top and simulations bottom), the two agree very well and the following description is valid for both. At small fluctuations and large separations, the cadherin agglomerate was a single, radially expanding domain with tightly packed bonds (A_1 panels in Fig. 5a). This is consistent with strong, membrane-induced cooperative effects obtained within the theoretical model and the associated simulations. Increasing the floppiness of the vesicle to produce only a 4 nm larger mean fluctuation amplitude, drastically changed the adhesion process (A_2). Consistently with the prediction that nucleation time should decreases by several orders of magnitude, many domains develop simultaneously over the entire contact area between the two membranes. Even at equilibrium, the bonds are not densely packed, suggesting that the

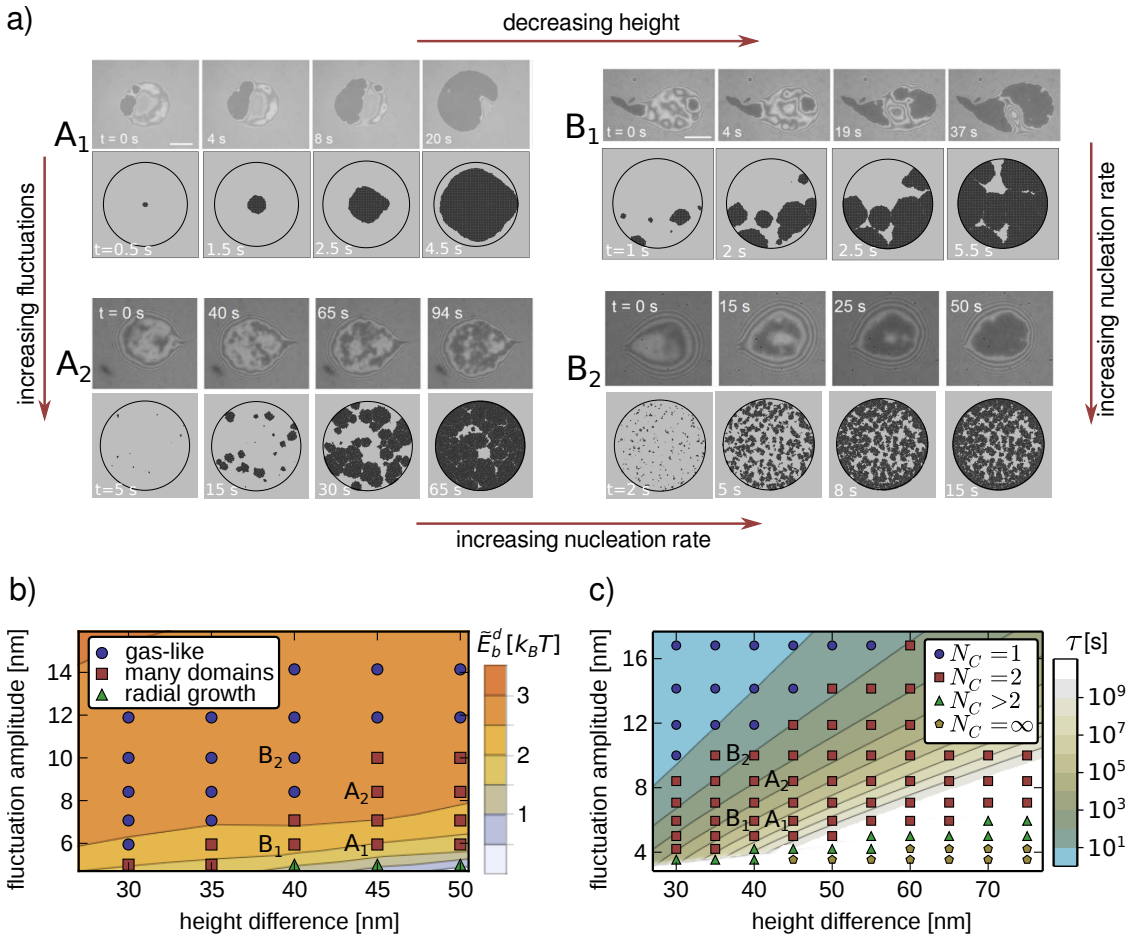

Figure 5: a) RICM images (top) and MC simulation snapshots (bottom) of growing cadherin adhesions A1, A2, B1, and B2. b) Map of the 2D binding affinity as determined from steady state distributions of bonds in simulations and Eq. (2). The result is overlaid with symbols denoting the type of growth (gas-like, small domains, radial growth of large domains), as determined from the morphological phase diagram (Fig. SI-1, section III in SI). c) Parameters determining the nucleation. The colored background represents the mean nucleation time $\bar{\tau}$, while the symbols mark the number N_c of *trans*-dimers necessary to form a stable seed. The intrinsic binding affinity was taken to be $\epsilon_b = 7\,k_BT$ [6] and $k_c = 5\times10^{-2}\,\mathrm{k_BT/nm^2}$, respectively. All simulations are performed for the experimental membrane stiffness $\kappa = 20\,\mathrm{k_BT}$, and diffusion constant of cadherins $D = 5\,\mu\mathrm{m}^2/\mathrm{s}$ as measured previously [**?**]. The attempt frequency k_0 was treated as a free parameter (identical across the whole phase diagrams), to obtain the macroscopic time-scale of growth, but kept constant over the whole phase diagram. In principle. all simulations were performed with $k_0 = 1\,\mathrm{s}^{-1}$. The exception are simulations of processes A_1 and B_1 in panel a) where we use $k_0 = 100\,\mathrm{s}^{-1}$ to combat the very low nucleation time. Experimentally, the average membrane to surface distance (h) and the average fluctuation amplitude (f) were determined from RICM data corrected for finite resolution (see SI for details). Reported h are absolute values and f are relative values.

membrane-induced cooperativity persists but is not as strong as in A_1. Similar decomposition of domains can be seen at lower initial separations between cadherins (B_1 compared to B_2). In B_2, at strongest fluctuations and smallest separations, the bonds are sparsely distributed over the entire contact zone in a gas-like fashion suggesting that N_c dropped to unity, further decreasing the nucleation time. Under these conditions, the correlations between *trans*-dimers completely vanish.

The described changes in morphology and the number of domains is summarized in Fig. 5b, where different symbols denote possible outcomes from the simulations (equilibrium contact zones presented in the SI). The phase diagram is clearly consistent with the scenario presented above.

While the our model experimental system relied on thermal fluctuations, in the cellular context, active membrane fluctuations, promoted by protrusions and retrac-

tions of filopodia, have recently been found necessary for the establishment of model junctions [3]. Active fluctuations may control the size of the domain, as well as the density of bonds within the domain, which is not the case in the passive membranes. In both active and passive systems, aggregates with low density of bonds (B2??) that densify under a retracting force can be obtained [41]. However, the regulation of the condensation process occurs in vesicles on the level of the system, while in cells, it can be performed locally by active forces.

Another intriguing phenomenon recently observed in cells [20] is that a ring of cadherin junctions forms spontaneously between two adherent cells or for cells binding to the substrate [3], upon which further cell spreading may be induced by forces acting on the ring [20]. The appearance of the ring can be understood in the context of the current work, which suggests that active membrane fluctuations, promote the initial ring-like organization of adhesions where cadherin is recruited from the outside of the contact zone, and after it enters the contact zone, it binds very quickly. Because the mobility of the construct is significantly affected, *trans*-dimers become obstacles for other cadherins penetrating the contact zone and a ring forms. This hypothesis is supported by the result that the formation of the ring is circumvented when the diffusion of cadherins is increased in the bilayer [3], due to a longer mean path of a free protein penetrating the contact zone [42].

A particularly interesting prediction of our model is the sensitivity of the two-dimensional effective binding affinity to the details of the membrane environment. The presented framework may therefore explain the significant spread of measured free energies for binding of membrane-embedded proteins with various techniques, in which the membrane environment was not strictly controlled [39, 44–46]. In the context of cadherin *trans*-dimerization, we find that the effective binding affinity does not exceed 3 k_BT units in the majority of the experimentally accessible phase space, making this system particularly vulnerable to small variations in experimental condition, as compared to the case of stronger ligand-receptor pairs [47, 48]. It is precisely this sensitivity that makes the cadherin model ideal for probing the presented theoretical framework. Further refinement of our approach should encompass the directionality of the cadherin *cis*-interaction, induced by the asymmetry of the cadherin *trans*-dimer which was previously identified as an important element for the lateral oligomerization [6, 49].

In addition to the static arguments which relate the classical 2D affinities to the effective affinities modulated by membrane fluctuations, this framework sets the foundation for an in-depth analysis of the two-dimensional protein transport and complexation dynamics, which control the formation of functional microdomains and rafts in cellular membranes. Indeed, the presented framework is consistent with the dynamics data available from the experiments where a cell is allowed to bind to a cadherin enriched substrate or another cell [3, 20]. Moreover, due to the generic nature of membrane mediated interactions, a very similar phase space exists for any other cell adhesion molecule, but due to their typically larger intrinsic affinity, in a broader range of separations and fluctuation amplitudes. Hence, the effects, identified here, may play a role in a number of intracellular and extracellular processes that involve the formation of macromolecular complexes between membranes.

[1] Leckband, D. & Sivasankar, S. Cadherin recognition and adhesion. *Curr. Opin. Cell Biol.* **24**, 620–627 (2012).

[2] Lecuit, T. & Yap, A. S. E-cadherin junctions as active mechanical integrators in tissue dynamics. *Nat. Cell Biol.* **17**, 533–539 (2015).

[3] Bazellières, E. *et al.* Control of cell-cell forces and collective cell dynamics by the intercellular adhesome. *Nat. Cell Biol.* **17**, 409–420 (2015).

[4] Volk, T., Cohen, O. & Geiger, B. Formation of heterotypic adherens-type junctions between L-CAM-containing liver cells and A-CAM-containing lens cells. *Cell* **50**, 987–994 (1987).

[5] Ayalon, O., Sabanai, H., Lampugnani, M.-G., Dejana, E. & Geiger, B. Spatial and temporal relationships between cadherins and pecam-1 in cell-cell junctions of human endothelial cells. *J. Cell Biol* **126**, 247–258 (1994).

[6] Wu, Y., Vendome, J., Shapiro, L., Ben-Shaul, A. & Honig, B. Transforming binding affinities from three dimensions to two with application to cadherin clustering. *Nature* **475**, 510–513 (2011).

[7] Bello, S. M., Millo, H., Rajebhosale, M. & Price, S. R. Catenin-dependent cadherin function drives divisional segregation of spinal motor neurons. *J. Neurosci.* **32**, 490–505 (2012).

[8] Katsamba, P. *et al.* Linking molecular affinity and cellular specificity in cadherin-mediated adhesion. *Proc. Natl. Acad. Sci. U.S.A.* **106**, 11594–11599 (2009).

[9] Gumbiner, B. M. Regulation of cadherin-mediated adhesion in morphogenesis. *Nat. Rev. Mol. Cell Biol.* **6**, 622–634 (2005).

[10] Jeanes, A., Gottardi, C. J. & Yap, A. S. Cadherins and cancer: How does cadherin dysfunction promote tumor progression? *Oncogene* **27**, 6920–6929 (2008).

[11] Biswas, K. H. *et al.* E-cadherin junction formation involves an active kinetic nucleation process. *Proc. Natl. Acad. Sci. U. S. A.* **112**, 10932–7 (2015).

[12] Rakshit, S. & Sivasankar, S. Biomechanics of cell adhesion: How force regulates the lifetime of adhesive bonds at the single molecule level. *Phys. Chem. Chem. Phys.* **16**, 2211–2223 (2014).

[13] Sivasankar, S., Zhang, Y., Nelson, W. J. & Chu, S. Characterizing the initial encounter complex in cadherin adhesion. *Structure* **17**, 1075–1081 (2009).

[14] Harrison, O. J. *et al.* Two-step adhesive binding by classical cadherins. *Nat. Struct. Mol. Biol.* **17**, 348–357 (2010).

[15] Boggon, T. J. *et al.* C-cadherin ectodomain structure and implications for cell adhesion mechanisms. *Science*

296, 1308–1313 (2002).

[16] Fenz, S. F. *et al.* Switching from ultraweak to strong adhesion. *Adv. Mater.* **23**, 2622–2626 (2011).

[17] Vendome, J. *et al.* Structural and energetic determinants of adhesive binding specificity in type I cadherins. *Proc. Natl. Acad. Sci. U.S.A.* **111**, E4175—-E4184 (2014).

[18] Brasch, J., Harrison, O. J., Honig, B. & Shapiro, L. Thinking outside the cell: How cadherins drive adhesion. *Trends Cell Biol.* **22**, 299–310 (2012).

[19] Hong, S., Troyanovsky, R. B. & Troyanovsky, S. M. Spontaneous assembly and active disassembly balance adherens junction homeostasis. *Proc. Natl. Acad. Sci. U.S.A.* **107**, 3528–3533 (2010).

[20] Engl, W., Arasi, B., Yap, L. L., Thiery, J. P. & Viasnoff, V. Actin dynamics modulate mechanosensitive immobilization of E-cadherin at adherens junctions. *Nat. Cell Biol.* **16**, 587–94 (2014).

[21] Taveau, J.-C. *et al.* Structure of artificial and natural VE-cadherin-based adherens junctions. *Biochem. Soc. Trans.* **36**, 189 (2008).

[22] Ozaki, C., Obata, S., Yamanaka, H., Tominaga, S. & Suzuki, S. T. The extracellular domains of E- and N-cadherin determine the scattered punctate localization in epithelial cells and the cytoplasmic domains modulate the localization. *J. Biochem.* **147**, 415–425 (2010).

[23] Harrison, O. J. *et al.* The extracellular architecture of adherens junctions revealed by crystal structures of type I cadherins. *Structure* **19**, 244–256 (2011).

[24] Hong, S., Troyanovsky, R. B. & Troyanovsky, S. M. Binding to F-actin guides cadherin cluster assembly, stability, and movement. *J. Cell Biol.* **201**, 131–143 (2013).

[25] Fenz, S. F., Merkel, R. & Sengupta, K. Diffusion and intermembrane distance: Case study of avidin and E-cadherin mediated adhesion. *Langmuir* **25**, 1074–1085 (2009).

[26] Limozin, L. & Sengupta, K. Quantitative reflection interference contrast microscopy (RICM) in soft matter and cell adhesion. *ChemPhysChem* **10**, 2752–2768 (2009).

[27] Rädler, J. O., Feder, T. J., Strey, H. H. & Sackmann, E. Fluctuation analysis of tension-controlled undulation forces between giant vesicles and solid substrates. *Phys. Rev. E* **51**, 4526–4536 (1995).

[28] Helfrich, W. Steric interaction of fluid membranes in multilayer systems. *Z. Naturforsch.* **33**, 305 (1978).

[29] Freund, L. B. Entropic pressure between biomembranes in a periodic stack due to thermal fluctuations. *Proc. Natl. Acad. Sci. U. S. A.* **110**, 2047–51 (2013).

[30] Bruinsma, R., Goulian, M. & Pincus, P. Self-assembly of membrane junctions. *Biophys. J.* **67**, 746–750 (1994).

[31] Bruinsma, R., Behrisch, A. & Sackmann, E. Adhesive switching of membranes: Experiment and theory. *Phys. Rev. E* **61**, 4253–4267 (2000).

[32] Schmidt, D. *et al.* Signature of a nonharmonic potential as revealed from a consistent shape and fluctuation analysis of an adherent membrane. *Phys. Rev. X* **4**, 021023 (2014).

[33] Bihr, T., Seifert, U. & Smith, A.-S. Nucleation of ligand-receptor domains in membrane adhesion. *Phys. Rev. Lett.* **109**, 258101 (2012).

[34] Schmidt, D., Bihr, T., Seifert, U. & Smith, A.-S. Coexistence of dilute and densely packed domains of ligand-receptor bonds in membrane adhesion. *Europhys. Lett.* **99**, 38003 (2012).

[35] Reister, E., Bihr, T., Seifert, U. & Smith, A. S. Two intertwined facets of adherent membranes: membrane roughness and correlations between ligand-receptors bonds. *New J. Phys.* **13**, 25003 (2011).

[36] Lipowsky, R. Adhesion of membranes via anchored stickers. *Phys. Rev. Lett.* **77**, 1652–1655 (1996).

[37] Bell, G. I. Models for the specific adhesion of cells to cells. *Science* **200**, 618–627 (1978).

[38] Dembo, M., Torney, D. C., Saxman, K. & Hammer, D. The reaction-limited kinetics of membrane-to-surface adhesion and detachment. *Proc. R. Soc. London, Ser. B* **234**, pp. 55–83 (1988).

[39] Bihr, T., Seifert, U. & Smith, A.-S. Multiscale approaches to protein-mediated interactions between membranes—relating microscopic and macroscopic dynamics in radially growing adhesions. *New J. Phys.* **17**, 083016 (2015).

[40] Bihr, T. *et al.* Association rates of membrane-coupled cell adhesion molecules. *Biophys. J.* **107**, L33 – L36 (2014).

[41] Smith, A.-S., Sengupta, K., Goennenwein, S., Seifert, U. & Sackmann, E. Force-induced growth of adhesion domains is controlled by receptor mobility. *Proc. Natl. Acad. Sci. U.S.A.* **105**, 6906–6911 (2008).

[42] Schmidt, D. *et al.* Crowding of receptors induces ring-like adhesions in model membranes. *BBA - Mol. Cell Res.* **1853**, 2984–2991 (2015).

[43] Fenz, S. F., Smith, A.-S., Merkel, R. & Sengupta, K. Inter-membrane adhesion mediated by mobile linkers: Effect of receptor shortage. *Soft Matter* **7**, 952–962 (2011).

[44] Dustin, M. L., Bromley, S. K., Davis, M. M. & Zhu, C. Identification of self through two-dimensional chemistry and synapses. *Annu. Rev. Cell Dev. Biol.* **17**, 133–157 (2001).

[45] Zhu, D.-M., Dustin, M. L., Cairo, C. W. & Golan, D. E. Analysis of two-dimensional dissociation constant of laterally mobile cell adhesion molecules. *Biophys. J.* **92**, 1022–1034 (2007).

[46] Hu, J., Lipowsky, R. & Weikl, T. R. Binding constants of membrane-anchored receptors and ligands depend strongly on the nanoscale roughness of membranes. *Proc. Natl. Acad. Sci. U.S.A.* **110**, 15283–15288 (2013).

[47] Boulbitch, A., Guttenberg, Z. & Sackmann, E. Kinetics of membrane adhesion mediated by ligand-receptor interaction studied with a biomimetic system. *Biophys. J.* **81**, 2743–2751 (2001).

[48] Lorz, B. G., Smith, A.-S., Gege, C. & Sackmann, E. Adhesion of giant vesicles mediated by weak binding of sialyl-lewisX to E-selectin in the presence of repelling poly(ethylene glycol) molecules. *Langmuir* **23**, 12293–12300 (2007).

[49] Wu, Y., Honig, B. & Ben-Shaul, A. Theory and simulations of adhesion receptor dimerization on membrane surfaces. *Biophys. J.* **104**, 1221–1229 (2013).

Acknowledgments

A.-S.S. and T.B. were funded from the grant ERC StG 2013-337283 and K.S. from ERC-StG 307104FP of the European Research Council. A.-S.S and D.S. were supported by the Research Training Group 1962 at the Friedrich-Alexander-Universität Erlangen-Nürnberg. This work has partly been supported by A*MIDEX (no. ANR-11-IDEX-0001-02).

Footnote

*both authors contributed equally

Author Contributions

The project was conceived and supervised by A.-S.S., K.S., U.S. and R.M. The experimental set-up was established by S.F. and K.S., and applied to the current problem by S.F. Data analysis was performed by S.F., D.S., K.S. and A.-S.S. The simulation setup was built by T.B and A.-S.S, and executed by T.B. The theoretical model was developed by D.S. and A.-S.S. with the help of T.B. and U.S. All authors contributed to the interpretation of results. The article was written by T.B., D.S., S.F. K.S. and A.-S.S.

Supplementary Information

Membrane as matchmaker in the cell adhesion process

Timo Bihr,[1,2] Susanne Fenz,[3,4] Daniel Schmidt,[1,2] Rudolf Merkel,[4]
Kheya Sengupta,[5] Udo Seifert,[2] and Ana-Sunčana Smith[1,6]

[1]*PULS Group, Institut für Theoretische Physik and the Excellence Cluster: Engineering of Advanced Materials, Universität Erlangen-Nürnberg, Nägelsbachstrasse 49b, 91052 Erlangen, Germany*

[2]*II. Institut für Theoretische Physik, Universität Stuttgart, Pfaffenwaldring 57, 70550 Stuttgart, Germany*

[3]*Department of Cell and Developmental Biology, Universität Würzburg, Am Hubland, 97074 Würzburg, Germany*

[4]*Institute of Complex Systems 7: Biomechanics Forschungszentrum Jülich GmbH, 52425 Jülich, Germany*

[5]*CNRS UPR 3118, Centre Interdisciplinaire de Nanosciences de Marseille, Aix-Marseille Université Campus de Luminy, 13288 Marseille cedex 9, France*

[6]*Institute Ruđer Bošković, Division of Physical Chemistry, Bijenička cesta 54, 10000 Zagreb, Croatia*

I. EXPERIMENTAL METHODS

A. Sample preparation

The measurements were performed following a procedure developed in previous work [1]. In short, supported lipid bilayers (SLBs) were prepared with a film balance (Nima, Coventry, UK) applying the Langmuir-Blodgett (proximal layer, pure SOPC) and Langmuir-Schäfer (distal layer, SOPC with 2 mol% DOPE-PEG2000 and 1 mol% DOGS-NTA) techniques. The SLBs were loaded with 2 μM nickel sulfate for 15 minutes and afterwards exposed to an E-cadherin Fc chimera (Fig. SI 1) exhibiting also an hexahistidin tag (R&D Systems, Minneapolis, MN) in a final concentration of 6 μg/ml for 3 hours.

GUVs consisting of SOPC with 2 mol% DOPE-PEG2000 and 1 mol% DOGS-NTA were produced via electro-swelling. The GUVs were functionalized with nickel sulfate and cadherin before exposure to the SLB in presence of 750 μM $CaCl_2$. All lipids were purchased from Avanti, Alabaster, AL.

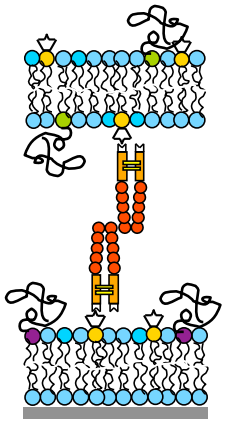

Fig. SI 1. Sketch of the E-cadherin Fc chimera bound to the lipid bilayer by a hexahistidin tag. The sizes of the individual constituents is estimated from structural considerations to be 19 nm (E-cadherin), 7 nm (Fc fragment) and 2 nm (hexahistidin tag). Consequently, the intermembrane distance is estimated to 52 nm considering the overlap of the outmost extracellular domains of both E-cadherins in the bound state [1].

B. Data acquisition and analysis - Extracting corrected fluctuations

Movies of GUVs were recorded with reflection interference contrast microscopy (RICM) at 10 Hz, with the lateral spatio-temporal resolution of $a \simeq 300\,\mathrm{nm}$ and $\tau \simeq 100\,\mathrm{ms}$, respectively. In the current set up, the absolute height resolution is 5 nm, while the relative height resolution is 2 nm (see [**?**] for details).

Because measured fluctuations of the membrane emerge from a signal recorded with a finite spatio-temporal resolution (apparent signal) and noise, some fluctuation modes of the membrane are not detectable, either because of being too small in size or decaying too fast in time. In order to extract corrected fluctuations, the noise needs to be deducted, and the effects of finite resolution de-convolved.

The camera noise $\langle\chi^2\rangle$ was measured for each vesicle independently in the background of the image. Consequently, we can extract the apparent fluctuation amplitude $\langle\Delta\bar{h}^2\rangle_a^\tau$ from the measured fluctuation amplitude $\langle\Delta\tilde{h}^2\rangle$ following the expression

$$\langle\Delta\bar{h}^2\rangle_a^\tau = \langle\Delta\tilde{h}^2\rangle - \langle\chi^2\rangle. \tag{SI-1}$$

By assuming the Gaussian nature of the fluctuations, and following a recently-developed procedure [**?**], we can relate the corrected fluctuation amplitude ($f \equiv 1/\sqrt{k_m}$) and the apparent fluctuation amplitude

$$\langle\Delta\bar{h}^2\rangle_a^\tau = \int \mathrm{d}\mathbf{q}\ \frac{1}{\kappa q^4 + k_m^2/(64\kappa)}\phi_a(\mathbf{q})\psi^\tau(\mathbf{q}) \tag{SI-2}$$

using

$$\phi_a(\mathbf{q}) = \frac{16}{a^4}\frac{\sin(aq_1/2)^2\sin(aq_2/2)^2}{(q_1q_2)^2}, \tag{SI-3}$$

and

$$\psi^\tau(\mathbf{q}) = \frac{\mathrm{e}^{-\Gamma(q)\tau} - 1 + \Gamma(q)\tau}{\Gamma^2(q)\tau^2}. \tag{SI-4}$$

Here, $\mathbf{q}$ are the wave vectors for which $\mathbf{q} \equiv (q_1, q_2)$, $q = |\mathbf{q}|$, and $\Gamma(q)$ denote the damping coefficients

$$\Gamma(q) = \frac{\kappa q^4 + k_m^2/(64\kappa)}{4\eta q}\frac{2\left(\sinh^2(qh_0) - (qh_0)^2\right)}{\sinh^2(qh_0) - (qh_0)^2 + \sinh(qh_0)\cosh(qh_0) + (qh_0)}. \tag{SI-5}$$

This form is used to account for the fact that the two interacting membranes are in relative proximity [4]. Here, η is the viscosity of the surrounding fluid.

name	Δh_r [nm]	$\sqrt{\langle \Delta\bar{h}^2 \rangle_a^\tau}$ [nm]	f [nm]
A1	6 ± 2	3 ± 2	12 ± 4
A2	6 ± 2	7 ± 2	15 ± 2
B1	reference state	6 ± 2	15 ± 2
B2	2 ± 2	8 ± 2	17 ± 2

Table SI-1. Measurement of height and fluctuations for the vesicles presented in Fig. 5 of the main text. The second column displays the separations between the other domains of cadherins on opposing membranes relative the the separation in the system B1 Δh_r. The separation Δh in the B1 system is obtained by measuring the absolute separation between two membranes $h_0 = 93$ nm and from that, deducing the length of the two cadherins is $2l_0 = 52\,\mathrm{nm}$ [6]. Consequently, the separation between cadherins in B1 is $\Delta h = 41 \pm 5\,\mathrm{nm}$. All other values are obtained relative to this separation. The third column is the apparent fluctuation amplitude, while the last column shows the corrected fluctuation f.

In our experiments the membrane bending rigidity was set to $\kappa = 20\,k_BT$ [5]. We measure h_0 for each vesicle from the mean membrane position in the unbound state and we find the corrected fluctuations f recursively from the apparent fluctuations. Finally, the corrected fluctuation amplitude is systematically downsized by $6 \pm 2\,\mathrm{nm}$, to systematically compare experiments and simulations (as shown in Fig. 5 of the main text).

II. 2D BINDING AFFINITY

A. Affinity of an isolated *trans*-dimer

The free energy for forming an isolated *trans*-dimer, can be calculated following [7] from the partition function of the unbound state $\mathcal{Z}_\mathrm{u}$, which takes the form

$$\begin{aligned}\mathcal{Z}_\mathrm{u} &= \int_{-\infty}^{\infty} \mathrm{d}h_1 \int_{-\infty}^{\infty} \mathrm{d}h_2 \ \exp\left[-\frac{1}{2}\frac{k_m k_c}{k_m + k_c}(h_2 - (h_0 - l_0))^2 - \frac{k_c}{2}(h_1 - l_0)^2\right], \\ &= \sqrt{\frac{2\pi}{k_c}}\sqrt{\frac{4(k_m + k_c)}{k_m k_c}}. \end{aligned} \tag{SI-6}$$

Here h_1 and h_2 are the coordinates of the outer cadherin domains on the two opposing membranes. Other symbols are defined in the main text and shown in Fig. 3c. We note

that the first and the second term in the exponent on the right hand side of eq. SI-6 account for the coupled fluctuations of the membrane and the associated cadherin, and the cadherin on the SLB, respectively. In the former case, the coupled contribution emerges through an effective elastic constant for two springs in series $k_m k_c/(k_m + k_c)$.

In a similar way, the partition function of the bound state $\mathcal{Z}_\mathrm{b}$ can be calculated from

$$\begin{aligned}\mathcal{Z}_\mathrm{b} &= \int_{-\infty}^{\infty} \mathrm{d}h_1 \int_{h_1}^{h_1+\alpha} \mathrm{d}h_2 \ \exp\left[-\frac{1}{2}\frac{k_m k_c}{k_m + k_c}(h_2 - (h_0 - l_0))^2 - \frac{k_c}{2}(h_1 - l_0)^2 + \epsilon_b\right], \\ &\simeq \sqrt{\frac{2\pi\alpha^2}{k_c}\frac{k_m + k_c}{2k_m + k_c}} \exp\left[-\frac{1}{2}\Omega_u(\Delta h)^2 + \epsilon_b\right], \end{aligned} \tag{SI-7}$$

with

$$\Omega_u \equiv \frac{k_m k_c}{2k_m + k_c}. \tag{SI-8}$$

The integration boundaries in eq. SI-7 now take into account only states in which the outmost domains of the two cadherins binding into a *trans*-dimer are within the binding pocket of the size α.

The free energy difference between the bound and the unbound state is then simply

$$\tilde{E}_b = \log\left(\frac{\mathcal{Z}_\mathrm{u}}{\mathcal{Z}_\mathrm{b}}\right) = \frac{1}{2}\Omega_u(\Delta h)^2 + \frac{1}{2}\ln\left[\frac{2\pi}{\Omega_u\alpha^2}\right] - \epsilon_b. \tag{SI-9}$$

If a formation of a *trans*-dimer is calculated within a mean-field approach, where all others create an environment in which the bond is formed or broken, membrane parameters Δh and k_m become position dependent yielding $\Delta h^{x_i} = h_0^{x_i} - 2l_0$, $k_m^{x_i}$ and

$$\Omega_u^{x_i} \equiv \frac{k_m^{x_i} k_c}{2k_m^{x_i} + k_c}. \tag{SI-10}$$

Using these local variables in eq. SI-9 gives rise to eq. 1 in the main text.

B. 2D affinity for *trans*-dimers within model junctions

To calculate the 2D binding affinity, we calculate the partition functions on the level of the entire junction consisting of N_b *trans*-dimers. In this case, the partition function for the

unbound and in the bound states, $\mathcal{Z}_{\rm u}^{N_b}$ and $\mathcal{Z}_{\rm b}^{N_b}$, become

$$\mathcal{Z}_{\rm u}^{N_b} = \prod_{i=1}^{N_b} \sqrt{\frac{2\pi}{k_c}} \sqrt{\frac{4(k_m + k_c)}{k_m k_c}}, \tag{SI-11}$$

$$\mathcal{Z}_{\rm b}^{N_b} = \prod_{i=1}^{N_b} \sqrt{\frac{2\pi\alpha^2}{k_c} \frac{k_m^{x_i} + k_c}{2k_m^{x_i} + k_c}} \exp\left[-\frac{1}{2} \frac{k_m^{x_i} k_c}{2k_m^{x_i} + k_c} (\Delta h^{x_i})^2 + \epsilon_b\right], \tag{SI-12}$$

and the 2D binding affinity is found as the average free energy gain for forming a *trans*-dimer

$$\begin{aligned} \tilde{E}_b^d &= \frac{1}{N_b} \log\left(\frac{\mathcal{Z}_{\rm u}^{N_b}}{\mathcal{Z}_{\rm b}^{N_b}}\right) = \frac{1}{N_b} \sum_{i=1}^{N_b} \left[\frac{1}{2}\Omega_u^{x_i} (\Delta h^{x_i})^2 - \epsilon_b + \frac{1}{2} \ln\left(\frac{2\pi}{\Omega_u^{x_i}\alpha^2} \frac{k_m + k_c}{k_m^{x_i} + k_c}\right)\right] \\ &= \frac{1}{N_b} \sum_{i=1}^{N_b} \left[E_b^{x_i} + \frac{1}{2} \ln\left(\frac{k_m + k_c}{k_m^{x_i} + k_c}\right)\right] \end{aligned} \tag{SI-13}$$

Since the reference state is the fully unbound membrane, an additional contribution to the free energy is obtained accounting for the entropic cost associated with the change of membrane fluctuations upon binding.

III. SIMULATION METHODS

The Monte Carlo simulation presented in the main text is based on a recently published protocol, which was shown to be in excellent agreement with a higher level theory [8], as well as with experiments [9, 10].

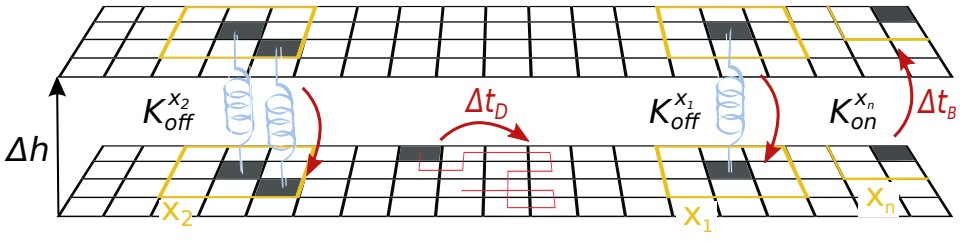

Fig. SI 2. Scheme for the Monte Carlo simulation.

For the current work, the protocol was adjusted to mimic the current experiments as closely as possible. More specifically, the GUV and SLB membranes were discretized into

square lattices (Fig. SI 2), thereby the unit edge of each lattice (40 nm) reflected the characteristic size of the cadherin chimera. The two lattices were aligned, and in the absence of bonds, the cadherin outer domains could be viewed as separated by a vertical distance Δh (Fig. 3c in the main text). Analogous to the initial densities in the vesicles and the substrate in the experiments, the simulation involved 3×10^5 cadherins (gray squares in Fig. SI 2) that diffuse on the GUV and the SLB consisting of 2^{24} sites (about $1,000\,\mu\mathrm{m}^2$) for over 100 s, with a microseconds resolution. The membrane was simulated with the bending rigidity of $20\,k_BT$ in all simulations. The binding range of the cadherins was set to $\alpha = 1\,\mathrm{nm}$, and the intrinsic binding affinity to $\epsilon_b = 7\,k_BT$ [11]. For the stiffness of cadherins we use $k_c = 5 \times 10^{-2}\,k_BT\mathrm{nm}^{-2}$.

In each simulation time step, if a binder on a vesicle grid-site is aligned with the binder on a substrate grid, an attempt to bind is performed with an effective rate $K_{\mathrm{on}}^{x_n}$. Existing bonds break with a rate $K_{\mathrm{off}}^{x_n}$. Here, the superscript x_n denotes the micro-environment (yellow squares in Fig. SI 2) consisting of neighbouring bonds (blue springs), detected and updated in each step of the simulation for each binder.

To calculate the effective reaction rates $K_{\mathrm{on}}^{x_i}$ and $K_{\mathrm{off}}^{x_i}$, we average instantaneous, height dependent reaction rates $k_{\mathrm{on}}\left(h(x_i,t)\right)$ and $k_{\mathrm{off}}\left(h(x_i,t)\right)$ by the height probability distribution $p^{x_i}(h)$

$$\begin{aligned} K_{\mathrm{off}}^{x_i} &\equiv \int \mathrm{d}h\, p^{x_i}(h) k_{\mathrm{off}}\left(h\right) \\ K_{\mathrm{on}}^{x_i} &\equiv \int \mathrm{d}h\, p^{x_i}(h) k_{\mathrm{on}}\left(h\right). \end{aligned} \tag{SI-14}$$

For the instantaneous reaction rates, we adjust the proposition from Dembo [8, 12]

$$k_{\mathrm{on}}\left(h(x_i,t)\right) = k_0 \sqrt{\frac{k_c\alpha^2}{4\pi}} \exp\left[-\frac{k_c}{4}\left(\Delta h_0^{x_i} - \alpha\right)^2\right], \tag{SI-15}$$

and from Bell [8, 13]

$$k_{\mathrm{off}}\left(h(x_i,t)\right) = k_0 \exp\left[\frac{k_c\alpha}{2}\Delta h_0^{x_i} - \frac{k_c\alpha^2}{4} - \epsilon_b\right]. \tag{SI-16}$$

Here, k_0 is the instrinsic reaction rate, α the binding range between the outer cadherin domains, and ϵ_b the binding enthalpy of the bond. The elastic constant k_c of the cadherin and instantaneous separation $\Delta h_0^{x_i} \equiv h(x_i,t) - 2l_0$ between outer cadherin domains have been introduced in the main text. For simplicity, we measure the energy in units of k_BT.

The membrane height distribution is calculated from the Helfrich-Hamiltonian [14, 15] for the membrane-bond system

$$\mathcal{H}[h(x)] = \int_A \mathrm{d}^2x \left(\frac{\kappa}{2}(\Delta h(x))^2 + \frac{1}{2}\frac{k_m^2}{64\kappa}\left[h(x) - h_0\right]^2 \right) + \sum_{\mathrm{i}=1}^{N_b} \left[\frac{k_c}{4}\left(\Delta h_0^{x_i}\right)^2 - \epsilon_b \right], \qquad \text{(SI-17)}$$

with bending rigidity κ of the membrane, effective elastic constant k_m of the unbound membrane fluctuating at the distance of h_0 from the other membrane (see Fig. 4c in the main text). Finally, N_b denotes the number of formed bonds at positions x_i .

The membrane height distribution for this Hamiltonian can be calculated semi-analytically for every possible bond configuration [14] and turns out (for the Hamiltonian that we consider) to be Gaussian. The height probability distribution becomes at the binding site x_i

$$p^{x_i}(h) = \frac{1}{\sqrt{2\pi k_m^{x_i}}} \exp\left[-\frac{k_m^{x_i}}{2}\left(h - \langle h^{x_i}\rangle\right)^2 \right] \qquad \text{(SI-18)}$$

with average membrane height

$$\langle h^{x_i}\rangle = -\frac{8}{\pi k_m^{x_i}} \sum_{jl} l_0 \left(G_{jl}^{x_i}\right)^{-1} \mathrm{kei}\left(q_0\ |x_i - x_j|\right) \qquad \text{(SI-19)}$$

and effective elastic constant of the membrane

$$k_m^{x_i} = k_m + \frac{16}{\pi^2} \sum_{jl} \mathrm{kei}\left(q_0\ |x_i - x_j|\right) \left(G_{jl}^{x_i}\right)^{-1} \mathrm{kei}\left(q_0\ |x_i - x_l|\right). \qquad \text{(SI-20)}$$

Thereby, we use the Kelvin-function $\mathrm{kei}(\cdot)$, the characteristic mode $q_0 \equiv \sqrt{8\kappa/k_m}$ and the coupling matrix $G_{jl}^{x_i}$ defined as

$$G_{jl}^{x_i} \equiv \frac{2\delta_{jl}}{k_c} - \frac{4}{\pi k_m} \mathrm{kei}\left(q_0|x_j - x_l|\right) - \frac{16}{\pi^2 k_m} \mathrm{kei}\left(q_0|x_i - x_j|\right) \mathrm{kei}\left(q_0|x_i - x_l|\right) \qquad \text{(SI-21)}$$

with Kronecker-delta δ_{jl}. Utilizing equations (SI-15), (SI-16) and (SI-18) we find the effective reaction rates, eq. (SI-14).

At the onset of the simulation, cadherins were randomly placed on the two membranes, and the contact zone of a fixed size was defined in the middle of the simulation box. The interaction between cadherins is enabled only for proteins within the contact zone, while the rest of the membrane provides the reservoir reconstructing the appropriate statistical ensemble. Specifically, the cadherins on the substrate are coupled to a reservoir of a constant chemical potential (mimicking the quasi-infinite surface of the bilayer), while in the vesicles,

the number of cadherins was set to a finite number (taking into account the finite vesicle size). This is important to set the proper equilibrium conditions [16] .

Typically, the simulation starts with $N_b = 0$. Exceptionally, if the expected nucleation time is exceedingly high (lower right corner in Fig. 5d), a stable seed was placed in the middle of the contact zone at $t = 0$. The simulations were ran until a steady state was reached. The final configuration was used to calculate the effective binding affinity (Fig. 5c).

To compare the simulations with the experiment, we systematically changed the initial separation between cadherins and the fluctuation amplitude of the membrane. Characteristic snapshots from this study are shown in figures SI 3 and SI 4 for intrinsic reaction rates $k_0 = 1\,s^{-1}$ and $k_0 = 100\,s^{-1}$, respectively. As can be seen from these phase diagrams, the intrinsic reaction rate does not significantly change the nature of the growth process, but affects the overall time-scale of the growth process from $N_b = 0$ to the equilibrium.

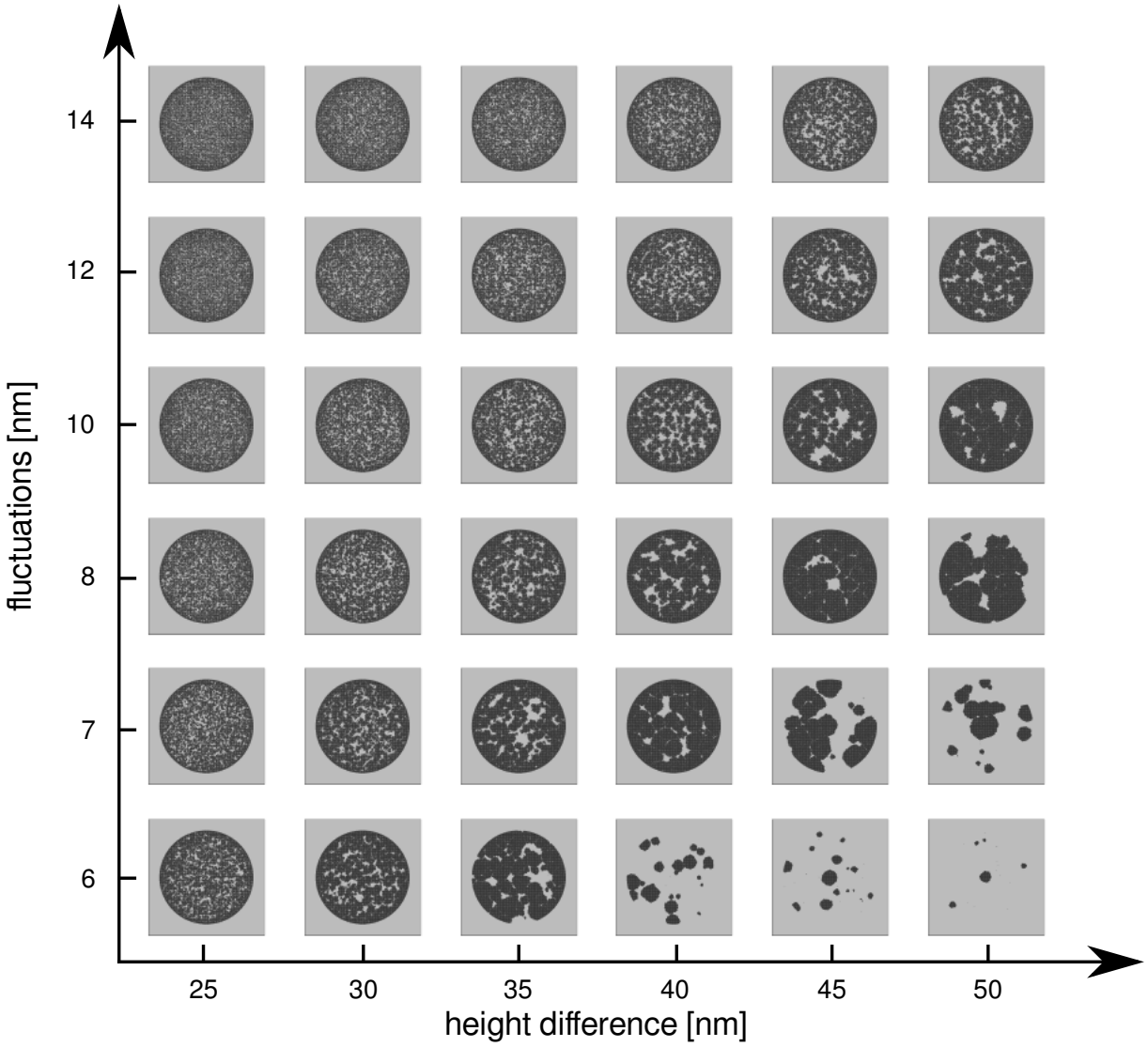

Fig. SI 3. Representative snapshots of the simulations in Fig. 5b and 5c of the main text. An increasing height and a decreasing fluctuation amplitude leads to a reduced number of seeds during the growth process ($k_0 = 1\,s^{-1}$).

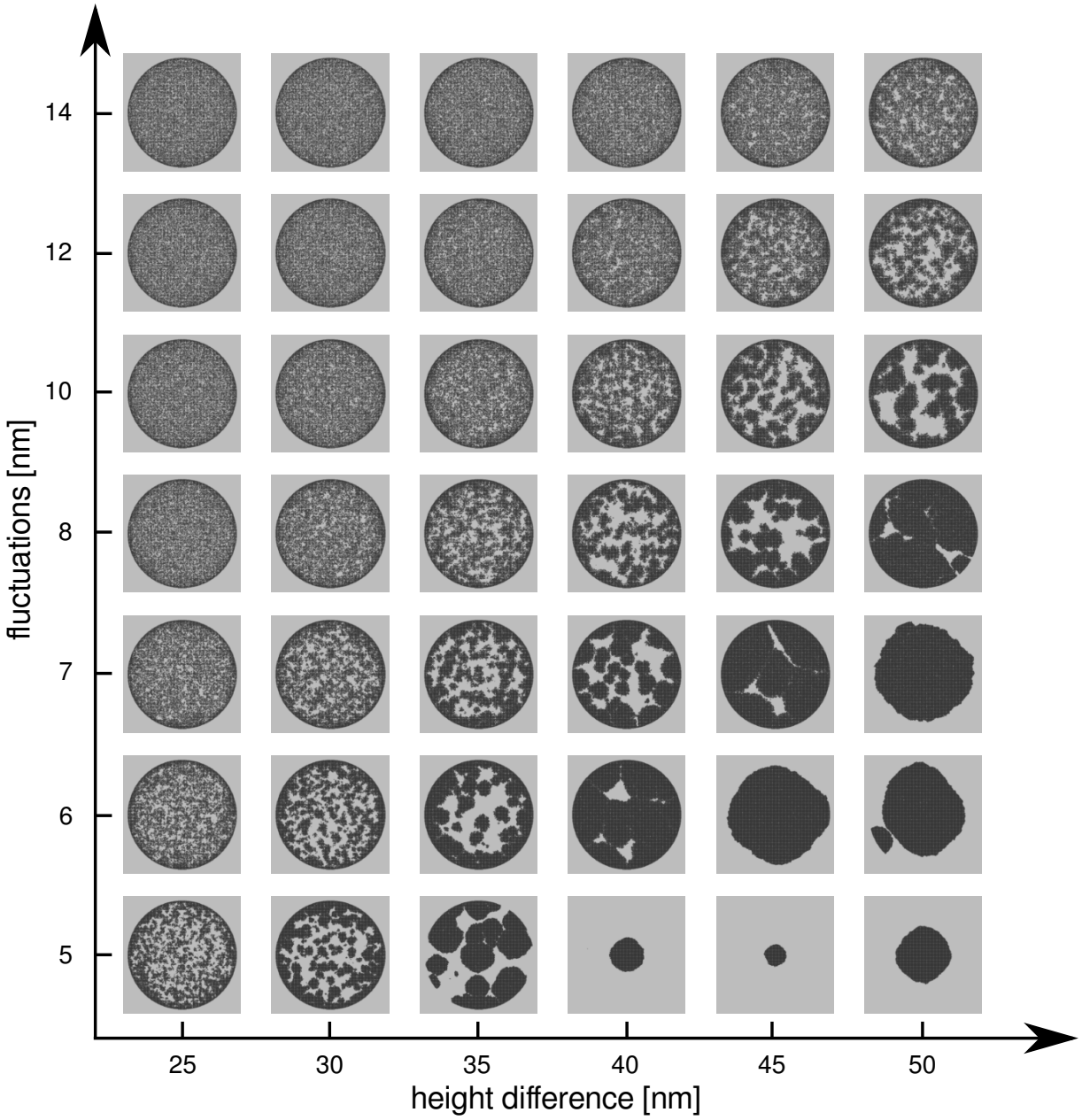

Fig. SI 4. Phase diagram for an increased intrinsic reaction $k_0 = 100\,s^{-1}$.

IV. REFERENCES

[1] Fenz, S. F., Merkel, R. & Sengupta, K. Diffusion and intermembrane distance: Case study of avidin and E-cadherin mediated adhesion. *Langmuir* **25**, 1074–1085 (2009).

[2] Limozin, L. & Sengupta, K. Quantitative reflection interference contrast microscopy (RICM) in soft matter and cell adhesion. *ChemPhysChem* **10**, 2752–2768 (2009).

[3] Schmidt, D. *et al.* Signature of a nonharmonic potential as revealed from a consistent shape and fluctuation analysis of an adherent membrane. *Phys. Rev. X* **4**, 021023 (2014).

[4] Seifert, U. Dynamics of a bound membrane. *Phys. Rev. E* **49**, 3124–3127 (1994).

[5] Evans, E. & Rawicz, W. Entropy-driven tension and bending elasticity in condensed-fluid membranes. *Phys. Rev. Lett.* **64**, 2094–2097 (1990).

[6] Boggon, T. J. *et al.* C-cadherin ectodomain structure and implications for cell adhesion mechanisms. *Science* **296**, 1308–1313 (2002).

[7] Schmidt, D., Bihr, T., Seifert, U. & Smith, A.-S. Coexistence of dilute and densely packed domains of ligand-receptor bonds in membrane adhesion. *Europhys. Lett.* **99**, 38003 (2012).

[8] Bihr, T., Seifert, U. & Smith, A.-S. Multiscale approaches to protein-mediated interactions between membranes—relating microscopic and macroscopic dynamics in radially growing adhesions. *New J. Phys.* **17**, 083016 (2015).

[9] Fenz, S. F. *et al.* Switching from ultraweak to strong adhesion. *Adv. Mater.* **23**, 2622–2626 (2011).

[10] Schmidt, D. *et al.* Crowding of receptors induces ring-like adhesions in model membranes. *BBA - Mol. Cell Res.* **1853**, 2984–2991 (2015).

[11] Wu, Y., Vendome, J., Shapiro, L., Ben-Shaul, A. & Honig, B. Transforming binding affinities from three dimensions to two with application to cadherin clustering. *Nature* **475**, 510–513 (2011).

[12] Dembo, M., Torney, D. C., Saxman, K. & Hammer, D. The reaction-limited kinetics of membrane-to-surface adhesion and detachment. *Proc. R. Soc. London, Ser. B* **234**, pp. 55–83 (1988).

[13] Bell, G. I. Models for the specific adhesion of cells to cells. *Science* **200**, 618–627 (1978).

[14] Bihr, T., Seifert, U. & Smith, A.-S. Nucleation of ligand-receptor domains in membrane adhesion. *Phys. Rev. Lett.* **109**, 258101 (2012).

[15] Reister, E., Bihr, T., Seifert, U. & Smith, A. S. Two intertwined facets of adherent membranes: membrane roughness and correlations between ligand-receptors bonds. *New J. Phys.* **13**, 25003 (2011).

[16] Smith, A.-S., Sengupta, K., Goennenwein, S., Seifert, U. & Sackmann, E. Force-induced growth of adhesion domains is controlled by receptor mobility. *Proc. Natl. Acad. Sci. U.S.A.* **105**, 6906–6911 (2008).

Part IV

Conclusion and Outlook

9 Conclusion

In this thesis, I investigated the effect of thermal fluctuations on the binding properties of membranes, especially in the context of specific adhesion. I presented solutions to a wide range of questions from contributions to a new experimental method measuring membrane fluctuations with an unprecedented resolution in time and space to simulation and theoretical understanding of mechanical membrane properties driving the growth of adhesion domains.

On the experimental level, I have demonstrated the importance of accounting for resolution limits of the experimental technique while measuring membrane fluctuations and, in parallel, presented a theoretical model to deduce the true membrane fluctuations from the measured ones (publication P1). This set of tools turned out to be the key for comparing membrane properties measured by different experimental techniques with different spatial and temporal resolution limits, e.g., comparing the novel technique DODS directly with RICM (publications P2 and P3). A nanometric vertical resolution of membrane fluctuations and an extraordinary temporal resolution of DODS, way below the characteristic time of membrane correlations, may turn DODS to the prospective standard technique measuring mechanical membrane properties of biological cells.

With the experimental techniques now available, the binding properties of biological and model membranes can be studied extensively. I contributed to the this field by first studying the limits of the harmonic approximation of the non-specific vesicle-substrate interaction (publication P1) and second by investigating specific membrane adhesion in great detail, from a single bond (publications P5 and P6) to infinite (publication P4) and finite domains (publications P7 and P8).

On the single bond level, I investigated the mutual interplay between

the membrane and the bond. On the one hand, the bond affects the mechanical static and dynamic properties of the membrane and, on the other hand, the membrane determines the binding kinetics and binding equilibrium of the bond. I showed that the effect of a permanent single bond on the static membrane properties can be homogenized in an effective potential. For the temporal correlations of a pinned membrane, I introduced a first order correction to the damping coefficients of the unbound membrane and found convincing agreement with simulations of the membrane fluctuations. For a stochastic single bond, the static and dynamic membrane properties are found by superposition of the findings for the unbound and the permanently bound membrane as well as a stochastic two-state process for association and dissociation of the bond. However, with a stochastic bond, the question of modelling the binding kinetics arises which I addressed in terms of reaction rates of the bond. On an almost molecular level, the instantaneous reactions rates, being a function the membrane and the receptor position, were constructed thermodynamically consistently, comparable to Arrhenius rates. By applying several levels of coarse-graining, I first recovered reaction rates that follow the form of phenomenologically introduced rates of Bell and Dembo, and second I obtained effective reaction rates that integrate both the membrane and the receptor fluctuations. These effective reaction rates allow for large scale simulations of domain growth in various situations.

With efficient simulations, I studied the growth of finite adhesion domains. I found first, for a vesicle adhering to a circular contact zone on the substrate, that dynamic spatial organisation of bonds can lead to crowding and the formation of adhesion domains in a ring-like structure. It is clear from analysis of the free energy landscape that a ring-like structure is not stable, however, due to crowding of the bonds, the growth dynamics is slowed down remarkably and the ring can exist for several minutes for a biological relevant system. Thus, speculations arise whether a cell might apply this type of non-regulated ring formation in, e.g., the initial stages of the formation of the immunological synapse. My second main result concerning finite adhesion domains exemplified for cadherins is that the adhesion properties depend strongly on the membrane parameters. I found, for instance, that the time until a stable nucleation is formed changes by several orders of magnitude if the fluctuation amplitude of the membrane changes by few nanometres. Moreover, the type of domain growth changes from multiple nucleations seeds to a single, radially growing domain. A cell might utilize this enormous sensitivity for initiating the adhesion process, which in its later stages will be regulated by the cell's biochemical network.

10 Outlook

The puzzles unravelled within this thesis may connect beyond the questions of specific or non-specific adhesion of model membranes to a broader range of cell interactions and cell mechanics. Describing cell mechanics by an interplay between membrane mechanics and mechanics of the cytoskeleton covers the picture of cell mechanics to a large extend. In a general scope, the biophysics of cell mechanics is nowadays on the edge of being applied in medical research. One famous example is the optical stretcher which deforms cells and, thus, gives insight into cell mechanics [159, 160]. Different cell types obey different cell mechanics due to different cell functions within the organism. Moreover, a metastasising cell embraces, typically, softer cell mechanics compared to a normal cell to maintain motility within the body. Consequently, measuring the "squeezability" of a cell with an optical stretcher is a possible tool to identify metastasising cells [161]. Each cell type is associated with its own cell mechanics and the mechanics of each individual cell of a specific type might express significant deviations from the mean values. Thus, especially for medical applications, large amounts of cells have to be analyzed and statistical analysis of the sample is a first step [160]. However, before this method may be used in medical detection further research on both, the experimental as well as the theoretical level, is required. Nevertheless, it exemplifies the progress of the whole field that approaches the edge of fundamental research to being applied beneficially for mankind.

The specific work within this thesis deepens our understanding of the importance of membrane properties, e.g., mean membrane distance or fluctuations, on cell interactions. One possible pathway of a cell to control interactions by physical means could be an active control of membrane fluctuations, e.g., by control of the osmotic pressure in the cell. Here, to

balance the osmotic pressure, water flows out of or into the cell, changing the reduced volume of the cell and, thus, the membrane fluctuations. However, experiments with microbeads pulling tethers from the cell membrane have shown that the cell has to have lipid reservoirs in or close to the biological membrane to keep the membrane tension at a constant [162, 163]. Nevertheless, if the cell has a mechanism to keep the membrane tension constant, it might have many regulatory mechanisms for mechanical membrane properties, too, and active control of cells to initiate or prohibit cellular interactions becomes realistic.

The mechanics of biological membranes are now well understood to increase, in a next step, the cell mechanics model beyond the membrane level. In recent years, the cell mechanics have been studied in a mean field approach [164] or on the molecular level [165]. However, how active forces connect the main players of cell mechanics, i.e., the cytoskeleton and the membrane, is poorly understood. The main source for active forces are molecular motors, which have been studied so far either for the cytoskeleton or attached to the membrane. In the next step, consequently the field of molecular motors connecting the cell membrane and the cytoskeleton is about to be tackled [166, 167]. Possibly, future models take into account the full membrane mechanics and the cytoskeleton and the field of active membrane fluctuations may be understood. In that spirit, the ever-since dream of mankind fabricating a man-made cell, at least mimicking the cell mechanics [168], becomes realistic by combining the cytoskeleton and the membrane.

List of Figures

Part V

Bibliography

Bibliography

[1] Fenz, S. F. & Sengupta, K. Giant vesicles as cell models. *Integr. Biol.* **4**, 982–995 (2012).

[2] Groves, J. T. Bending mechanics and molecular organization in biological membranes. *Annu. Rev. Phys. Chem.* **58**, 697–717 (2007).

[3] Fenz, S. F., Merkel, R. & Sengupta, K. Diffusion and intermembrane distance: Case study of avidin and e-cadherin mediated adhesion. *Langmuir* **25**, 1074–1085 (2009).

[4] Enderlein, J. Polymer dynamics, fluorescence correlation spectroscopy, and the limits of optical resolution. *Phys. Rev. Lett.* **108**, 108101 (2012).

[5] Hsieh, C.-L., Spindler, S., Ehrig, J. & Sandoghdar, V. Tracking single particles on supported lipid membranes: Multimobility diffusion and nanoscopic confinement. *J. Phys. Chem. B* **118**, 1545–1554 (2014). PMID: 24433014.

[6] Lipowsky, R. Remodeling of membrane compartments: some consequences of membrane fluidity. *Biol. Chem.* **395**, 253–274 (2014).

[7] Gov, N., Zilman, A. G. & Safran, S. Cytoskeleton confinement and tension of red blood cell membranes. *Phys. Rev. Lett.* **90**, 228101 (2003).

[8] Mizuno, D., Tardin, C., Schmidt, C. F. & MacKintosh, F. C. Nonequilibrium mechanics of active cytoskeletal networks. *Science* **315**, 370–373 (2007).

[9] Bischofs, I. B., Klein, F., Lehnert, D., Bastmeyer, M. & Schwarz, U. S. Filamentous network mechanics and active contractility determine cell and tissue shape. *Biophys. J.* **95**, 3488–3496 (2008).

[10] Sabass, B. & Schwarz, U. S. Modeling cytoskeletal flow over adhesion sites: competition between stochastic bond dynamics and intracellular relaxation. *J. Phys.: Condens. Matter* **22**, 194112 (2010).

[11] Toyota, T., Head, D. A., Schmidt, C. F. & Mizuno, D. Non-gaussian athermal fluctuations in active gels. *Soft Matter* **7**, 3234 (2011).

[12] Jülicher, F., Ajdari, A. & Prost, J. Modeling molecular motors. *Rev. Mod. Phys.* **69**, 1269 (1997).

[13] Nan, X., Sims, P. A., Chen, P. & Xie, X. S. Observation of individual microtubule motor steps in living cells with endocytosed quantum dots. *J. Phys. Chem. B* **109**, 24220–24224 (2005).

[14] Klumpp, S. & Lipowsky, R. Cooperative cargo transport by several molecular motors. *Proc. Natl. Acad. Sci. U. S. A.* **102**, 17284–17289 (2005).

[15] Koenderink, G. H. *et al.* An active biopolymer network controlled by molecular motors. *Proc. Natl. Acad. Sci. U. S. A.* **106**, 15192–15197 (2009).

[16] Nelson, S. R., Trybus, K. M. & Warshaw, D. M. Motor coupling through lipid membranes enhances transport velocities for ensembles of myosin va. *Proc. Natl. Acad. Sci. U. S. A.* **111**, E3986–E3995 (2014).

[17] Klumpp, S., Keller, C., Berger, F. & Lipowsky, R. Molecular motors: Cooperative phenomena of multiple molecular motors. In *Multiscale Modeling in Biomechanics and Mechanobiology*, 27–61 (Springer, 2015). URL `http://www.mpikg.mpg.de/rl/P/archive/383.pdf`.

[18] Toyabe, S. *et al.* Nonequilibrium energetics of a single f 1-atpase molecule. *Phys. Rev. Lett.* **104**, 198103 (2010).

[19] Zimmermann, E. & Seifert, U. Effective rates from thermodynamically consistent coarse-graining of models for molecular motors with probe particles. *Phys. Rev. E* **91**, 022709 (2015).

[20] Grakoui, A. *et al.* The immunological synapse: a molecular machine controlling t cell activation. *Science* **285**, 221–227 (1999).

[21] Kaizuka, Y., Douglass, A. D., Varma, R., Dustin, M. L. & Vale, R. D. Mechanisms for segregating T cell receptor and adhesion molecules during immunological synapse formation in jurkat T cells. *Proc. Nat. Acad. Sci. U.S.A.* **104**, 20296–20301 (2007).

[22] Huppa, J. B. *et al.* TCR–peptide–MHC interactions in situ show accelerated kinetics and increased affinity. *Nature* **463**, 963 (2010).

[23] Dustin, M. L., Chakraborty, A. K. & Shaw, A. S. Understanding the structure and function of the immunological synapse. *Cold Spring Harbor perspectives in biology* **2**, a002311 (2010).

[24] Dustin, M. L. & Groves, J. T. Receptor signaling clusters in the immune synapse. *Ann. Rev. Biophys.* **41**, 543 (2012).

[25] Dustin, M. L. What counts in the immunological synapse? *Mol. Cell* **54**, 255–262 (2014).

[26] Dillard, P., Varma, R., Sengupta, K. & Limozin, L. Ligand-mediated friction determines morphodynamics of spreading t cells. *Biophys. J.* **107**, 2629–2638 (2014).

[27] Biswas, K. H. *et al.* E-cadherin junction formation involves an active kinetic nucleation process. *Proc. Natl. Acad. Sci. U. S. A.* **112**, 10932–10937 (2015).

[28] Lipowsky, R. The conformation of membranes. *Nature* **349**, 475–481 (1991).

[29] Lipowsky, R. Generic interactions of flexible membranes. In Lipowsky, R. & Sackmann, E. (eds.) *Structure and dynamics of membranes*, chap. 11, 521–602 (Elsevier, 1995).

[30] Seifert, U. Configuratios of fluid membranes and vesicles. *Adv. Phys.* **46**, 13–137 (1997).

[31] Miao, L., Seifert, U., Wortis, M. & H.-G.Döbereiner. Budding transitions of fluid-bilayer vesicles: The effect of area-difference elasticity. *Phys. Rev. E* **49**, 5389–5407 (1994).

[32] Auth, T. & Gompper, G. Budding and vesiculation induced by conical membrane inclusions. *Phys. Rev. E* **80**, 031901 (2009).

[33] Šarić, A. & Cacciuto, A. Self-assembly of nanoparticles adsorbed on fluid and elastic membranes. *Soft Matter* **9**, 6677 (2013).

[34] Dasgupta, S., Auth, T. & Gompper, G. Wrapping of ellipsoidal nanoparticles by fluid membranes. *Soft Matter* **9**, 5473–5482 (2013).

[35] Boulbitch, A., Guttenberg, Z. & Sackmann, E. Kinetics of membrane adhesion mediated by ligand–receptor interaction studied with a biomimetic system. *Biophys. J.* **81**, 2743–2751 (2001).

[36] Gao, H., Shi, W. & Freund, L. B. Mechanics of receptor-mediated endocytosis. *Proc. Natl. Acad. Sci. U. S. A.* **102**, 27 (2005).

[37] Shenoy, V. B. & Freund, L. B. Growth and shape stability of a biological membrane adhesion complex in the diffusion-mediated regime. *Proc. Natl. Acad. Sci. U. S. A.* **102**, 9 (2005).

[38] Alberts, B. *et al. Molecular Biology of the Cell* (Garland Science, Taylor & Francis Group, LLC, 2007), 5th edn.

[39] Israelachvili, J. N., Marčelja, S. & Horn, R. G. Physical principles of membrane organization. *Q. Rev. Biophys.* **13**, 121–200 (1980).

[40] Phillips, R., Kondev, J. & Theriot, J. *Physical Biology of the Cell* (Garland Science, 2008).

[41] Singer, S. J. & Nicolson, G. L. The fluid mosaic model of the structure of cell membranes. *Science* **175**, 720–731 (1972).

[42] Engelman, D. Membranes are more mosaic than fluid. *Nature* **438**, 578–580 (2005).

[43] Takamori, S. *et al.* Molecular anatomy of a trafficking organelle. *Cell* **127**, 831–846 (2006).

[44] Schrödinger, E. *What is life?: With mind and matter and autobiographical sketches* (Cambridge University Press, 1992).

[45] Smith, A.-S. Physics challenged by cells. *Nat. Phys.* **6**, 726–729 (2010).

[46] Lewis, B. A. & Engelman, D. M. Lipid bilayer thickness varies linearly with acyl chain length in fluid phosphatidylcholine vesicles. *J. Mol. Biol.* **166**, 211–217 (1983).

[47] Brochard, F. & Lennon, J. F. Frequency spectrum of the flicker phenomenon in erythrocytes. *J. Phys. France* **36**, 11 (1975).

[48] Helfrich, W. Elastic properties of lipid bilayers: Theory and possible experiments. *Z. Naturforsch., C: J. Biosci.* **28**, 693–703 (1973).

[49] Edidin, M. Lipids on the frontier: a century of cell-membrane bilayers. *Nat. Rev. Mol. Cell Biol.* **4**, 414–418 (2003).

[50] Brown, F. L. H. Elastic modeling of biomembranes and lipid bilayers. *Annu. Rev. Phys. Chem.* **59**, 685–712 (2008).

[51] Deserno, M. Mesoscopic membrane physics: Concepts, simulations, and selected applications. *Macromol. Rapid Commun.* **30**, 752–771 (2009).

[52] Tanaka, M. & Sackmann, E. Polymer-supported membranes as models of the cell surface. *Nature* **437**, 656–663 (2005).

[53] Liu, A. P. & Fletcher, D. A. Biology under construction: in vitro reconstitution of cellular function. *Nat. Rev. Mol. Cell Biol.* **10**, 644 (2009).

[54] Sackmann, E. & Smith, A.-S. Physics of cell adhesion: some lessons from cell-mimetic systems. *Soft Matter* **10**, 1644 (2014).

[55] Sackmann, E. Supported membranes: Scientific and practical applications. *Science* **271**, 43–48 (1996).

[56] Curtis, A. S. G. The mechanism of adhesion of cells to glass: A study by interference reflection microscopy. *J. Cell Biol.* **20**, 199–215 (1964).

[57] Limozin, L. & Sengupta, K. Quantitative reflection interference contrast microscopy (RICM) in soft matter and cell adhesion. *ChemPhysChem* **10**, 2752–2768 (2009).

[58] Filler, T. J. & Peuker, E. T. Reflection contrast microscopy (rcm): a forgotten technique? *J. Pathol.* **190**, 635–638 (2000).

[59] Schilling, J., Sengupta, K., Goennenwein, S., Bausch, A. & Sackmann, E. Absolute interfacial distance measurements by dual-wavelength reflection interference contrast microscopy. *Phys. Rev. E* **69**, 021901 (2004).

[60] Monzel, C., Fenz, S. F., Giesen, M., Merkel, R. & Sengupta, K. Mapping fluctuations in biomembranes adhered to micropatterns. *Soft Matter* **8**, 6128–6138 (2012).

[61] Browicz, T. Weitere Beobachtungen über Bewegungsphänomene an Roten Blutkörperchen in pathologischen Zuständen. *Zbl Med. Wissen* **28**, 625–627 (1890).

[62] Canham, P. The minimum energy of bending as a possible explanation of the biconcave shape of the human red blood cell. *J. Theor. Biol.* **26**, 61–81 (1970).

[63] Helfrich, W. Steric interaction of fluid membranes in multilayer systems. *Z. Naturforsch., A: Phys. Sci.* **33**, 305 (1978).

[64] Deserno, M. Fluid lipid membranes: From differential geometry to curvature stresses. *Chem. Phys. Lipids* **185**, 11 (2014).

[65] Seifert, U. The concept of effective tension for fluctuating vesicles. *Z. Phys. B-Condens. Mat.* **97**, 299–309 (1995).

[66] Schmid, F. Are stress-free membranes really "tensionless"? *Europhys. Lett.* **95**, 28008 (2011).

[67] Fournier, J.-B. Comment on "are stress-free membranes really "tensionless"?" by schmid f. *Europhys. Lett.* **97**, 18001 (2012).

[68] Schmid, F. Reply to the comment by j.-b. fournier. *Europhys. Lett.* **97**, 18002 (2012).

[69] Bassereau, P., Sorre, B. & Lévy, A. Bending lipid membranes: Experiments after w. helfrich's model. *Adv. Colloid Interfac.* **208**, 47–57 (2014).

[70] Pécréaux, J., Döbereiner, H.-G., Prost, J., Joanny, J.-F. & Bassereau, P. Refined contour analysis of giant unilamellar vesicles. *Eur. Phys. J. E* **13**, 277–290 (2004).

[71] Rädler, J. O., Feder, T. J., Strey, H. H. & Sackmann, E. Fluctuation analysis of tension-controlled undulation forces between giant vesicles and solid substrates. *Phys. Rev. E* **51**, 4526–4536 (1995).

[72] Schmid, F. Fluctuations in lipid bilayers: Are they understood? *Biophys. Rev. Lett.* **8**, 1–20 (2013).

[73] Seifert, U., Berndl, K. & Lipowsky, R. Shape transformations of vesicles: Phase diagram for spontaneous-curvature and bilayer-coupling models. *Phys. Rev. A* **44**, 1182–1202 (1991).

[74] Jarić, M., Seifert, U., Wintz, W. & Wortis, M. Vesicular instabilities: The prolate-to-oblate transition and other shape instabilities of fluid bilayer membranes. *Phys. Rev. E* **52**, 6623 (1995).

[75] Ziherl, P. & Svetina, S. Nonaxisymmetric phospholipid vesicles: Rackets, boomerangs, and starfish. *EPL* **70**, 690 (2005).

[76] Schneider, M. B., Jenkins, J. T. & Webb, W. W. Thermal fluctuations of large quasi-spherical bimolecular phospholipid vesicles. *J. Phys. France* **45**, 1457–1472 (1984).

[77] Milner, S. T. & Safran, S. A. Dynamical fluctuations of droplet microemulsions and vesicles. *Phys. Rev. A* **36**, 4371 (1987).

[78] Gompper, G. & Kroll, D. M. Steric interactions in multimembrane systems: a monte carlo study. *Europhys. Lett.* **9**, 59 (1989).

[79] Lipowsky, R. & Zielinska, B. Binding and unbinding of lipid membranes: A monte carlo study. *Phys. Rev. Lett.* **62**, 1572 (1989).

[80] Netz, R. R. & Lipowsky, R. Stacks of fluid membranes under pressure and tension. *Europhys. Lett.* **29**, 345–350 (1995).

[81] Bachmann, M., Kleinert, H. & Pelster, A. Strong-coupling calculation of fluctuation pressure of a membrane between walls. *Phys. Lett. A* **261**, 127–133 (1999).

[82] Netz, R. R. Complete unbinding of fluid membranes in the presence of short-ranged forces. *Phys. Rev. E* **51:3**, 2286–2294 (1995).

[83] Weikl, T. R. & Lipowsky, R. Unbinding transitions and phase separation of multicomponent membranes. *Phys. Rev. E* **62**, 1 (2000).

[84] Komura, S. & Andelman, D. Adhesion-induced lateral phase separation in membranes. *Eur. Phys. J. E* **3**, 259–271 (2000).

[85] Breidenich, M., Netz, R. R. & Lipowsky, R. The shape of polymer-decorated membranes. *Europhys. Lett.* **49**, 431–437 (2000).

[86] Auth, T. & Gompper, G. Fluctuation spectrum of membranes with anchored linear and star polymers. *Phys. Rev. E* **72**, 031904 (2005).

[87] Lipowsky, R. & Seifert, U. Adhesion of membranes: a theroetical perspective. *Langmuir* **7**, 1867–1873 (1991).

[88] Weikl, T. R., Andelman, D., Komura, S. & Lipowsky, R. Adhesion of membranes with competing specific and generic interactions. *Eur. Phys. J. E* **8**, 59–66 (2002).

[89] Smirnova, Y. G., Marrink, S.-J., Lipowsky, R. & Knecht, V. Solvent-exposed tails as prestalk transition states for membrane fusion at low hydration. *J. Am. Chem. Soc.* **132**, 6710–6718 (2010).

[90] Yang, K. & Ma, Y.-Q. Computer simulations of fusion, fission and shape deformation in lipid membranes. *Soft Matter* **8**, 606–618 (2012).

[91] Venable, R. M., Zhang, Y., Hardy, B. J. & Pastor, R. W. Molecular dynamics simulations of a lipid bilayer and of hexadecane: an investigation of membrane fluidity. *Science* **262**, 223–226 (1993).

[92] Noguchi, H. Membrane simulation models from nanometer to micrometer scale. *J. Phys. Soc. Jap.* **78**, 041007 (2009).

[93] Neder, J., West, B., Nielaba, P. & Schmid, F. Coarse-grained simulations of membranes under tension. *J. Chem. Phys.* **132**, 115101 (2010).

[94] Müller, M. Studying amphiphilic self-assembly with soft coarse-grained models. *J. Stat. Phys.* **145**, 967–1016 (2011).

[95] Schneck, E., Sedlmeier, F. & Netz, R. R. Hydration repulsion between biomembranes results from an interplay of dehydration and depolarization. *Proc. Natl. Acad. Sci. U. S. A.* **109**, 14405–14409 (2012).

[96] Lyman, E. & Patel, S. Molecular dynamics of lipid bilayers. *Liposomes, Lipid Bilayers and Model Membranes: From Basic Research to Application* 69 (2014).

[97] Evans, E. A. & Parsegian, V. A. Thermal-mechanical fluctuations enhance repulsion between bimolecular layers. *Proc. Natl. Acad. Sci. U. S. A.* **83**, 7132 (1986).

[98] Pincus, P., Joanny, J.-F. & Andelman, D. Electrostatic interactions, curvature elasticity, and steric repulsion in multimembrane systems. *Europhys. Lett.* **11**, 763 (1990).

[99] Israelachvili, J. N. *Intermolecular and Surface Forces* (Academic Press, 1992), 2. edn.

[100] Parsegian, A. *Van Der Waals Forces* (Cambridge University Press, 2006).

[101] Mecke, K. R., Charitat, T. & Graner, F. Fluctuating lipid bilayer in an arbitrary potential: theory and experimental determination of bending rigidity. *Langmuir* **19**, 2080–2087 (2003).

[102] Speck, T., Reister, E. & Seifert, U. Specific adhesion of membranes: Mapping to an effective bond lattice gas. *Phys. Rev. E* **82**, 021923 (2010).

[103] Seifert, U. Dynamics of a bound membrane. *Phys. Rev. E* **49**, 3124–3127 (1994).

[104] Geiger, B., Spatz, J. P. & Bershadsky, A. D. Environmental sensing through focal adhesion. *Nat. Rev. Mol. Cell Biol.* **10**, 21 (2009).

[105] Cavalcanti-Adam, E. A. *et al.* Cell spreading and focal adhesion dynamics are regulated by spacing of integrin ligands. *Biophys. J.* **92**, 2964–2974 (2007).

[106] Bruinsma, R., Behrisch, A. & Sackmann, E. Adhesive switching of membranes: Experiment and theory. *Phys. Rev. E* **61**, 4253–4267 (2000).

[107] Sengupta, K. & Limozin, L. Adhesion of soft membranes controlled by tension and interfacial polymers. *Phys. Rev. Lett.* **104**, 088101 (2010).

[108] Sackmann, E. & Bruinsma, R. Cell adhesion as wetting transition? *ChemPhysChem* **3**, 262–269 (2002).

[109] Bihr, T., Seifert, U. & Smith, A.-S. Multiscale approaches to protein-mediated interactions between membranes—relating microscopic and macroscopic dynamics in radially growing adhesions. *New J. Phys.* **17**, 083016 (2015).

[110] Bongrand, P. Ligand-receptor interactions. *Rep. Prog. Phys.* **62**, 921 (1999).

[111] Bell, G. I., Dembo, M. & Bongrand, P. Cell adhesion. competition between nonspecific repulsion and specific bonding. *Biophys. J.* **45**, 1051 (1984).

[112] Wu, Y., Vendome, J., Shapiro, L., Ben-Shaul, A. & Honig, B. Transforming binding affinities from three dimensions to two with application to cadherin clustering. *Nature* **475**, 510–513 (2011).

[113] Bihr, T. *et al.* Association rates of membrane-coupled cell adhesion molecules. *Biophys. J.* **107**, L33–L36 (2014).

[114] Smith, A.-S. & Seifert, U. Vesicles as a model for controlled (de-)adhesion of cells: a thermodynamic approach. *Soft Matter* **3**, 275–289 (2007).

[115] Weikl, T. R., Asfaw, M., Krobath, H., Rózycki, B. & Lipowsky, R. Adhesion of membranes via receptor–ligand complexes: Domain formation, binding cooperativity, and active processes. *Soft Matter* **5**, 3213–3224 (2009).

[116] Benoit, M., Gabriel, D., Gerisch, G. & Gaub, H. E. Discrete interactions in cell adhesion measured by single-molecule force spectroscopy. *Nat. Cell Biol.* **2**, 313–317 (2000).

[117] Lee, G. U., Kidwell, D. A. & Colton, R. J. Sensing discrete streptavidin-biotin interactions with atomic force microscopy. *Langmuir* **10**, 354–357 (1994).

[118] Florin, E. L., Moy, V. T. & Gaub, H. E. Adhesion forces between individual ligand-receptor pairs. *Science* **264**, 415–417 (1994).

[119] Moy, V. T., Florin, E.-L. & Gaub, H. E. Intermolecular forces and energies between ligands and receptors. *Science* **266**, 257–259 (1994).

[120] Baumgartner, W. *et al.* Cadherin interaction probed by atomic force microscopy. *Proc. Natl. Acad. Sci. U. S. A.* **97**, 4005–4010 (2000).

[121] Lorenz, B. *et al.* Model system for cell adhesion mediated by weak carbohydrate−carbohydrate interactions. *J. Am. Chem. Soc.* **134**, 3326–3329 (2012).

[122] Neuman, K. C. & Nagy, A. Single-molecule force spectroscopy: optical tweezers, magnetic tweezers and atomic force microscopy. *Nat. Methods* **5**, 491–505 (2008).

[123] Dufrêne, Y. F. *et al.* Five challenges to bringing single-molecule force spectroscopy into living cells. *Nat. Methods* **8**, 123–127 (2011).

[124] Smith, S. B., Finzi, L. & Bustamante, C. Direct mechanical measurements of the elasticity of single dna molecules by using magnetic beads. *Science* **258**, 1122–1126 (1992).

[125] Essevaz-Roulet, B., Bockelmann, U. & Heslot, F. Mechanical separation of the complementary strands of dna. *Proc. Natl. Acad. Sci. U. S. A.* **94**, 11935–11940 (1997).

[126] Woodside, M. T. *et al.* Nanomechanical measurements of the sequence-dependent folding landscapes of single nucleic acid hairpins. *Proc. Natl. Acad. Sci. U. S. A.* **103**, 6190–6195 (2006).

[127] Huguet, J. M. *et al.* Single-molecule derivation of salt dependent base-pair free energies in dna. *Proc. Natl. Acad. Sci. U. S. A.* **107**, 15431–15436 (2010).

[128] Dieterich, E., Camunas-Soler, J., Ribezzi-Crivellari, M., Seifert, U. & Ritort, F. Single-molecule measurement of the effective temperature in non-equilibrium steady states. *Nat. Phys.* (2015).

[129] Clausen-Schaumann, H., Seitz, M., Krautbauer, R. & Gaub, H. E. Force spectroscopy with single bio-molecules. *Curr. Opin. Chem. Biol.* **4**, 524–530 (2000).

[130] Bruinsma, R., Goulian, M. & Pincus, P. Self-assambly of membrane junctions. *Biophys. J.* **67**, 746–750 (1994).

[131] Bihr, T., Seifert, U. & Smith, A.-S. Nucleation of ligand-receptor domains in membrane adhesion. *Phys. Rev. Lett.* **109**, 258101 (2012).

[132] Betz, T., Lenz, M., Joanny, J.-F. & Sykes, C. Atp-dependent mechanics of red blood cells. *Proc. Natl. Acad. Sci. U. S. A.* **106**, 15320–15325 (2009).

[133] Betz, T. & Sykes, C. Time resolved membrane fluctuation spectroscopy. *Soft Matter* **8**, 5317–5326 (2012).

[134] Gov, N. S. & Safran, S. A. Red blood cell membrane fluctuations and shape controlled by atp-induced cytoskeletal defects. *Biophys. J.* **88**, 1859–1874 (2005).

[135] Lin, L. C.-L. & Brown, F. L. H. Dynamic simulations of membranes with cytoskeletal interactions. *Phys. Rev. E* **72**, 011910 (2005).

[136] Fournier, J.-B., Lacoste, D. & Raphaël, E. Fluctuation spectrum of fluid membranes coupled to an elastic meshwork: jump of the effective surface tension at the mesh size. *Phys. Rev. Lett.* **92**, 018102 (2004).

[137] Merath, R.-J. & Seifert, U. Nonmonotonic fluctuation spectra of membranes pinned or tethered discretely to a substrate. *Phys. Rev. E* **73**, 010401 (2006).

[138] Bell, G. Models for the specific adhesion of cells to cells. *Science* **200**, 618–627 (1978).

[139] Alón, R., Hammer, D. A. & Springer, T. A. Lifetime of the p-selectin-carbohydrate bond and its response to tensile force in hydrodynamic flow. *Nature* **374**, 539–542 (1995).

[140] Merkel, R., Nassoy, P., Leung, A., Ritchie, K. & Evans, E. Energy landscapes of receptor–ligand bonds explored with dynamic force spectroscopy. *Nature* **397**, 50–53 (1999).

[141] Chen, S. & Springer, T. A. Selectin receptor–ligand bonds: Formation limited by shear rate and dissociation governed by the bell model. *Proc. Natl. Acad. Sci. U. S. A.* **98**, 950–955 (2001).

[142] Thomas, W. E., Vogel, V. & Sokurenko, E. Biophysics of catch bonds. *Annu. Rev. Biophys.* **37** (2008).

[143] Hertig, S. & Vogel, V. Catch bonds. *Curr. Biol.* **22**, R823 – R825 (2012).

[144] Dembo, M., Torney, D., Saxman, K. & Hammer, D. The reaction-limited kinetics of membrane-to-surface adhesion and detachment. *P. Roy. Soc. Lond. B Bio.* **234**, 55–83 (1988).

[145] Marshall, B. T. *et al.* Direct observation of catch bonds involving cell-adhesion molecules. *Nature* **423**, 190–193 (2003).

[146] Manibog, K., Li, H., Rakshit, S. & Sivasankar, S. Resolving the molecular mechanism of cadherin catch bond formation. *Nat. Commun.* **5** (2014).

[147] Rakshit, S., Zhang, Y., Manibog, K., Shafraz, O. & Sivasankar, S. Ideal, catch, and slip bonds in cadherin adhesion. *Proc. Natl. Acad. Sci. U. S. A.* **109**, 18815–18820 (2012).

[148] Atkins, P. & De Paula, J. Atkins' physical chemistry. *Oxford Univ. Press, Oxford, ed* **7** (2002).

[149] Fenz, S. F. *et al.* Switching from ultraweak to strong adhesion. *Adv. Mater.* **XX**, 1–5 (2011).

[150] Speck, T. Effective free energy for pinned membranes. *Phys. Rev. E* **83**, 050901 (2011).

[151] Speck, T. & Vink, R. L. C. Random pinning limits the size of membrane adhesion domains. *Phys. Rev. E* **86**, 031923 (2012).

[152] Cavalcanti-Adam, E. A. & Spatz, J. P. Receptor clustering control and associated force sensing by surface patterning: when force matters. *Nanomedicine-UK* **10**, 681–684 (2015).

[153] Weikl, T. R. & Lipowsky, R. Pattern formation during t-cell adhesion. *Biophys. J.* **87**, 3665–3678 (2004).

[154] Farago, O. Statistical thermodynamics of adhesion points in supported membranes. In Iglič, A. (ed.) *Advances in Planar Lipid Bilayers and Liposomes*, vol. 14, chap. 5, 129–155 (Elsevier, 2011).

[155] Weil, N. & Farago, O. Entropic attraction of adhesion bonds toward cell boundaries. *Phys. Rev. E* **84**, 051907 (2011).

[156] Noguchi, H. Entropy-driven aggregation in multilamellar membranes. *Europhys. Lett.* **102**, 68001 (2013).

[157] Avrami, M. Kinetics of phase change. II transformation-time relations for random distribution of nuclei. *J. Chem. Phys.* **8**, 212–224 (1940). URL `http://link.aip.org/link/?JCP/8/212/1`.

[158] Krapivsky, P. L., Redner, S. & Ben-Naim, E. *A kinetic view of statistical physics* (Cambridge University Press, 2010).

[159] Guck, J. *et al.* The optical stretcher: a novel laser tool to micromanipulate cells. *Biophys. K.* **81**, 767–784 (2001).

[160] Delabre, U. *et al.* Deformation of phospholipid vesicles in an optical stretcher. *Soft Matter* **11**, 6075–6088 (2015).

[161] Otto, O. *et al.* Real-time deformability cytometry: on-the-fly cell mechanical phenotyping. *Nat. Meth.* (2015).

[162] Raucher, D. & Sheetz, M. P. Characteristics of a membrane reservoir buffering membrane tension. *Biophys. J.* **77**, 1992 – 2002 (1999).

[163] Morris, C. E. & Homann, U. Cell surface area regulation and membrane tension. *J. Membrane Biol.* **179**, 79–102 (2001).

[164] Marchetti, M. C. *et al.* Hydrodynamics of soft active matter. *Rev. Mod. Phys.* **85**, 1143–1189 (2013).

[165] Köster, S., Weitz, D. A., Goldman, R. D., Aebi, U. & Herrmann, H. Intermediate filament mechanics in vitro and in the cell: from coiled coils to filaments, fibers and networks. *Curr. Opin. Cell Biol.* **32**, 82–91 (2015).

[166] Sakai, T., Umeki, N., Ikebe, R. & Ikebe, M. Cargo binding activates myosin viia motor function in cells. *Proc. Natl. Acad. Sci. U. S. A.* **108**, 7028–7033 (2011).

[167] Umeki, N. *et al.* Phospholipid-dependent regulation of the motor activity of myosin x. *Nat. Struct. Mol. Biol.* **18**, 783–788 (2011).

[168] Frohnmayer, J. P. *et al.* Minimal synthetic cells to study integrin-mediated adhesion. *Angew. Chem. Int. Ed.* **54**, 12472–12478 (2015).

Part VI

Miscellaneous

Curriculum vitae

DANIEL SCHMIDT

Personal details

Date of birth	21 October 1985
Place of birth	Stuttgart, Germany
Nationality	German

Educational

since 10/2011	**PhD studies** in theoretical physics *Friedrich-Alexander Universität Erlangen-Nürnberg*, Germany Member of the Research Training Group 1962 „Dynamic Interactions at Biological Membranes – from Single Molecules to Tissue“ Thesis: “Effect of thermal fluctuations on the binding properties of biological membranes” Supervisors: Prof. Dr. A.-S. Smith, FAU Erlangen-Nürnberg, Germany Prof. Dr. U. Seifert, Universität Stuttgart, Germany
10/2006-07/2011	**Diplom** in Physics, *Universität Stuttgart*, Germany Thesis: “Fluctuation effects for bound membranes” Supervisor: Prof. Dr. U. Seifert, Universität Stuttgart, Germany
10/2005-09/2006	part-time studies of Physics at *TU Kaiserslautern*, Germany FiPS (Früheinstieg ins Physikstudium)
07/1999-08/2005	**Abitur** (German university entrance qualification) *Solitude-Gymnasium* (grammar school), Stuttgart, Germany
09/1996-06/1999	*Eschbach-Gymnasium* (grammar school), Stuttgart, Germany
09/1992-08/1996	*Herbert-Hoover-Schule* (primary school), Stuttgart, Germany

Additional experience

08/2005-04/2006	Social service (in lieu of military service) in a hospital

Language skills

German (mother tongue)
English (fluent)
French (basics)
Russian (basics)

List of publications (chronologically)

- **D. Schmidt**, T. Bihr, U. Seifert, and A.-S. Smith, "Coexistence of dilute and densely packed domains of ligand-receptor bonds in membrane adhesion", *EPL* **99**, 38003 (2012).
(publication P4)

- **D. Schmidt**, C. Monzel, T. Bihr, R. Merkel, U. Seifert, K. Sengupta, and A.-S. Smith, "Signature of a Nonharmonic Potential as Revealed from a Consistent Shape and Fluctuation Analysis of an Adherent Membrane", *Phys. Rev. X* **4**, 021023 (2014).
(publication P1)

- **D. Schmidt**, T. Bihr, S. Fenz, R. Merkel, U. Seifert, K. Sengupta, and A.-S. Smith, "Crowding of receptors induces ring-like adhesions in model membranes", *BBA: Mol. Cell Res.* **1894**, 2984-2991 (2015).
(publication P7)

- C. Monzel, **D. Schmidt**, C. Kleusch, D. Kirchenbüchler, U. Seifert, A.-S. Smith, K. Sengupta, and R. Merkel, "Measuring Fast Stochastic Displacements of Bio-Membranes with Dynamic Optical Displacement Spectroscopy", *Nat. Commun.*, **6**, 8162 (2015).
(publication P2)

- C. Monzel, **D. Schmidt**, U. Seifert, A.-S. Smith, R. Merkel, and K. Sengupta, "Nanometric Thermal Fluctuations of Weakly Confined Bio-membranes Measured with Microsecond Time-Resolution", *Soft Matter*, accepted (2016).
(publication P3)

- T. Bihr, S. Fenz, **D. Schmidt**, R. Merkel, K. Sengupta, U. Seifert, and A.-S. Smith, "Membrane promoted cis-interactions influence nucleation and growth of cadherin adhesions", in preparation (2016). (publication P8)

- **D. Schmidt**, U. Seifert, and A.-S. Smith, "A model for spectral properties of a pinned membrane", in preparation (2016). (publication P5)

- **D. Schmidt**, U. Seifert, and A.-S. Smith, "Spectral properties of a stochastically bound membrane", in preparation (2016). (publication P6)

List of conferences (chronologically)

1. **PhysCell2009** (1st of conference series) in Primošten, Croatia (09/2009)

2. D. Schmidt, U. Seifert, and A.-S. Smith, *Conformation of bonds in adhesion clusters*, **Spring meeting German Physical Society (DPG)**, Regensburg, Germany (03/2010, poster)

3. D. Schmidt, U. Seifert, and A.-S. Smith, *Distribution of ligand-receptor bonds in membrane adhesion clusters*, **467. WE-Hereaus-Seminar "Biophysics of Membrane Transformations"**, Bad Honnef, Germany (10/2010, poster)

4. D. Schmidt, U. Seifert, and A.-S. Smith, *Shape and fluctuations of a membrane pinned to a patterned substrate*, **Spring meeting German Physical Society (DPG)**, Dresden, Germany (03/2011, poster)

5. D. Schmidt, U. Seifert, and A.-S. Smith, *Shape and fluctuations of a membrane pinned to a patterned substrate*, **Young Researcher Day** of the Excellence Cluster: Engineering of Advanced Materials, Erlangen, Germany (07/2011, poster)

6. D. Schmidt, T. Bihr, U. Seifert, and A.-S. Smith, *Towards the understanding of bond organization in adhesion domains: Coexistence of the dilute and the dense packing*, **Spring meeting German Physical Society (DPG)**, Berlin, Germany (03/2012, talk)

7. D. Schmidt, T. Bihr, U. Seifert, and A.-S. Smith, *Towards the understanding of adhesion domains: Coexistence of the dilute and dense*

packing, **MaterialsScienceEngineering (MSE)**, Darmstadt, Germany (09/2012, talk)

8. D. Schmidt, T. Bihr, U. Seifert, and A.-S. Smith, *The puzzle of domain formation in vesicle adhesion*, **PhysCell2012** (2nd of conference series), Hyeres, France (09/2012)

9. D. Schmidt, U. Seifert, and A.-S. Smith, *Quantitative understanding of the nonspecific vesicle-substrate adhesion*, **Spring meeting German Physical Society (DPG)**, Regensburg, Germany (03/2013, talk)

10. D. Schmidt, U. Seifert, and A.-S. Smith, *Beyond the standard model for membrane-scaffold interactions as revealed by fluctuations*, **International Soft Matter Conference (ISMC)**, Rome, Italy (09/2013, poster)

11. D. Schmidt, U. Seifert, and A.-S. Smith, *Quantitative understanding of the nonspecific vesicle-substrate adhesion*, **Young Researcher Day** of the Excellence Cluster: Engineering of Advanced Materials (EAM), Erlangen, Germany (02/2014, talk)

12. D. Schmidt, T. Bihr, U. Seifert, and A.-S. Smith, *Modeling ring formation in cell adhesion*, **Spring meeting German Physical Society (DPG)**, Dresden, Germany (03/2014, talk)

13. D. Schmidt, T. Bihr, S. Fenz, R. Merkel, K. Sengupta, U. Seifert, and A.-S. Smith, *Reconstituting the immunological ring-like domain in adhesive liposomes*, **Biomembrane Days**, Berlin, Germany (09/2014, poster)

14. D. Schmidt, T. Bihr, S. F. Fenz, R. Merkel, K. Sengupta, U. Seifert, and A.-S. Smith, *Reconstituting the immunological ring-like domain in adhesive liposomes*, **Proteins & Nanoparticles @ Membranes (PAM)**, Jülich, Germany (10/2014, talk)

15. D. Schmidt, U. Seifert, and A.-S. Smith, *A microscopic model for the Red Blood Cell membrane: What can we learn from measuring membrane fluctuations?*, **Spring meeting German Physical Society (DPG)**, Berlin, Germany (03/2015, poster)

16. D. Schmidt, T. Bihr, S. F. Fenz, R. Merkel, K. Sengupta, U. Seifert, and A.-S. Smith, *The membrane as matchmaker for cadherin adhesion clusters*, **PhyBio International Workshop on Cell Motility**, Paris, France (04/2015, talk)

17. D. Schmidt, T. Bihr, S. F. Fenz, R. Merkel, K. Sengupta, U. Seifert, and A.-S. Smith, *Membranes as matchmaker for cadherin adhesions*, **PhysCell2015** (3rd of conference series), Bad Staffelstein, Germany (09/2015, poster)

18. D. Schmidt, T. Bihr, S. F. Fenz, R. Merkel, K. Sengupta, U. Seifert, and A.-S. Smith, *The Membrane as a matchmaker in the cell adhesion process*, **Spring meeting German Physical Society (DPG)**, Regensburg, Germany (03/2016, talk)

Articles in co-authorship

According to §10, Absatz (3) der Promotionsordnung der Universität Erlangen-Nürnberg and §6, Absatz (5) der Promotionsordnung für die Naturwissenschaftlichen Fakultät der Friedrich-Alexander-Universität Erlangen-Nürnberg it is necessary for scientific contributions in Co-authorship to declare unambiguously which part of such a contribution originate from the candidate. This has to be confirmed by the other co-authors. On the following pages, the respective documents for the publications P2, P3, and P8 can be found. In the other publications in this thesis, the author of this thesis is the first author.

Measuring Fast Stochastic Displacements of Bio-Membranes with Dynamic Optical Displacement Spectroscopy

Declaration The article in Chapter P2 of this thesis with the title "Measuring Fast Stochastic Displacements of Bio-Membranes with Dynamic Optical Displacement Spectroscopy", published in Nature Communications, was written with the collaboration of the author of this thesis (hereafter author).
The author was involved in developing the theoretical model and analyzed experimental data.

I hereby declare the correctness of the above statements.

C. Monzel — Cornelia Monzel
D. Schmidt — Daniel Schmidt
C. Kleusch — Christian Kleusch

David Kirchenbüchler — David Kirchenbüchler
U. Seifert — Udo Seifert
Ana-Sunčana Smith

Kheya Sengupta — Kheya Sengupta
Rudolf Merkel — Rudolf Merkel

Nanometric Thermal Fluctuations of Weakly Confined Biomembranes Measured with Microsecond Time-Resolution

Declaration The article in Chapter P3 of this thesis with the title "Nanometric Thermal Fluctuations of Weakly Confined Biomembranes Measured with Microsecond Time-Resolution" (hereafter article) published in Soft Matter was written with the collaboration of the author of this thesis (hereafter author).
The author was involved in developing the theoretical models and analyzed the experimental data. Furthermore, the author wrote parts of the article.

I hereby declare the correctness of the above statements.

Cornelia Monzel | Daniel Schmidt | Udo Seifert

Ana-Sunčana Smith | Kheya Sengupta | Rudolf Merkel

Membrane fluctuations mediate lateral interactions between bonds

Declaration The article in Chapter P8 of this thesis with the title "Membrane fluctuations mediate lateral interactions between bonds" submitted to a peer-reviewed journal was written with the collaboration of the author of this thesis (hereafter author).
The author participated in developing the theoretical model especially to link the membrane model to a model of harmonic springs. Moreover, the author analyzed experimental data to gain true membrane parameters which were described by the author in a chapter in the supporting information.

I hereby declare the correctness of the above statements.

Timo Bihr | Susanne Fenz | Daniel Schmidt

Rudolf Merkel | Kheya Sengupta

Udo Seifert | Ana-Sunčana Smith

Statuary declaration

Ehrenwörtliche Erklärung

Ich erkläre hiermit, dass ich diese Arbeit selbstständig verfasst und keine anderen als die angegebenen Quellen und Hilfsmittel verwendet habe.

Erlangen, den 11. Mai 2016

Daniel Schmidt